
Probabilistic Based Nonlinear Seismic Analysis of Nuclear Containment Vessel Structures with AAR

TASK 3-B

DECEMBER 2017

BY

VICTOR E. SAOUMA

MOHAMMAD AMIN HARIRI-ARDEBILI

University of Colorado, Boulder

NRC-HQ-60-14-G-0010: REPORTS

1-A: *Design of an AAR Prone Concrete Mix for Large Scale Testing*

1-B: *AAR Expansion; Effect of Reinforcement, Specimen Type, and Temperature*

1-C: *Effect of AAR on Shear Strength of Panels*

2: *Diagnosis & Prognosis of AAR in Existing Structures*

3-A: *Risk Based Assessment of the Effect of AAR on Shear Walls Strength*

3-B: *Probabilistic Based Nonlinear Seismic Analysis of Nuclear Containment Vessel Structures with AAR*

This page intentionally left blank.

Contents

1	Introduction	2
1.1	Challenges	2
1.2	Codes Philosophy	2
1.2.1	LRFD	3
1.2.2	Performance Base Earthquake Engineering (PBEE)	4
1.3	Complexities of a Nonlinear Analysis.	5
1.4	Inadequate Codes	6
I	Theory	9
2	Probabilistic Risk Evaluation	11
2.1	Introduction	11
2.2	Performance Based Earthquake Engineering	13
2.2.1	First Generation of PBEE	14
2.2.2	Second Generation of PBEE	15
2.3	Seismic Hazard Analysis	17
2.3.1	Location and Site Condition	18
2.3.1.1	Seismic Environment and Hazard	18
2.3.1.2	Site	18
2.3.1.3	Local Geotechnical Effects	19
2.3.2	Attenuation Relationships	19
2.3.3	Probabilistic vs. Deterministic Hazard Analysis	20
2.3.3.1	Deterministic Seismic Hazard Analysis	20
2.3.3.2	Probabilistic Seismic Hazard Analysis	20
2.3.4	Seismic Hazard Curves	20
2.3.5	Seismic Hazard De-aggregation	23
2.3.6	Ground motion Selecting and Scaling	23
2.3.6.1	Target Acceleration Response Spectra	23
2.3.6.2	Ground Motion Scaling Methods	24
2.3.6.3	Ground Motion Selection and Scaling	25
2.3.7	Potential Intensity measure Parameter	26
2.4	Sensitivity and Uncertainty Quantification	26
2.4.1	Analyses	27

2.4.1.1	Sensitivity	27
2.4.1.2	Uncertainty	28
2.4.2	Data Preparation	29
2.4.2.1	Sampling Techniques	29
2.4.2.2	Type of RV Correlation	30
2.5	Nonlinear Structural Analyses	31
2.5.1	Cloud Analysis	32
2.5.2	Incremental Dynamic Analysis	32
2.5.3	Multiple Stripe Analysis	34
2.5.4	Endurance Time Analysis	34
2.6	Capacity Functions	35
2.7	Damage Index	36
2.8	Fragility Analyses	38
2.8.1	Fundamentals	38
2.8.1.1	Fragility Curve <i>vs.</i> Surface	38
2.8.1.2	Fragility <i>vs.</i> Vulnerability <i>vs.</i> Hazard	39
2.8.1.3	Continuous Function <i>vs.</i> Discrete Matrix	40
2.8.1.4	Fragility in the Context of PBEE	41
2.8.1.5	Treatment of Collapse (Large Data Point)	42
2.8.2	Fragility Curve Determination	42
2.8.2.1	Empirical	42
2.8.2.2	Heuristic	42
2.8.2.3	Experimental	42
2.8.2.4	Hybrid	43
2.8.2.5	Analytical	43
2.8.2.5.1	Generalized Linear Models	43
2.8.2.5.2	Lognormal	44
2.8.2.5.2.1	IM-based Rule	45
2.8.2.5.2.2	EDP-based Rule	45
2.8.2.6	Analysis Techniques and Data Fitting	46
2.8.2.6.1	Incremental Dynamic Analysis (IDA)	46
2.8.2.6.2	Multiple Stripe Analysis (MSA)	48
3	Soil Structure Interaction	51
3.1	Deconvolution	51
3.1.1	Introduction	51
3.1.2	Fourier Transform	52
3.1.3	Butterworth Filter	52
3.1.4	Transfer Function	53
3.1.5	Algorithm	54
3.1.5.1	One-Dimensional	54
3.1.5.2	Three-Dimensional	55
3.1.5.3	Simplification	55
3.2	Soil Structure Interaction	56

3.2.1	Wave Equation	56
3.2.2	Lysmer Model	57
3.2.3	Other SSI Models	59
3.2.4	Miura-Saouma (MS) Model	60
3.2.4.1	Internal Virtual Work	62
3.2.4.2	External Virtual Work	63
3.2.4.2.1	Forces Caused by Velocity	63
3.2.4.2.2	Forces Caused by Displacements	64
3.2.5	Validation Problems	66
3.2.6	Viscous Boundary Conditions; Lysmer Model	69
3.2.6.1	Active/Flexible Boundary; Miura-Saouma	70
3.2.6.2	Finite Element Implementation	71
4	Alkali Silica reaction Modeling	77
4.1	Introduction	77
4.1.1	Life Extension	77
4.1.2	Reported Cases	77
4.2	Finite Element Modeling of AAR	80
4.2.1	Scale and Models	80
4.2.2	Overview of Coupled Chemo-Mechanical Models	81
4.2.3	Minimum Requirements for a “Modern” AAR Numerical Model	83
4.3	Author’s Model	84
4.3.1	Kinetics	85
4.3.1.1	Sensitivity to Temperature	86
4.3.1.2	Sensitivity to Integration Scheme	87
4.3.1.3	Sensitivity to Activation Energies	88
4.3.1.4	Sensitivity to Time	88
4.3.2	Retardation	88
4.3.2.1	Hydrostatic Compressive Stress	88
4.3.2.2	Role of Cracking	93
4.3.2.2.1	Tensile Macrocrack	93
4.3.2.2.2	Compressive Microcracks	94
4.3.3	Humidity	95
4.3.4	AAR Strain	96
4.3.4.1	Weights	97
4.3.4.2	AAR Linear Strains	100
4.3.4.3	Deterioration	100
4.3.5	Validation	100
II	Modeling	103
5	Science and Art of Finite Element Modeling	105
5.1	Modelling	105

5.1.1	Introduction	105
5.1.2	Tasks	105
5.1.2.1	Problem Definition	105
5.1.2.2	Mathematical Model	107
5.1.2.3	Finite Element Analyses	107
5.1.2.4	Final Evaluation	107
5.1.3	Key Considerations	107
5.1.3.1	Modeling	107
5.1.3.2	Finite Element Mesh	108
5.1.3.3	Loads and Boundary Conditions	109
5.1.3.4	Material Properties	110
5.1.3.5	Software Selection	112
5.1.4	Verification and Validation <i>vs.</i> Calibration	113
5.1.5	Expert Selection	115
5.1.6	Singularities	115
5.2	Some Theoretical Considerations	116
5.2.1	Material Nonlinearity	116
5.2.1.1	Explicit	117
5.2.1.2	Implicit	117
5.2.2	Fracture Mechanics of Concrete	118
5.2.2.1	Theoretical Considerations	118
5.2.2.2	Finite Element Modeling	120
5.2.2.2.1	Discrete Crack Model	120
5.2.2.2.2	Smeared Crack Model	122
5.2.3	Fragility Curves	123
5.3	Sensitivity Analyses	123
5.4	Uncertainty Analyses or Risk Informed Conditional Assessment	124
6	Computational Tools for Probabilistic Analyses	127
6.1	Introduction	127
6.2	isk rinformed rconditional rassessmentrProbabilistic rPerformance rAssessment rof rStructure- sProbabilistic Performance Assessment of Structures	127
6.3	Detailed Steps	129
6.3.1	P0.m	129
6.3.2	P1.m	129
6.3.3	P2.m	134
6.3.4	P3.m	134
6.3.5	P4.m	134
6.3.6	P5.m	136
7	Numerical Modeling for Seismic Analysis	139
7.1	Deconvolution	139
7.1.1	Example	139
7.2	Preliminary Considerations	140

7.2.1	Mass and Gravity	140
7.2.2	Two Step Analysis	140
7.2.3	wo tstep tanalysistLateral tRigid tBody tMotionLateral Rigid Body Motion	142
7.2.4	Rocking	143
7.2.4.1	ockingRFoundation RSupportFoundation Support	143
7.2.4.2	ockingRConcrete-Rock RInterfaceConcrete-Rock Interface	143
7.3	Modeling Soil Structure Interaction	145
7.3.1	ockingRSoil-StructureSoil-Structure	145
7.3.2	ockingRRock-RockRock-Rock	145
7.3.3	Model 1	146
7.3.4	Model 2	146
7.3.5	Model 3	146
7.3.6	Model 4	146
7.3.7	Model 5	146
7.3.8	Model 6	148
7.3.9	Model 7	148
7.3.10	Model 8	148
8	Modelling AAR	151
8.1	Introduction	151
8.2	Kinetics Related Variables	151
8.2.1	Temperatures	152
8.2.2	AR Amaterial ApropertiesALatency Aand Acharacteristic AtimesLatency and characteristic times	152
8.2.3	AR Amaterial ApropertiesAAactivation AenergiesActivation energies	152
8.3	AR Amaterial ApropertiesAAanalysis ATime AUnit A(ATU)Analysis Time Unit (ATU)	153
8.4	AAR; Numerical Modeling	154
III	Case Study	157
9	Problem Definition	159
9.1	Motivation	159
9.2	Preliminary Considerations	159
9.3	Geometry	160
9.4	Finite Element Model	161
9.5	Material Properties	161
9.6	Finite Element Mesh	164
9.7	Earthquake Characteristics	164
9.8	AAR Volumetric Expansion	166
9.9	uried bcontainerbIndex bPointsIndex Points	168
10	Results of Analyses	169
10.1	Introduction	169
10.2	Analyses	169

10.2.1 Static Analysis	169
10.2.2 Static + AAR Analysis	170
10.2.3 Static + Seismic Analysis	170
10.2.4 Static + AAR + Seismic	170
10.3 Impact of AAR on Seismic Response of a NCVS	171
10.3.1 Results	171
10.3.2 Observations	173
10.4 Conclusions	175
11 Conclusions	177
11.1 Summary	177
11.2 Recommendation for Future Work	177
References	179
Index	179
12 Acronyms	183

List of Figures

1.1	Probabilistic aspects of LRFD	4
2.1	Summary of the proposed method	12
2.2	Recommended minimum seismic performance design objectives for buildings	14
2.3	Conceptual description of first generation PBEE (WHITTAKER)	15
2.4	General framework of PEER PBEE methodology (Porter2003)	16
2.5	Comparison of ground motion selection and scaling for IBPA, SBPA and TBPA	17
2.6	Steps toward seismic hazard analysis of nuclear containment vessel structures	18
2.7	Sample of mean and fractile hazard curves	21
2.8	Ground motion annual rate of exceedance (Cornell1968).	22
2.9	Connection between Hazard curve and annual rate of ground motion exceedance	22
2.10	Sample seismic de-aggregation plots	23
2.11	Uniform seismic hazard spectra for Pine Flat dam	24
2.12	Different time-domain scaling of the ground motions	25
2.13	Sensitivity analysis using Tornado diagram	28
2.14	Sampling of a system with two RVs	30
2.15	Multivariate partial correlation matrix for fracture mechanics-based zero thickness joint element at the dam-foundation interface	31
2.16	Spatial correlation of fracture energy, G_f , at the dam-foundation interface area; three sample realization for each correlation length	31
2.17	Temporal correlation in concrete tensile strength, f_t , of an AAR-affected structure over the 100 years time period	32
2.18	Application of advanced nonlinear analysis techniques on concrete dams	33
2.19	Application of IDA on concrete dams	34
2.20	Characteristics of a sample ETAF (hariri2016new)	35
2.21	Schematic of ETA-based capacity function for arch dams (hariri2016new)	36
2.22	Relationships between a DI and two DVs	37
2.23	Comparison of seismic fragility, vulnerability and hazard curves	39
2.24	Different aspects of seismic fragility surfaces	40
2.25	Relationship between fragility curve and damage probability matrix	41
2.26	Link functions for binomial data and their relationship	44
2.27	Conceptual collapse fragility curves based on IDA method	48
2.28	Conceptual collapse fragility curves based on MSA method	50

3.1	Seismic Attenuation/Amplification (pires)	51
3.2	Deconvolution	52
3.3	Comparison of filters	53
3.4	Transfer function	53
3.5	Deconvolution applied in finite element analysis	54
3.6	Infinitesimal element subjected to elastic wave	56
3.7	Elastic waves in an infinite medium	58
3.8	Lysmer Modeling for Lateral Excitation	59
3.9	Viscous elements (dash-pots)	59
3.10	Conceptual Model	61
3.11	2D Idealization and Γ_x Plane	63
3.12	Selected results for 2D analyses with free boundaries; Crest accelerations, deformed shapes with contour lines of V_X and V_Y	66
3.13	Selected results for 2D Lysmer analyses; Crest accelerations, deformed shapes with contour lines of V_X and V_Y	67
3.14	Selected results for 2D Miura-Saouma analyses; Crest accelerations, deformed shapes with contour lines of V_X and V_Y	67
3.15	Selected results for 3D Lysmer analyses; Crest accelerations, accelerations at $h = 0, h/8, h/4, 3h/8, h/2, 5h/8, 3h/4, 7h/8$ and h ; deformed shapes with contour lines of V_X	67
3.16	Selected results for 3D Miura-Saouma analyses; Crest accelerations, accelerations at $h = 0, h/8, h/4, 3h/8, h/2, 5h/8, 3h/4, 7h/8$ and h ; deformed shapes with contour lines of V_X	68
3.17	Elastic waves in an infinite medium	69
3.18	Foundation Model, Radiating Flexible Foundation	70
3.19	Finite Element Discretization of the free field	72
3.20	Finite Element Discretization of Dam Foundation in Account of Free Field Velocities	72
3.21	Finite Element Discretization of the free field	73
3.22	Finite Element Discretization of the Corner free field	73
3.23	Finite Element Discretization of the Side free field	73
3.24	Finite Element Discretization of the Side free field, X Acceleration	74
3.25	Finite Element Discretization of the Side free field, Y Acceleration	74
3.26	Finite Element Discretization of the Side free field, Z Acceleration	74
3.27	Finite Element Discretization of the free field; Transfer of Velocities	75
3.28	Finite Element Discretization of the free field; Rock Foundation	75
3.29	Finite Element Discretization of the free field; Outline of Procedure	75
4.1	ASR in Seabrook nuclear power plant, (ML12199A300)	79
4.2	Concept of performance based earthquake engineering design, (fema445)	80
4.3	Rheological Chemo-Mechanical Models	83
4.4	Definition of the expansion curve	85
4.5	Effect of Temperature on AAR Expansion	87
4.6	Effect of time integration scheme for a harmonic temperature variation	89
4.7	Effect of time integration scheme for temperature variation in Coimbra Portugal	90
4.8	Effects of activation energy variations on characteristic and latency times	91
4.9	Time Evolution	91

4.10	Uniaxially-restrained expansion model	92
4.11	Tests on reactive concrete subjected to compressive stresses and confinement by Multon (comi09)	92
4.12	Stress-Induced Cracks with Potential Gel Absorption, (scrivener03)	93
4.13	Graphical representation of normalized retardation parameters Γ_c and Γ_t	94
4.14	Effect of relative humidity	95
4.15	Weight of volumetric AAR redistribution in selected cases	97
4.16	Weight domain	98
4.17	Relative Weights	101
4.18	Degradation of E and f'_t	102
5.1	Finite Element Process (inspired by bathe)	106
5.2	Uniformly distributed model complexity	109
5.3	Shape functions for isoparametric. elements	110
5.4	Unstructured <i>vs.</i> structured <i>vs.</i> Shell meshes (meshed with ryp1	111
5.5	Meshing in the presence of stress singularity in a re-entry corner https://www.comsol.com/blogs/how-identify-resolve-singularities-model-meshing/	115
5.6	Numerical integration schemes for nonlinear structural analysis	116
5.7	Integration schemes	118
5.8	Test highlighting localization	119
5.9	Gradual strain localization	120
5.10	Fracture of concrete; Cohesive crack	121
5.11	Discrete and smeared crack models in concrete	121
5.12	Yield function for the fracture mechanics based interface element	122
5.13	Fragility function	123
5.14	Tornado diagram for sensitivity analysis	124
5.15	Fragility curves (saouma2017riskinformed)	125
5.16	Engineering interpretation of results (saouma2017riskinformed)	126
6.1	Interaction among KumoNoSu, Merlin and Spider	128
6.2	Interaction among different programs in Matlab-based code	130
6.3	General algorithm in P0.m	131
6.4	Different types of uncertainties in PPACD	132
6.5	General algorithm in P1Sta.m	132
6.6	User defined Excel file with distribution models, mean, standard deviation and L/U bounds.	133
6.7	User defined Excel file with possible correlation coefficients.	133
6.8	Sampling the material properties based on algorithm in figure 6.5	134
6.9	General algorithm in P1Dyn.m	135
6.10	Different types of dynamic analysis methodologies in PPACD	135
6.11	Treatment of IMs in P4.m	136
7.1	Deconvolution feature in Merlin	139
7.2	Accelerograms of the input and output	140
7.3	Transfer functions	140

7.4	Deconvoluted signals	141
7.5	Comparison between original and deconvoluted signals	141
7.6	Results of deconvolution analysis	142
7.7	Insertion of springs to mitigate rigid body motions in a dynamic analysis	143
7.8	Rocking due to finite size foundation support	144
7.9	Rocking due to concrete-rock interface	144
7.10	Spring joint element	145
7.11	SSI: Concrete-Rock Interaction	145
7.12	Soil structure interaction model 1	146
7.13	Soil structure interaction model 2	147
7.14	Soil structure interaction model 3	147
7.15	Soil structure interaction model 4	147
7.16	Soil structure interaction model 5	148
7.17	Soil structure interaction model 6	148
7.18	Soil structure interaction model 7	149
7.19	Soil structure interaction model 8	149
8.1	Normalized AAR expansion in terms of temperature and relative humidity (saouma2014AARBook)	154
9.1	Potential rocking in a seismic analysis of a NCVS	160
9.2	Need for radiation damping	160
9.3	Two part analysis to mitigate effect of rocking	160
9.4	Geometry of a generic NCVS	161
9.5	Adopted geometry of the generic NCVS	162
9.6	Finite element mesh of the NCVS	164
9.7	Reinforcement details	165
9.8	Site characterization around the NCVS site	165
9.9	Hazard de-aggregation plot	166
9.10	Sample ETAF (endurance time acceleration functions)	167
9.11	Imposed AAR expansion model (kinetics)	167
9.12	Index points to extract the displacement response	168
10.1	Schematic representation of analysis to be performed.	169
10.2	NCVS response: Static analysis	170
10.3	Response of NPP under AAR analysis	171
10.4	Seismic response without AAR	171
10.5	Response of NCVS under AAR and seismic	172
10.6	Principal stress time histories from seismic analysis	173
10.7	Crack profile from seismic analysis	174

List of Tables

1.1	Target β values for different types of loads and members, (asce-7).	4
1.2	Damage control and building performance levels (fema356)	5
2.1	Comprehensive list of candidate IM parameters	27
4.1	Variation of $\epsilon(\infty)$, τ_c and τ_l for 4 specimens, (larive98)	86
4.2	Coefficients for moisture influence on expansion and kinetics (li04)	95
4.3	Triaxial Weights	99
5.1	Sample of Excel file storing load information	111
5.2	Example of Data Repository	112
5.3	Example of Correlation Between Random variables	112
5.4	Highlights of integration schemes	117
7.1	Evaluation of Various Boundary Conditions	146
8.1	Characteristics of the ASR model. ATU: AR Amaterial ApropertiesAarbitrary Atime Auni- tarbitrary time unit	152
8.2	Activation energy for different rock types (adapted from Katayama)	153
9.1	Concrete mechanical properties	163
9.2	Characteristics of the ASR model	163
9.3	Foundation rock mechanical properties	163
9.4	rebar mechanical properties	163

this is a test **aci349p3**

1— Introduction

1.1 Challenges

The nuclear industry is confronted with mounting challenges concerning the safety assessment of a Nuclear Containment Structure (NCS):

Beyond Design Basis Loads Fukushima’s earthquake¹ forced us to reconsider the seismic safety of NCS (miller11). Conceivably some of the NCS deemed seismically safe prior to the incident, may no longer be so. As a result, orders were issued by the NRC for requirements to develop mitigation strategies for beyond design-basis external events ml12054A735.

Accidental and unanticipated damage may occur in what may be perceived as a routine operation. Detensioning of Crystal-River 3 is such an example, as it has resulted in unanticipated splitting cracks along the post-tension cable shields (danielson09). Despite attempts to properly repair, the unit was ultimately decommissioned.

Ageing of some NCS is of a recent concern. This is primarily due to alkali silica reaction (ASR). Indeed, the Nuclear Regulatory Commission (NRC) issued Information Notice (IN) 2011-20, *Concrete Degradation by Alkali Silica Reaction* on November 18, 2011, related to the ASR identified at Seabrook (saouma13b).

Second License Renewal: Beyond 60 By the end of 2015, more than one-third of the existing domestic fleet will have passed their 40th anniversary of power operations, and about one-half of the fleet will reach the same 40-year mark within this decade. A regulatory process exists (nrc54) for obtaining approval from NRC on extended nuclear power plant operations beyond 60 years.

These challenges beg for a modern solutions suitable for the structural safety assessment of an existing structure as opposed to one originally tailored for the design of new structures.

1.2 Codes Philosophy

This document will advocate the use of modern nonlinear analysis in assessing the structural safety and integrity of NCS. Yet, many engineers continue on relying on prevailing codes (addressed below in Sect. 1.4), hence a critical review of the philosophy behind codes is hereby presented.

Design codes are essential documents regulating the construction industry. Historically, they have evolved in response to needs but were always fueled by improved knowledge. Without dwelling on specific codes (ACI, ASCE, AASHTO, EuroCodes and many others), a code provides a mean to ensure the design (and

¹It should be emphasized that despite its magnitude 6.6 M_w , the earthquake did not directly cause substantial failure. Failure was caused by the ensuing tsunami.

construction) of a structure with an adequate *factor of safety*.

The concept of factor of safety has evolved over the years. Schematically the following three approaches have evolved sequentially:

Allowable Stress Design (ASD) Oldest, simplest approach where a factor of safety is assigned to the strength only (typically a 40% reduction). Furthermore, failure of a structural component at a time is considered (i.e. no interaction or coupling amongst them is considered to determine the failure of a *system*).

Load Resistance Factor Design (LRFD) is the prevailing design methodology for both concrete and steel structural components. It was introduced in the ACI code in 1977, and in the AISC steel code in 1986, and is discussed below in Sect. 1.2.1.

Performance Based Engineering 1 (council2009nehrp) Goes beyond the LRFD approaches and focuses on the performance of the structure and introduces the concepts of fragility curves, Sect. 1.2.2.

Performance based Engineering 2 extends the previous PBEE (porter2003overview).

1.2.1 LRFD

The premise of the method is that both capacity and demands (or resistance and loads) have normal distribution functions as shown in Fig. 1.1(a) (ellingwood1980development). Since, by definition, the normal distribution function is defined from minus to plus infinity, there will always be a small region where $D > C$. Hence, the method can not ensure zero risk, however the risk will be reduced to an “acceptable” value (around one in one hundred thousand).

The method will then assign two different sets of properly balanced factors (loads and resistance) and since we are considering failure, a limit state analysis (plastic mechanism) is used (i.e concrete strain at 0.003, and fully plastified cross section for steel section).

$$\begin{aligned} \text{Reinforced Concrete: } M_d &= \phi A_s f_y \left(d - \frac{a}{2}\right) \\ \text{Steel Section: } M_z &= \Phi Z f_Y \end{aligned} \tag{1.1}$$

To ensure safety, load is multiplied by a factor α , and the ultimate resistance is reduced by Φ . α and Φ are assigned such that the probability of failure does not exceed a certain value:

$$\Phi C_n \geq \Sigma \alpha_i D_i \tag{1.2}$$

where C_n and D are the nominal capacity and demands (or nominal resistance and load). The method explicitly accounts for uncertainties in loads and strength, and can implicitly account for consequences of failure.

The reliability index, defined in Fig. 1.1(b) is a “universal” indicator on the adequacy of a structure, and can be used as a metric to 1) assess the health of a structure, and 2) compare different structures targeted for possible remediation. Relationship between the reliability index β and the probability of failure is shown in Fig. 1.1(c)

LRFD seeks to have a *Reliability Index* such that $\beta > \sim 3.5$, and thus it was determined that this is nearly achievable for the values of α shown in Table 1.1, (asce-7): The load and resistance factors are statistically determined to produce a probability of failure of about 10^{-5} . Nevertheless, the LRFD method has the following severe limitation:

1. Inconsistent: Linear analysis, but plastic design.

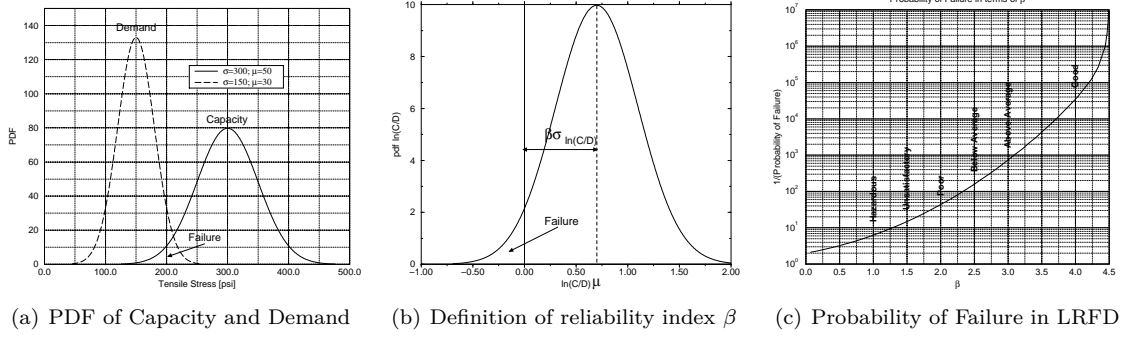


Figure 1.1: Probabilistic aspects of LRFD

Type of Load/Member	β
AISC	
DL + LL; Members	3.0
DL + LL; Connections	4.5
DL + LL + WL; Members	3.5
DL + LL + EL; Members	1.75
ACI	
Ductile Failure	3-3.5
Brittle Failures	3.5-4

Table 1.1: Target β values for different types of loads and members, (**asce-7**).

2. Ignores load redistribution near failure (though ACI implicitly accounts for some of it through reduction of negative moments).
3. Addresses only one level of hazard: failure of one structural component (and not the entire system), but how about quantification of damage due to more frequent events?

1.2.2 Performance Base Earthquake Engineering (PBEE)

Though this approach was originally developed in the context of earthquake engineering by the Pacific Earthquake Engineering Research center, it has subsequently evolved into procedures endorsed by ASCE (**asce-sei-31**) and FEMA (**fema356**). Contrarily to LRFD:

- it does not limit itself to one level of hazard, but up to four hazard performance levels, Table 1.2.
- It considers the whole structure as opposed to an individual member collapse.

This approach was recently espoused by the author (**HaririSaoumaPSDM**) (**hariri2016seismicfragility**) for concrete dams.

Conceptually, it may not differ much from the original risk assessments pioneered for the nuclear industry, (**ellingwood1985probabilistic**).

The PBEE method ultimately yields one or more fragility curves. A fragility function quantifies the probability of exceeding a particular level of damage (limit state or structural collapse in the end) as a function of a stressor (such as ground motion intensity measure). More coverage on fragility curves can be found in Sect. 5.2.3

The concept of a fragility curve in earthquake engineering goes back at least to 1980 (**kennedy1980probabilistic**), who define a fragility function as a probabilistic relationship between frequency of failure (in this work a component of nuclear power plant) and environmental excitation (these authors speak exclusively of earthquakes

	Collapse tion	Preven- tion	Life Safety	Immediate pancy	Occu- pancy	Operational
Overall Damage	Severe		Moderate	Light		Very Light
General	Little residual stiffness and strength, but load bearing columns and walls function. Large permanent drifts. Some exits blocked. Infills and unbraced parapets failed or at incipient failure. Building is near collapse.		Some residual strength and stiffness left in all stories. Gravity-load bearing elements function. No out-of plane failure of walls or tipping of parapets. Some permanent drift. Damage to partitions. Building may be beyond economical repair.	No permanent drift. Structure substantially retains original strength and stiffness. Minor cracking of facades, partitions, and ceilings as well as structural elements. Elevators can be restarted. Fire protection operable.		No permanent drift. Structure substantially retains original strength and stiffness. Minor cracking of facades, partitions, and ceilings as well as structural elements. All systems important to normal operation are functional.
Nonstructural components	Extensive damage.		Falling hazards mitigated but many architectural, mechanical, and electrical systems are damaged.	Equipment and contents are generally secure, but may not operate due to mechanical failure or lack of utilities.		Negligible damage occurs. Power and other utilities are available, possibly from standby sources.

Table 1.2: Damage control and building performance levels (**fema356**)

and PGA). Other important references are (**ellingwood1998issues**) and (**braverman2004degradation**). It should be noted that this concept has not yielded many additional archived journal articles.

1.3 Complexities of a Nonlinear Analysis.

Linear analysis is typically performed during the design process, whereas a nonlinear one is performed to assess actual safety of an existing structure. Nonlinear analyses is thus performed when the material response (stress-strain or load-displacement) is no longer linear elastic, but depends on the applied load. For reinforced concrete structures, this is the case when concrete has cracked compressive stresses exceed about 0.45 the compressive strength or when the tensile stress exceeds the tensile strength resulting in structural cracks (such as delamination) and not in the anticipated hairline cracks found in properly designed reinforced concrete structures. Nonlinear analysis will also be needed when the reinforcement stress reaches the yield stress resulting in excessive deformation. Finally, nonlinear analysis may be required in the presence of “large” deformation, but this is very rarely the case in **NCS**. In the former case we deal with material nonlinearity and in the second geometric nonlinearity.

In the presence of material nonlinearity, there is not a unique solution. The solution will greatly depend on the model adopted, and its implementation. On the other hand, linear elastic analysis results should all be identical (assuming the exact model has been analysed).

The concept of performance based, and accompanying fragility curve is inseparable from nonlinear analysis which will be reviewed next.

Design, code constraints aside, is relatively “easy”, and the analyst is mostly confined to a linear elastic analysis on the basis of known material properties. Accurate (to the extent possible) safety assessment of an existing structure for any load is a challenge for the following reasons:

Material Physical Properties two ranges to be considered

Elastic: are no longer the ones stipulated by the designer but the actual ones which are likely to be different than the one stipulated many years earlier in a design office and are seldom uniform

within the entire structure.

Inelastic properties are necessary for the failure load assessment, yet they are unlikely to have ever been envisioned before. Compressive strength f'_c is no longer the universal metric, and additional tests would have to be performed to determine the tensile strength, stress-strain curve, creep characteristics, fracture energy and others.

Loads Beside the design loads which were well defined in the design process, one must also consider

Beyond design basis loads that may not have been anticipated. One such example is the increased seismic excitation that the structure must resist. This increase is likely to be the result of improved knowledge, past recent experience, stricter safety requirements than those envisioned many years earlier during the design process.

Accidental loads such as improper detensioning of cables, but also blast loadings of a magnitude never previously anticipated.

Ageing of structures likely to jeopardize its integrity. The most common one being Alkali-Aggregate Reaction (AAR) which is already afflicting some NCS.

Lack of Guidance Design codes are for design and not for safety assessment. With the ageing of the nuclear infrastructure, and the impetus to extend life to 80 years, there is an urgent need to develop new codes specifically written for structural assessment.

Computational Models used for design are mostly limited to the linear elastic range under amplified loads (1.4, 1.7 factors) with the implicit assumption that the sufficiently large factors of safety provide sufficient safeguard for problems that should really be uncovered by nonlinear analysis. Thus, regulators do not know what is the true factor safety of a structure other than it is greater than 1.0 (i.e. is it 1.1 or 3?). On the other hand, for safety assessment we must be capable of handling full nonlinear analyses up to collapse with the gradually increasing service load.

Fragmented Knowledge is a major handicap. The knowledge for the structural safety assessment of NCS is present and mostly in publications from few major companies or researchers in academic settings. That knowledge needs to be combed, reviewed, distilled and made palpable to the engineering community for a major revisit of the NCS park.

Human Resources Engineers trained for design, are not as well equipped to handle safety failure analysis. On the other hand, those few researchers from academia who know how to perform a full nonlinear analysis are seldom in tune with the necessity to analyse holistically a structure without occasional simplifications to accommodate overly complex models.

1.4 Inadequate Codes

In light of the previously described complexities associated with a modern safety assessment of NCS, and governed by existing regulations, engineers have taken the safe (and easier) path of a strict adherence to existing codes. Yet those codes may yet be inadequate to fully address the challenges described in Sect. 1.1 and thus fully ensure public safety.

The prevailing code for NCS design and Reinforced Concrete (RC) design are (aci349) and aci318) respectively. The former code explicitly states

The standard covers the proper design and construction of concrete structures that form part of a nuclear power plant and that have nuclear safety-related functions, *but does not cover*

*concrete reactor vessels and concrete containment structures*² (as defined by joint ACI-ASMR Committee 359).

Hence, **aci349** explicitly does not address the analysis of the containment structures, but only the frame-like internal ones. A complementary document (**aci349p3**) provides

... guidelines for the evaluation of existing nuclear safety-related concrete structures. The purpose of [this report] is to provide the plant owner and engineering staff with an appropriate procedure and background for examining the performance of facility structures and taking appropriate actions based on observed conditions. Methods of examination, including visual inspection and testing techniques, and their recommended applications are cited. Guidance related to acceptance criteria for various forms of degradation is provided.

Yet, these codes were used to assess the structural integrity of Crystal-River 3.

Unfortunately, (**aci349p3**) is very general and qualitative in nature as it provides guidelines as opposed to specific quantitative assessment methods. As a result, engineers confronted with the engineering assessment of existing structures, have to consult (**aci349**). This may lead to either incomplete or erroneous conclusions which may not necessarily err on the conservative side.

(**aci365p1R00**), (Service Life Prediction) addresses concrete deteriorations (mostly carbonation, chloride diffusion, spalling) in some details. However, it does not address the critical issue of the ensuing structural analysis after deterioration has been observed. This limitation has already been identified and acted upon in Europe (**bruhwiler2012swiss**) (**iso201013822**).

In the absence of a specific code for the safety evaluation of **NCS**, and complementing **aci349p3**, this document is a partial attempt to encourage the nuclear engineering community to consider the development of new codes for the detailed assessment of existing structures based on nonlinear analyses and adequate field inspections and experimental techniques.

²Author's italic for emphasis.

This page intentionally left blank.

Part I

Theory

This page intentionally left blank.

2— Probabilistic Risk Evaluation

2.1 Introduction

The previously reported document of **pires** made some very relevant and timely recommendations that include:

1. Move away from *seismic hazard assessment* to *risk evaluation*.
2. Evaluate different methodologies for soil structure interaction recognizing the epistemic uncertainty.
3. Identifying consistent, efficient, robust methods for developing fragility estimates utilizing available design data to support probabilistic risk analyses.
4. Incorporation of earthquake experience data into assessment.

This chapter will (in great part) address those recommendations based on a methodology developed at the University of Colorado: (**HaririSaoumaCollapseFragility**), (**HaririSaoumaPSDM**), (**HaririSaouma2014DI**), (**HaririSaoumaPorter2015**), (**HaririSaoumaSensitivity**), (**hariri2016new**), which are all based on the PhD thesis of **HaririPHD2015** for concrete dams and will be extended to nuclear containment vessel structures (NCVS).

Keeping in mind that ultimately, it is the fragility curve/surface which is sought, the proposed procedure is first illustrated in Fig. 2.1 and described synthetically as follows:

Site and NCVS Characteristics Determine *NCVS Site Seismicity Map* (Section 2.3.1, 2.3.4 and 2.3.5), examine the NCVS (*Physical Model*), select *Instrumentation*, analyze *Long Term Field Monitoring* data, and possibly perform *Forced Vibration Testing*.

Finite Element Model based on the previous data and *Material Characteristics*, determine desirable *Features* of the analyses and of the *Constitutive Models* Finally, select appropriate *F.E. Package*. The soil structure interaction is separately addressed in Chapter 3.

Finite Element Model based on the previous data and *Material Characteristics*, determine desirable *Features* of the analyses and of the *Constitutive Models*. Finally, select appropriate *F.E. Package*. The soil structure interaction is separately addressed in Chapter 3.

Initial Deterministic analysis to assess the model, to be followed by a set of *Parametric Analyses* with initially $N1$ identifiable unknown parameters, which may be reduced to $N2$ through calibration with *Forced Vibration Testing* and *Long Term Field Monitoring*.

Sensitivity Analysis Assuming that each of the remaining $N2$ variables has a minimum and maximum, then $2 \times N2 + 1$ sensitivity analyses are performed. The first has all variables set to their mean value, and then each variable is assigned the minimum or maximum, one at a time. Results are then displayed in the so-called *Tornado Diagram* from which the most sensitive $N3$ random variables are selected and

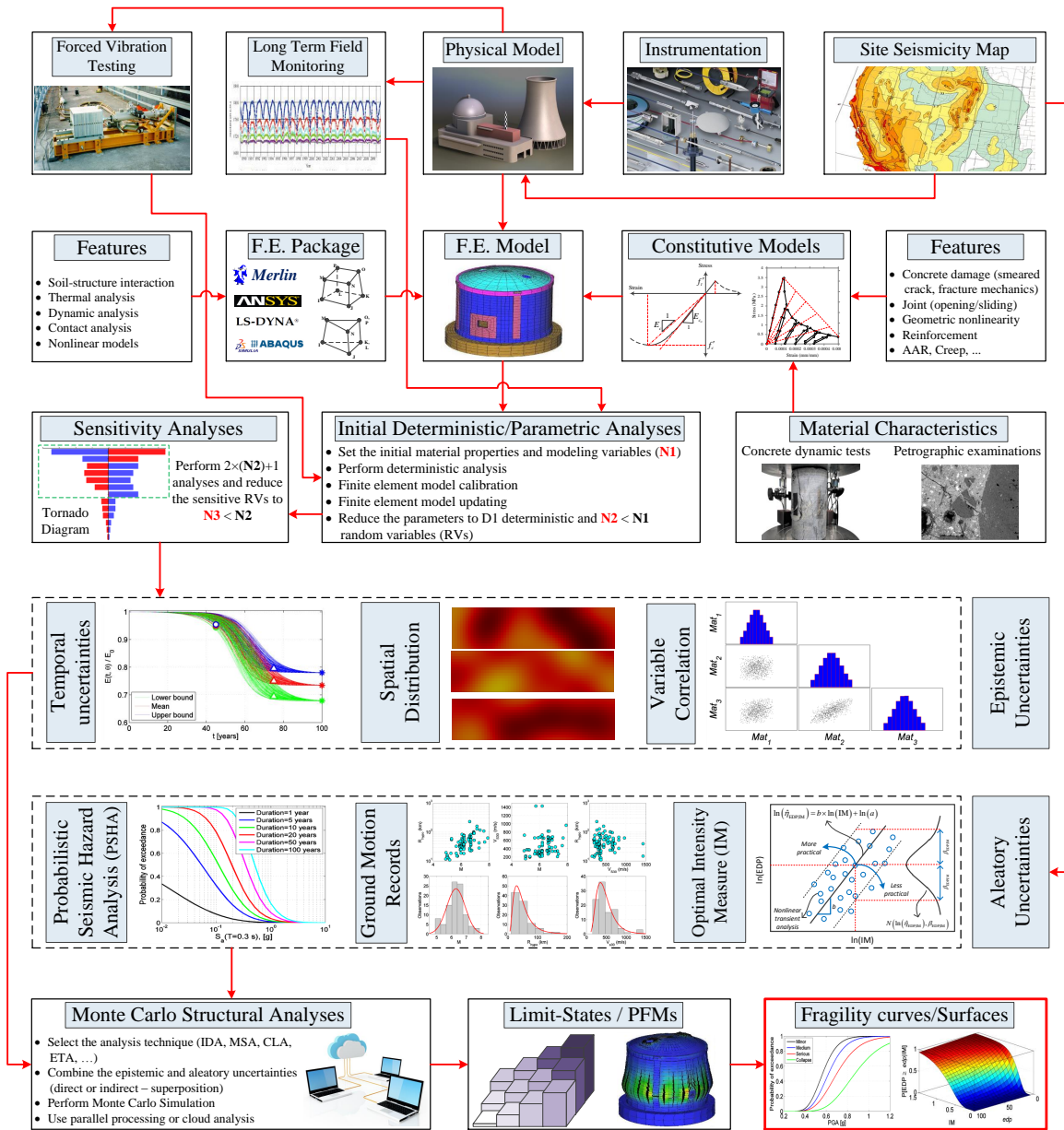


Figure 2.1: Summary of the proposed method

kept in further studie, Section 2.4.

Epistemic Uncertainties are those associated with quantities that should be known, but practically impossible to quantify, such as material property *Spatial Distribution* [olsen2002latin](#) or *Temporal Uncertainties* (e.g. time dependent material degradation). Either one of those two may have two or more random variables (such as tensile strength and compressive strength) and a possible *Variable Correlation* matrix, Section 2.4.2.

Aleatory Uncertainties are those due to unsurmountable lack of knowledge such as seismicity at a given site and at a given time. First, a *Probabilistic Seismic Hazard Analysis* is performed to determine the

hazard curves. Then, corresponding *Ground Motion Records* are selected **PEERWS**, and finally the *Optimal Intensity Measure* parameter is determined (such as PGA, $S_a(T_1)$) **PadgettNielsonDesRoches**, Section 2.3.6.2.

Monte Carlo Structural Analysis Outcome of both epistemic and aleatory uncertainties are combined by performing *Monte Carlo Structural Analyses*, figure 2.14. This is by far the most computationally expensive step, Section 2.5

Capacity Functions *Limit States and Potential Failure Modes* are then extracted through data mining. Examples of limit states include crest displacements and joint opening/sliding, Section 2.6.

Fragility Curves/Surface are derived from the previous through a statistical interpretation and a cumulative distribution function Section 2.8.

First a section will briefly review the conceptual paradigm which inspired the proposed approach. It is based on many years of research by the Pacific Earthquake Engineering Research (PEER) center (**Porter2000PHD**), and later adopted by FEMA (**femap581**).

2.2 Performance Based Earthquake Engineering

First let us distinguish among the following terms:

Performance-Based Engineering (PBE) is defined as consisting of the selection of design criteria, appropriate structural systems, layout, proportioning, and detailing for a structure and its non-structural components and contents, and the assurance and control of construction quality and long-term maintenance, such that at specified levels of all the excitation and with defined levels of reliability, the structure or facility will not be damaged beyond certain limit states (**Bertero2002**).

Performance-Based Earthquake Engineering (PBEE) is defined as the application of PBE to the case that seismic hazard controls the design. Therefore, PBEE involves the complete design, construction and control (monitoring) of the maintenance and function of the structure to assure that the constructed structures will resist the effects of earthquake ground motions with different severity within specified limiting levels of damage (**Bertero2000**).

Performance-Based Seismic Design (PBSD) is the subset of activities of PBEE that focus on the design process.

Performance-Based Assessment (PBA) is the implementation of the PBEE in quantitative evaluation of the performance of a given structure (even an existing structure or a completed design of a new structure) (**Zareian2009**).

In the US, interest in PBSD initiated in the 1980s among engineers engaged in seismic retrofit of existing buildings. Owners of existing buildings would not commit to investment in retrofit construction unless they had an understanding of the probable performance of their buildings in future earthquakes, decided that this performance was undesirable, and that acceptable performance could be obtained at reasonable cost. Thus, engineers began to develop rudimentary procedures for assessing the likely earthquake performance of existing buildings so that they could evaluate whether collapse or other life-threatening damage was likely (**hamburger04**).

Based on Structural Engineers Association of California (SEAOC) Vision 2000 the first step in PBEE is the definition and selection of the performance objectives (PO). A PO is a coupling of expected performance levels with levels of seismic ground motions. A performance level represents a distinct band in the spectrum of damage to the structural and non-structural components and contents, and also considers the consequences

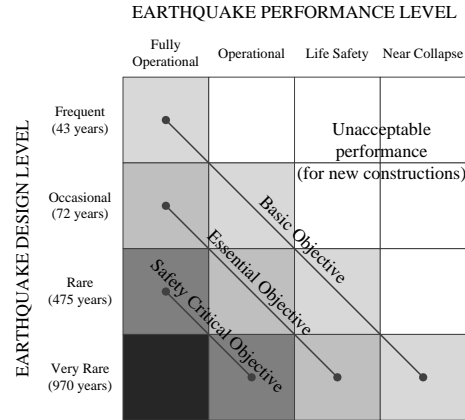


Figure 2.2: Recommended minimum seismic performance design objectives for buildings

of the damage to the occupants and functions of the facility (**Bertero2002**). Four discrete performance levels in this document are: 1) fully operational, 2) operational, 3) life safety, and 4) near collapse in terms of damage to structural and non-structural components and consequences to the occupants and functions carried on within the facility as shown in figure 4.2 (**SEAOC1995**). Earthquake design levels are shown as earthquake with specific return period. The diagonal lines represent different *objectives* correspond to different facility types.

2.2.1 First Generation of PBEE

First Generation of PBEE (also known as PBEE-1) is shown conceptually in figure 2.3 and it is assumed that a structure is loaded by earthquake-induced lateral forces that produce nonlinear response in structural components. Relations were established between structural responses (inter-story drift ratio, inelastic member deformation, and member force) and performance-oriented descriptions (such as immediate occupancy, life safety and collapse prevention) (**MOEHLE-DEIERLEIN2004**).

The first-generation of PBEE represents a significant improvement over past practice. It includes standard methods of defining performance in terms of quantified performance levels that relate to calculated seismic response parameters and incorporate a formal methodology for simulating building response to earthquake motions and assessing performance capability based on the predicted magnitude of a series of structural response parameters (**hamburger04**). Considering all these developments also they had shortcomings which need to be improved:

- PBEE-1 has evaluated performance on the basis of the demands and capacities of individual components, rather than global building behavior. So the weakest or the least ductile elements in a structure were controlled the estimation of overall structural performance.
- The reliability of PBEE-1 is questionable because many of the acceptance criteria contained in the documents are based on the engineering judgment.
- The procedures that evaluate non-structural components are limited.
- The reliability of the procedures in PBEE-1 and their ability to achieve the desired performance has never been established.
- The basic process of performance-based engineering carries with it significant potential liability as many

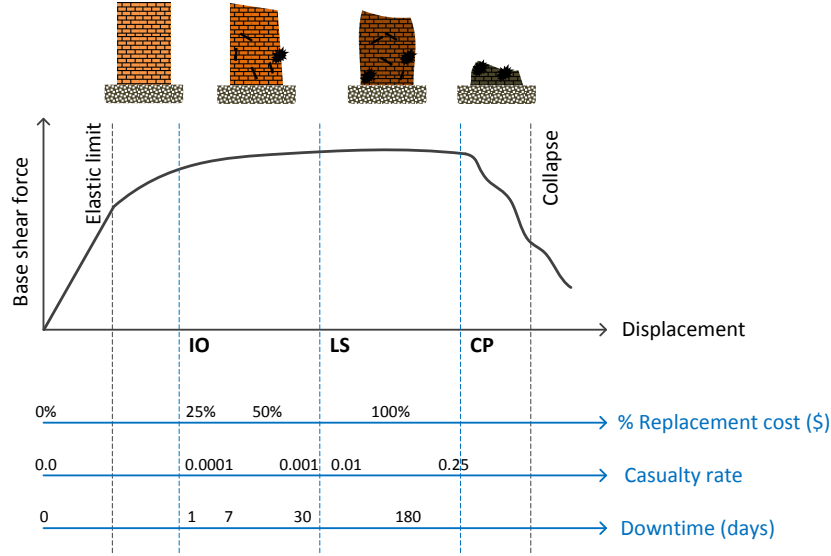


Figure 2.3: Conceptual description of first generation PBEE (**WHITTAKER**)

building owners may perceive that the design professional has provided a warranty on the design's performance capability.

2.2.2 Second Generation of PBEE

Although there are many research about the different aspects of PBEE (theoretical models and case studies), historical development of this framework can be addressed briefly based on the works by **Czarnecki1973**, **KustuMillerBroken1982**, **Porter2000PHD**, **aslani2005probabilistic**, **MitraniReiser2007**, **YangMoehleStojadinovic2012advancement**.

In 1997 the Pacific Earthquake Engineering Research Center (PEER) decided to develop a more robust methodology for performance-based earthquake engineering, called as next generation PBEE (also called as PBEE-2 or PEER PBEE). The PEER PBEE framework developed by PEER facilitates direct calculation of the effects of uncertainty and randomness on each step in the performance based procedure (**Porter2003**).

The general framework for PEER PBEE is shown in figure 2.4. It breaks the seismic performance assessment into four primary steps: 1) ground motion hazard characterization, 2) structural response analysis, 3) damage analysis, and 4) loss assessment (**PEER-RCFrame**). The results of each of these steps are represented as generalized variables, Intensity Measure (IM), Engineering Demand Parameter (EDP), Damage Measure (DM), and Decision Variable (DV). This process can be expressed in terms of a triple integral that is an application of the total probability theorem (**Porter2003**) :

$$g[DV|D] = \int \int \int p[DV|DM,D] p[DM|EDP,D] p[EDP|IM,D] g[IM|D] dIM.dEDP.dDM \quad (2.1)$$

where $p[X|Y]$ denotes the complementary cumulative distribution function of X conditioned on Y , $g[X|Y]$ denotes the mean annual occurrence rate of X given Y , and D denotes facility location, structural, non-structural, and other features. Note that in future we omit conditioning on D for simplicity.

IM: describes the characteristics of the earthquake ground motion quantitatively. This parameter is ex-

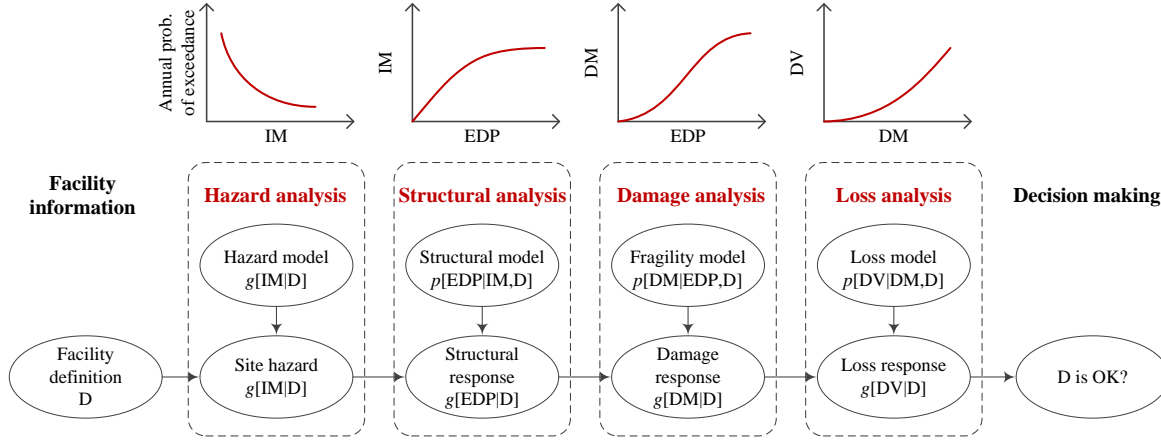


Figure 2.4: General framework of PEER PBEE methodology (**Porter2003**)

pressed typically as a function of mean annual probability of exceedance, $g[IM]$.

EDP: describes the response of the structural and the non-structural components and contents to earthquake shaking. The products of this step are conditional probabilities, $p[EDP|IM]$.

DM: describes the physical condition of structural and non-structural components. DMs include effective descriptions of damage to characterize the functionality, occupancy-ready, life safety and necessary repairs of the building. The products of this step are conditional probabilities, $p[DM|EDP]$.

DV: serves to translate damage estimates into quantities that are useful to those tasked with making risk-related decisions. Currently used DVs which are identified as decision metrics are direct dollar losses, downtime (or restoration time) and deaths (casualties). The products of this step are conditional probabilities, $p[DV|DM]$.

As mentioned before direct dollar losses, downtime and casualties are used as decision variables in PBEE-2 methodology for performance assessment of structures. **ATC-58-1** uses three types of performance assessment methodologies:

Intensity-Based Performance Assessments (IBPA) evaluates a structure's performance assuming that it is subjected to a specific intensity of shaking. This assessment usually is used when the structure is subjected to the earthquake shaking with specific response spectrum (such as design response spectrum).

Scenario-Based Performance Assessments (SBPA) evaluates a structure's performance assuming that it is subjected to the effects of a specific magnitude earthquake occurring at a specific location relative to the structure site. Scenario assessments may be useful for decision makers with structures located close to one or more known active faults.

Time-Based Performance Assessments (TBPA) evaluates a structure's performance over a period of time considering all earthquakes that may occur in that period of time, and the probability that each will occur. It considers uncertainty in the magnitude and location of future earthquakes as well as the intensity of motion resulting from these earthquakes.

Figure 2.5 compares the step-by-step procedure for ground motion selection and scaling based on the three above mentioned methods. It is noteworthy that in TBPA, the recommended values for the parameters introduced in figure 2.5 are as follows: $(S_a)_{min} = 0.05 \text{ g}$ and $(S_a)_{max}$ is associated with annual frequency of exceedance of $0.00002/\text{yr}$ (that is, 1 occurrence in 50,000 years). Number of intervals m usually is

recommended to be 8.

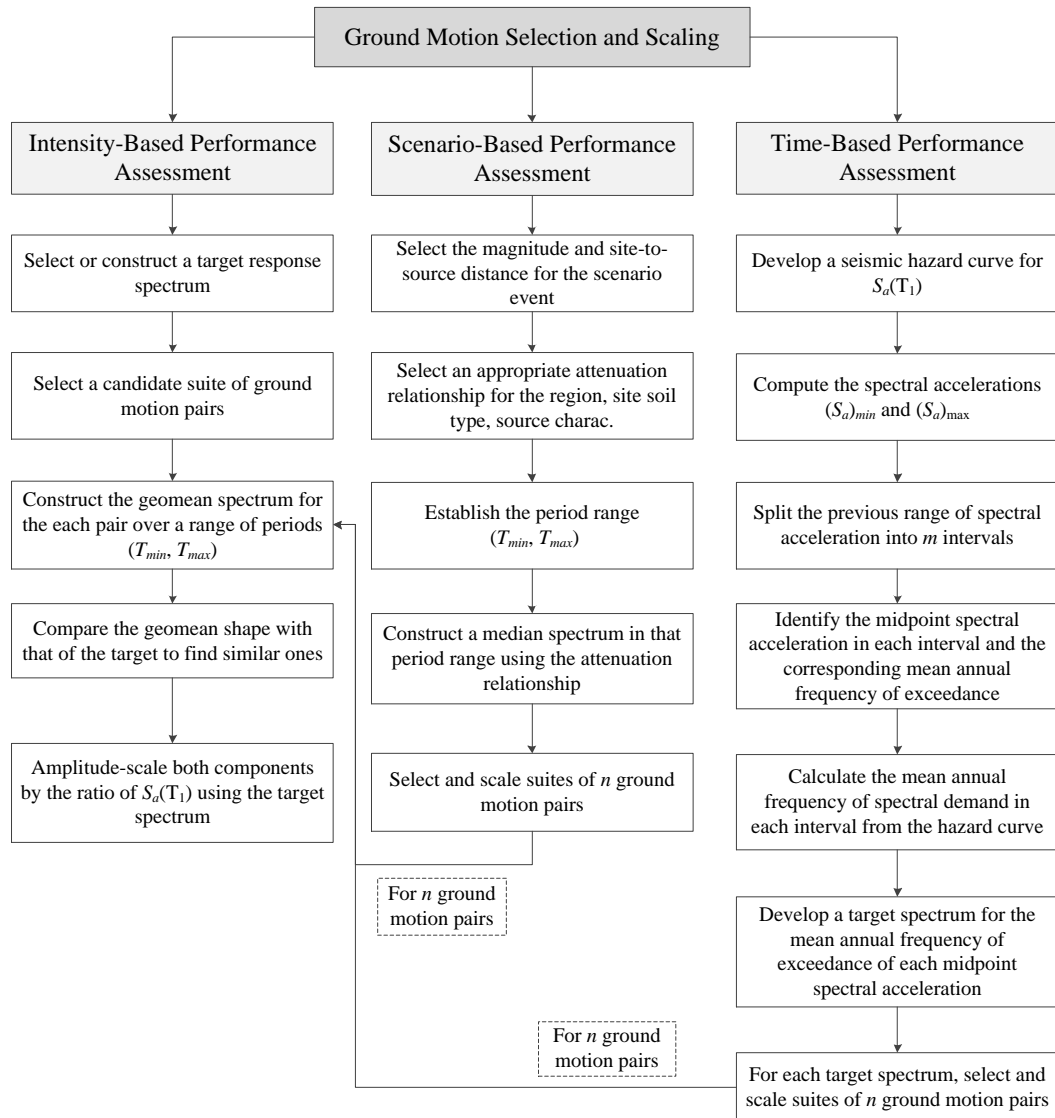


Figure 2.5: Comparison of ground motion selection and scaling for IBPA, SBPA and TBPA

2.3 Seismic Hazard Analysis

Seismic design of many structures, especially critical infrastructures such as nuclear power plants (NPP) and dams needs to a clear vision on seismic potential of the region that the structure is going to be constructed. Parameters such as importance of the structure, risk of the failure, financial concerns, and even the technological problems may affects the method of the seismic hazard analysis. Flowchart 2.6 shows the different steps that are required for seismic hazard analysis of a nuclear containment vessel structure in context of the PBEE.

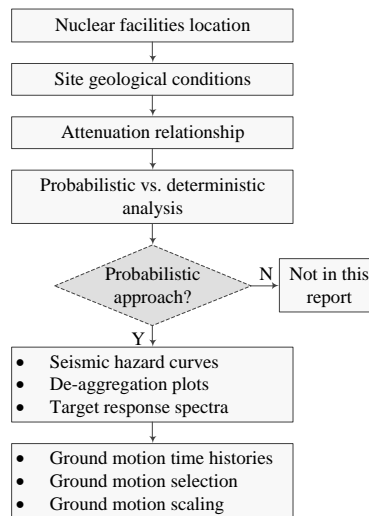


Figure 2.6: Steps toward seismic hazard analysis of nuclear containment vessel structures

2.3.1 Location and Site Condition

2.3.1.1 Seismic Environment and Hazard

Earthquake shaking hazards are dependent on site location with respect to seismic sources and, regional and site-specific geologic characteristics. Seismic source is characterized by identification of all the potential earthquake sources. Earthquake sources typically are either faults or areal seismic source zones. Local topographic conditions (e.g., hills, valleys, canyons) can also modify the character of shaking. Determine from the earthquake rupture forecast whether any part of the structure stands within 500 m of the trace of a known active fault. In such a case, the site is not suitable for construction of a dam. Otherwise, determine from the earthquake rupture forecast the distance from the site to every seismic source within 200 km capable of producing an earthquake of magnitude M_{min} or greater (e.g. $M_{min} = 5.0$), and determine from the earthquake rupture forecast its annual frequency of producing such an earthquake at such a distance. It should be noticed that for critical facilities, such as dams and NPPs, even fault with fairly low slip rates (~ 0.01 mm/yr) can be important.

2.3.1.2 Site

The assessments recommended here require seismic hazard curves that predict the annual frequency of exceedance of key spectral response parameters. To develop hazard curves, the NCVS site's exact location (longitude and latitude) must be identified. Latitude and longitude should be defined to three decimal places (approximately 100 m).

For *Time-Based Performance Assessment* it is required to have seismic hazard curves which shows the annual frequency of exceedance of key spectral response parameters so the site's exact location must be identified. For *Scenario-Based Performance Assessment*, the distance from the structure site to the causative fault must be known. For *Intensity-Based Performance Assessment*, the site location need not be defined (ATC-58-1).

2.3.1.3 Local Geotechnical Effects

It is assumed here that the containment vessel is founded on rock or hard rock. Rock is defined here consistently with ASCE 7-10 Section 20.3 (**ASCE-710**), as having shear wave velocity of 760 m/s to 1520 m/s. Hard rock is defined here as having a minimum shear wave velocity of 1520 m/s. As a minimum, it will be necessary to have sufficient data to characterize the Site Class in accordance with the ASCE 7-10 Standard (**ASCE-710**) so that site coefficients can be assigned. This information will generally include the depth, classification and shear wave velocity of materials in the soil column above bedrock, if the NCVS is not founded on rock or hard rock. Alternatively, the main parameters of site condition, i.e. average shear wave velocity at top 30 m of the soil/rock column, V_{S30} , depth to 1.0 km/s shear wave velocity, $Z_{1.0}$, and depth to 2.5 km/s shear wave velocity, $Z_{2.5}$, can be obtained using the application at [OpenSHA](#) (**Field2003**).

2.3.2 Attenuation Relationships

Attenuation relationships are used to derive acceleration response spectra for use in *Scenario-Based Performance Assessment* and also form the basis for probabilistic seismic hazard analysis (PSHA) used to develop the hazard curves needed for *Time-Based Performance Assessment*. Attenuation relationships provide estimated values of ground shaking intensity parameters, such as peak ground acceleration (PGA), peak ground velocity (PGV) and spectral response acceleration at particular structural periods, $S_a(T_i)$, for user-specified combinations of earthquake magnitude and site-to-source distance (**ATC-58-1**).

Attenuation relationships are derived by performing regression analyses of the values of intensity parameters obtained from strong motion recordings of past earthquakes against distance, magnitude and other parameters. Most attenuation relationships provide geometric mean spectral response accelerations, $S_{gm}(T)$ which represents the quantity:

$$S_{gm}(T) = \sqrt{S_x(T) \times S_y(T)} \quad (2.2)$$

where $S_x(T)$ and $S_y(T)$ are orthogonal components of spectral response acceleration at period T . The x and y directions may represent the actual recorded orientations, or may represent a rotated axis orientation. $S_{gm}(T)$ approximately represents a statistical mean response, with actual shaking response in any direction as likely to be higher as it is lower than the geometric mean (**ATC-58-1**).

Time-Based Performance Assessment can be used to assess the effects of a repeat of a historic earthquake or to explore the effects of a maximum-magnitude event on a nearby fault. Many of attenuation relationships can be written in simple form as:

$$\ln(Y) = c_1 + c_2 M - c_3 \ln(R) - c_4 R + \gamma \quad (2.3)$$

where Y is the median value of the strong-motion parameter of interest, e.g. $S_a(T_i)$, M is the earthquake magnitude, R is the source-to-site distance, γ is a standard error term and c_1 to c_4 are constant coefficient can be obtained from regression. Additional terms can be used to account for other effects including near-source directivity, faulting mechanism, site condition, and hanging wall/footwall location of the site. The complete list of ground motion prediction equations proposed and developed in last 50 years can be found at (**Douglas2011**).

If the site is within 20 km to 30 km of the presumed zone of fault rupture and the selected earthquake magnitude is $M_w \geq 6$, fault directivity effects should be considered. Fault directivity characterizes

whether the progression of rupture along the fault is towards the site or away from the site and can have substantial effect on the amplitude, duration and period content of shaking. Directivity should be specified as: forward directivity (rupture progresses towards the site); reverse directivity (rupture progresses away from the site); null directivity; or unspecified directivity (random direction of rupture progression).

At sites located within the forward directivity region, and within 20 km of the rupture zone of large magnitude ($M_w \geq 6$) strike-slip faulting, shaking in the fault normal direction often exhibits significant velocity pulses as well as significantly larger amplitude than does shaking in the fault parallel direction. This effect is known as directionality. Hazard assessments on sites within this distance should account for these effects.

2.3.3 Probabilistic vs. Deterministic Hazard Analysis

In general, there are two approaches for obtaining site-specific ground motions, i.e. probabilistic seismic hazard analysis (PSHA) and deterministic seismic hazard analysis (DSHA). Within the PBEE concept, PSHA is used to obtain the appropriate suit of ground motions.

2.3.3.1 Deterministic Seismic Hazard Analysis

DSHA uses the known seismic sources near the site and available historical seismic and geological data to generate discrete single-valued events or models of ground motion at the site. Typically, one or more earthquakes that will produce the greatest ground motion at the site are specified by magnitude and location with respect to the site. Usually, the earthquakes are assumed to occur on the portion of the source closest to the site. The site ground motion parameters are estimated deterministically for each source, given the magnitude, source-to-site distance, and site conditions, using an attenuation relationship and/or theoretical models (**FEMA-65**). DSHA typically specify a maximum earthquake magnitude, often referred to as the maximum credible earthquake (MCE).

2.3.3.2 Probabilistic Seismic Hazard Analysis

PSHA approach uses the elements of the DSHA and adds an assessment of the likelihood that ground motions of a given magnitude would occur. The probability or frequency of occurrence of different magnitude earthquakes on each significant seismic source and inherent uncertainties are directly accounted for in the analysis. The possible occurrence of each magnitude earthquake at any part of a source is directly incorporated in a PSHA. The results of a PSHA are used to select the design earthquake ground motion parameters based on the probability of exceeding a given parameter level during the service life of the structure or for a given return period. Results from the PSHA approach can also be used to identify which combinations of magnitudes and distance is the largest contributor to hazard. Identification of these controlling earthquakes can then be used in scenario or DSHA analyses (**FEMA-65**).

2.3.4 Seismic Hazard Curves

The fundamental outcome of a PSHA is the seismic hazard curve, which shows the annual rate or probability at which a specific ground motion level will be exceeded at the site. In any hazard curve, the vertical axis presents annual probability of exceedence (or return period), and the horizontal axis is intensity measure (IM)

parameter. Seismic hazard curves are usually an important and useful tool in risk analysis of containment vessels. Figure 9.8(b) shows a typical seismic hazard curves at a known site.

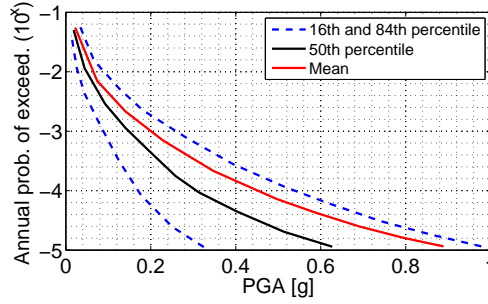


Figure 2.7: Sample of mean and fractile hazard curves

Having access to the earthquake rupture forecast and ground-motion prediction equations, the seismic hazard curve is estimated as follows:

$$\lambda(Y \geq y) = \sum_{f=1}^{N_f} \sum_{m=M_{min}}^{M_{max,f}} \sum_{\varrho=1}^{N_{\varrho,f,m}} (\lambda(f, m, \varrho) - \lambda(f, m + \Delta m, \varrho)) \cdot (1 - F_{Y|f,m,\varrho}(y)) \quad (2.4)$$

where,

$$F_{Y|f,m,\varrho}(y) = \frac{1}{N_a} \sum_{a=1}^{N_a} \Phi \left(\frac{\ln \left(\frac{y}{\exp(\mu_{\ln Y,a})} \right)}{\sigma_{\ln Y,a}} \right) \quad (2.5)$$

- Y is site shaking IM parameter, usually $S_a(T_1, \xi = 5\%)$,
- y is a particular value of Y ,
- $\lambda(Y \geq y)$ is mean rate at which the site can experience shaking of intensity y or greater, referred to here as the seismic hazard,
- f is an index to faults in the earthquake rupture forecast, $f = 1, 2, \dots, N_f$,
- N_f is number of faults in the earthquake rupture forecast,
- m is moment magnitude, in $\Delta m = 0.1$ -magnitude increments; $m = M_{min}, M_{min} + \Delta m, M_{min} + 2\Delta m, \dots, M_{max,f}$,
- M_{min} is minimum magnitude considered, such as 5.0,
- $M_{max,f}$ is maximum magnitude that fault f is believed to be capable of producing, according to the earthquake rupture forecast,
- ϱ is an index to discrete locations along a fault trace at which earthquake epicenters are discretized, $\varrho = 1, 2, \dots, N_{\varrho,f,m}$,
- $N_{\varrho,f,m}$ is number of discrete locations along fault f at which an earthquake of magnitude m can be centered,
- $\lambda(f, m, \varrho)$ is mean frequency with which fault f can produce earthquakes of magnitude m or greater at location ϱ , according to the earthquake rupture forecast,
- $F_{Y|f,m,\varrho}(y)$ is probability that shaking intensity $Y \leq y$ given an earthquake on fault f of magnitude m with epicenter located at ϱ ,
- a is an index to the ground motion prediction equations used here, $a = 1, 2, \dots, N_a$,

- N_a is number of ground motion prediction equations used,
- Φ is standard normal cumulative distribution function evaluated at the term in parentheses. This thesis assumes that all ground motion prediction equations assume that Y is log-normally distributed conditioned on magnitude, distance, mechanism, etc.
- $\mu_{\ln Y, a}$ is expected value of the natural logarithm of Y under ground motion prediction equation a .
- $\sigma_{\ln Y, a}$ is total standard deviation of the natural logarithm of Y under ground motion prediction equation a .

The annual rate of exceedance of the ground motion amplitude, λ , (inverse of return period T_R) for any seismic intensity level (such as Maximum Design Level - MDL) is determined from a Poisson probability model, (Cornell1968), figure 2.8:

$$\lambda = -\frac{\ln(1 - P_E)}{t} \quad (2.6)$$

where P_E is the probability of occurrence of at least one event (i.e. an earthquake) during the life time t , t is usually taken as 50 years for buildings, and 100 years for dams, 2.9.

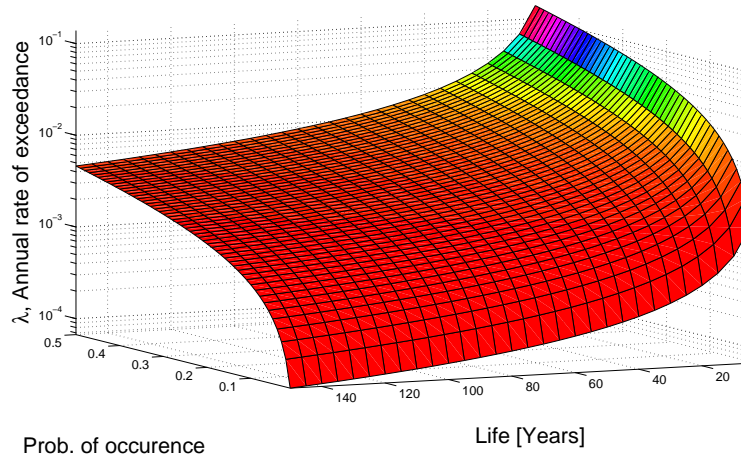


Figure 2.8: Ground motion annual rate of exceedance (Cornell1968).

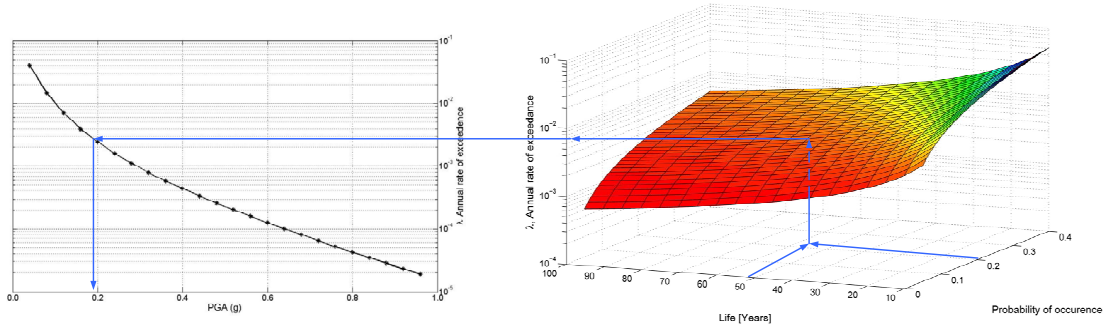


Figure 2.9: Connection between Hazard curve and annual rate of ground motion exceedance

2.3.5 Seismic Hazard De-aggregation

Seismic hazard de-aggregation plots are useful since they can provide a clear vision on contribution of the different parameters in record selection process. Also they can be used for the source identification controlling the hazard at the NCVS site. Figure 9.9 shows the seismic hazard de-aggregation plots for a known site based on different return periods (**USGS2003**). The modal distance, magnitude, and inter-event term can be found in each case.

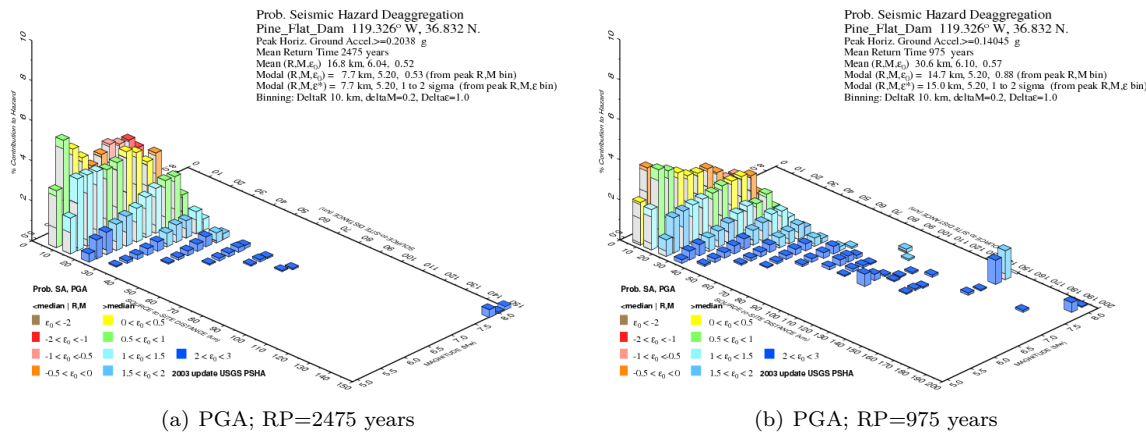


Figure 2.10: Sample seismic de-aggregation plots

2.3.6 Ground motion Selecting and Scaling

2.3.6.1 Target Acceleration Response Spectra

One spectrum is required for each of the several seismic hazard intervals used for analysis which are selected from the site seismic hazard curve. Three types of spectra are acceptable:

- Uniform Hazard Spectra (UHS)
- Conditional Mean Spectra (CMS), and
- Conditional Spectra (CS)

UHS are computed from the seismic hazard curves. This is done by developing hazard curves for several vibration periods to define the response spectra. Then, for a given exceedance probability or return period, the ordinates are taken from the hazard curves for each spectral acceleration, and an “equal hazard response spectrum” is generated. Thus, the response spectra curves are generated for specified return periods of interest, usually 10,000 and 50,000 years, but often at either lower, intermediate, or even higher return periods. Figure 2.11 shows the UHS for only the horizontal direction at the Pine Flat NCVS site.

For frequent events, the UHS and CMS should have similar shape. For infrequent events, the amplitude of a CMS will be smaller at some periods than the UHS as the conditional mean spectrum quantifies a less conservative and more realistic spectrum for a single earthquake. The conditional spectrum differs from the conditional mean spectrum only in that it considers uncertainty in spectral values. The use of either conditional mean spectra or conditional spectra will provide more accurate estimates of response for a given intensity of earthquake shaking than the UHS, but additional effort is required to generate these types of spectra.

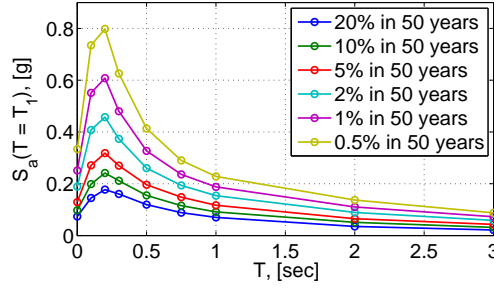


Figure 2.11: Uniform seismic hazard spectra for Pine Flat dam

It should be mentioned that the aforementioned procedure deals with spectra for horizontal motion. The vertical acceleration response spectrum, $S_a^V(T)$, can be constructed by scaling the corresponding ordinates of the horizontal response spectrum, $S_a^H(T)$, as follows:

$$S_a^V(T) = S_a^H(T) \times \begin{cases} 1 & T \leq 0.1\text{sec} \\ 1 - 1.048(\log(T) + 1) & 0.1\text{sec} < T \leq 0.3\text{sec} \\ 0.5 & 0.3\text{sec} < T \leq 1.0\text{sec} \end{cases} \quad (2.7)$$

For IBPA any spectrum of the user's choice can be used. The spectral shape should be consistent with the site's geologic characteristics. For SBPA the target spectrum should be derived directly from appropriate attenuation relationships. For TBPA one spectrum is required for each of the several seismic hazard intervals, selected from the seismic hazard curve for the site (**ATC-58-1**).

2.3.6.2 Ground Motion Scaling Methods

include selection of ground motions: a) peer site; b) matlab/Baker

This section provides a brief description on different ground motion scaling methods for nonlinear analysis. There are four widely-used categories in which a ground motion (or a set of ground motions) can be fitted to the desired target response spectrum:

Ground motion scaling in time domain, where the selected ground motion(s) is (are) scaled up or down using a constant coefficient to match the target response spectrum. This method can be divided into four categories:

- Scaling the response spectrum of a single ground motion to match the target spectrum only at the peak ground acceleration (PGA), figure 2.12(a).
- Scaling the response spectrum of a single ground motion to match the target spectrum only at the specific period, usually fundamental vibrational period ($S_a(T_1)$), figure 2.12(b).
- Scaling the response spectrum of a single ground motion to match the target spectrum at the desired period range by minimizing the error function, figure 2.12(c).
- Scaling the response spectra of a set of ground motions to the target spectrum. In this method median spectrum of the selected ground motions is scaled to match the target one in the desired period range, figure 2.12(d).

Spectral matching in frequency domain, where a real ground motion record is used in order to generate the acceleration time history that matches the target response spectrum. In this method, an iterative procedure is repeated to filter the ground motion in the frequency domain.

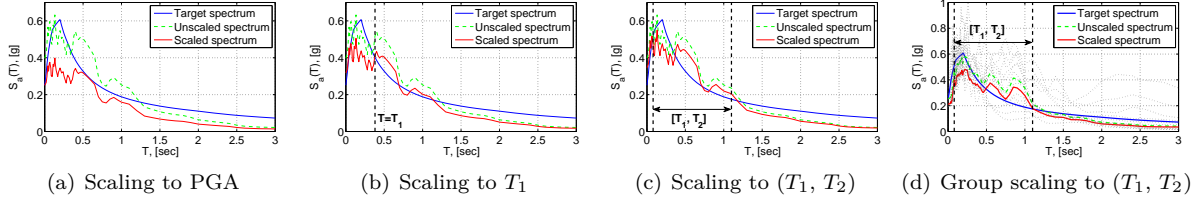


Figure 2.12: Different time-domain scaling of the ground motions

Spectral matching by Wavelets tries to match the ground motion response spectrum iteratively to the target response spectrum by adding wavelets having specified period range and limited duration to the initial (original) time history.

Spectrum compatible artificial ground motion is generated in a way that its acceleration response spectrum matches to the target one with the predefined accuracy. They can be generated with different duration and shape. Usually seismic hazard analysis of the site is required to find out the appropriate combination of the magnitude and distance (seismic hazard de-aggregation plots).

2.3.6.3 Ground Motion Selection and Scaling

It is recommended to amplitude scaling of the ground motions in a way that provide acceptable consistency, both individually and in a mean sense, to the target spectrum over a desired period range, T_{min} to T_{max} . The structures's small-amplitude fundamental period of vibration is denoted here by T_1 . Motions are scaled at this period. After a target spectrum has been defined ground motions are selected and scaled to be consistent with the target spectrum over a period range $[T_{min}, T_{max}]$. T_{max} is taken as $2T_1$ and period T_{min} should typically be taken as $0.2T_1$ (**ATC-58-1**). If substantial response and damage can occur due to response in modes having periods smaller than T_{min} , T_{min} should be selected to be sufficiently small to capture these important behaviors.

Let's also point out that the selected period range should considers all the effective modes contributing to the vibrational response of the structures(i.e. the contributed effective mass equals at least 90% of the total mass).

The intent of ground motion selection is to obtain a set of motions that will produce unbiased estimates of structural response when used with nonlinear response-history analysis. When there is significant scatter in spectral shape of the selected records or a poor fit to the target spectrum, 11 or more triplets of motions may be needed to produce reasonable estimates of median response. Use of fewer than 7 motion pairs is not recommended regardless of the goodness of fit of the spectra of the selected motions to that of the target. We denote by n the number of ground motion triplets required for each level of excitation. For simplicity, we recommend $n = 11$, although more may be used. In any case the number of required ground motions for the IBPA is estimated as (**Huang2011**):

$$n \approx \left(\frac{\beta}{X_{bound}} \Phi^{-1} \left(1 + \frac{C_L}{2} \right) \right)^2 \quad (2.8)$$

where X_{bound} is the bound for the required accuracy (e.g., $1 \pm X_{bound}$ of the true value), C_L is the required confidence level, and β is the dispersion in the displacement response given the scaling procedure. Note that $n = 11$ is selected because it generally produces a reasonable estimate of median structural response (within

$X_{bound} = \pm 20\%$) with reasonable confidence ($C_L = 75\%$) for the system with relatively large dispersion ($\beta = 0.52$). Using $n = 11$ structural analyses for each level of seismic excitation is practical for 2D models, but may be impractical for 3D model when the analyst lacks access to super-computing or massively parallel computing resources.

To the extent possible, select triplets of earthquake ground motions whose horizontal components have spectral shape similar to that of the target spectrum over the range of periods $[T_{min}, T_{max}]$. Additional factors to consider include selecting records having faulting mechanism, earthquake magnitude, site-to-source distance and local geology that are similar to those that dominate the seismic hazard at the particular intensity level, although these are not as significant as the overall spectral shape.

2.3.7 Potential Intensity measure Parameter

As mentioned in the previous sections, the first step in the PBEE-2 framework is to determine the ground motion intensity measure (IM) parameter. **HaririSaoumaPSDM** provided a comprehensive list of possible IM parameters for concrete dams, Table 2.1. They are reviewed here and the “optimal” one will be selected in the next sections. Those seven distinct categories are:

- Category I: Unscalable IMs
- Category II: Ground Motion Dependent Scalar IMs
- Category III: Ground Motion Dependent Compound IMs
- Category VI: Structure-Independent Spectral IMs
- Category V: Structure-Dependent Spectral IMs
- Category VI: Vector-Based IMs
- Category VII: IM for Multiple-Component Ground Motions

2.4 Sensitivity and Uncertainty Quantification

The random variables (RVs) can be categorized as aleatory or epistemic (**KiureghianDitlevsen2009**). An aleatory uncertainty is presumed to be the intrinsic randomness of a phenomenon, while an epistemic one is due to lack of knowledge. The basic qualifier refers to directly observable quantities such as material properties (strength and stiffness), loads (earthquake magnitude and sea wave height), environmental phenomena (temperature, alkali-aggregate reaction), and geometric dimensions (section size).

Note that there is a third source of uncertainty usually referred to “lexical uncertainty” which is due to subjective definition of parameters and hence, shows the lack of definite or sharp distinction (**moller2003safety**).

After developing the detailed finite element model of the dam-reservoir-foundation system, appropriate properties should be assigned to the numerical model. This can be performed by system identification and micro-geodesic measurements. Even though there is still some uncertainty in the material property due to heterogeneous distribution of the material properties. On the other hand, some of the advanced nonlinear models (e.g. cohesive crack models) contains many parameters that either cannot be directly determined in the field or are very expensive to determine. In any case, sensitivity and uncertainty analyses should be performed first to determine the impact of each RV on the results.

Table 2.1: Comprehensive list of candidate IM parameters

Category	Description	IM	Mathematical definition
I	Moment magnitude	M_w	-
	Rapture distance	R_{rup}	-
	Significant duration	t_{sig}	$t_{0.95I_A} - t_{0.05I_A}$
	Seismological duration	D_{5-75}	$t_{0.75I_A} - t_{0.05I_A}$
	Predominant period (acceleration)	T_p^{accel}	-
	Predominant period (velocity)	T_p^{vel}	-
II	Peak ground acceleration	PGA	$\max(\ddot{u}(t))$
	Peak ground velocity	PGV	$\max(\dot{u}(t))$
	Peak ground displacement	PGD	$\max(u(t))$
	Root-mean-square of acceleration	a_{RMS}	$\sqrt{\frac{1}{t_{tot}} \int_0^{t_{tot}} (\ddot{u}(t))^2 dt}$
	Root-mean-square of velocity	v_{RMS}	$\sqrt{\frac{1}{t_{tot}} \int_0^{t_{tot}} (\dot{u}(t))^2 dt}$
	Root-mean-square of displacement	u_{RMS}	$\sqrt{\frac{1}{t_{tot}} \int_0^{t_{tot}} (u(t))^2 dt}$
	Arias intensity	I_A	$\frac{\pi}{2g} \int_0^{t_{tot}} (\ddot{u}(t))^2 dt$
	Specific energy density	SED	$\int_0^{t_{tot}} (\dot{u}(t))^2 dt$
	Cumulative absolute velocity	CAV	$\int_0^{t_{tot}} \dot{u}(t) dt$
	Cumulative absolute displacement	CAD	$\int_0^{t_{tot}} \dot{u}(t) dt$
III	Peak velocity to acceleration ratio	$I_{v/a}$	$(PGA)^{-1} (PGV)^{+1}$
	Characteristics intensity	I_C	$(a_{RMS})^{+3/2} (t_{sig})^{+1/2}$
	Riddell Garcia acceleration index	I_a	$(PGA)^{+1} (t_{sig})^{+1/3}$
	Riddell Garcia velocity index	I_v	$(PGV)^{+2/3} (t_{sig})^{+1/3}$
	Riddell Garcia displacement index	I_d	$(PGD)^{+1} (t_{sig})^{+1/3}$
	Fajfar index	I_F	$(PGV)^{+1} (t_{sig})^{+1/4}$
	Cosenza index	I_D	$\frac{2g}{\pi} (PGA)^{-1} (PGV)^{-1} (I_A)^{+1}$
	Shaking intensity rate	SIR	$(I_{A5-75})(D_{5-75})^{-1}$
VI	Acceleration spectrum intensity	ASI	$\int_{0.1}^{0.5} S_a(T, \xi = 5\%) dT$
	Velocity spectrum intensity	VSI	$\int_{0.1}^{2.5} S_v(T, \xi = 5\%) dT$
	Displacement spectrum intensity	DSI	$\int_{2.0}^{5.0} S_d(T, \xi = 5\%) dT$
	Effective peak acceleration	EPA	$\frac{1}{2.5 \times 0.4} \times \int_{0.1}^{0.5} S_a(T, \xi = 5\%) dT$
	Effective peak velocity	EPV	$\frac{1}{2.5 \times 0.4} \times \int_{0.1}^{1.2} S_v(T, \xi = 5\%) dT$
V	First-mode spectral acceleration	$S_a(T_1)$	$S_a(T_1, \xi = 5\%)$
	First-mode spectral velocity	$S_v(T_1)$	$S_v(T_1, \xi = 5\%)$
	First-mode spectral displacement	$S_d(T_1)$	$S_d(T_1, \xi = 5\%)$
	Spectral acceleration at predominant period	$S_a(T_p^{accel})$	-
	Spectral velocity at predominant period	$S_v(T_p^{vel})$	-
	Combined (mode 1 to 2) spectral acceleration	S_a^{1-to-2}	$\sum_{i=1}^2 (S_a(T_i, \xi))^{\alpha_i}, \alpha_i = \frac{m_i^{eff}}{\sum_{i=1}^2 m_i^{eff}}$
	Combined (mode 1 to 3) spectral acceleration	S_a^{1-to-3}	$\sum_{i=1}^3 (S_a(T_i, \xi))^{\alpha_i}, \alpha_i = \frac{m_i^{eff}}{\sum_{i=1}^3 m_i^{eff}}$
	Combined (mode 1 to 4) spectral acceleration	S_a^{1-to-4}	$\sum_{i=1}^4 (S_a(T_i, \xi))^{\alpha_i}, \alpha_i = \frac{m_i^{eff}}{\sum_{i=1}^4 m_i^{eff}}$
	Combined (mode 1 to 5) spectral acceleration	S_a^{1-to-5}	$\sum_{i=1}^5 (S_a(T_i, \xi))^{\alpha_i}, \alpha_i = \frac{m_i^{eff}}{\sum_{i=1}^5 m_i^{eff}}$

2.4.1 Analyses

2.4.1.1 Sensitivity

Sensitivity analysis determines the impact of a variation in an input parameter on output results. Mathematically, this corresponds to the partial derivative of the output function with respect to an input parameter at a given design point.

The procedure starts with the identification of the basic RVs, $\mathbf{X} = (X_1, \dots, X_n)$, and their corresponding distributional model (e.g. normal, log-normal). Then, $2n + 1$ analyses are performed **etlr1** using mean (X_i^{mean}), minimum (X_i^{min}) and maximum (X_i^{max}) values of the RVs. The response can be mathematically

expressed in terms of

$$\Theta = f(X_1, X_2, \dots, X_i, \dots, X_n) \quad (2.9)$$

A reference response Θ^{Ref} is first computed in terms of the n RVs in $S = \{1, 2, \dots, n\}$ equal to their mean values

$$\Theta^{\text{Ref}} = f(X_i^{\text{mean}}), \forall i \in S \quad (2.10)$$

Then $2n$ analyses are performed, each corresponding to a given maximum or minimum of a RV, while all others are set to their mean value

$$\begin{aligned} \Theta_i^{\min} &= f(X_i^{\min}, X_j^{\text{mean}}), i = RV, \forall j \in S \wedge j \neq i \\ \Theta_i^{\max} &= f(X_i^{\max}, X_j^{\text{mean}}), i = RV, \forall j \in S \wedge j \neq i \end{aligned} \quad (2.11)$$

The swing for each of the n RVs is computed next

$$\Theta_i^{\text{swing}} = |\Theta_i^{\max} - \Theta_i^{\min}| \quad (2.12)$$

and are sorted in descending order. Finally, the Tornado diagram is plotted and one has to arbitrarily decide what are the most sensitive RVs, figure 2.13.

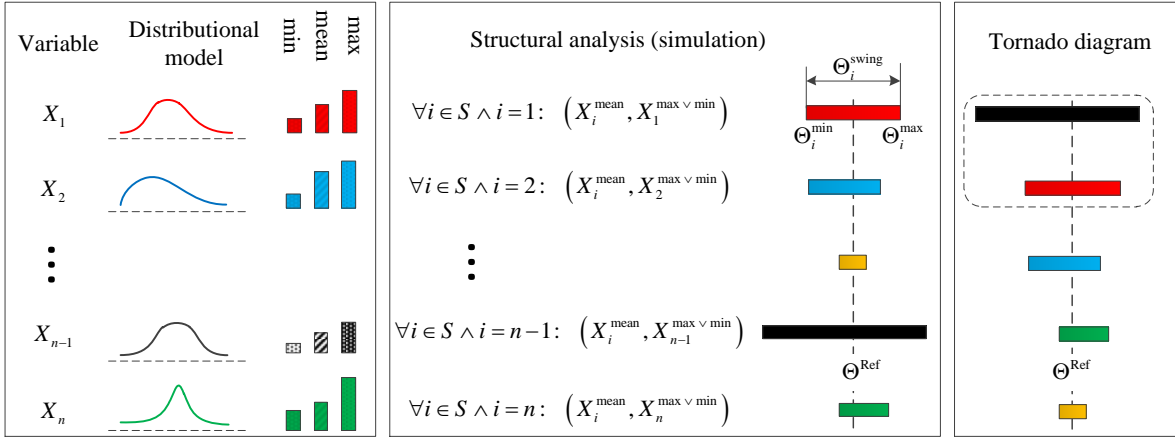


Figure 2.13: Sensitivity analysis using Tornado diagram

2.4.1.2 Uncertainty

The input factors of models are unfortunately not always known with a sufficient degree of certainty which can be caused by natural variations as well as by errors and uncertainties associated with measurements.

The uncertainty of input parameters is often expressed in terms of probability distributions; it can also be specified by samples of measured values, i.e. empirical probability distributions. The uncertainties of the different input parameters may have dependencies on each other, i.e. they may be correlated. Generally, the main reason of performing an uncertainty analysis is to assess the uncertainty in the model output that arises from uncertainty in the input RVs.

If we consider the distribution of the uncertain input RV x , the cumulative distribution function $\Phi(x)$

(CDF) gives the probability P that the variable X will be less than or equal to x :

$$\Phi(x) = P(X \leq x) \quad (2.13)$$

Also, the uncertainty of the input RVs can be described with probability density functions (PDF) $\phi(x)$ (the gradient of the CDF):

$$\phi(x) = \frac{d\Phi(x)}{dx} \quad (2.14)$$

Following are the PDF for some of the most important distributional models used to quantify the material and modeling uncertainty in NCVS engineering:

$$\phi(x) = \begin{cases} \frac{1}{\sigma\sqrt{2\pi}} e^{-\frac{1}{2}\left(\frac{x-\mu}{\sigma}\right)^2} & \text{Normal} \\ \frac{1}{x\sigma\sqrt{2\pi}} e^{-\frac{1}{2}\left(\frac{\log x - \mu}{\sigma}\right)^2} & \text{Log-normal} \\ 0 & \text{for } x \notin (a, b) \\ \frac{1}{b-a} & \text{for } x \in (a, b) \\ \alpha e^{\alpha x} & \text{Exponential} \\ \frac{\frac{\mu-x}{\sigma}}{e^{\frac{\mu-x}{\sigma}} - e^{-\frac{\mu-x}{\sigma}}} & \text{Gumbel} \end{cases} \quad (2.15)$$

2.4.2 Data Preparation

2.4.2.1 Sampling Techniques

Sampling of the distributional model is indeed a key element of an uncertainty analysis. By far, the most widely used sampling method is the so-called Monte Carlo Simulation (MCS). In crude MCS, probability of failure P_f is estimated by:

$$P_f = \frac{1}{n} \sum_{i=1}^n I(g(\mathbf{u}_i)) ; \quad I(g(\mathbf{u}_i)) = \begin{cases} 0 & \text{if } g(\mathbf{u}) > 0 \\ 1 & \text{if } g(\mathbf{u}) \leq 0 \end{cases} \quad (2.16)$$

where n is the number of simulations, $g(\mathbf{u})$ is failure function, \mathbf{u}_i is sample number, and I is failure indicator function. The standard error of P_f is estimated by:

$$s_{err} = \sqrt{\frac{P_f(1 - P_f)}{n}} \quad (2.17)$$

Success of the crude MCS depends on a very large number of analysis. As a palliative to this handicap, an improved sampling method is achieved through the so-called Latin Hypercube Sampling (LHS) **ImanConover1982**. LHS guarantees samples to be drawn over the whole range of the distribution and proceeds as follows. Given a system with basic RVs, $\mathbf{X} = (X_1, \dots, X_n)$ and corresponding distributions D_1, \dots, D_n , first the range of each variable is split into m non-overlapping intervals of equal marginal probability $1/m$. Then, sampling starts with the random selection of an interval followed by another random selection of a point inside it. The procedure is repeated until all intervals have been accessed, and none of them more than once. This procedure is repeated for each of the n RVs. It is noteworthy that should there be a single RV, then one could evaluate each interval sequentially. However should there be two or more RVs, then the random access of the combination of interval is essential. So far, the maximum number of combinations for

a LHS with m divisions and n RVs can be computed as:

$$N_{combo}^{LHS} = \left(\prod_{i=0}^{m-1} (m-i) \right)^{n-1} = (m!)^{n-1} \quad (2.18)$$

Although there is no specific value for the minimum or optimum sample size in LHS, the following recommendation can be used for different confidence levels, C_L :

$$n > \frac{-\ln(1 - C_L)}{P_f} \quad (2.19)$$

2.4.2.2 Type of RV Correlation

It is possible to account for the correlation among the RVs. The correlation coefficient is bounded by $[-1, +1]$. It will have value of zero when the covariance (among the RVs) is zero and value of ± 1 when the RVs are perfectly correlated or anti-correlated. Figure 2.14 illustrated three case with MCS, LHS and correlation effect, where only two RVs are assumed to exists.

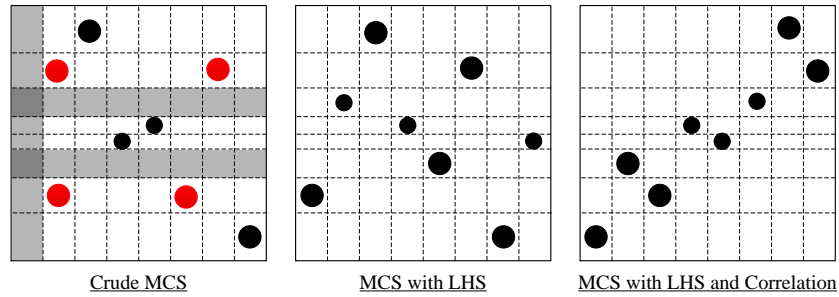


Figure 2.14: Sampling of a system with two RVs

In general, it is possible to account for three types of correlations in NCVS engineering problems:

- **Multivariate correlation:** For the real world application on concrete dams, many of the material properties in mass concrete, foundation rock, interface joint, ... may be assumed as RVs. Usually there are partial correlation among these individual RVs (e.g. concrete modulus of elasticity and compressive strength). Figure 2.15 shows the correlation matrix for the concrete-rock interface joint element adapted from **HaririSaoumaSensitivity**.
- **Spatial correlation:** Spatial variability of structural properties (i.e. material properties) is very important which can have substantial impact on the structural damage and failure (e.g. crack initiation and localization in homogeneous stress state region). Figure 2.16 shows three realizations based on LHS and “random fields” theory (**olsson2002latin**) for the fracture energy, G_f , at the concrete-rock interface (60 m \times 15 m area). Three different correlation lengths are assumed $d_{corr} = 2, 10$ and 20 m (which follows the square exponential model). Applications of material spatial correlation in NCVS engineering can be found in **deAraujoAwruch1998**, **krounis2015effects**, **bernier2015seismic** and **altarejos2015advances**.
- **Temporal correlation:** Temporal uncertainty are related to time-dependent variability and can be considered in two levels (**nokland2009review**):
 - Temporal prediction: (1) uncertainty in future states; (2) apparent inherent randomness of nature;

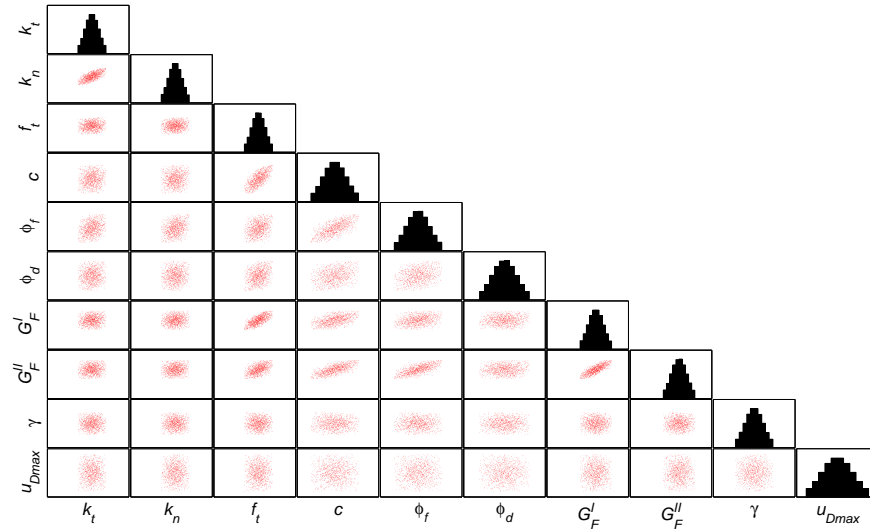


Figure 2.15: Multivariate partial correlation matrix for fracture mechanics-based zero thickness joint element at the dam-foundation interface

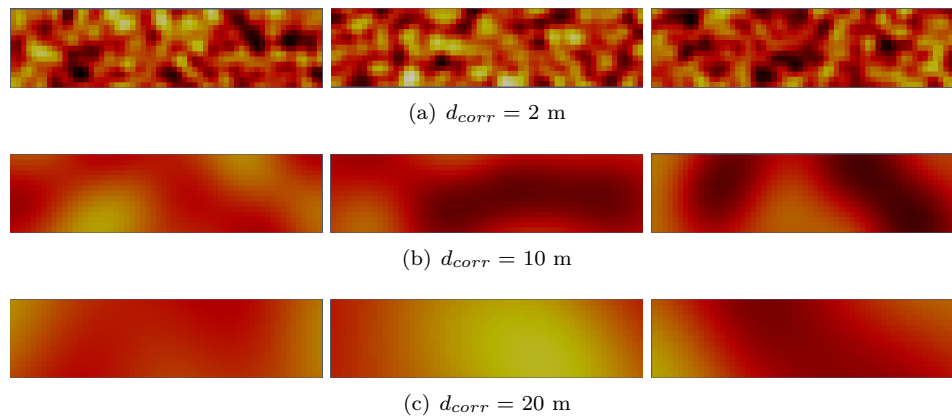


Figure 2.16: Spatial correlation of fracture energy, G_f , at the dam-foundation interface area; three sample realization for each correlation length

- (3) luck in the short run (unusual combination of outcomes); (4) Inconsistent human behavior;
- (5) nonlinear dynamic (chaotic) systems behavior; individual vs. expected values behavior.
- Temporal retrodiction: (1) uncertainty in past state; (2) incomplete historical data (measurement error); (3) biased history (bias error); (4) changing system parameters preventing identical conditions to be revisited (systematic error).

Figure 2.17 shows the temporal correlation in concrete tensile strength, f_t , of an AAR-affected structure over the 100 years time period. Time-dependent strength reduction is quantified for over 100 LHS-based simulations.

2.5 Nonlinear Structural Analyses

Having a detailed finite element model, with the capability of accounting for the material and modeling uncertainties, one of the following advanced structural analysis techniques can be adapted to apply the

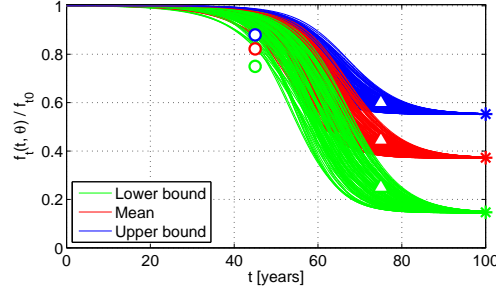


Figure 2.17: Temporal correlation in concrete tensile strength, f_t , of an AAR-affected structure over the 100 years time period

ground motion record-to-record variability as well: 1) Cloud Analysis (CLA), 2) Multiple stripe analysis (MSA), 3) Incremental Dynamic Analysis (IDA), and 4) Endurance Time Analysis (ETA).

2.5.1 Cloud Analysis

CLA is a procedure in which first a NCVS is subjected to a (relatively large) set of (un-scaled or as-recorded) ground motions and is analyzed numerically. If the ground motion records are taken from a bin, they can represent an earthquake scenario defined by (M_{bin}, R_{bin}) , the magnitude and distance representative of the bin (**JalayerPHD2003**). Then, from the results, EDP *vs.* IM are determined and form the so-called cloud response, figure 6.10(a). CLA method usually is used in conjunction with probabilistic seismic demand analysis (PSDA). Application of CLA and PSDA for concrete gravity dams was discussed by (**HaririSaoumaPSDM**). It is a well-accepted assumption that the discrete data points resulted from CLA have linear trend in the logarithmic scale implying a power form in the arithmetic scale (**PadgettNielsonDesRoches**), (**JankovicStojadinovic2004**), (**RamamoorthyGardoniBracci2006**):

$$\eta_{\text{EDP}|\text{IM}} = a \cdot \text{IM}^b \quad (2.20)$$

where a and b are the regression constants and $\eta_{\text{EDP}|\text{IM}}$ is the median value of EDP given IM. Also, the logarithmic standard deviation is:

$$\beta_{\text{EDP}|\text{IM}} = \sigma_{\ln(\text{EDP}|\text{IM})} \cong \sqrt{\frac{\sum \left(\ln(\text{edp}_i) - \ln(a \cdot \text{IM}^b) \right)^2}{n - 2}} \quad (2.21)$$

where n is the number of nonlinear transient analyses

2.5.2 Incremental Dynamic Analysis

IDA is a dynamic procedure in which first a set of N (usually ~ 30) ground motions are selected. Each ground motion is scaled successively to multiple IM levels (**Vamvatsikos2002a**). Let $\ddot{\mathbf{x}}_g$ be a representative un-scaled acceleration time history (it may already filtered, rotated, or baseline corrected). In order to consider the stronger and weaker scenarios, the ground motion can be scaled uniformly using a scale factor $\lambda_{SF} \in [0, +\infty)$. The scaled ground motion will be $\ddot{\mathbf{x}}_g^{\lambda_{SF}} = \lambda_{SF} \ddot{\mathbf{x}}_g$.

Each of the scaled ground motions, $\ddot{\mathbf{x}}_g^{\lambda_{SF}}$, are then applied to the NCVS separately and the maximum EDP is computed. A single-record IDA curve connects the resulting EDPs corresponding to each ground mo-

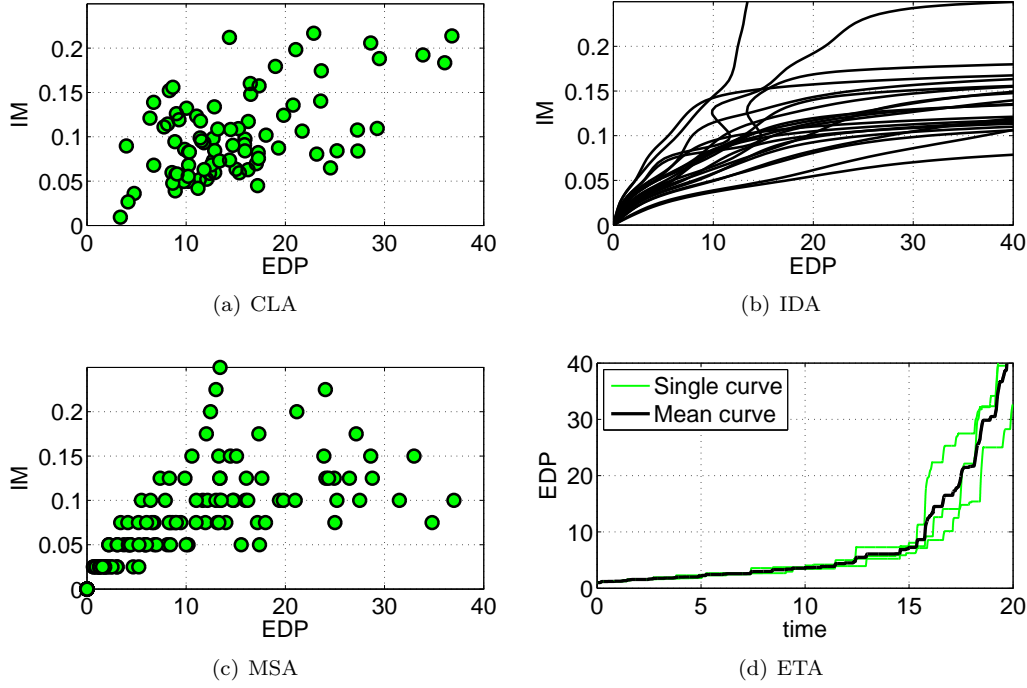


Figure 2.18: Application of advanced nonlinear analysis techniques on concrete dams

tion. Finally, a multiple-record IDA curve is developed, which is a group of N single-record IDA curves, figure 6.10(d). A full IDA procedure for each ground motion results NCVS failure under high scale factors. It corresponds to a flat-line in IDA curve. The IDA method has the capability to extract probabilistic information that describes the global instability collapse limit state (LS) of the dam. Using IDA results, the percentiles of response can be calculated as continuous curves, e.g., the median (50%), the 16th and 84th fractile IDA curves, figure 2.19(a). Record-to-record dispersion in IDA may be estimated directly from the sample curves, or it can be approximated from the corresponding fractile IDAs as (VamvatsikosFragiadakis2010):

$$\begin{aligned}\beta_{\text{IM}|\text{EDP}} &\approx \frac{1}{2} \left(\ln(\text{IM}^{84\%}) - \ln(\text{IM}^{16\%}) \right) \\ \beta_{\text{EDP}|\text{IM}} &\approx \frac{1}{2} \left(\ln(\text{EDP}^{84\%}) - \ln(\text{EDP}^{16\%}) \right)\end{aligned}\quad (2.22)$$

where $\text{IM}^{84\%}$ and $\text{IM}^{16\%}$ are the 84% and 16% values of IM-capacity, while $\text{EDP}^{84\%}$ and $\text{EDP}^{16\%}$ are the 84% and 16% fractiles of the EDP-demand.

Note that if the failure of the NCVS is not the objective of performing nonlinear analysis, the IDA procedure may truncated at any desired level which is usually called truncated IDA method (Baker021113EQS025M). Also, in the case of direct combination of the epistemic and aleatory uncertainties (based on Monte Carlo family methods), the resulted procedure is called extended IDA method DolsekEIDA2011. It is noteworthy that scaling the ground motions with large scale factors may generate records with unrealistic shape Haselton2011.

In the classical IDA application on buildings, it is shown that in an IDA curve a first failure triggered by an im_j may be followed by a non-failure at im_{j+1} and failure again at im_{j+2} . The transition from j to $j+1$ has been labeled as “resurrection” (Vamvatsikos2002a). It was determined that to capture such a

phenomena in concrete dams one must model the concrete nonlinearity (using smeared cracks) in addition to the discrete nonlinear rock/concrete interface (multiple source of failure modes). Figure 2.19 shows three IDA curves associated with three different ground motions for a gravity dam. Also shown in this figure is the resurrection phenomenon for “severe hardening” curve (a failed IM between two non-failed IMs).

Application of IDA for concrete gravity and arch dams were discussed by [Alembagheri2012](#), [Alembagheri2013IDA](#), [alembagheri2013incremental](#), [amirpour2014quantifying](#), [PanXuJin2015](#), [wang2015xfem](#) and [soysal2015investig](#)

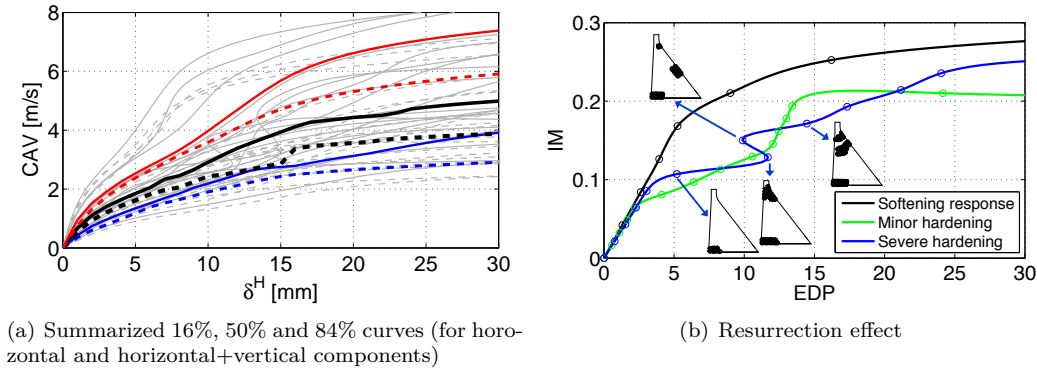


Figure 2.19: Application of IDA on concrete dams

2.5.3 Multiple Stripe Analysis

MSA is a procedure in which a set of m seismic intensity levels (SIL) or stripes are selected first. If $m = 1$ or 2 , this method is called single- or double-stripe analysis (SSA/DSA), respectively. Each stripe in this method corresponds to a specific SIL and it is possible to perform a probabilistic seismic hazard analysis (PSHA) for each one separately. Consequently, N different ground motions may be selected for each of the m stripes ([Cornell-Jalayer2002](#)).

The resulted $N \times m$ ground motions are then used for nonlinear transient analyses of the NCVS and the EDPs are computed. Shown in figure 6.10(c) is a sample plot of MSA with m up to 10. Discrete data points in each strip follow a log-normal distributional model. No scaling is used in MSA and thus it provides more realistic picture of NCVS performance under different earthquake scenarios. Considering that the ground motions are changed in each strip, one cannot connect the discrete data points (similar to IDA) to generate a continuous plot [Baker2007](#).

Application of MSA for a concrete arch NCVS with $m = 3$ SILs and $N = 9$ ground motions in each one is discussed in [HaririSaoumaPorter2015](#). Also, [BernierMonteiroPaultre2016](#) shows the application of MSA for a gravity NCVS in conjunction with conditional spectrum in each hazard level.

2.5.4 Endurance Time Analysis

All the CLA, IDA and MSA methods require large number of nonlinear dynamic analyses and are computationally demanding for dam-reservoir-foundation system. ETA is a dynamic pushover procedure which estimates the seismic performance of the NCVS when subjected to limited number of pre-designed intensifying excitation, which are called endurance time acceleration functions (ETAF). The ETAFs are aimed to shake the NCVS from a low excitation level — with a response in the elastic range — to a medium excitation

level — where the NCVS experiences some nonlinearity — and finally to a high excitation level, which causes the failure. All these responses ranges are experienced in a single time history analysis.

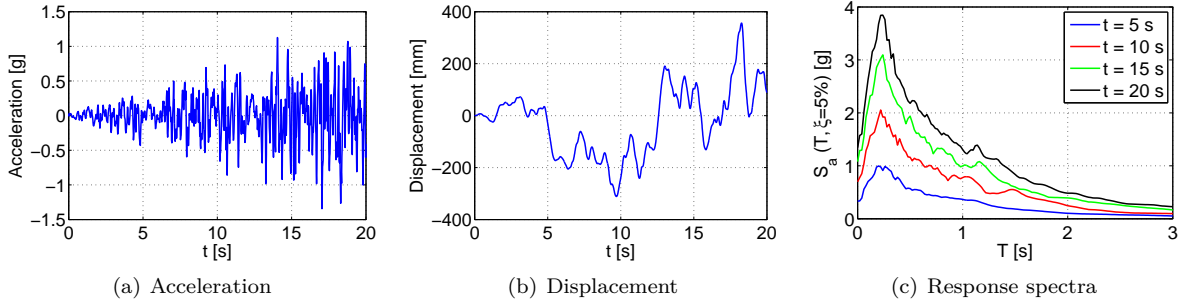


Figure 2.20: Characteristics of a sample ETAF ([hariri2016new](#))

Generation of an ETAF is explained by ([Hariri2014ES](#)). Considering that ETAFs have random nature, usually at least three of them are required to reduce the uncertainty. ETA procedure is identical to a conventional time history analysis except that ETAFs are used as input for the dynamic analyses instead of the real ground motions. Figures 2.20(a) and 2.20(b) show the acceleration and displacement time histories of a sample ETAF, whereas the response spectra are shown in figure 2.20(c) for different time periods. It should be noted that in any given period of time, the response spectrum of the ETAF remains proportional to the target one, i.e. the response spectrum at $t = 10$ s is twice the intensity of the spectrum at $t = 5$ s and half the intensity at $t = 20$ s.

Figure 6.10(b) shows the results of three ETA and also the mean curve. In this method, failure corresponds to a vertical line in ETA curve. The mean ETA curve is analogous to the one of the pushover analysis (POA) or median of IDA ([HaririSaoumaPorter2015](#)). Note that in figure 6.10(b) the vertical axis refers to the maximum absolute values of EDP during the time interval from 0 to t , (see Eq. 10.1) and the horizontal axis is time.

$$\Omega(\text{EDP}(t)) \equiv \max \{ \text{Abs}(\text{EDP}(\tau)) : \tau \in [0, t] \} \quad (2.23)$$

Finally, the “time” parameter may be converted to any desired IM parameter, e.g. peak ground acceleration (PGA), first-mode spectral acceleration ($S_a(T_1)$), etc. Application of this method for gravity and arch dams can be found in [HaririSaouma2014DI](#), [MeghellaFurgani2014](#), [hariri2014AJST](#), [hariri2014ksce](#).

2.6 Capacity Functions

whereas the conventional capacity curve is referred to a nonlinear force-displacement curve ([Freeman1978](#)), a “capacity function” is defined as a relationship between an external (or internal) parameter affects the capacity of the structure, referred as “stressor” and “response” of the system in the macro level ([HaririPHD2015](#)). The capacity function is a more general concept and can be used by any initiators and is not limited to only seismic action.

Stressor: can be 1) incrementally increasing monotonic, cyclic or time-dependent load (or displacement, acceleration, pressure); 2) incrementally decreasing the resistance parameter or degradation of the

strength properties; and 3) discrete increasing/decreasing critical parameter in a system leads to failure. In PBEE language, stressor should be referred to IM parameter (**Porter2003**).

Response: is a representative of the system behavior under the varying stressor. It is represented either in an absolute sense or relative one. Response can be 1) single damage variable (DV) such as drift and energy dissipation, 2) combination of several DVs in term of damage index (DI); and 3) any safety monitoring index (**WangGuBao2013**). In PBEE language, the un-processed response is usually called EDP (**Vamvatsikos2004a**).

Under the seismic action, the capacity function represents the continuous 2D (curve) or 3D (surface) plot of stressor (i.e. IM) vs. response (i.e. EDP). Some of the structural analysis techniques are capable of generating this plot by default, e.g. ETA (figure 6.10(b)); some requires interpolation, e.g. IDA (figure 6.10(d)); some other requires curve fitting, e.g. CLA (figure 6.10(a)), while some other cannot produce such a continuous plot due to nature of analyses, e.g. MSA (figure 6.10(c)).

Figure 2.21 shows a smoothed 2D capacity function for an arch NCVS obtained from ETA method. The evolution of damage and different limit states can be recognized on this figure. Although this figure shows a qualitative measure of the LSs, the next step in the proposed hybrid method discusses on the quantification of them in term of performance and damage indices.

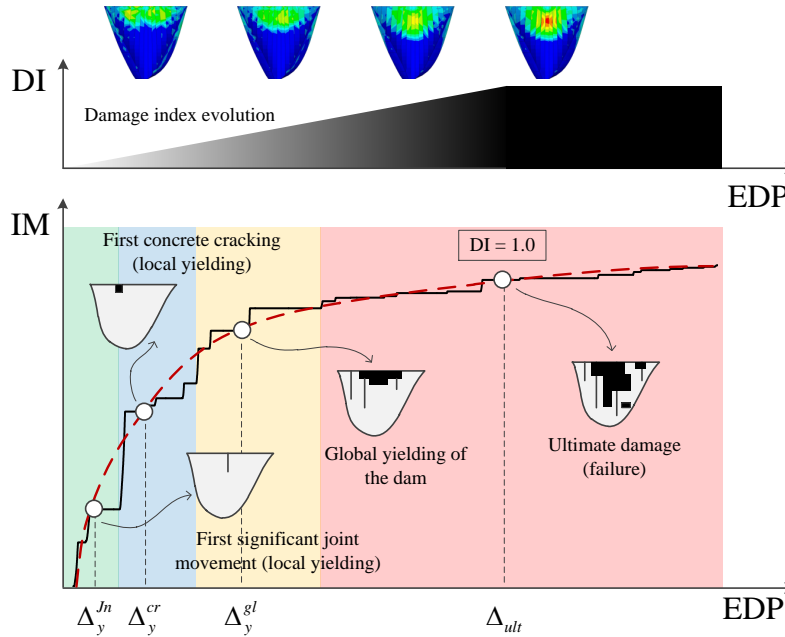


Figure 2.21: Schematic of ETA-based capacity function for arch dams (**hariri2016new**)

2.7 Damage Index

Damage index (DI) is defined as a function of one or more damage variable (DVs). It is a quantity set to zero in the absence of any damage and unity when failure or collapse occurs, $DI \in [0, 1]$ (**hariri2016new**):

$$DI = f(DV_i) , \quad i = 1, \dots, N \quad (2.24)$$

where n is the number of contributor DVs. If $n = 1$, it is called single-variable DI and if $n > 1$, it is a multiple-variable DI (**Kappos1997**). The most popular form for the evolution of damage index can be written as:

$$DI = \prod_{i=1}^N \left(\frac{DV_i - DV_{L_i}}{DV_i - DV_{U_i}} \right)^{\kappa_i} \quad (2.25)$$

where DV_{L_i} and DV_{U_i} are the lower and upper boundaries (threshold) of the i^{th} damage variable and κ is an exponent related to the rate of the changes in damage index at different stages of the damage variable. Figure 2.22 illustrates four different models based on combination of κ_i for a hypothetical DI with two DVs.

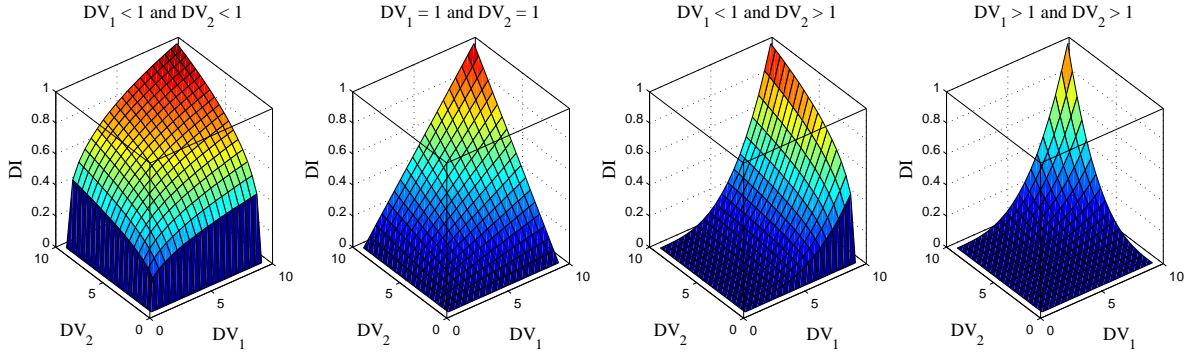


Figure 2.22: Relationships between a DI and two DVs

Damage indices can be classified based on different applications (**HaririSaouma2014DI**):

- *Local* vs. *Global*: Local DI is an indicator of damage in an element, member, or limited part of the structure. The global DI on the other hand captures damage state in an entire. The global DI can be computed by weighted summation of the local DIs.
- *Single-variable* vs. *Multi-variable*: The DI can be computed either from a single variable or from a combination of several ones. Usually combined DI takes into account different parameters and provides a more comprehensive indicator of the damage progress.
- *Cumulative* vs. *Non-cumulative*: A cumulative DI is capable of capturing the accumulation of the damage during the transient analysis, whereas a non-cumulative one can only capture the end state.
- *Deterministic* vs. *Stochastic*: As all materials are heterogeneous, the DI may or may not capture this heterogeneity through stochastic or deterministic expressions.
- *Damage index* vs. *Damage spectrum*: Damage spectrum represents variation of the damage index versus the structural period for a series of single-degree-of-freedom systems subjected to a ground motion record **BozorgniaBertero2003**.
- *Structural* vs. *Economical*: Structural DI captures the damage in terms of structural parameters. On the other hand, an economical DI would introduce concepts of cost such as the ratio of repair cost to corresponding replacement cost.

In this paper the main DVs used to characterize the DIs are displacement, cracking (either smeared crack or discrete one), and energy-dissipation which are combined based on NCVS type:

2.8 Fragility Analyses

2.8.1 Fundamentals

First it is important to distinguish among some terms, their definition and their relationship. In general, a “fragility function”, as described by **PorterEEE2015**, *expresses the probability that an undesirable event will occur as a function of the value of some (potentially uncertain) environmental excitation*.

2.8.1.1 Fragility Curve vs. Surface

Fragility function is a general term and may be referred to 2D “fragility curve” or 3D “fragility surface”:

- Fragility curve is a continuous function showing the probability of exceedance of a certain limit state (LS) for specific level of ground motion intensity measure (IM) (**Ellingwood2009179**), figure 5.13:

$$\text{Fragility} = P[\text{LS}|\text{IM} = im] \quad (2.26)$$

where $P[A|B]$ is the conditional probability that A is true given that B is true. In addition, im refers to a particular value of IM, i.e., there is no uncertainty.

Alternatively, fragility can be defined as (**JalayerFranchinPinto2007**):

$$\text{Fragility} = P[D \geq C_{\text{LS}}|\text{IM} = im] = P\left[\frac{D}{C_{\text{LS}}} \geq 1|\text{IM} = im\right] = P[Y \geq 1|\text{IM} = im] \quad (2.27)$$

where D is the demand parameter and C_{LS} is the capacity associated with the given LS. Note that Y may be in the component or structure level.

In the context of performance-based earthquake engineering (PBEE), where the structural responses are expressed as engineering demand parameter (EDP), the fragility can be defined as:

$$\text{Fragility} = P[\text{EDP} \geq edp|\text{IM} = im] \quad (2.28)$$

where edp is a specific threshold value of EDP.

- Fragility surface is a three-dimensional version of fragility curves and can be expressed in one of the following ways:
 - Fragility surface with vectorized IM is a continuous function showing the probability of exceedance of a certain LS conditioned on two IM parameters. For such a system the fragility definition in Eq. 5.1 should be replaced with (**Bojorquez2013**):

$$\text{Fragility} = P[\text{LS}|\text{IM}_1 = im_1, \text{IM}_2 = im_2] \quad (2.29)$$

The two IMs can be among un-scalable parameters, e.g. $\langle M_w, R_{rup} \rangle$ (earthquake magnitude and distance), or the scalable ones, e.g. $\langle S_a(T_1), I_A \rangle$ (first-mode spectral acceleration and Arias intensity) (**modica2014vector**), figure 2.24(a).

- Fragility surface which is a function of an external parameter (or variable). Usually this parameter is time. The resulted fragility surface showing the time-dependent seismic behavior (aging, deterioration, creep) of the structural system. For such a system the fragility is defined

as (ghosh2010aging):

$$\text{Fragility} = P[\text{LS}(t)|\text{IM} = im] \quad (2.30)$$

Sample of a fragility surface for a system with the capability of aging in 30 years is plotted in figure 2.24(b). As seen, aging reduces the capacity and increases probability of exceedance of a certain LS.

- Fragility surface with scalar IM but for a range of $\text{LS} \in [\text{LS}_{\min}, \text{LS}_{\max}]$ as a continuous function. This can be used when there is a no established criterion for the LS in a new structure. Note that the governing equation in this case is again similar to Eq. 5.1 while a “for loop” is required on LS from LS_{\min} to LS_{\max} . Figure 2.24(c) shows a sample of fragility surface with varying LS that normalized based on $\frac{\text{LS} - \text{LS}_{\min}}{\text{LS}_{\max} - \text{LS}_{\min}}$.

2.8.1.2 Fragility vs. Vulnerability vs. Hazard

Although the main focus of this paper is on fragility curves; however, two other terms need to be clearly defined and distinguished, i.e. vulnerability curves and hazard curves:

- Vulnerability curves: Vulnerability is different from fragility (PorterEEE2015). The former measures loss (in terms dollars, deaths, and downtime) while the later measures probability. A vulnerability curve expresses the loss as a function of IM parameter. Three major types of vulnerability curves are:
 - Measuring repair cost: In such a case the repair cost is normalized by the replacement cost new and is called damage factor. The expected value of damage factor conditioned on IM parameter is called mean damage factor, figure 2.23(b).
 - Measuring life-safety: In such a case the number of casualties is normalized by the number of indoor occupants and expressed as a function of IM parameter.
 - Measuring downtime: It is measured in terms of fraction of a year during which the structure cannot be used.
- Hazard curves: It expresses a plot where the horizontal axis is the IM at a site and the vertical one is annual frequency of exceedance, λ , (inverse of the return period, T_R), figure 2.23(c). Hazard curves are usually obtained by performing a probabilistic seismic hazard analysis (PSHA).

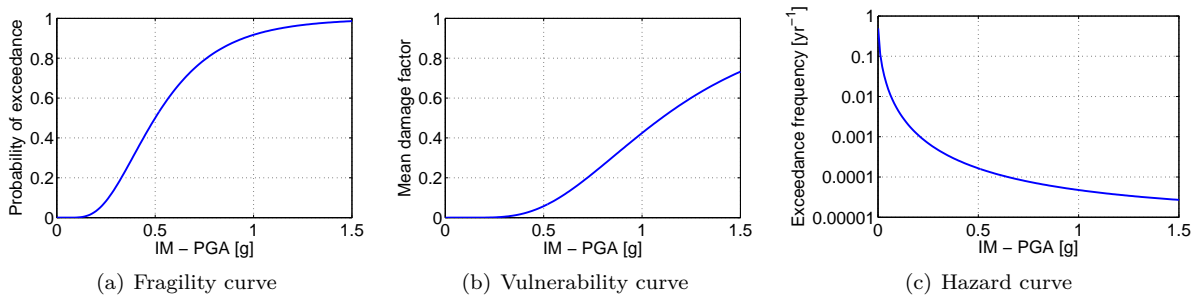


Figure 2.23: Comparison of seismic fragility, vulnerability and hazard curves

Note that the seismic hazard curve for an IM, λ_{IM} , (result of PSHA) can be combined with seismic fragility curve (the result of structural analysis) to obtain the mean annual frequency of exceeding a specified EDP

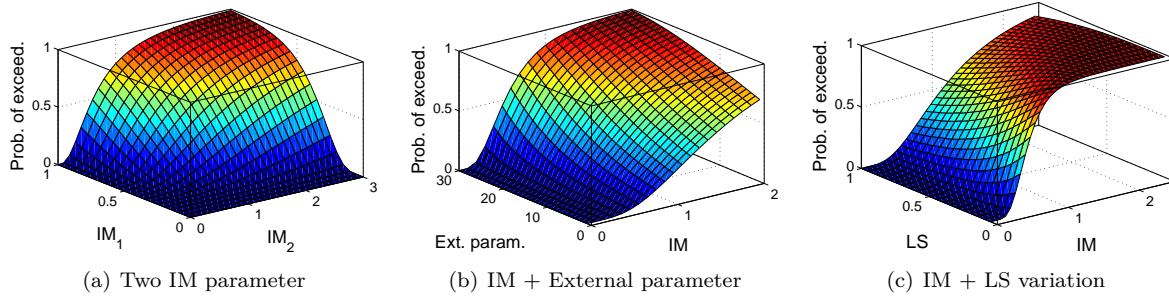


Figure 2.24: Different aspects of seismic fragility surfaces

value, λ_{EDP} , as (TothongLuco2007):

$$\lambda_{EDP}(edp) = \int_{im} P[EDP \geq edp | IM = im] \cdot |d\lambda_{IM}(im)| \quad (2.31)$$

where $d\lambda_{IM}(im)$ is the slope of hazard curve and the absolute value is used because the slope is negative.

2.8.1.3 Continuous Function vs. Discrete Matrix

Based on another classification, the results of a fragility analysis can be represented either as a continuous function, i.e. fragility curve or table of discrete values, i.e. damage probability matrix (DPM) (ErberikFragility2015):

- Single vs. multiple fragility curves: So far figure 5.13 presented single fragility curve based on a certain LS in Eq. 5.1 or a certain edp in Eq. 2.28. However, it is also possible to define the fragility of a structural system using multiple LSs or EDP threshold values.

LSs are the borders between different damage states (DS) in a structure. DS has a (mainly) qualitative definition, e.g. slight damage, moderate damage, etc. However, it can be presented quantitatively using damage index (DI) concept. For a system with N_{LS} limit states ($N_{LS} = 1, 2, \dots$), there are $N_{DS} = N_{LS} + 1$ damage states ($N_{DS} = 0, 1, 2, \dots$). DS_0 corresponds to “undamaged state” and there is a one-to-one correspondence between the other LSs and DSs, i.e. LS_i and DS_i ($i = 1, 2, \dots$). Figure 2.25(a) shows a set of fragility curves for a structural system with five DS and 4 LS.

In such a condition, one of the following situations may occur:

- DSs are series (Sequential): In this condition, DS_i should be reached before DS_{i+1} and so on. The order does matter. The probability of being in a specific DS can be computed as:

$$P[DS = ds_i | IM = im] = \begin{cases} 1 - P[LS_1 | IM = im] & i = 0 \\ P[LS_i | IM = im] - P[LS_{i+1} | IM = im] & 1 \leq i < N_{DS} \\ P[LS_i | IM = im] & i = N_{DS} \end{cases} \quad (2.32)$$

- DSs are parallel (Simultaneous): In this condition, probability of being in one DS can be evaluated independently from the others. The order does not matter. The probability of being in a specific DS can be computed as:

$$P[DS = ds_i | IM = im] = \begin{cases} 1 - P[LS_1 | IM = im] & i = 0 \\ P[LS_1 | IM = im] \cdot P[DS = ds_i | LS_1] & 1 \leq i \leq N_{DS} \end{cases} \quad (2.33)$$

where $P[DS = ds_i | LS_1]$ is the probability that, if damaged, it is in ds_i (or others as well) (**Porter2015**). Note that since the damage states are simultaneous it is possible to have $\left(\sum_{i=1}^{N_{DS}} P[DS = ds_i | LS_1]\right) > 1.0$.

- DPM is a matrix of data showing the discrete values of DS probabilities at some specified seismic intensity levels (SIL). The columns represent the discrete SILs and the rows are different DSs, figure 2.25(b). Note that this DPM corresponds to the multiple fragility curves shown in figure 2.25(a) which is extracted only for four SILs.

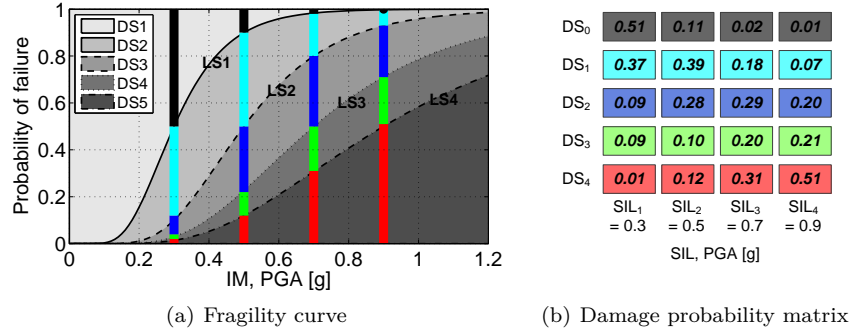


Figure 2.25: Relationship between fragility curve and damage probability matrix

2.8.1.4 Fragility in the Context of PBEE

The explicit determination of the performance measures, e.g. monetary losses, casualties, downtime in a probabilistic manner accounting for all sources uncertainty, e.g. earthquake ground motion, structural properties, damage, and loss can be performed in the context of the pacific earthquake engineering research center (PEER) PBEE (also known as PBEE-2). The primary steps in PEER PBEE are (**Porter2003**): 1) seismic hazard analysis, 2) structural response analysis, 3) damage analysis, and 4) loss assessment. The results of each of these steps are represented as generalized variables, IM, EDP, damage measure (DM), and decision variable (DV). Based on total probability theorem, the mean annual frequency of exceedance of a DV is (**Baker2008236**) (**Kiureghianergodicity**):

$$\lambda_{DV}(dv) = \int_{dm} \int_{edp} \int_{im} G_{DV|DM}[dv|dm] |dG_{DM|EDP}[dm|edp]| |dG_{EDP|IM}[edp|im]| |d\lambda_{IM}(im)| \quad (2.34)$$

where $G_{X|Y}[x|y] = P[X > x | Y = y]$ denotes the conditional complementary cumulative distribution function (CCDF) of random variable X given Y = y. Thus Eq. 2.34 can be rephrased as:

$$\lambda_{DV}(dv) = \int_{dm} \int_{edp} \int_{im} P[DV \geq dv | DM = dm] dP[DM \geq dm | EDP = edp] dP[EDP \geq edp | IM = im] |d\lambda_{IM}(im)| \quad (2.35)$$

As mentioned already in Eq. 2.28, the conditional probability $P[EDP \geq edp | IM = im]$ is called fragility or “demand fragility” (**mackie2005fragility**). However, to be used in the context of the PEER PBEE the fragility is defined as (**PorterKennedyBachman2007**) (**GunayMosalam2013**):

$$\text{Fragility} = P[DM \geq dm | EDP = edp] \quad (2.36)$$

Note that both the Eqs. 2.32 and 2.33 can be converted to a format of Eq. 2.36.

2.8.1.5 Treatment of Collapse (Large Data Point)

All the Eqs. 5.1, 2.27 and 2.28 were written assuming that there is no collapse or structural stability among the data points (usually resulted from analytical procedures). Should there be real collapse or numerical instability in analyses, the fragility has an alternative expression (**JalayerFranchinPinto2007**):

$$P[\text{EDP} \geq \text{edp} | \text{IM} = im] = P[\text{EDP} \geq \text{edp} | \text{IM} = im, \text{NLg}] \cdot (1 - P[\text{Lg} | \text{IM} = im]) + P[\text{Lg} | \text{IM} = im] \quad (2.37)$$

where Lg and NLg are referred to “very large” and “no very large” EDPs. In some references, they corresponds to “collapse” and “non collapse” data points and are shown with C and \bar{C} , respectively, (**RajeevFranchinPinto2008**). $P[\text{Lg} | \text{IM} = im]$ is the probability of having “very large” EDP for a given IM and can be computed based on relative frequency method (RFM):

$$P[\text{Lg} | \text{IM} = im] = P[C | \text{IM} = im] = \frac{N_C}{N_T} \quad (2.38)$$

where N_C and N_T are number of demands causing collapse and total number of realizations, respectively.

Note that similar to Eq. 2.31, the mean annual frequency of collapse, $\lambda_{\text{collapse}}$, can be computed as (**Baker021113EQS025M**):

$$\lambda_{\text{collapse}} = \int_{im} P[C | \text{IM} = im] \cdot |d\lambda_{\text{IM}}(im)| \quad (2.39)$$

2.8.2 Fragility Curve Determination

2.8.2.1 Empirical

Emperical based fragility curves are constructed based on post-earthquake surveys which are usually the most reliable source for this purpose. The reason is that they are real world damage observations accounting for all the details of ground motion and structure characteristics. However, they are lack of generality and usually there are large uncertainty in their determination mainly due to inconsistency in DS definitions and different inspection techniques (**MuntasirShahria2015**).

2.8.2.2 Heuristic

Heuristic fragility curves are based on expert elicitation and is useful where the empirical information about damage data is very limited or when the analytical approach is difficult or impossible to practically perform. **ATC-13** report is one of the most practical examples of the expert opinion-based fragility curves (in fact DPM) for the California infrastructure system (including concrete dam).

2.8.2.3 Experimental

Experimental fragility curves can be constructed based on large- or small-scale experimental tests; however, this method is not common because it is expensive and the required data is limited (**vosooghi2012experimental**).

2.8.2.4 Hybrid

Hybrid fragility curves are based on combination of the above sources. The objective is to reduce the computational effort of the analytical simulations and to compensate the subjective bias of the expert elicitation approach (**KapposPanagopoulos2006**).

2.8.2.5 Analytical

2.8.2.5.1 Generalized Linear Models In statistics, the generalized linear model (GLM) is a generalization of the general linear model (linear regression) and consists of three components:

- A *random component*, specifying the conditional distribution of the response variable, y , given the values of the explanatory variables in the model. The distribution of response variable is one of the exponential family members, e.g. Gaussian, binomial, Poisson, gamma, or inverse-Gaussian.
- A *linear predictor*, γ , that is a linear function of regressors.
- A smooth and invertible linearizing *link function*, $g(\Delta)$, which transforms the expectation of the response variable, $\mu \equiv E(Y)$, (also mean of the distribution) to the linear predictor.

$$g(\mu) = \gamma = \theta_0 + \sum_{i=1}^n \theta_i x_i \quad (2.40)$$

where x_i are independent variables, and θ_i are coefficients.

Commonly used link functions for seismic fragility curves are summarized in Eq. 2.41. These functions are used because they are for binomial data where the LS status can be defined as 0 and 1.

$$g(\mu) = \begin{cases} \text{Probit} & \Phi^{-1}(\mu) \\ \text{Logit} & \ln(\mu) - \ln(1 - \mu) \\ \text{log-log} & -\ln(-\ln(\mu)) \\ \text{Complementary log-log} & \ln(-\ln(1 - \mu)) \end{cases} \quad (2.41)$$

where Φ is the cumulative distribution function (CDF) of the standard-normal distribution.

The link function is invertible and the inverse link $g^{-1}(\Delta)$ is called the *mean function*:

$$\mu = g^{-1}(\gamma) = g^{-1}\left(\theta_0 + \sum_{i=1}^n \theta_i X_i\right) \quad (2.42)$$

Subsequently, the inverse of the functions in Eq. 2.41 are:

$$g^{-1}(\gamma) = \begin{cases} \text{Probit} & \Phi(\gamma) \\ \text{Logit} & 1/(1 + \exp(-\gamma)) \\ \text{log-log} & \exp(-\exp(-\gamma)) \\ \text{Complementary log-log} & 1 - \exp(-\exp(\gamma)) \end{cases} \quad (2.43)$$

Note that in the context of seismic fragility curves, a single independent variable, x_1 , is used with two coefficients which represent the slope and the intercept of the linear model. The independent variable, x_1 , is assumed to be IM parameter and μ is the probability of the LS exceeding (fragility itself). The two common forms of Eq. 2.40 for the seismic fragility curves are: $\theta_0 + \theta_1 \text{IM}$ (simple linear form) and $\theta_0 + \theta_1 \ln(\text{IM})$ (Logarithmic form) (**IoannouRossetto2014**). Combination of these two forms with those four link

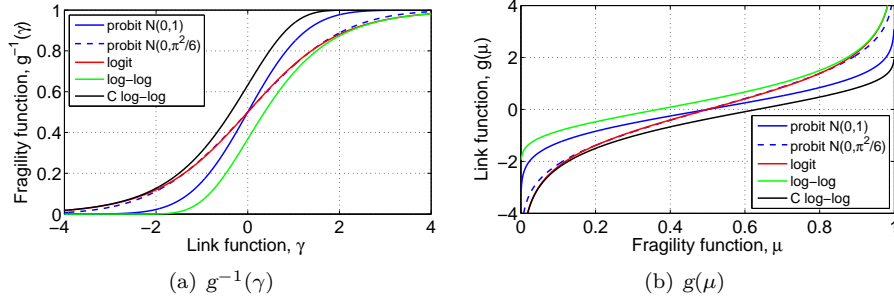


Figure 2.26: Link functions for binomial data and their relationship

functions in Eq. 2.41 provides at least eight possible seismic fragility curve representations. Four out of eight representations (which are mentioned already in the literature (**LallemantKiremidjianBurton2015**)) in the form of Eq. 2.28 are summarized here:

- Probit GLM with logarithmic IM form (**CharvetIoannouRossetto2014**):

$$\begin{aligned}\Phi^{-1}(P[\text{EDP} \geq \text{edp} | \text{IM} = im]) &= \theta_0 + \theta_1 \ln(im) \Rightarrow \\ P[\text{EDP} \geq \text{edp} | \text{IM} = im] &= \Phi(\theta_0 + \theta_1 \ln(im))\end{aligned}\quad (2.44)$$

- Logit GLM with linear IM form (**oRourke2000seismic**):

$$\begin{aligned}\ln\left(\frac{P[\text{EDP} \geq \text{edp} | \text{IM} = im]}{1 - P[\text{EDP} \geq \text{edp} | \text{IM} = im]}\right) &= \theta_0 + \theta_1(im) \Rightarrow \\ P[\text{EDP} \geq \text{edp} | \text{IM} = im] &= \frac{\exp(\theta_0 + \theta_1(im))}{1 + \exp(\theta_0 + \theta_1(im))}\end{aligned}\quad (2.45)$$

- Logit GLM with logarithmic IM form:

$$\begin{aligned}\ln\left(\frac{P[\text{EDP} \geq \text{edp} | \text{IM} = im]}{1 - P[\text{EDP} \geq \text{edp} | \text{IM} = im]}\right) &= \theta_0 + \theta_1 \ln(im) \Rightarrow \\ P[\text{EDP} \geq \text{edp} | \text{IM} = im] &= \frac{\exp(\theta_0 + \theta_1 \ln(im))}{1 + \exp(\theta_0 + \theta_1 \ln(im))} = \frac{e^{\theta_0} im^{\theta_1}}{1 + e^{\theta_0} im^{\theta_1}}\end{aligned}\quad (2.46)$$

- Complementary log-log GLM with logarithmic IM form:

$$\begin{aligned}\ln(-\ln(1 - P[\text{EDP} \geq \text{edp} | \text{IM} = im])) &= \theta_0 + \theta_1 \ln(im) \Rightarrow \\ P[\text{EDP} \geq \text{edp} | \text{IM} = im] &= 1 - \exp(-\exp(\theta_0 + \theta_1 \ln(im))) = 1 - e^{-e^{\theta_0} im^{\theta_1}}\end{aligned}\quad (2.47)$$

2.8.2.5.2 Lognormal Among different models, lognormal CDF is the most often form used to define a fragility function. There are two rules to present the fragility curves based on lognormal model, i.e. 1) IM-based rule, and 2) EDP-based rule.

2.8.2.5.2.1 IM-based Rule In this condition, Eq. 5.1 can take the following form (DolsekAnalytic2015):

$$P[\text{LS}|\text{IM} = im] = \Phi\left(\frac{\ln(im) - \ln(\eta_{im,LS})}{\beta_{im,LS}}\right) \quad (2.48)$$

where $\eta_{im,LS}$ $\beta_{im,LS}$ are the median LS intensity and the corresponding logarithmic standard deviation (also called dispersion). Note that $\beta_{im,LS}$ is also shown as $\sigma_{\ln(im,LS)}$ which is the standard deviation of the natural logarithms of the LS intensity.

Mathematically, the standard-normal CDF is represented in one of the following forms:

$$\begin{aligned} \Phi(t) &= \frac{1}{\sqrt{2\pi}} \int_{-\infty}^t e^{-u^2/2} du \\ \Phi(t) &= \frac{1}{2} \left(1 + \operatorname{erf}\left(\frac{t}{\sqrt{2}}\right) \right) \end{aligned} \quad (2.49)$$

where $\operatorname{erf}(t) = \frac{1}{\sqrt{\pi}} \int_{-t}^{+t} e^{-u^2} du$ is the error function and is defined as the probability of a random variable with normal distribution of mean 0 and variance 1/2 falling in the range $[-t, t]$.

Combination of Eqs. 2.48 and 2.49 gives:

$$P[\text{LS}|\text{IM} = im] = \int_0^{im} \frac{1}{\sqrt{2\pi} \cdot \beta_{extupim,LS} \cdot im} \exp\left[-\frac{(\ln(im) - \eta_{im,LS})^2}{2\beta_{im,LS}^2}\right] d im \quad (2.50)$$

In the same way, the lognormal-based fragility curve for Eq. 2.28 can be written as:

$$P[\text{EDP} \geq edp|\text{IM} = im] = \Phi\left(\frac{\ln(im) - \ln(\eta_{im,edp})}{\beta_{im,edp}}\right) \quad (2.51)$$

Finally, note that Eq. 2.51 is the other form of Eq. 2.44 assuming $\theta_0 = -\frac{\ln(\eta)}{\beta}$ and $\theta_1 = \frac{1}{\beta}$.

2.8.2.5.2.2 EDP-based Rule In this condition, Eq. 2.28 can take the following form (JalayerPHD2003):

$$P[\text{EDP} \geq edp|\text{IM} = im] = 1 - \Phi\left(\frac{\ln(edp) - \ln(\eta_{\text{EDP}|\text{IM}=im})}{\beta_{\text{EDP}|\text{IM}=im}}\right) \quad (2.52)$$

where $\eta_{\text{EDP}|\text{IM}=im}$ and $\beta_{\text{EDP}|\text{IM}=im}$ are the median value and the logarithmic standard deviation of EDP given IM.

Combination of Eqs. 2.52 and 2.49 gives:

$$\begin{aligned} P[\text{EDP} \geq edp|\text{IM} = im] &= 1 - \int_0^{edp} \frac{1}{\sqrt{2\pi} \cdot \beta_{\text{EDP}|\text{IM}=im} \cdot edp} \\ &\quad \exp\left[-\frac{1}{2} \left(\frac{\ln(edp) - \ln(\eta_{\text{EDP}|\text{IM}=im})}{\beta_{\text{EDP}|\text{IM}=im}}\right)^2\right] d edp \end{aligned} \quad (2.53)$$

Last but not least, two questions rise: 1) how one can obtain the empirical data points to be used for fragility analysis? and 2) How one can estimate the parameters in Eqs. 2.51 and 2.52 properly? The next section will discuss on different nonlinear analysis techniques to get the data points and also data fitting.

2.8.2.6 Analysis Techniques and Data Fitting

2.8.2.6.1 Incremental Dynamic Analysis (IDA) In this method, each ground motion is scaled successively to multiple IM levels and the maximum EDP is computed at each scale level (**Vamvatsikos2002a**). The IDA curve connects the resulting EDPs corresponding to each ground motion, usually based on the spline fitting (**Vamvatsikos2004a**). Using IDA results, the percentiles of response can be calculated as continuous curves, e.g., the median IDA curve or the 16th and 84th fractile IDA curves.

This is a famous method because the researchers are usually interested in collapse probability of structures and IDA guarantee the collapse of the structures at the higher intensities. However, scaling the ground motions may lead to generating records with non-realistic shape, which in turn implies that the shape of the records should be considered **Haselton2011**.

Thus, the focus will be on calculating $P[C|IM = im]$. Three approaches can be used: 1) EDP capacity based with full IDA results, 2) IM capacity based with full IDA results, and 3) IM capacity based with truncated IDA results. The only difference between the full and truncated IDA methods is that in the former one all the ground motions are incrementally scaled up to collapse of the structure, while in the later one there is a limitation in scaling ground motion to no more than IM_{trunc} . Thus, some of the scaled ground motions may not leads to collapse eventually.

- EDP capacity based with full IDA: First, a full IDA is performed and the IDA curves are plotted, figure 2.27(a). In this approach, the structure is assumed to be collapsed when the EDP demand, EDP_d , exceeds the EDP capacity, EDP_c (**zareian2010basic**):

$$P[C|IM = im] = P[EDP_d \geq EDP_c | IM = im] \\ = \sum_{\text{all } edp_c} P[EDP_d \geq EDP_c | EDP_c = edp_c, IM = im] P[EDP_c = edp_c] \quad (2.54)$$

where the first term inside the summation sign is the probability that the demand exceeds a specific capacity value, edp_c , at $IM = im$ and the second term is the probability that capacity is equal to edp_c . Figure 2.27(a) shows the EDP capacity points for different records, as well as the EDP demand at two specific IM level. Then, for each IM (low to high) the probability of collapse is computed, Eq. 2.54, and plotted as a cumulative histogram. A log-normal CDF can be fitted to the empirical collapse points.

- IM capacity based with full IDA: After performing IDA, the IM collapse capacity, IM_{cap} , approximately is tagged as an asymptotic point on each IDA curve, figure 2.27(b). The probability of collapse is:

$$P[C|IM = im] = P[IM_{cap} < IM = im] \quad (2.55)$$

The empirical fragility is computed simply by Eq. 2.38 at each IM_{cap} level. A log-normal CDF, Eq. 2.48 can be fitted to the collapse data point. Subsequently, the median and logarithmic standard deviation can be estimated by one of the following methods:

- Method of Moments (MM) seeks $\hat{\eta}$ and $\hat{\beta}$ in a way that the resulting log-normal distribution has the same moments (mean and standard deviation) as the collapse data points:

$$\hat{\eta} = \exp\left(\frac{\sum_{i=1}^{N_T} \ln(IM_{cap_i})}{N_T}\right), \quad \hat{\beta} = \sqrt{\frac{\sum_{i=1}^{N_T} (\ln(IM_{cap_i}) - \ln(\hat{\eta}))^2}{N_T - 1}} \quad (2.56)$$

where N_T is total number of ground motions and superscript $\hat{\cdot}$ refers to an estimated value.

- Maximum Likelihood Estimation (MLE) seeks the parameters in a way to maximize a “likelihood function”. For the readers not familiar with the MLE concept, assume a generic form of a n -dimensional random vector \mathbf{U} with probability density function (PDF) $f(\mathbf{u} | \theta)$. Assuming \mathbf{U} is independent and identically distributed (iid) observations, the PDF can be written as $f(\mathbf{u} | \theta) = f(u_1 | \theta) \times f(u_2 | \theta) \times \dots \times f(u_n | \theta)$. Further, it is assumed that θ is a fixed and unknown constant. The “complete-data likelihood function” of θ is defined as:

$$\mathcal{L}(\theta; \mathbf{u}) = f(\mathbf{u} | \theta) = \prod_{i=1}^n f(u_i | \theta) \quad (2.57)$$

where \mathbf{u} is assumed to be fixed, and θ as the variable for \mathcal{L} . In practice, it is convenient to work with the logarithmic version of 2.57. The “average log-likelihood function” is then $\ell = \frac{1}{n} \ln \mathcal{L}$. The MLE method estimates $\hat{\theta}$ by maximizing $\ell(\theta; \mathbf{u})$:

$$\{\hat{\theta}\} = \underset{\hat{\theta}}{\operatorname{argmax}} \ell(\theta; \mathbf{u}) = \underset{\hat{\theta}}{\operatorname{argmax}} \frac{1}{n} \sum_{i=1}^n \ln(f(u_i | \theta)) \quad (2.58)$$

In the case of N_T seismic data, it is assumed that the observation of each ground motion is either collapsed or safe and also is independent of the other ground motions. Thus, Eq. 2.58 takes the following form:

$$\{\hat{\eta}, \hat{\beta}\} = \underset{\hat{\eta}, \hat{\beta}}{\operatorname{argmax}} \ell(\eta, \beta; \mathbf{IM}_{cap}) = \underset{\hat{\eta}, \hat{\beta}}{\operatorname{argmax}} \sum_{i=1}^{N_T} \ln \left\{ \phi \left(\frac{\ln(\mathbf{IM}_{cap_i}) - \ln(\eta)}{\beta} \right) \right\} \quad (2.59)$$

Note that Eq. 2.59 has an analytical solution, where the $\hat{\eta}$ is exactly same as Eq. 2.56, while for the $\hat{\beta}$, the $(N_T - 1)$ should be replaced with N_T .

- IM capacity based with truncated IDA: First \mathbf{IM}_{trunc} is selected and then the truncated IDA is performed. The \mathbf{IM}_{cap} , and the number of ground motions leading to failure, N_C are defined, figure 2.27(c). The probability of collapse can be computed based on Eq. 2.55. Considering that the collapse data are incomplete (censored), the method of moment, Eq. 2.56, can not be used for data fitting. The alternative method is:

- Maximum Likelihood Estimation with Censored Data (MLECD) can be used for fitting the type I censored data. Assume during the T hours of a test with n sample, there are r observed failure with the (exact) failure times as t_1, t_2, \dots, t_r . Thus, there are $(n - r)$ samples that are survived the entire T -hour test without failing. This type of censoring is also called “right censored data” since the failure times to the right are missing. The “censored likelihood function” for such a system is defined as:

$$\mathcal{L}(\theta; \mathbf{t}, T) = c_0 \left(\prod_{i=1}^r f(t_i | \theta) \right) (1 - F(T | \theta))^{n-r} \quad (2.60)$$

where $F(t)$ is the CDF of $f(t)$, and c_0 is a constant has no effect in MLE process.

In the same way, “censored likelihood function” for truncated IDA can be written as:

$$\mathcal{L}(\eta, \beta; \mathbf{IM}_{cap}, \mathbf{IM}_{trunc}) = \left(\prod_{i=1}^{N_C} \phi \left(\frac{\ln(\mathbf{IM}_{cap_i}) - \ln(\eta)}{\beta} \right) \right) \left(1 - \Phi \left(\frac{\ln(\mathbf{IM}_{trunc}) - \ln(\eta)}{\beta} \right) \right)^{N_T - N_C} \quad (2.61)$$

Again, similar to Eqs. 2.58 and 2.59 it is easier to maximize the logarithm of the censored likelihood function. The estimated parameters will be (**Baker021113EQS025M**):

$$\{\hat{\eta}, \hat{\beta}\} = \underset{\hat{\eta}, \hat{\beta}}{\operatorname{argmax}} \sum_{i=1}^{N_C} \left\{ \ln \phi \left(\frac{\ln(\mathbf{IM}_{cap_i}) - \ln(\eta)}{\beta} \right) \right\} + (N_T - N_C) \ln \left(1 - \Phi \left(\frac{\ln(\mathbf{IM}_{trunc}) - \ln(\eta)}{\beta} \right) \right) \quad (2.62)$$

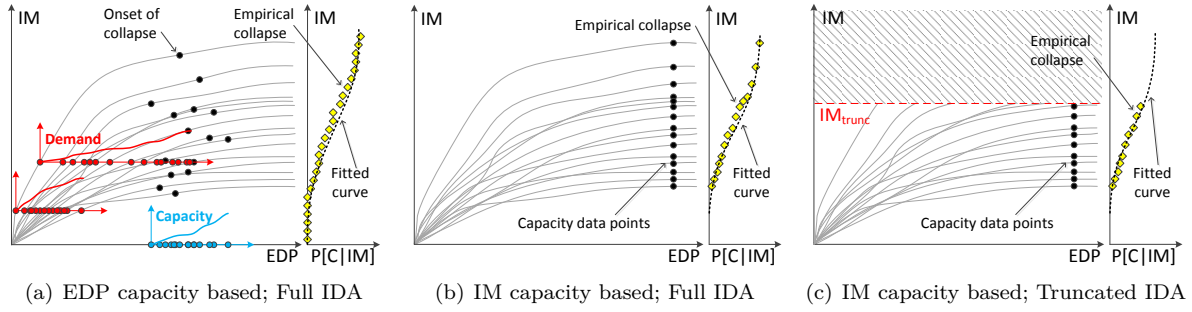


Figure 2.27: Conceptual collapse fragility curves based on IDA method

2.8.2.6.2 Multiple Stripe Analysis (MSA) Instead of selecting a fixed set of ground motions and scaling them (i.e. IDA), the analyses can be performed in several discrete SILs. Having three or more SILs this new method is called multiple stripe analysis (MSA) (**Cornell-Jalayer2002**). If the analyses are performed for one or two stripes, the method is called single stripe analysis (SSA) and double stripe analysis (DSA), respectively. Some important points in MSA are:

- Interval between two sequential SILs are not necessarily identical. For example, in figure 2.28(a) distance between SIL_2 and SIL_3 and also between SIL_6 and SIL_7 is more than others. The reason can be attributed to the desired frequency of exceedance for the project/analyzer.
- The number of ground motions in each stripe can be different from the others.
- The selected ground motions in each stripe may be different from other stripes, specially when the conditional spectrum is used to select the ground motions.
- The number of selected SILs is optimal. Increasing the number of SILs, increases the accuracy of future curve fitting. In figure 2.28(a), the analyses are performed only for 8 SIL, while it can be extended up to collapse of all ground motions (this is computationally demanding).
- The empirical collapse in each SIL can be obtained using Eq. 2.38.
- Considering different ground motions in each stripe, the empirical collapse for SIL_i may be equal or more than SIL_{i+1} . In figure 2.28(a), SIL_4 leads to higher empirical collapse than SIL_5 . Also, the number of collapse data points in SIL_7 and SIL_8 are equal.

One of the following two methods can be used to estimate the median and logarithmic standard deviation:

- Sum of Squared Error (SSE) tries to minimize the sum of squared error between the observed fractions

of collapse data and probabilities predicted by the fragility function:

$$\{\hat{\eta}, \hat{\beta}\} = \underset{\hat{\eta}, \hat{\beta}}{\operatorname{argmin}} \sum_{i=1}^m \left(\frac{N_{C_i}}{N_{T_i}} - \Phi \left(\frac{\ln(im_i) - \ln(\eta)}{\beta} \right) \right)^2 \quad (2.63)$$

where N_{C_i} and N_{T_i} are number of collapsed data and total ground motions at level $IM = im_i$, and m is the number of IM levels. Note that $\frac{N_{C_i}}{N_{T_i}}$ is similar to that showed in Eq. 2.38.

- Maximum Likelihood Estimation (MLE) can be used assuming that the collapse and non-collapse data at each SIL are independent. In such a case the binomial distribution assumption is valid. Recall that the PDF for the binomial distribution with parameter p is $\binom{u}{v} p^v (1-p)^{u-v}$ where v is successes in u trials. Substituting in Eq. 2.57, the “likelihood function” for this system is defined as:

$$\mathcal{L}(p; \mathbf{u}, \mathbf{v}) = \prod_{i=1}^m \binom{u_i}{v_i} p_i^{v_i} (1-p_i)^{u_i-v_i} \quad (2.64)$$

In the same way, the “likelihood function” for the MSA can be written in the form of Eq. 2.65 considering that p (in Eq. 2.64) is the probability of collapse for a ground motion at $IM = im_i$.

$$\mathcal{L}(\eta, \beta; \mathbf{IM}, \mathbf{N}_T, \mathbf{N}_C) = \prod_{i=1}^m \binom{N_{T_i}}{N_{C_i}} \Phi \left(\frac{\ln(im_i) - \ln(\eta)}{\beta} \right)^{N_{C_i}} \left(1 - \Phi \left(\frac{\ln(im_i) - \ln(\eta)}{\beta} \right) \right)^{N_{T_i} - N_{C_i}} \quad (2.65)$$

Again, similar to Eq. 2.58 it is easier to maximize the logarithm of the likelihood function. The estimated parameters will be (**Baker021113EQS025M**):

$$\{\hat{\eta}, \hat{\beta}\} = \underset{\hat{\eta}, \hat{\beta}}{\operatorname{argmax}} \sum_{i=1}^m \left(\ln \binom{N_{T_i}}{N_{C_i}} + N_{C_i} \ln \left(\Phi \left(\frac{\ln(im_i) - \ln(\eta)}{\beta} \right) \right) + (N_{T_i} - N_{C_i}) \ln \left(1 - \Phi \left(\frac{\ln(im_i) - \ln(\eta)}{\beta} \right) \right) \right) \quad (2.66)$$

- Linear Regression in Transferred Space (LRTS) or Method B in **PorterKennedyBachman2007**: As it is stated already, in MSA the ground motions are selected in stripes to have (almost) identical IM, figure 2.28(a). The primarily option for IM in different structures is $S_a(T_1)$. However, sometimes it is required to present the results based on an alternative IM, here is called IM' . In such a case the data points do not rest on the specific stripes and they speared in the space, figure 2.28(b). Thus, SSE and MLE are not applicable any more. In this case, LRTS can be used as summarized in the following steps:

- For all the data points (i.e. collapse and non-collapse), O_i , identify the corresponding IM'_i value.
- Assuming total number of data points to be M , divide them into N bins, where $N = \lfloor \sqrt{M} \rfloor$. Each bin should have approximately equal number of data points. **PorterKennedyBachman2007** recommend the minimum M to be 25.
- For each bin j determine the exact number of data point, M_j , the mean intensity measure, $\overline{IM'}_j$, and the number of collapse data points, m_j . Thus,

$$\overline{IM'}_j = \frac{1}{M_j} \sum_{k=1}^{M_j} IM'_j ; \quad M = \sum_{i=1}^N M_j \quad (2.67)$$

- Determine the X and Y coordinates as:

$$X_j = \ln \left(\overline{IM'}_j \right) ; \quad Y_j = \Phi^{-1} \left(\frac{m_j + 1}{M_j + 1} \right) \quad (2.68)$$

- Fit a line, $\hat{Y} = A_1 X + A_0$, to the data points, $\langle X_j, Y_j \rangle$, using least-squares approach, and estimate the slope, A_1 , and the intercept, A_0 .
- Determine the random logarithmic standard deviation, β , and the median, η , as:

$$\beta = \frac{1}{A_1} ; \quad \eta = \exp \left(-\frac{A_0}{A_1} \right) \quad (2.69)$$

Having these two parameters, a lognormal fragility curve can be plotted, figure 2.28(b).

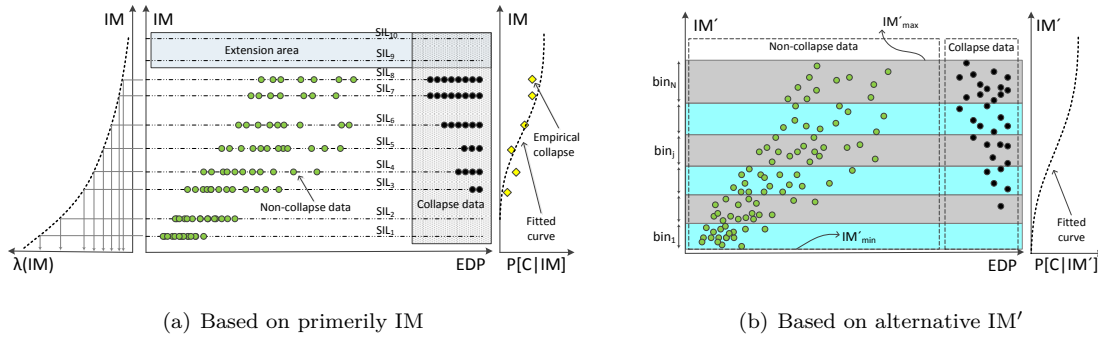


Figure 2.28: Conceptual collapse fragility curves based on MSA method

3— Soil Structure Interaction

3.1 Deconvolution

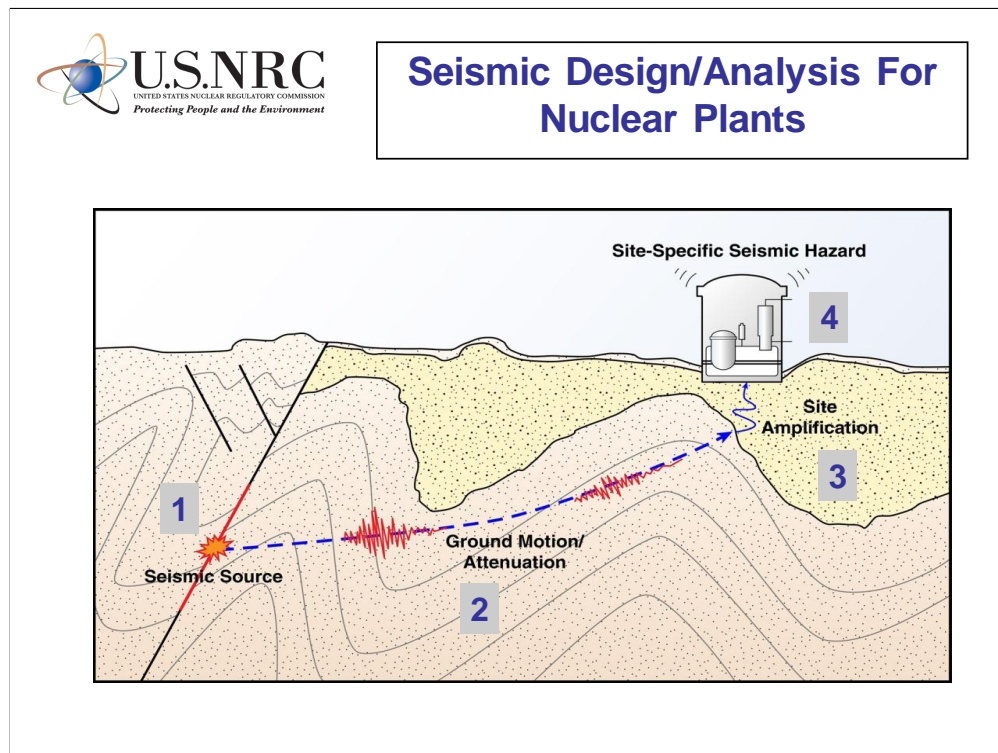


Figure 3.1: Seismic Attenuation/Amplification (pires)

3.1.1 Introduction

Seismic events originate through tectonic slips and elastic (p- and s-) waves traveling through rock/soil foundation up to the surface. Hence, the seismographs (usually installed at the foot of the dam) record only the manifestation of the event.

On the other hand, modeling the foundation is essential for proper and comprehensive analysis of the dam, and as such the seismic excitation will have to be applied at the base of the foundation.

However, figure 3.2, if we were to apply at the base the accelerogram recorded on the surface $I(t)$, the output signal $A(t)$ at the surface will be different than the one originally recorded (unless we have rigid

foundation). Hence, the accelerogram recorded on the surface must be de-convoluted into a new one $I'(t)$, such that when the new signal is applied at the base of the foundation, the computed signal at the dam base matches the one recorded by the accelerogram.

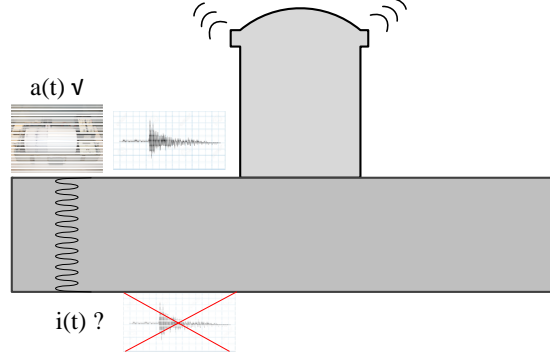


Figure 3.2: Deconvolution

3.1.2 Fourier Transform

Fourier transforms enables us to transfer a signal from the time domain to the frequency domain through the following equation:

$$X(\omega) = \int_{-\infty}^{\infty} x(t) e^{-2i\pi\omega t} dt \quad (3.1)$$

$$x(t) \xrightarrow{\text{FFT}} X(\omega) \quad (3.2)$$

while the inverse FFT takes us back from the frequency domain to the time domain through:

$$x(t) = \int_{-\infty}^{\infty} X(\omega) e^{2i\pi\omega t} d\omega \quad (3.3)$$

$$X(\omega) \xrightarrow{\text{FFT}^{-1}} x(t) \quad (3.4)$$

3.1.3 Butterworth Filter

Spider has the following filters implemented in its de-convolution feature, figure 3.3.

$$|H(j\omega)|^2 = \begin{cases} \text{Low pass} & \frac{1}{1 + \left(\frac{\omega}{\omega_L}\right)^{2n}} \\ \text{High pass} & \frac{1}{1 + \left(\frac{\omega_U}{\omega}\right)^{2n}} \\ \text{Band pass} & \frac{1}{1 + \left(\frac{\omega}{\omega_L}\right)^{2n}} \frac{1}{1 + \left(\frac{\omega_U}{\omega}\right)^{2n}} \\ \text{Band stop} & \frac{1}{1 + \left(\frac{\omega_L}{\omega}\right)^{2n}} \frac{1}{1 + \left(\frac{\omega}{\omega_U}\right)^{2n}} \end{cases} \quad (3.5)$$

where ω , ω_L , ω_U and n are the frequency, the lower and upper filter frequencies, and the order of the filter, respectively.

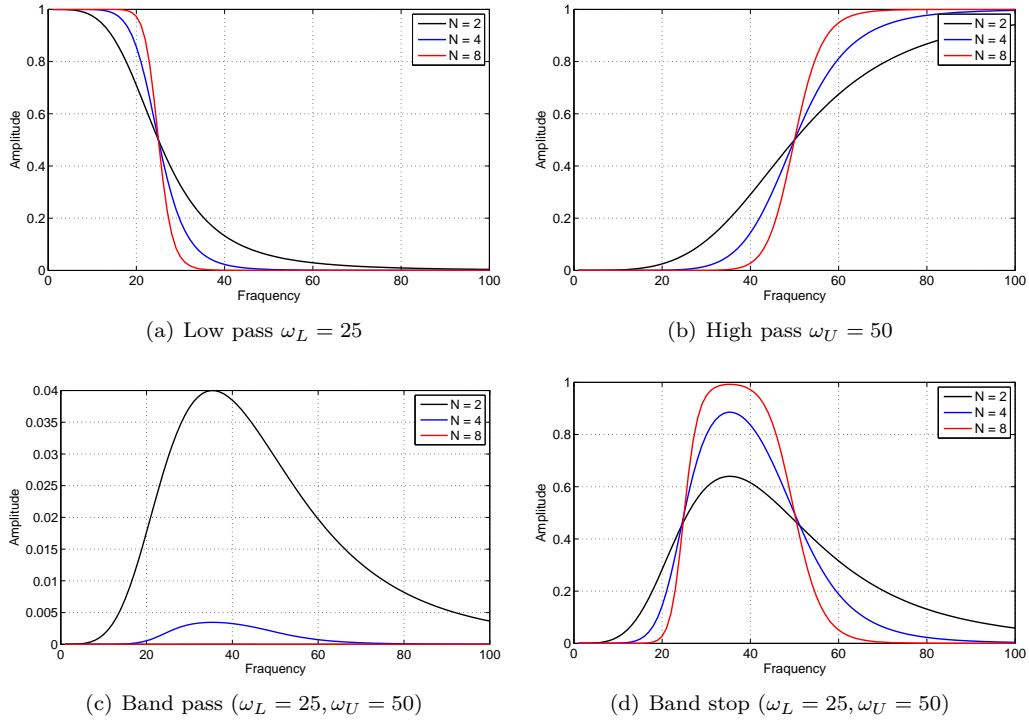


Figure 3.3: Comparison of filters

3.1.4 Transfer Function

In dynamic event, we can define an input record $i(t)$ which is amplified by $h(t)$ resulting in an output signal $o(t)$, figure 3.4. Similarly, the operation can be defined in the frequency domain. This output to input relationship is of major importance in many disciplines. The transfer function is the “Laplace” transform of the output divided by the Laplace transform of the input. Hence, in 1D, we can determine the transfer function as follows:

1. $i(t) \xrightarrow{\text{FFT}} I(\omega)$
2. $o(t) \xrightarrow{\text{FFT}} O(\omega)$
3. Transfer Function is $TF_{I-O} = \frac{O(\omega)}{I(\omega)}$

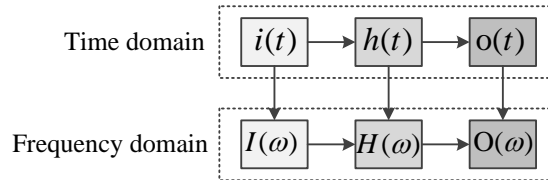


Figure 3.4: Transfer function

3.1.5 Algorithm

3.1.5.1 One-Dimensional

Extending our discussion one step further, we introduce the concept of deconvolution which addresses the dilemma posed above, and will now require one (or more) finite element analyses. With reference to figure 3.5.

1. Record the earthquake induced acceleration on the surface $a'(t)$, and apply it as $i'(t)$ at the base of the foundation.
2. Perform a transient finite element analysis.
3. Determine the surface acceleration $a(t)$ (which is obviously different from $i(t)$).
4. Compute the following FFTs:

$$i'(t) \xrightarrow{\text{FFT}} I'(\omega) = A'(\omega) \quad (3.6)$$

$$a(t) \xrightarrow{\text{FFT}} A(\omega) \quad (3.7)$$

5. Compute transfer function from the base to surface as

$$TF_{I'-A} = A(\omega)/I'(\omega) \quad (3.8)$$

6. Compute the inverse transfer function $TF_{I'-A}^{-1}$.
7. Determine the updated excitation record in the frequency domain

$$I(\omega) = TF_{I'-A}^{-1} \times A'(\omega) = \frac{I'(\omega)}{A(\omega)} A'(\omega) \quad (3.9)$$

8. Determine the updated excitation in the time domain

$$I(\omega) \xrightarrow{\text{FFT}^{-1}} i(t) \quad (3.10)$$

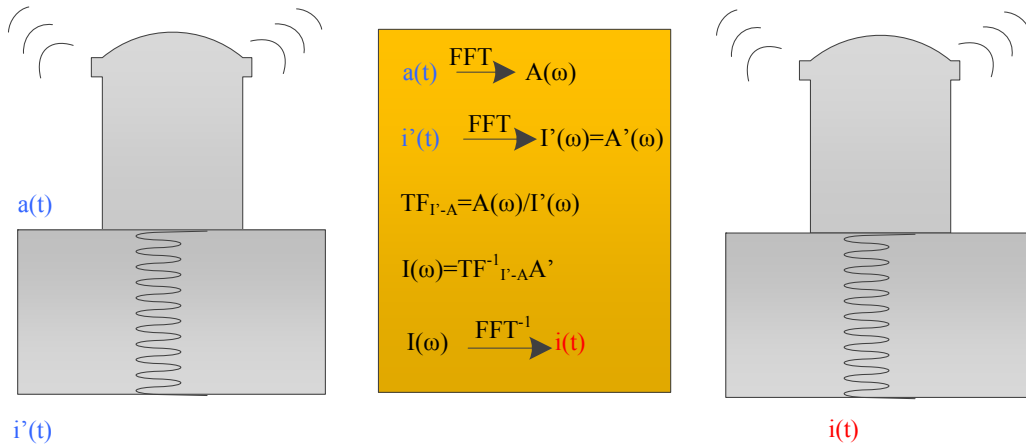


Figure 3.5: Deconvolution applied in finite element analysis

3.1.5.2 Three-Dimensional

In 3D applications, the transfer function is a 3×3 matrix, each row corresponds to the response to an excitation in a given direction, and each column corresponds to the response in a given direction. Hence, three separate analysis must be performed [I'_x I'_y I'_z] and for each excitation, we must determine the three components of the surface acceleration. Then, we will compute the 3D transfer function:

$$[TF] = \underbrace{\begin{bmatrix} TF_{xx} & TF_{xy} & TF_{xz} \\ TF_{yx} & TF_{yy} & TF_{yz} \\ TF_{zx} & TF_{zy} & TF_{zz} \end{bmatrix}}_{TF_{I'-A}} = \begin{bmatrix} \frac{A_{xx}(\omega)}{I'_x(\omega)} & \frac{A_{xy}(\omega)}{I'_x(\omega)} & \frac{A_{xz}(\omega)}{I'_x(\omega)} \\ \frac{A_{yx}(\omega)}{I'_y(\omega)} & \frac{A_{yy}(\omega)}{I'_y(\omega)} & \frac{A_{yz}(\omega)}{I'_y(\omega)} \\ \frac{A_{zx}(\omega)}{I'_z(\omega)} & \frac{A_{zy}(\omega)}{I'_z(\omega)} & \frac{A_{zz}(\omega)}{I'_z(\omega)} \end{bmatrix} \quad (3.11)$$

Hence, the excitation to be applied in the frequency domain is given by:

$$\begin{Bmatrix} I_x(\omega) \\ I_y(\omega) \\ I_z(\omega) \end{Bmatrix} = [TF_{I'-A}]^{-1} \begin{Bmatrix} A'_x(\omega) \\ A'_y(\omega) \\ A'_z(\omega) \end{Bmatrix} \quad (3.12)$$

while in the time domain it is

$$\begin{Bmatrix} I_x(\omega) \\ I_y(\omega) \\ I_z(\omega) \end{Bmatrix} \xrightarrow{\text{FFT}^{-1}} \begin{Bmatrix} i_x(t) \\ i_y(t) \\ i_z(t) \end{Bmatrix} \quad (3.13)$$

3.1.5.3 Simplification

The preceding 3D generalized procedure can be simplified by ignoring the off-diagonal terms

$$[TF] = \begin{bmatrix} TF_{xx} & 0 & 0 \\ 0 & TF_{yy} & 0 \\ 0 & 0 & TF_{zz} \end{bmatrix} = \begin{bmatrix} \frac{A_{xx}(\omega)}{I'_x(\omega)} & 0 & 0 \\ 0 & \frac{A_{yy}(\omega)}{I'_y(\omega)} & 0 \\ 0 & 0 & \frac{A_{zz}(\omega)}{I'_z(\omega)} \end{bmatrix} \quad (3.14)$$

which will greatly simplify the inversion of the transfer function.

$$\begin{Bmatrix} I_x(\omega) \\ I_y(\omega) \\ I_z(\omega) \end{Bmatrix} = [TF_{I'-A}]^{-1} \begin{Bmatrix} A'_x(\omega) \\ A'_y(\omega) \\ A'_z(\omega) \end{Bmatrix} = \begin{bmatrix} \frac{I'_x(\omega)}{A_{xx}(\omega)} & 0 & 0 \\ 0 & \frac{I'_y(\omega)}{A_{yy}(\omega)} & 0 \\ 0 & 0 & \frac{I'_z(\omega)}{A_{zz}(\omega)} \end{bmatrix} \begin{Bmatrix} A'_x(\omega) \\ A'_y(\omega) \\ A'_z(\omega) \end{Bmatrix} \quad (3.15)$$

and finally,

$$\begin{Bmatrix} I_x(\omega) \\ I_y(\omega) \\ I_z(\omega) \end{Bmatrix} = \begin{bmatrix} \frac{I'_x(\omega)}{A_{xx}(\omega)} A'_x(\omega) & 0 & 0 \\ 0 & \frac{I'_y(\omega)}{A_{yy}(\omega)} A'_y(\omega) & 0 \\ 0 & 0 & \frac{I'_z(\omega)}{A_{zz}(\omega)} A'_z(\omega) \end{bmatrix} \xrightarrow{\text{FFT}^{-1}} \begin{Bmatrix} i_x(t) \\ i_y(t) \\ i_z(t) \end{Bmatrix} \quad (3.16)$$

3.2 Soil Structure Interaction

All operating plants in the United States must quantify the margin for beyond design basis events and take necessary actions to improve the margin if required. This effort is mostly completed by performing Seismic Probabilistic Risk Assessment (SPRA) requiring Soil-Structure Interaction (SSI) analysis as part of the overall analysis. Given the site profile data and the structural model developed as part of the Final Safety Analysis Report (FSAR) are generated many years ago, it is necessary to evaluate the SSI effects for structures founded on rock sites which were considered as fixed base condition during the original analysis.

It is often assumed that dynamic analysis for existing plants that are rock-founded (i.e. with shear wave velocity > 3500 fps) may be completed without consideration of soil structure interaction (SSI) effects (hashemi2012).

3.2.1 Wave Equation

Considering an infinitesimal element at rest, figure 3.6, with elastic modulus E , and mass density ρ , we seek to determine the governing differential equation under dynamic condition.

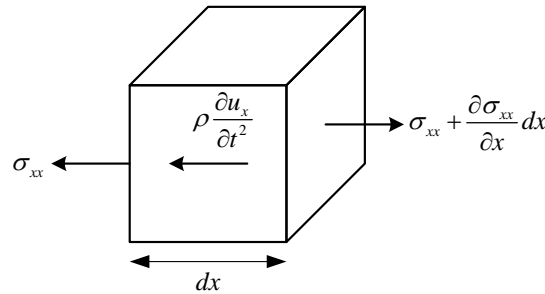


Figure 3.6: Infinitesimal element subjected to elastic wave

Thinking in terms of equilibrium of forces, it is more appealing to invoke D'Alembert's principle of **dynamic equilibrium** rather than Newton's second law of motion. This principle is based on the notion of a fictitious **inertia force**, equal to the product of mass times acceleration and acting in a direction opposite to the acceleration. Hence, the element force equilibrium requirements of a typical differential element are, using D'Alembert's principle which states that with inertia forces included, a system is in equilibrium at each time instant.

$$\frac{\partial \sigma_{xx}}{\partial x} dx - \rho \frac{\partial^2 u_x}{\partial t^2} dx = 0 \quad (3.17)$$

Since $\sigma_{xx} = \lambda \varepsilon_{xx} = \lambda \frac{\partial u_x}{\partial x}$, substituting, we obtain

$$\frac{\partial^2 u_x}{\partial t^2} - V_p^2 \frac{\partial^2 u_x}{\partial x^2} = 0 \quad (3.18)$$

where $V_p = \sqrt{\frac{\lambda}{\rho}}$

The solution of this equation, for harmonic wave propagation in the positive x-direction, is

$$u(t, x) = U \left[\sin\left(\omega t - \frac{\omega x}{V_p}\right) + \cos\left(\omega t - \frac{\omega x}{V_p}\right) \right] \quad (3.19)$$

where ω is the arbitrary frequency of the harmonic motion. The velocity, $\frac{\partial u}{\partial t}$ of a particle at location x is

$$\dot{u}(t, x) = U\omega \left[\cos\left(\omega t - \frac{\omega x}{V_p}\right) - \sin\left(\omega t - \frac{\omega x}{V_p}\right) \right] \quad (3.20)$$

and the strain in the x direction is

$$\varepsilon(x, t) = \frac{\partial u}{\partial x} = -\frac{\dot{u}(x, t)}{V_p} \quad (3.21)$$

The corresponding stress is now

$$\sigma(x, t) = \lambda \varepsilon(x, t) = -V_p \rho \dot{u}(x, t) \quad (3.22)$$

Thus, the compressive stress is equal to the force on a viscous damper with constant damping coefficient equal to ρV_p per unit area of boundary. It can be easily shown that the shear wave radiation boundary condition parallel to a free boundary, is satisfied if damping value is equal to ρV_s .

When modeling the wave motion in a spatial domain, it is essential to introduce artificial boundaries to limit the bounded domain to a reasonable size. The simple Dirichlet boundary condition, in which displacements are fixed, is unsuitable as substantial reflection (through Snell's law) will occur at the boundary and reflected waves will degrade the solution. A solution to this nagging problem could be to enlarge the numerical mesh, thus delaying the side reflections. Obviously this solution considerably increases the expense of computation and is not viable unless artificial damping can be introduced in the material near the far field, (**quad4m**). Thus, a numerical model (finite element in our case) should absorb the incoming waves just as they would be absorbed by the free field physically.

3.2.2 Lysmer Model

lysmer69 were the first to investigate this problem. Their solution is simple, elegant and quite effective. It is based on the premises that one can surround the rock boundary by *viscous boundaries* (through energy absorbent dashpots) with

$$t_n = \rho V_P \dot{u}; \quad t_{s1} = \rho V_S \dot{v}; \quad t_{s2} = \rho V_S \dot{w}; \quad (3.23)$$

where t_n and t_s are the normal and shear tractions respectively; \dot{u} , \dot{v} and \dot{w} the normal and two tangential particle velocities at the boundary; ρ is the mass density; V_S and V_P are the shear and pressure waves velocities respectively given by

$$V_S = \sqrt{\frac{\mu}{\rho}} \quad \text{and} \quad V_P = \frac{1}{s} V_S \quad \text{where} \quad s^2 = \frac{1 - 2\nu}{2(1 - \nu)} \quad (3.24)$$

where μ and ν are the shear modulus and the Poisson ratio respectively.

Lysmer determined the ratio of the reflected energy to incident energy (of the P waves per unit time per unit area) as

$$\frac{E_r}{E_i} = A^2 + s \frac{\sin \beta}{\sin \alpha} B^2 \quad (3.25)$$

where a unit ratio corresponds to a perfect reflection (undesired), while a zero ratio corresponds to complete

absorption (desired). A similar equation was determined for S waves. In both cases, it was found that a viscous boundary defined by $a = b = 1$ is: a) 95% effective in absorbing S waves; and b) absorbs nearly all waves for $\alpha > 30^\circ$ (some reflection occurs at smaller angles), Figure 3.17.

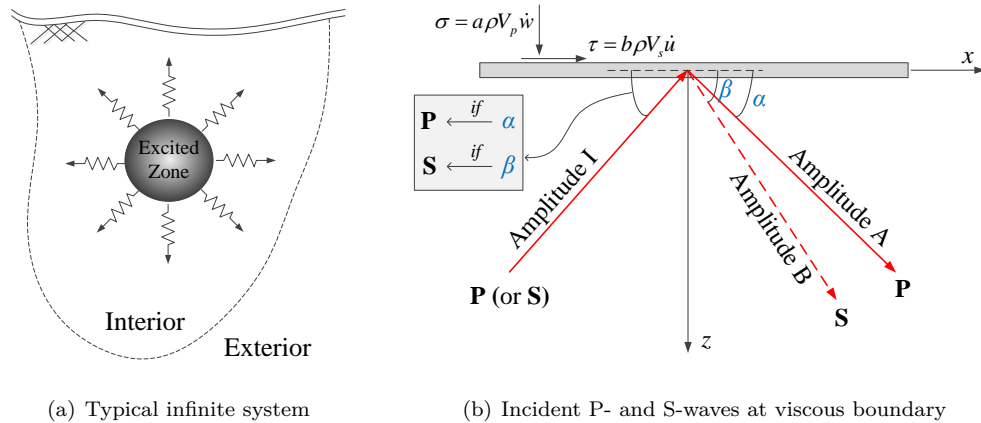


Figure 3.7: Elastic waves in an infinite medium

Strictly speaking, one must thus enforce the so-called Sommerfeld boundary condition, (**sommerfeld**) which is more casually referred to as Lysmer-Kuhlemeyer boundary condition. It is an exact solution if the P and S waves impinge at a right angle the artificial boundary. However they are only approximate solutions for inclined body waves where the reflected energy is only a small part of the total energy. In many cases, the farther one chooses the artificial boundary to be from a source which radiates waves, the more the angle of incidence with respect to the artificial boundary will approach 90° , and, thus, the better the viscous dampers will perform, (**wolf88**).

A major limitation of this approach is that the required damping coefficients are frequency dependent and consequently they can (strictly speaking) only be used in frequency domain calculations, though they are also often used in time domain analyses such as in (**zhang03**).

From a practical point of view, in the context of a finite element simulation, Fig. 3.8 illustrates the dashpot distribution for a mesh subjected to only lateral excitation. Should there be a vertical component, then the vertical support at the base of the dashpots should also be removed (which would raise some problems in the presence of body forces). This model has been implemented in the SHAKE program for the frequency-domain analysis for shear-wave propagation in layered soils (**schnabel72**).

Whereas the viscous boundary model eliminated wave reflections, it did not necessarily account for the proper boundary conditions. This was addressed by **lysmer72** in an *energy transmitting boundary* model. This model assumed a linear variation of shear strain, and those in turn are transformed into equivalent nodal forces to be applied on the numerical one. This model was implemented in (frequency domain) program FLUSH, (**lysmer75**).

Finally, Lysmer boundary conditions can be modeled in Merlin using either one of two models, figure 3.9: lumped or distributed.

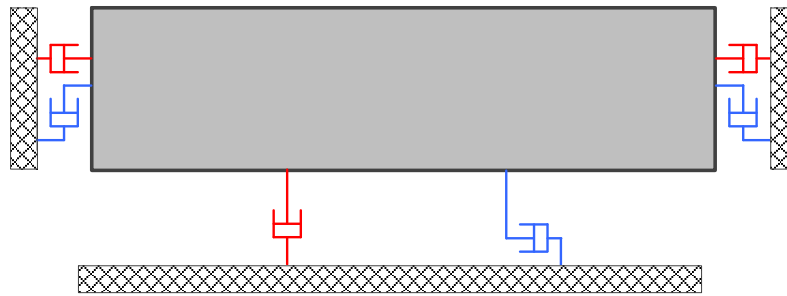


Figure 3.8: Lysmer Modeling for Lateral Excitation

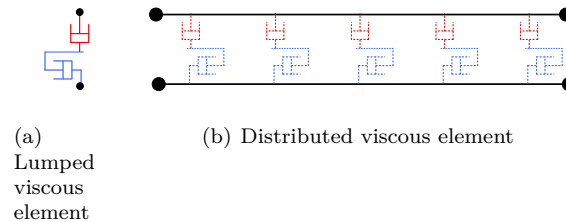


Figure 3.9: Viscous elements (dash-pots)

3.2.3 Other SSI Models

A *Superimposing boundaries* approach was proposed by **smith74** who showed that the reflection from the boundary of a model can be completely eliminated by simply adding the solutions of the Dirichlet and Neumann problems (corresponding to free and fixed boundaries respectively). Hence two separate analyses are performed with different boundary conditions. The first with fixed in normal and free in the tangential, the second free in normal and fixed in tangential directions. Furthermore, if n boundary faces are required to be nonreflecting, than 2^n solutions will be necessary for a full solution. **cundall79** refined this method by summing incrementally the Dirichlet and Neumann solutions at the boundaries of the finite element (or finite difference). This had the advantage of eliminating the reflections as soon as they occur, and thus multiple reflections (encountered by Smith) are voided and only one solution must be performed. However, the fixed-free boundary conditions of Smith are replaced by constant velocity, constant stress ones. In a two dimensional analysis, this corresponds to a) constant velocity in the x and constant stress in the y ; and b) constant stress in the x and constant velocity in the y . Again, rather than performing the same calculation twice with different boundary conditions (as suggested by Smith), two overlapping grids are employed (modeling the free field) with each of the two boundary conditions used separately for each grid. Boundary being represented by four elements, all variables of the two grids are added every three or four time-steps. Hence, the Lysmer-Kuhlemeyer model with absorbing dashpots on the side and bottom is now enriched with a simultaneous free-field calculation that imposes stress conditions on the side boundaries. This model was implemented in the time-history program NEESI, (**cundall80**). Analysis of a dam using analogous boundary conditions was performed by **lemos99** (albeit with a discrete element system) in which one-dimensional calculations representing the left and right free-field conditions are performed in parallel

with the main model. The free field is represented by a one-dimensional finite-difference mesh.

bielak84 introduced an effective seismic input model in which the soil-structure interaction problem is transformed into one in which the source is exclusively inside the computation domain, thus eliminating the need to explicitly transmit seismic excitation through the boundary (which has to simply absorb the outgoing waves).

These two step approaches are analogous to the one of **bielak01** where heterogeneity and scale are accounted for through a two tier approach. The first at the macro scale represents the “far-field” in great details and simulates the earthquake source and propagation path effects with a detailed model. The second models local site effects and presumably includes the structure of interest. Those two analyses are coupled through continuity of displacements and transfer of forces from the first subdomain to the other.

A most recent and noteworthy development, which alleviates the restriction placed on the orientation of the incoming wave, is the Perfectly Matched Layer (PML) (originally developed for electromagnetic wave propagation). When this layer is placed adjacent to a truncated model of an unbounded domain, waves of all frequencies and all angles of incidence are absorbed into without any reflection from the interface: the PML is thus “perfectly matched” to the truncated domain, (**basu04**) and (**basu08**).

It should be noted that the implementation of both the effective seismic input and the perfectly matched layer require substantial modification of the computer code. This is not the case in the proposed model.

Despite the numerous innovative models in SSI, even applications continue to use the Lysmer-Kuhlmeyer model as is the case in **zhang03**.

3.2.4 Miura-Saouma (MS) Model

Section adapted from **lebon-1**

In an earlier publication (in Japanese) **miura87** and (**jsce00**) considered both viscous boundary and energy transmitting boundaries. Those are divided into a) absorption of scattering wave energy on the sides and the bottom; and b) energy inflow from outer free fields.

The model was investigated by Saouma through his contract with the Tokyo Electric Power Service Company (TEPCO) which required its implementation in Merlin. The model was deemed to be incomplete, and lacking proper traceable derivations by the first author. More specifically, there is no derivation of the matrices, how the method is to be actually implemented in a finite element analysis, and is limited to 2D homogeneous models. A closer examination of the Japanese version of the model, (**miura89**), indicates that the free field is analysed in parallel with the main body, and the principle of virtual work is invoked in the derivation. Regretfully, the derivation is again limited to 2D problems, and many critical steps are omitted. Finally, a 2D implementation of this model is reported to be in (**super-flush**).

Hence, the author has revisited the original model of Miura, systematically rederived all the equations, extended it to three dimensional non-homogeneous problems and provided the reader with all necessary analytical expressions for the finite element implementation (**lebon-1**).

It will be shown that implementation of this method does not require internal modification of a finite element code, however extensive data transfer between separate analyses would have to be performed. **lebon-2** reports on the results of a parametric investigation contrasting Lysmer’s model, Miura’s model, and the lack of absorbing boundary conditions in the context of transient analysis of a concrete dam.

The model seeks to concurrently account for 1) absorption of the outgoing scattered wave motion (or radiation damping); and 2) input of the free field ground motion into the numerical model.

The former will be addressed by the classical Lysmer-Kuhlemeyer model. On the other hand, the input

from the free field will be addressed through separate analysis, and resulting displacements and velocities will be transferred as discrete forces to the model.

A key advantage of this method, is the simplicity of the model, and the fact that it is purely a pre or post processing operation which (contrarily to some prevailing methods) does not require modification of the source code. All relevant equations (including 3D) are given, thus greatly facilitating implementation of the model with existing finite element codes.

The interaction between the free field and the foundation is examined first, Fig. 3.10. We identify four

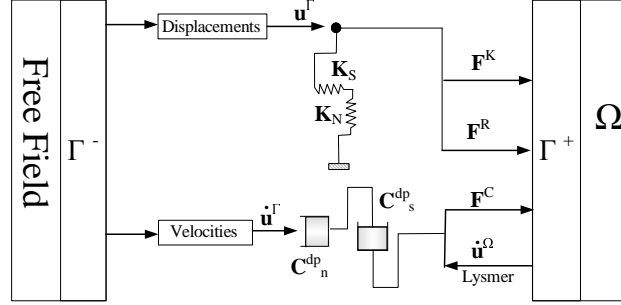


Figure 3.10: Conceptual Model

distinct parts: 1) The free field itself (F) without its contact surface Γ^- ; 2) The contact surface of the free field Γ^- ; 3) the contact surface of the model Γ^+ ; and 4) the model Ω without its contact surface Γ^+ . Hence, mass, damping, and stiffness matrices can each be decomposed into four parts as

$$\left[\begin{array}{cc|cc} FF & F\Gamma^- & F\Gamma^+ & F\Omega \\ \Gamma^-F & \Gamma^-\Gamma^- & \Gamma^-\Gamma^+ & \Gamma^-\Omega \\ \hline \Gamma^+F & \Gamma^+\Gamma^- & \Gamma^+\Gamma^+ & \Gamma^+\Omega \\ \Omega F & \Omega\Gamma^- & \Omega\Gamma^+ & \Omega\Omega \end{array} \right] \quad (3.26)$$

where each term XY infers the effect of Y on X . This is clearly a tightly coupled problem, however if we neglect the influence of the model on the free field response, this reduces to

$$\left[\begin{array}{cc|cc} FF & F\Gamma^- & 0 & 0 \\ \Gamma^-F & \Gamma^-\Gamma^- & 0 & 0 \\ \hline 0 & 0 & \Gamma^+\Gamma^+ & \Gamma^+\Omega \\ 0 & 0 & \Omega\Gamma^+ & \Omega\Omega \end{array} \right] \rightarrow \left[\begin{array}{c|c} F & 0 \\ \hline 0 & \Omega^* \end{array} \right] \quad (3.27)$$

then $\Gamma^-\Gamma^+$ becomes zero we now have a loosely coupled system through $\Gamma^+\Gamma^-$. Hence we can consider the equation of motion for the free field by itself, and will account for the interaction in the equation of motion in Ω by adding forces, stemming from $\Gamma^+\Gamma^-$, on the right hand side. We next write the first equation of motion for the free field:

$$\mathbf{M}^F \ddot{\mathbf{u}}^F + \mathbf{C}^F \dot{\mathbf{u}}^F + \mathbf{K}^F \mathbf{u}^F = \mathbf{t}^F \quad (3.28)$$

solving this equation, we determine the displacements and velocities along Γ^- , and then solve for the equation

of motion in the model:

$$\mathbf{M}^\Omega \ddot{\mathbf{u}}^\Omega + \mathbf{C}^\Omega \dot{\mathbf{u}}^\Omega + \mathbf{K}^\Omega \mathbf{u}^\Omega = \mathbf{t}_{\text{bot}}^\Omega - \underbrace{\left(\mathbf{C}_{\text{lift}}^R \dot{\mathbf{u}}_{\text{lift}}^{\Gamma^-} + \mathbf{K}_{\text{lift}} \mathbf{u}_{\text{lift}}^{\Gamma^-} \right)}_{\text{Left Virtual Interface}} - \underbrace{\left(\mathbf{C}_{\text{rgt}}^R \dot{\mathbf{u}}_{\text{rgt}}^{\Gamma^-} + \mathbf{K}_{\text{rgt}} \mathbf{u}_{\text{rgt}}^{\Gamma^-} \right)}_{\text{Right Virtual Interface}} \quad (3.29)$$

where \mathbf{M} , \mathbf{C} , and \mathbf{K} are the usual mass, damping and stiffness matrices respectively; the subscripts lift , rgt , and bot correspond to left, right, and bottom; the superscript R corresponds to Rayleigh damping.

So far, we have not accounted for one of the premises of the model, that is absorbtion of the outgoing scattered wave, this is simply added through the inclusion of the dashpots in accordance with the Lysmer-Kuhlmeyer model. We note that the viscous forces should be expressed in terms of the relative displacements between Γ^+ and Γ^- .

$$\begin{aligned} \mathbf{M}^\Omega \ddot{\mathbf{u}}^\Omega + \mathbf{C}^\Omega \dot{\mathbf{u}}^\Omega + \mathbf{K}^\Omega \mathbf{u}^\Omega + \mathbf{C}_{\text{lift}}^{dp} \left(\dot{\mathbf{u}}_{\text{lift}}^{\Gamma^+} - \dot{\mathbf{u}}_{\text{lift}}^{\Gamma^-} \right) + \mathbf{C}_{\text{rgt}}^{dp} \left(\dot{\mathbf{u}}_{\text{rgt}}^{\Gamma^+} - \dot{\mathbf{u}}_{\text{rgt}}^{\Gamma^-} \right) + \mathbf{C}_{\text{bot}}^{dp} \dot{\mathbf{u}}_{\text{bot}}^\Omega \\ = \mathbf{t}_{\text{bot}}^\Omega - \left(\mathbf{C}_{\text{lift}}^R \dot{\mathbf{u}}_{\text{lift}}^{\Gamma^-} + \mathbf{K}_{\text{lift}} \mathbf{u}_{\text{lift}}^{\Gamma^-} \right) - \left(\mathbf{C}_{\text{rgt}}^R \dot{\mathbf{u}}_{\text{rgt}}^{\Gamma^-} + \mathbf{K}_{\text{rgt}} \mathbf{u}_{\text{rgt}}^{\Gamma^-} \right) \end{aligned} \quad (3.30)$$

This equation can be rewritten by separating known and unknown quantities, and : substituting the effects of the free field displacements and velocities by their corresponding nodal equivalent forces

$$\begin{aligned} [\mathbf{M}^\Omega \ddot{\mathbf{u}}^\Omega + \mathbf{C}^\Omega \dot{\mathbf{u}}^\Omega + \mathbf{K}^\Omega \mathbf{u}^\Omega] + [\mathbf{C}_{\text{lift}}^{dp} \dot{\mathbf{u}}_{\text{lift}}^\Omega + \mathbf{C}_{\text{rgt}}^{dp} \dot{\mathbf{u}}_{\text{rgt}}^\Omega + \mathbf{C}_{\text{bot}}^{dp} \dot{\mathbf{u}}_B^\Omega] \\ = \mathbf{t}_{\text{bot}}^\Omega + [\mathbf{F}_{\text{lift}}^C + \mathbf{F}_{\text{lift}}^K + \mathbf{F}_{\text{lift}}^R] + [\mathbf{F}_{\text{rgt}}^C + \mathbf{F}_{\text{rgt}}^K + \mathbf{F}_{\text{rgt}}^R] \end{aligned} \quad (3.31)$$

Where \mathbf{F}^C , \mathbf{F}^K , and \mathbf{F}^R are the vectors of nodal equivalent forces caused by the free field velocities, stiffness and damping respectively. They will be separately derived later. The corresponding three dimensional equation would be

$$\begin{aligned} [\mathbf{M}^\Omega \ddot{\mathbf{u}}^\Omega + \mathbf{C}^\Omega \dot{\mathbf{u}}^\Omega + \mathbf{K}^\Omega \mathbf{u}^\Omega] + [\mathbf{C}_{\text{lift}}^{dp} \dot{\mathbf{u}}_{\text{lift}}^\Omega + \mathbf{C}_{\text{rgt}}^{dp} \dot{\mathbf{u}}_{\text{rgt}}^\Omega + \mathbf{C}_{\text{bck}}^{dp} \dot{\mathbf{u}}_{\text{bck}}^\Omega + \mathbf{C}_{\text{fro}}^{dp} \dot{\mathbf{u}}_{\text{fro}}^\Omega + \mathbf{C}_{\text{bot}}^{dp} \dot{\mathbf{u}}_B^\Omega] \\ = \mathbf{t}_{\text{bot}}^\Omega + [\mathbf{F}_{\text{lift}}^C + \mathbf{F}_{\text{lift}}^K + \mathbf{F}_{\text{lift}}^R] + [\mathbf{F}_{\text{rgt}}^C + \mathbf{F}_{\text{rgt}}^K + \mathbf{F}_{\text{rgt}}^R] + [\mathbf{F}_{\text{bck}}^C + \mathbf{F}_{\text{bck}}^K + \mathbf{F}_{\text{bck}}^R] + [\mathbf{F}_{\text{fro}}^C + \mathbf{F}_{\text{fro}}^K + \mathbf{F}_{\text{fro}}^R] \end{aligned} \quad (3.32)$$

where bck and fro correspond to the back and front sides respectively.

To derive the expressions of the forces in the right hand side of Eq. 3.32 we apply the principle of virtual work to the *system*

$$\int_{\Omega} \delta \mathbf{u} \cdot [\rho \ddot{\mathbf{u}} + \eta \dot{\mathbf{u}} + \mathbf{F}] d\Omega = \int_{\Gamma} \delta \mathbf{u} \cdot (\mathbf{t}^{\text{bot}} + \mathbf{t}^{\Gamma^-}) d\Gamma \quad (3.33)$$

where ρ is the mass density, η the viscosity parameter, \mathbf{F} the internal force, \mathbf{u} the displacement vector, \mathbf{t}^{bot} and \mathbf{t}^{Γ^-} are the surface traction on the boundary Γ (base and free field). It can be readily shown that the left and right hand sides of Eq. 3.33 corresponds to the integral form of the left and right hand sides of Eq. 3.32 respectively.

3.2.4.1 Internal Virtual Work

Discretizing the continuum through shape function, (Zienkiewicz and Taylor V'1), it can be readily shown that the left hand side and the first right hand side term of Eq. 3.33 correspond to the classical form of the equation of motion

$$\mathbf{M}^\Omega \ddot{\mathbf{u}}^\Omega + \mathbf{C}^\Omega \dot{\mathbf{u}}^\Omega + \mathbf{K} \mathbf{u}^\Omega$$

In the context of the present analysis, this can be generalized to the right hand side of Eq. 3.32.

3.2.4.2 External Virtual Work

Focusing on the remaining term of the external virtual force can be expressed as

$$\int_{\Gamma} \delta \mathbf{u} \cdot \mathbf{t}^{\Gamma^-} d\Gamma = \int_0^{t_y} \int_0^{t_z} [\delta u t_n + \delta v t_{s1} + \delta w t_{s2}] dz dy \quad (3.34)$$

In the next sections we will separately determine the tractions caused by presence of dashpots or the free field displacements.

3.2.4.2.1 Forces Caused by Velocity Due to the presence of the dashpots around the bounded model, we substitute Eq. 3.24 into Eq. 3.34. It should be noted that in the model, the velocities will actually correspond to difference in velocities between the free field and the bounded model: $\dot{\mathbf{u}}_{\text{ift}}^{\Omega} - \dot{\mathbf{u}}_{\text{ift}}^{\Gamma^-}$ as in Eq. 3.30. The nodal displacements along the surface boundary can be expressed in terms of the known nodal ones through the shape functions (assuming a linear variation). Considering the x -plane the finite element discretization yields

$$\begin{cases} u = \mathbf{N}_u \bar{\mathbf{u}}; & \delta u = \mathbf{N}_u \delta \bar{\mathbf{u}}; & V_p \dot{u} = V_p \mathbf{N}_u \dot{\bar{\mathbf{u}}} \\ v = \mathbf{N}_v \bar{\mathbf{u}}; & \delta v = \mathbf{N}_v \delta \bar{\mathbf{u}}; & V_s \dot{v} = V_s \mathbf{N}_v \dot{\bar{\mathbf{u}}} \\ w = \mathbf{N}_w \bar{\mathbf{u}}; & \delta w = \mathbf{N}_w \delta \bar{\mathbf{u}}; & V_s \dot{w} = V_s \mathbf{N}_w \dot{\bar{\mathbf{u}}} \end{cases} \quad (3.35)$$

where the shape functions, for the bilinear element shown in Fig. 3.11, are given by

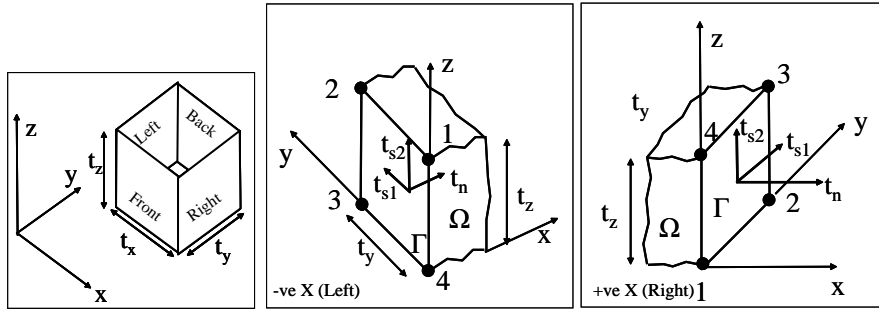


Figure 3.11: 2D Idealization and Γ_x Plane

$$\begin{aligned} \mathbf{N}_u &= \frac{1}{t_y t_z} \begin{bmatrix} (t_y - y)(t_z - z) & 0 & 0 & (t_z - z)y & 0 & 0 & zy & 0 & 0 & z(t_y - y) & 0 & 0 \end{bmatrix}^T \\ \mathbf{N}_v &= \frac{1}{t_y t_z} \begin{bmatrix} 0 & (t_y - y)(t_z - z) & 0 & 0 & (t_z - z)y & 0 & 0 & zy & 0 & 0 & z(t_y - y) & 0 \end{bmatrix}^T \\ \mathbf{N}_w &= \frac{1}{t_y t_z} \begin{bmatrix} 0 & 0 & (t_y - y)(t_z - z) & 0 & 0 & (t_z - z)y & 0 & 0 & zy & 0 & 0 & z(t_y - y) \end{bmatrix}^T \end{aligned} \quad (3.36)$$

and

$$\bar{\mathbf{u}} = [\bar{u}_1 \quad \bar{v}_1 \quad \bar{w}_1 \quad \bar{u}_2 \quad \bar{v}_2 \quad \bar{w}_2 \quad \bar{u}_3 \quad \bar{v}_3 \quad \bar{w}_3 \quad \bar{u}_4 \quad \bar{v}_4 \quad \bar{w}_4]^T \quad (3.37)$$

Substituting¹ in Eq. 3.34,

$$\int_{\Gamma} \delta \mathbf{u} \cdot \mathbf{t} d\Gamma = \rho \int_0^{t_z} \int_0^{t_y} V_p \mathbf{N}_u \cdot \mathbf{N}_u^T + V_s (\mathbf{N}_v \cdot \mathbf{N}_v^T + \mathbf{N}_w \cdot \mathbf{N}_w^T) dy dz \quad (3.38)$$

¹All operations performed by *Mathematica*.

or $\mathbf{F}^C = \mathbf{C}_x^{dp} \dot{\mathbf{u}}$ where

$$\mathbf{C}_x^L = \frac{\rho t_y t_z}{36} \begin{bmatrix} 4V_p & 0 & 0 & 2V_p & 0 & 0 & V_p & 0 & 0 & 2V_p & 0 & 0 \\ 0 & 4V_s & 0 & 0 & 2V_s & 0 & 0 & V_s & 0 & 0 & 2V_s & 0 \\ 0 & 0 & 4V_s & 0 & 0 & 2V_s & 0 & 0 & V_s & 0 & 0 & 2V_s \\ 2V_p & 0 & 0 & 4V_p & 0 & 0 & 2V_p & 0 & 0 & V_p & 0 & 0 \\ 0 & 2V_s & 0 & 0 & 4V_s & 0 & 0 & 2V_s & 0 & 0 & V_s & 0 \\ 0 & 0 & 2V_s & 0 & 0 & 4V_s & 0 & 0 & 2V_s & 0 & 0 & V_s \\ V_p & 0 & 0 & 2V_p & 0 & 0 & 4V_p & 0 & 0 & 2V_p & 0 & 0 \\ 0 & V_s & 0 & 0 & 2V_s & 0 & 0 & 4V_s & 0 & 0 & 2V_s & 0 \\ 0 & 0 & V_s & 0 & 0 & 2V_s & 0 & 0 & 4V_s & 0 & 0 & 2V_s \\ 2V_p & 0 & 0 & V_p & 0 & 0 & 2V_p & 0 & 0 & 4V_p & 0 & 0 \\ 0 & 2V_s & 0 & 0 & V_s & 0 & 0 & 2V_s & 0 & 0 & 4V_s & 0 \\ 0 & 0 & 2V_s & 0 & 0 & V_s & 0 & 0 & 2V_s & 0 & 0 & 4V_s \end{bmatrix} \quad (3.39)$$

The same expression applies on the positive and negative faces.

The two dimensional equivalent matrix is obtained by simply adding rows and columns 1-4, 3-6, 7-10, 9-12 (while dropping rows and columns 2, 5, 8 and 11) in Eq. 3.39. This reduces to

$$\mathbf{F}^C = \frac{\rho t_z}{6} \begin{bmatrix} 2V_p & 0 & V_p & 0 \\ 0 & 2V_s & 0 & V_s \\ V_p & 0 & 2V_p & 0 \\ 0 & V_s & 0 & 2V_s \end{bmatrix} \begin{Bmatrix} \dot{u}_1 \\ \dot{v}_1 \\ \dot{u}_2 \\ \dot{v}_2 \end{Bmatrix} \quad (3.40)$$

It should be noted that both the left and right sides will be subjected to the same \mathbf{C}_x^L matrix.

3.2.4.2.2 Forces Caused by Displacements The lateral forces exerted on the bounded domain by the free field displacements are determined next. The free field will be modeled as a shear beam (where $\frac{\partial u}{\partial x} = 0$) and in the most general case, Fig. 3.11, there will be displacements along the three axis x , y and z . Hence, unsymmetric and non-homogeneous boundaries could be accounted for. The traction terms to be substituted in Eq. 3.34 are thus

$$\begin{cases} t_n &= \sigma_{xx} &= \lambda(\epsilon_{xx} + \epsilon_{yy} + \epsilon_{zz}) + 2\mu\epsilon_{xx} &= \lambda\left(\frac{\partial v}{\partial y} + \frac{\partial w}{\partial z}\right) \\ t_{s1} &= \tau_{xy} &= \mu\gamma_{xy} &= \mu\frac{\partial u}{\partial y} \\ t_{s2} &= \tau_{xz} &= \mu\gamma_{xz} &= \mu\frac{\partial u}{\partial z} \end{cases} \quad (3.41)$$

where λ and μ are the classical Lamé's parameters,

$$\lambda = \frac{\nu E}{(1 + \nu)(1 - 2\nu)}; \quad \mu = \frac{E}{2(1 + \nu)} \quad (3.42)$$

The internal displacements can be expressed in terms of the known nodal ones through the shape functions, Eq. 3.36. Substituting into Eq. 3.34, we obtain:

$$\delta W_{ext} = \delta \bar{\mathbf{u}} \int_0^{t_z} \int_0^{t_y} \left[\mathbf{N}_u \cdot \left[\lambda \left(\frac{\partial \mathbf{N}_v}{\partial y} + \frac{\partial \mathbf{N}_w}{\partial z} \right) \right] + \mathbf{N}_v \cdot \left(\mu \frac{\partial \mathbf{N}_u}{\partial y} \right) + \mathbf{N}_w \cdot \left(\mu \frac{\partial \mathbf{N}_u}{\partial z} \right) \right] dy dz \bar{\mathbf{u}} \quad (3.43)$$

Or

$$\mathbf{F}^K = \mathbf{K}_x^+ \bar{\mathbf{u}} \quad (3.44)$$

where

$$\mathbf{F}^K = [F_{1,u} \ F_{1,v} \ F_{1,w} \ F_{2,u} \ F_{2,v} \ F_{2,w} \ F_{3,u} \ F_{3,v} \ F_{3,w} \ F_{4,u} \ F_{4,v} \ F_{4,w}]^T \quad (3.45)$$

and the corresponding stiffness matrix is given by

$$\mathbf{K}_x^+ = \frac{1}{12} \begin{bmatrix} 0 & -2t_z\lambda & -2t_y\lambda & 0 & 2t_z\lambda & -t_y\lambda & 0 & t_z\lambda & t_y\lambda & 0 & -t_z\lambda & 2t_y\lambda \\ -2t_z\mu & 0 & 0 & 2t_z\mu & 0 & 0 & t_z\mu & 0 & 0 & -t_z\mu & 0 & 0 \\ -2t_y\mu & 0 & 0 & -t_y\mu & 0 & 0 & t_y\mu & 0 & 0 & 2t_y\mu & 0 & 0 \\ 0 & -2t_z\lambda & -t_y\lambda & 0 & 2t_z\lambda & -2t_y\lambda & 0 & t_z\lambda & 2t_y\lambda & 0 & -t_z\lambda & t_y\lambda \\ -2t_z\mu & 0 & 0 & 2t_z\mu & 0 & 0 & t_z\mu & 0 & 0 & -t_z\mu & 0 & 0 \\ -t_y\mu & 0 & 0 & -2t_y\mu & 0 & 0 & 2t_y\mu & 0 & 0 & t_y\mu & 0 & 0 \\ 0 & -t_z\lambda & -t_y\lambda & 0 & t_z\lambda & -2t_y\lambda & 0 & 2t_z\lambda & 2t_y\lambda & 0 & -2t_z\lambda & t_y\lambda \\ -t_z\mu & 0 & 0 & t_z\mu & 0 & 0 & 2t_z\mu & 0 & 0 & -2t_z\mu & 0 & 0 \\ -t_y\mu & 0 & 0 & -2t_y\mu & 0 & 0 & 2t_y\mu & 0 & 0 & t_y\mu & 0 & 0 \\ 0 & -t_z\lambda & -2t_y\lambda & 0 & t_z\lambda & -t_y\lambda & 0 & 2t_z\lambda & t_y\lambda & 0 & -2t_z\lambda & 2t_y\lambda \\ -t_z\mu & 0 & 0 & t_z\mu & 0 & 0 & 2t_z\mu & 0 & 0 & -2t_z\mu & 0 & 0 \\ -2t_y\mu & 0 & 0 & -t_y\mu & 0 & 0 & t_y\mu & 0 & 0 & 2t_y\mu & 0 & 0 \end{bmatrix} \quad (3.46)$$

Rayleigh damping is introduced

$$[\mathbf{F}^R] = \frac{\zeta}{\pi f} [\mathbf{K}] \quad (3.47)$$

where ζ is the damping factor at frequency f . We note that this is stiffness proportional only since we are dealing with a massless element.

Again, the two dimensional equivalent matrix is obtained by simply adding rows and columns 1-4, 3-6, 7-10, 9-12 (while dropping rows and columns 2, 5, 8 and 11). This reduces to If we were to limit ourselves to the two dimensional case, then on the lateral boundary

$$\delta W_{ext} = \delta \mathbf{u} \cdot \mathbf{t} = t \int_0^h [\delta u t_n + \delta w t_s] dz \quad (3.48)$$

and

$$\begin{cases} t_n &= \sigma_{xx} &= \lambda(\epsilon_{xx} + \epsilon_{zz}) + 2\mu\epsilon_{xx} &= \lambda \frac{\partial w}{\partial z} \\ t_s &= \tau_{xz} &= \mu\epsilon_{xz} &= \mu \frac{\partial u}{\partial z} \end{cases} \quad (3.49)$$

The internal displacements can be expressed in terms of the known nodal ones through the linear shape functions. Substituting into equation 3.48, we obtain:

$$\delta W = t\delta \bar{\mathbf{u}} \int_0^h \left[\underbrace{\mathbf{N}_u \cdot \lambda \frac{\partial \mathbf{N}_w}{\partial z}}_{K_n} + \underbrace{\mathbf{N}_w \cdot \mu \frac{\partial \mathbf{N}_u}{\partial z}}_{K_s} \right] \bar{\mathbf{u}} dz \quad (3.50)$$

or $\mathbf{F}^K = \mathbf{K} \bar{\mathbf{u}}$ where

$$\mathbf{F}^K = [F_{1,u} \ F_{1,v} \ F_{2,u} \ F_{2,v}]^T \quad (3.51)$$

These equations are similar to the one of Miura in the Super flush manual (**super-flush**).

$$\mathbf{K}_x^+ = \frac{t}{2} \begin{bmatrix} 0 & -\lambda & 0 & \lambda \\ -\mu & 0 & \mu & 0 \\ 0 & -\lambda & 0 & \lambda \\ -\mu & 0 & \mu & 0 \end{bmatrix} \quad (3.52)$$

3.2.5 Validation Problems

To assess the effectiveness of the method in dissipating elastic waves an extensive parametric study is performed. We consider a soft foundation with E , ρ and ν equal to 1.563×10^3 MN/m², 2,500 kg/m³ and 0.25 respectively. This corresponds to a shear wave velocity (V_S from Eq. 3.24) of 500 m/sec. Hence by exciting the base with a harmonic excitation with period of 0.4 sec, a full wave length develops over 200 m which is the height of the model. Length is set to 800 m, and the 3D model in turn is 200 by 800 by 800 m. Since the base excitation has a magnitude of 1 m/sec.², ideally we should have a similar (though with a phase lag) response at the top of the bounded domain. In both cases element size was 25 m (except for a fine 2D mesh with half this size). Results are assessed by examining the acceleration at the top, distribution of accelerations at $h/8$ increments, deformed shapes and velocity or acceleration contour lines. From this investigation we conclude that:

1. When the boundaries are left bare (for both 2D and 3D analyses), results are totally unacceptable, Fig. 3.12.

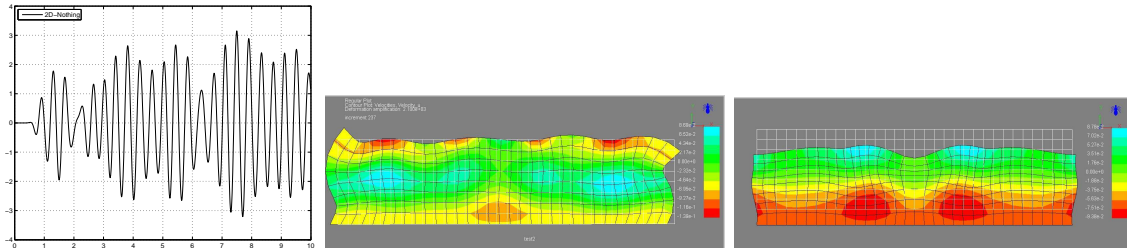


Figure 3.12: Selected results for 2D analyses with free boundaries; Crest accelerations, deformed shapes with contour lines of V_X and V_Y

2. 2D Lysmer yields nearly perfect (0.9) acceleration at h , nearly zero accelerations at the knots ($h/4$ and $3h/4$) barely acceptable displacements for horizontal excitation, and very bad ones for a vertical excitation. Top accelerations due to vertical excitation were slightly better than when a horizontal was applied, Fig. 3.13.
3. 2D Present model gave excellent top acceleration (~ 1.0), nearly zero ones at the knots (have as large as those predicted by Lysmer), and a deformation which indeed is consistent with a shear beam. It should be noted that best results are achieved when both terms were included (C and K). Similarly, excellent results were obtained for vertical excitation (the importance of including both terms was more accentuated than for the horizontal acceleration), Fig. 3.14.
4. The 3D analysis based on Lysmer's model yields top acceleration slightly higher than 1.0, a good deformation, and not quite a homogeneous velocity distribution, Fig. 3.15.
5. the 3D analysis based on the present model yielded a nearly perfect acceleration distribution from

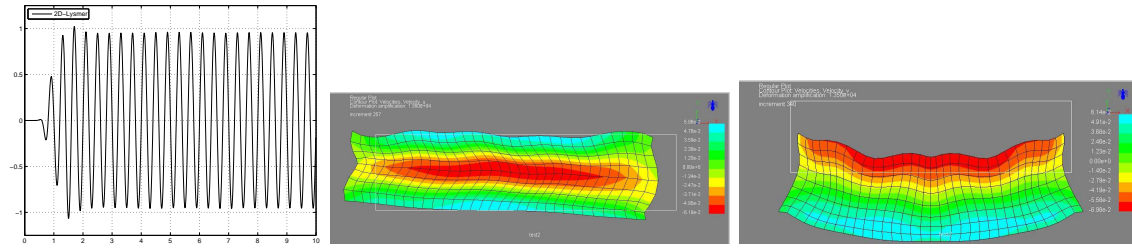


Figure 3.13: Selected results for 2D Lysmer analyses; Crest accelerations, deformed shapes with contour lines of V_X and V_Y

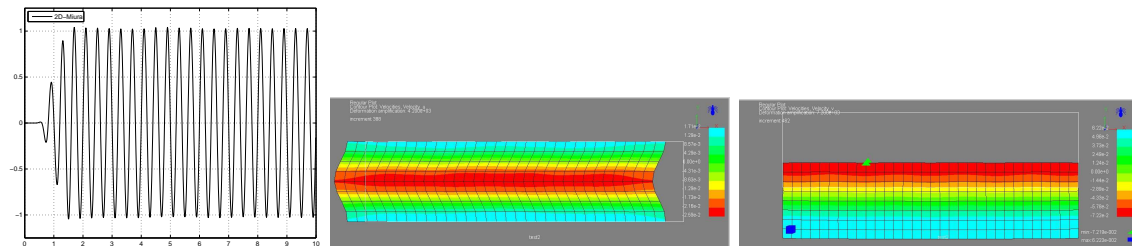


Figure 3.14: Selected results for 2D Miura-Saouma analyses; Crest accelerations, deformed shapes with contour lines of V_X and V_Y

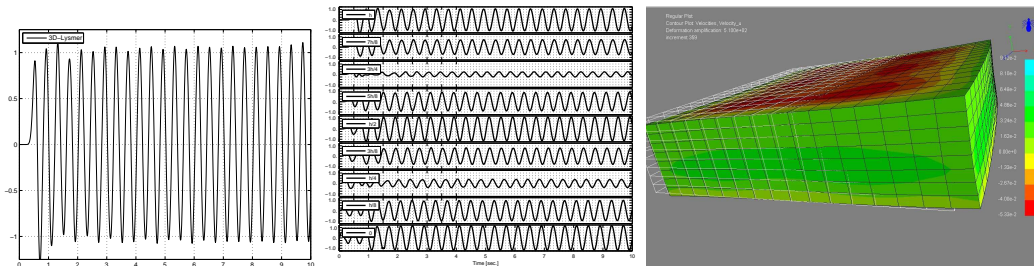


Figure 3.15: Selected results for 3D Lysmer analyses; Crest accelerations, accelerations at $h = 0, h/8, h/4, 3h/8, h/2, 5h/8, 3h/4, 7h/8$ and h ; deformed shapes with contour lines of V_X

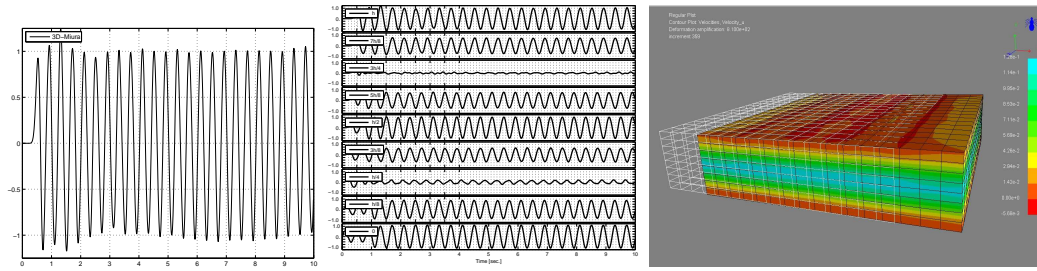


Figure 3.16: Selected results for 3D Miura-Saouma analyses; Crest accelerations, accelerations at $h = 0, h/8, h/4, 3h/8, h/2, 5h/8, 3h/4, 7h/8$ and h ; deformed shapes with contour lines of V_x

bottom to top, a very smooth deformation, and internal velocity distribution, Fig. 3.16.

In summary, Lysmer's model performs better in 3D than in 2D, whereas the present one yields excellent results in all analyses.

3.2.6 Viscous Boundary Conditions; Lysmer Model

When modeling a dynamic problem involving soil-structure interaction, particular attention must be given to the soil boundary conditions. Ideally, infinite boundary conditions should be surrounding the excited zone. Propagation of energy will occur from the interior to the exterior region. Since the exterior region is non-reflecting, it absorbs all the incoming energy. Yet, in a finite element analysis, we are constrained into applying finite size boundaries for the foundations. Those boundaries in turn will reflect the elastic waves which is contrary to the physics of the problem.

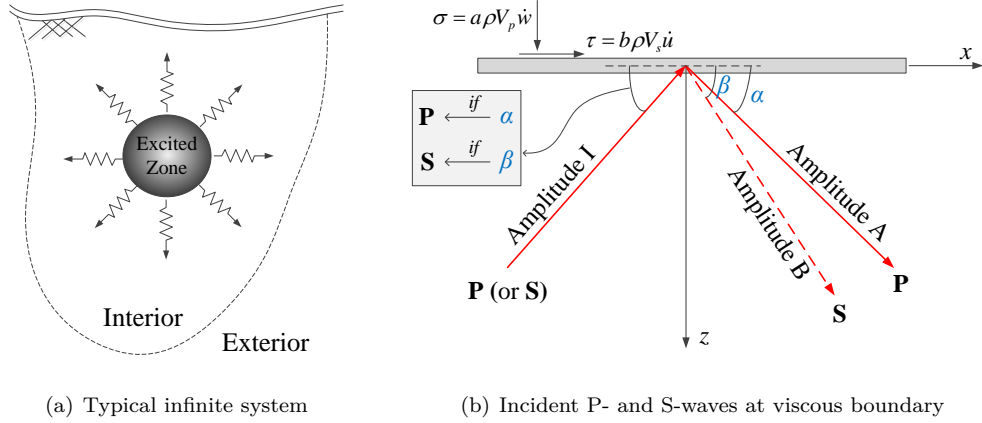


Figure 3.17: Elastic waves in an infinite medium

lysmer69 was the first to investigate this problem, and he proposed a model through which the boundary of a finite element mesh is surrounded by (energy absorbent) dashpots where

$$\sigma = a\rho V_P \dot{w} \quad (3.53)$$

$$\tau = b\rho V_S \dot{u} \quad (3.54)$$

where σ and τ are the normal and shear stresses respectively; \dot{w} and \dot{u} are the normal and tangential velocities; ρ is the mass density; V_s and V_p are the shear and pressure waves respectively given by

$$V_s = \sqrt{\frac{G}{\rho}} \quad (3.55)$$

$$V_p = \frac{1}{s} V_s \quad \text{where} \quad s^2 = \frac{1-2\nu}{2(1-\nu)} \quad (3.56)$$

where G and ν are the shear modulus and the Poisson's ratio respectively.

The directions of the incident and reflected waves are related through Snell's Law

$$\cos \beta = s \cos \alpha \quad (3.57)$$

Lysmer determined the ratio of the reflected energy to incident energy (of the P waves per unit time per unit area) as

$$\frac{E_r}{E_i} = A^2 + s \frac{\sin \beta}{\sin \alpha} B^2 \quad (3.58)$$

where a unit ratio corresponds to a perfect reflection (undesired), while a zero ratio corresponds to complete absorption (desired). A similar equation was determined for S waves. In both cases, it was found that a viscous boundary defined by $a = b = 1$ is: a) 95% effective in absorbing S waves; and b) absorbs nearly all waves for $\alpha > 30^\circ$ (some reflection occurs at smaller angles).

3.2.6.1 Active/Flexible Boundary; Miura-Saouma

Recognizing that in practice we do not have a rigid support for the foundation, but rather a flexible one, we need to account for this added variability, Fig. 3.18.

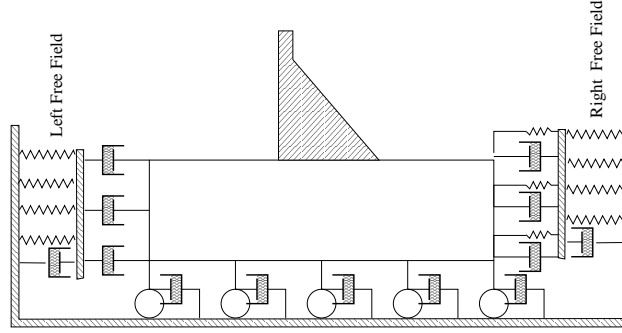


Figure 3.18: Foundation Model, Radiating Flexible Foundation

The methodology here adopted here is based on the work of **miura87**.

The governing equation for a dam foundation system in an infinite flexible medium is given by

$$[\mathbf{M}] \{\ddot{\mathbf{x}}\} + ([\mathbf{C}] + [\mathbf{C}_B] + [\mathbf{C}_L] + [\mathbf{C}_R]) \{\dot{\mathbf{x}}\} + [\mathbf{K}] \{\mathbf{x}\} = \{\mathbf{f}\} + [\mathbf{C}_L] \{\dot{\mathbf{x}}_L\} + [\mathbf{C}_R] \{\dot{\mathbf{x}}_R\} + [\mathbf{G}_{CL}] \{\dot{\mathbf{x}}_L\} + [\mathbf{G}_{CR}] \{\dot{\mathbf{x}}_R\} + [\mathbf{G}_L] \{\mathbf{x}_L\} + [\mathbf{G}_R] \{\mathbf{x}_R\} \quad (3.59)$$

This equation can be rewritten as

$$= \begin{bmatrix} M_{II} & M_{IB} & M_{IL} & M_{IR} \\ M_{BI} & M_{BB} & M_{BL} & M_{BR} \\ M_{LI} & M_{LB} & M_{LL} & 0 \\ M_{RI} & M_{RB} & 0 & M_{RR} \end{bmatrix} \begin{Bmatrix} \ddot{x}_B \\ \ddot{x}_L \\ \ddot{x}_R \end{Bmatrix} + \begin{bmatrix} C_{II} & C_{IB} & C_{IL} & C_{IR} \\ C_{BI} & C_{BB} & C_{BL} & C_{BR} \\ C_{LI} & C_{LB} & C_{LL} & 0 \\ C_{RI} & C_{RB} & 0 & C_{RR} \end{bmatrix} \begin{Bmatrix} \dot{x}_B \\ \dot{x}_L \\ \dot{x}_R \end{Bmatrix} + \begin{bmatrix} K_{II} & K_{IB} & K_{IL} & K_{IR} \\ K_{BI} & K_{BB} & K_{BL} & K_{BR} \\ K_{LI} & K_{LB} & K_{LL} & 0 \\ K_{RI} & K_{RB} & 0 & K_{RR} \end{bmatrix} \begin{Bmatrix} x_B \\ x_L \\ x_R \end{Bmatrix} + \begin{bmatrix} 0 \\ 0 \\ C_{LL} + G_{CL} \\ C_{RR} + G_{CR} \end{bmatrix} \begin{Bmatrix} \dot{x}_I \\ \dot{x}_B \\ \dot{x}_L \\ \dot{x}_R \end{Bmatrix} + \begin{bmatrix} 0 \\ 0 \\ G_L \\ G_R \end{bmatrix} \begin{Bmatrix} x_B \\ x_L \\ x_R \end{Bmatrix}$$

where $[\mathbf{M}]$ is the mass matrix, $[\mathbf{C}]$ damping matrix, $[\mathbf{K}]$ stiffness matrix and subscripts I, B, L, R refer to interior, bottom, left and right nodes; $\{\mathbf{x}\}$, $\{\dot{\mathbf{x}}\}$, $\{\ddot{\mathbf{x}}\}$ are the nodal displacements, velocities and accelerations.

$[\mathbf{C}_B]$ is Lysmer (dashpot) viscous boundary conditions at the bottom (tuned to shear wave for lateral excitation and to pressure waves for vertical excitation).

$$[\mathbf{C}_B] = \frac{\rho L}{2} \begin{bmatrix} V_H & 0 & 0 & 0 \\ 0 & V_V & 0 & 0 \\ 0 & 0 & V_H & 0 \\ 0 & 0 & 0 & V_V \end{bmatrix} \quad (3.60)$$

$$\begin{cases} V_H = V_S \cos \theta + V_P \sin \theta \\ V_V = V_P \cos \theta + V_S \sin \theta \end{cases} \quad (3.61)$$

$[\mathbf{C}_L], [\mathbf{C}_R]$ are Lysmer (dashpot) left and right boundary conditions, tuned to pressure wave for lateral excitation and shear waves for vertical excitation. $[\mathbf{G}_L], [\mathbf{G}_R]$ are the boundary stiffness matrices associated with the displacement of the free field.

$$[\mathbf{G}] = \frac{1}{2} \begin{bmatrix} 0 & -\lambda & 0 & \lambda \\ -\mu & 0 & \mu & 0 \\ 0 & -\lambda & 0 & \lambda \\ -\mu & 0 & \mu & 0 \end{bmatrix} \quad (3.62)$$

where λ and μ are the Lamé parameters, $\lambda = \frac{\nu E}{(1-2\nu)(1+\nu)} = K - \frac{2}{3}G$, and $\mu = \frac{E}{2(1+\nu)} = G$. For symmetric foundation ($\mathbf{x}_L = -\mathbf{x}_R$) we can ignore this term. $[\mathbf{G}_{CL}], [\mathbf{G}_{CR}]$ are the boundary damping matrices associated with the free field. Their effect do also cancel out for symmetric cases.

Hence, for symmetric boundary conditions, we can ignore $[\mathbf{G}_R], [\mathbf{G}_L], [\mathbf{G}_{CR}], [\mathbf{G}_{CL}], \mathbf{x}_R, \mathbf{x}_L$, and the resulting governing partial differential equation to be solved is reduced to:

$$[\mathbf{M}] \{\ddot{\mathbf{x}}\} + ([\mathbf{C}] + [\mathbf{C}_b] + [\mathbf{C}_L] + [\mathbf{C}_R]) \{\dot{\mathbf{x}}\} + [\mathbf{K}] \{\mathbf{x}\} = \{\mathbf{f}\} + [\mathbf{C}_L] \{\dot{\mathbf{x}}_L\} + [\mathbf{C}_R] \{\dot{\mathbf{x}}_R\} \quad (3.63)$$

or

$$\begin{aligned} & \left[\begin{array}{cc|cc} \mathbf{M}_{II} & \mathbf{M}_{IB} & \mathbf{M}_{IL} & \mathbf{M}_{IR} \\ \mathbf{M}_{BI} & \mathbf{M}_{BB} & \mathbf{M}_{BL} & \mathbf{M}_{BR} \\ \mathbf{M}_{LI} & \mathbf{M}_{LB} & \mathbf{M}_{LL} & 0 \\ \mathbf{M}_{RI} & \mathbf{M}_{RB} & 0 & \mathbf{M}_{RR} \end{array} \right] \begin{Bmatrix} \dot{\mathbf{x}}_I \\ \dot{\mathbf{x}}_B \\ \dot{\mathbf{x}}_L \\ \dot{\mathbf{x}}_R \end{Bmatrix} + \left[\begin{array}{cc|cc} \mathbf{C}_{II} & \mathbf{C}_{IB} & \mathbf{C}_{IL} & \mathbf{C}_{IR} \\ \mathbf{C}_{BI} & \mathbf{C}_{BB} & \mathbf{C}_{BL} & \mathbf{C}_{BR} \\ \mathbf{C}_{LI} & \mathbf{C}_{LB} & \mathbf{C}_{LL} & 0 \\ \mathbf{C}_{RI} & \mathbf{C}_{RB} & 0 & \mathbf{C}_{RR} \end{array} \right] \begin{Bmatrix} \dot{\mathbf{x}}_I \\ \dot{\mathbf{x}}_B \\ \dot{\mathbf{x}}_L \\ \dot{\mathbf{x}}_R \end{Bmatrix} + \left[\begin{array}{cc|cc} \mathbf{K}_{II} & \mathbf{K}_{IB} & \mathbf{K}_{IL} & \mathbf{K}_{IR} \\ \mathbf{K}_{BI} & \mathbf{K}_{BB} & \mathbf{K}_{BL} & \mathbf{K}_{BR} \\ \mathbf{K}_{LI} & \mathbf{K}_{LB} & \mathbf{K}_{LL} & 0 \\ \mathbf{K}_{RI} & \mathbf{K}_{RB} & 0 & \mathbf{K}_{RR} \end{array} \right] \begin{Bmatrix} \mathbf{x}_I \\ \mathbf{x}_B \\ \mathbf{x}_L \\ \mathbf{x}_R \end{Bmatrix} \\ & = \begin{Bmatrix} \mathbf{f}_I \\ \mathbf{f}_B \\ \mathbf{f}_L \\ \mathbf{f}_R \end{Bmatrix} + \left[\begin{array}{cc|cc} 0 & & & \\ & 0 & & \\ & & \mathbf{C}_{LL} & \\ & & & \mathbf{C}_{RR} \end{array} \right] \begin{Bmatrix} \dot{\mathbf{x}}_I \\ \dot{\mathbf{x}}_B \\ \dot{\mathbf{x}}_L \\ \dot{\mathbf{x}}_R \end{Bmatrix} \end{aligned}$$

In order to solve this equation, we still need some quantities on the right hand side of the equation, namely $\dot{\mathbf{x}}_L$ and $\dot{\mathbf{x}}_R$. These can be obtained from two separate (one if we take advantage of symmetry) analyses of the free field which can be discretized as shown in Fig. 3.19. We note the vertical restraint for lateral excitation, and the lateral restraint for vertical excitation in order to respect the far field boundary conditions. Thus the governing differential equations for these analyses are

$$[\mathbf{M}_L] \{\ddot{\mathbf{x}}_L^?\} + [\mathbf{C}_L] \{\dot{\mathbf{x}}_L^?\} + [\mathbf{K}_L] \{\mathbf{x}_L^?\} = \{\mathbf{f}_L\sqrt{\}\} \quad (3.64)$$

$$[\mathbf{M}_R] \{\ddot{\mathbf{x}}_R^?\} + [\mathbf{C}_R] \{\dot{\mathbf{x}}_R^?\} + [\mathbf{K}_R] \{\mathbf{x}_R^?\} = \{\mathbf{f}_R\sqrt{\}\} \quad (3.65)$$

from which we solve for $\dot{\mathbf{x}}_L$ and $\dot{\mathbf{x}}_R$.

Once the free field velocities have been obtained, they can in turn be used in the full 2D analysis of the dam/foundation discretization shown in 3.20.

$$\begin{aligned} & \left[\begin{array}{cc|cc} \mathbf{M}_{II} & \mathbf{M}_{IB} & \mathbf{M}_{IL} & \mathbf{M}_{IR} \\ \mathbf{M}_{BI} & \mathbf{M}_{BB} & \mathbf{M}_{BL} & \mathbf{M}_{BR} \\ \mathbf{M}_{LI} & \mathbf{M}_{LB} & \mathbf{M}_{LL} & 0 \\ \mathbf{M}_{RI} & \mathbf{M}_{RB} & 0 & \mathbf{M}_{RR} \end{array} \right] \begin{Bmatrix} \dot{\mathbf{x}}_I^? \\ \dot{\mathbf{x}}_B^? \\ \dot{\mathbf{x}}_L^? \\ \dot{\mathbf{x}}_R^? \end{Bmatrix} + \left[\begin{array}{cc|cc} \mathbf{C}_{II} & \mathbf{C}_{IB} & \mathbf{C}_{IL} & \mathbf{C}_{IR} \\ \mathbf{C}_{BI} & \mathbf{C}_{BB} & \mathbf{C}_{BL} & \mathbf{C}_{BR} \\ \mathbf{C}_{LI} & \mathbf{C}_{LB} & \mathbf{C}_{LL} & 0 \\ \mathbf{C}_{RI} & \mathbf{C}_{RB} & 0 & \mathbf{C}_{RR} \end{array} \right] \begin{Bmatrix} \dot{\mathbf{x}}_I^? \\ \dot{\mathbf{x}}_B^? \\ \dot{\mathbf{x}}_L^? \\ \dot{\mathbf{x}}_R^? \end{Bmatrix} + \left[\begin{array}{cc|cc} \mathbf{K}_{II} & \mathbf{K}_{IB} & \mathbf{K}_{IL} & \mathbf{K}_{IR} \\ \mathbf{K}_{BI} & \mathbf{K}_{BB} & \mathbf{K}_{BL} & \mathbf{K}_{BR} \\ \mathbf{K}_{LI} & \mathbf{K}_{LB} & \mathbf{K}_{LL} & 0 \\ \mathbf{K}_{RI} & \mathbf{K}_{RB} & 0 & \mathbf{K}_{RR} \end{array} \right] \begin{Bmatrix} \mathbf{x}_I^? \\ \mathbf{x}_B^? \\ \mathbf{x}_L^? \\ \mathbf{x}_R^? \end{Bmatrix} \\ & = \begin{Bmatrix} \mathbf{f}_I\sqrt{} \\ \mathbf{f}_B\sqrt{} \\ \mathbf{f}_L\sqrt{} \\ \mathbf{f}_R\sqrt{} \end{Bmatrix} + \left[\begin{array}{cc|cc} 0 & & & \\ & 0 & & \\ & & \mathbf{C}_{LL} & \\ & & & \mathbf{C}_{RR} \end{array} \right] \begin{Bmatrix} \dot{\mathbf{x}}_I^? \\ \dot{\mathbf{x}}_B^? \\ \dot{\mathbf{x}}_L\sqrt{} \\ \dot{\mathbf{x}}_R\sqrt{} \end{Bmatrix} \end{aligned}$$

3.2.6.2 Finite Element Implementation

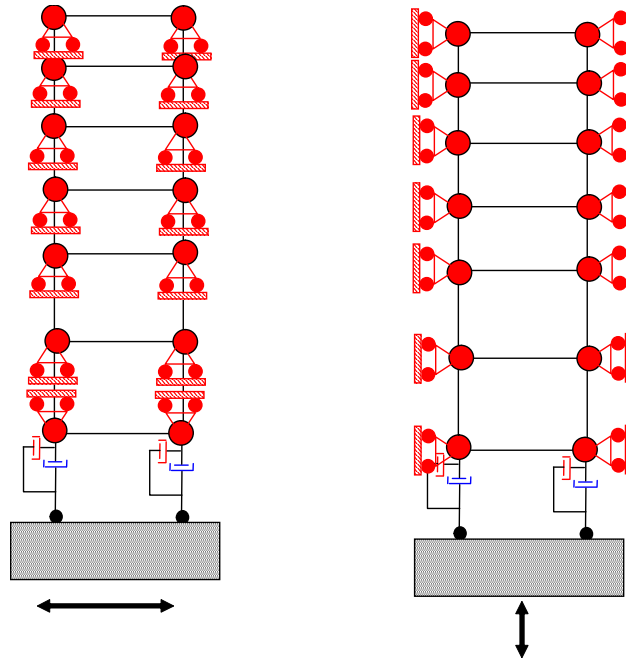


Figure 3.19: Finite Element Discretization of the free field

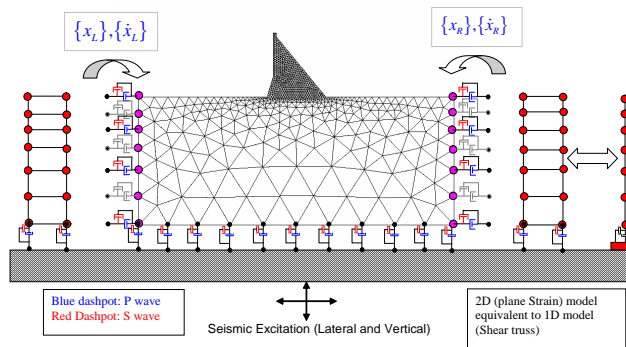


Figure 3.20: Finite Element Discretization of Dam Foundation in Account of Free Field Velocities

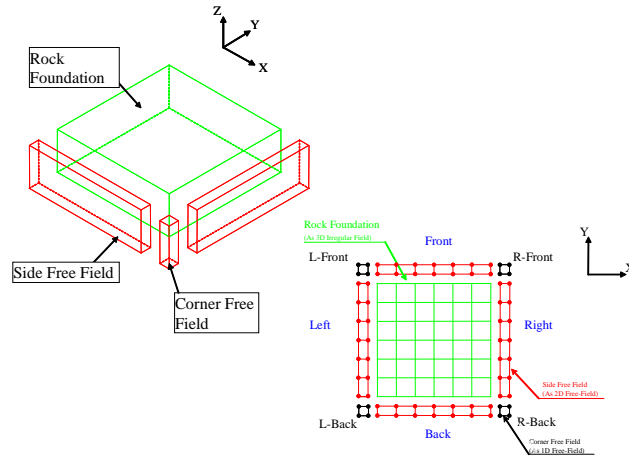


Figure 3.21: Finite Element Discretization of the free field

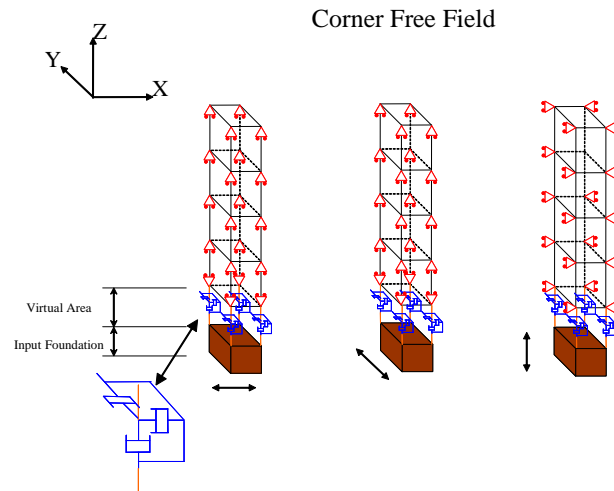


Figure 3.22: Finite Element Discretization of the Corner free field

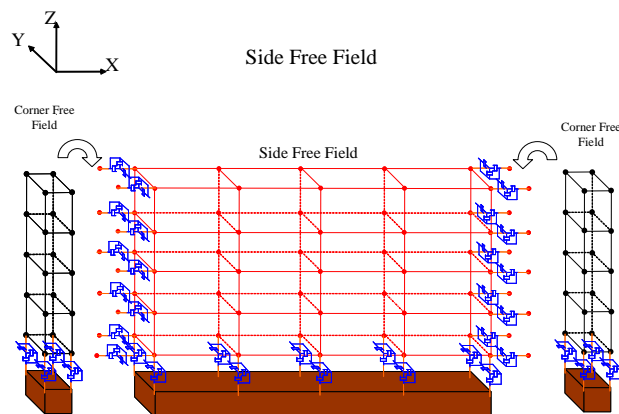


Figure 3.23: Finite Element Discretization of the Side free field

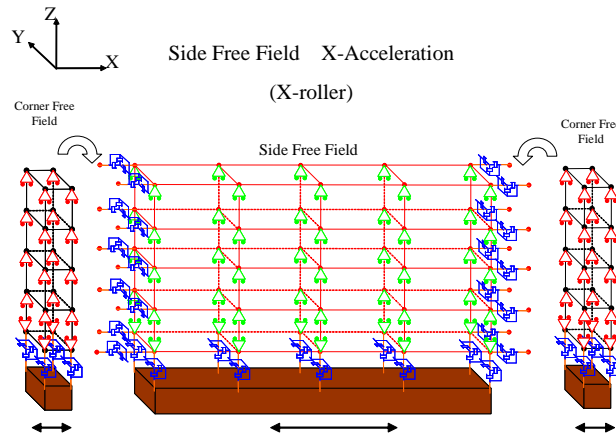


Figure 3.24: Finite Element Discretization of the Side free field, X Acceleration

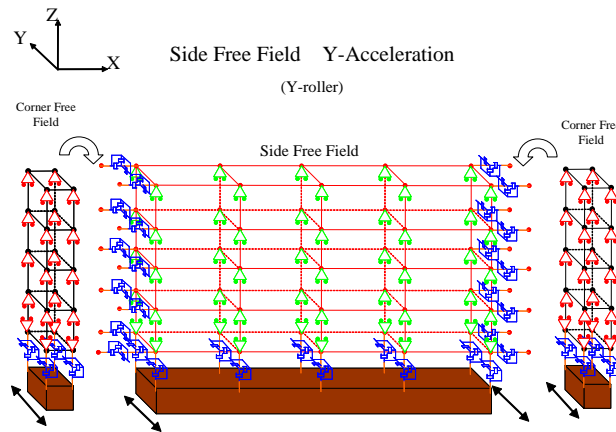


Figure 3.25: Finite Element Discretization of the Side free field, Y Acceleration

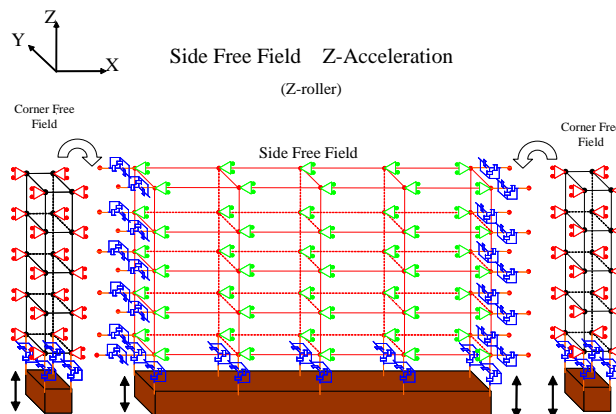


Figure 3.26: Finite Element Discretization of the Side free field, Z Acceleration

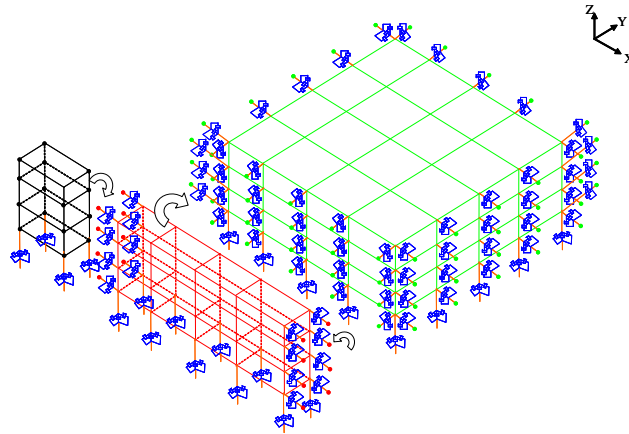


Figure 3.27: Finite Element Discretization of the free field; Transfer of Velocities

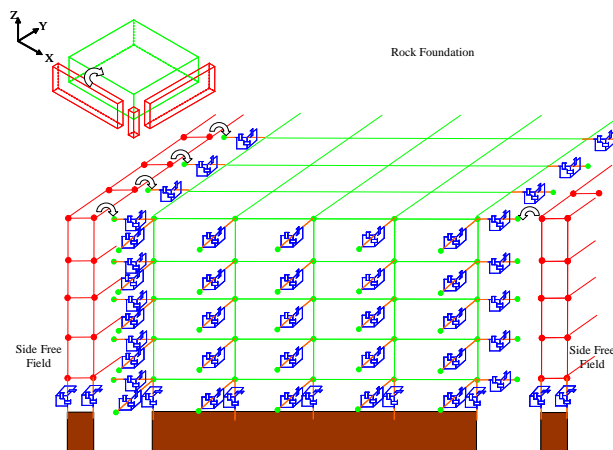


Figure 3.28: Finite Element Discretization of the free field; Rock Foundation

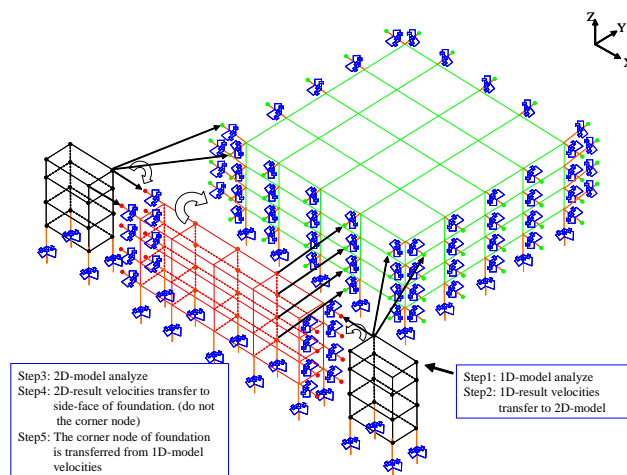


Figure 3.29: Finite Element Discretization of the free field; Outline of Procedure

This page intentionally left blank.

4— Alkali Silica reaction Modeling

4.1 Introduction

4.1.1 Life Extension

According to the Atomic Energy Act of 1954, (**nureg-0980**) and Nuclear Regulatory Commission (NRC) regulations, the operating licenses for commercial power reactors are issued for 40 years and can be renewed for an additional 20 years, with no limit to the number of renewals. The original 40-year license term was selected on the basis of economic and antitrust considerations rather than technical limitations. Henceforth, many plants have sought (and obtained) a 20-year life extension. In the United States, the average structural life is 32 years (**nppageinus**).

Also in the U.S., most NPP have already had a life extension from 40 to 60 year, and serious consideration is now being given to a further extension to 80 years. It is in this context that **emda03** offered a comprehensive evaluation of potential aging-related degradation modes for light-water reactor materials and components. This work was based on the levels of existing technical and operating experience, knowledge, the expected severity of degradation, and the likelihood of occurrence. The report produced thus detailed an *expanded materials degradation analysis* of the degradation mechanisms capable of affecting concrete.

The report concluded that three (of the five) high-ranked degradation modes could potentially affect the concrete containment, which is the safety-related structure of primary interest.

Creep of the post-tensioned concrete containment.

Irradiation of concrete (which, as shown below, may accelerate ASR).

Alkali-silica reaction *Though this degradation has been well documented through operating experience (for bridges and dams in particular) and the scientific literature, its high ranking in this EMDA analysis underscores the need to assess its potential consequences on the structural integrity of the containment.*

4.1.2 Reported Cases

As late as 2007, it was reported that *to date, no incidences of ASR-related damage have been identified in U.S. nuclear power plants* (**naus07**). Yet, there has been recently mounting evidence of such occurrences in Nuclear Power Plants (**NPPs**).

In Japan, the (reinforced concrete) turbine generator foundation at Ikata No. 1 NPP (owned by Shihoku Electric Power) exhibits ASR expansion and has thus been the subject of many studies. **Ikata-7** reports on the field investigation work underway: location, extent of cracking, variation in concrete elastic modulus and compressive strength, expansion in sufficient detail to adequately understand the extent of damage. The influence of ASR on mechanical properties (in particular, the influence of rebar) and on structural behavior

has been discussed by **Ikata-3** and **Ikata-2**, respectively. In the latter study, beams made from reactive concrete were tested for shear and flexure. These beams were cured at 40°C and 100% relative humidity for about six weeks. Some doubt remains, however, as to how representative such a beam is for those NPP where ASR has been occurring for over 30 years. A study of the material properties introduced in the structural analysis was first reported by **Ikata-5**. An investigation of the safety margin for the turbine generator foundation has also been conducted (**Ikata-4**). Moreover, vibration measurements and simulation analyses have been performed (**Ikata-1**). **Takakura-07** has recently reported on an update of the safety assessment at this NPP.

In Canada, Gentilly 2 NPP is known to have suffered ASR (**orbovic2011**). An early study by **Tcherner-09** actually assessed the effects of ASR on a CANDUTM6 NPP (such as Gentilly 2). In 2012 however, following an early attempt to extend the life of Gentilly 2 until 2040 (with an approx. \$1.9B overhaul), Hydro-Quebec announced its decommissioning after 29 years for economic reasons.

In the US, the first reported (and possibly not only) nuclear power plant to possibly suffer from ASR is Seabrook. In summary, what is publically known is:

Description NextEra Energy Seabrook, LLC submitted an application for renewal of the Seabrook Station NPP Unit 1 operating license for another 20 years (beyond the current licensing date of May 15, 2030), (**ML12160A374**). This renewal process consisted of two concurrent reviews, i.e. a technical review of safety issues and an environmental review. For the safety review, the License Renewal Rule process and application requirements for commercial power reactors are based on two key principles: a) that the current regulatory process, continued into the extended period of operation, is adequate to ensure that the continuing license basis of all currently operating plants provides an acceptable level of safety, with the possible exception of the detrimental effects of aging on certain systems, structures, and components (SSCs), and possibly a few other issues related to safety only during the period of extended operation; and b) each plant's continuing license basis is required to be maintained.

As part of the license renewal process, an aging management program (AMP) is to be identified that is determined to be acceptable to manage potential problems such as ASR.

In 2009-2010, it was determined that groundwater infiltrated into the annular space between the concrete enclosure building and concrete containment. The bottom 6 ft of the concrete containment wall was in contact with groundwater for an extended period of time. Cracks due to the alkali-silica reaction had been observed in various Seabrook plant concrete structures, including the concrete enclosure building ((**ML12160A374**), Fig. 4.1). As a consequence, the NRC identified ASR as an open item indicating that it had not been adequately addressed in the Structures Monitoring AMP (OI 3.0.3.2.18-1).

A total of 131 cores (4" diameter, 14" - 16" deep) in the affected areas were tested to determine their compressive strength and modulus of elasticity and then compared with test results from standard concrete cylinders cast during the original concrete construction placements. In addition, petrographic examinations, as per ASTM C856, were performed. It was determined that the areas affected were highly localized, and core samples extracted from adjacent locations did not show signs of ASR. Furthermore, when the core lengths were evaluated (i.e. depth into the wall), it was observed that cracking was most severe at the exposed surface and reduced towards the center of the wall, (**ML12199A295**). As a consequence, the NRC initiated an *Open Item* (OI 3.0.3.2.18-1) related to the AMP.

As a result of this identification of ASR, it was reported that NRC officials informed the power plant's owners that in order for the plant to gain approval for its license extension, proof needed to be pro-

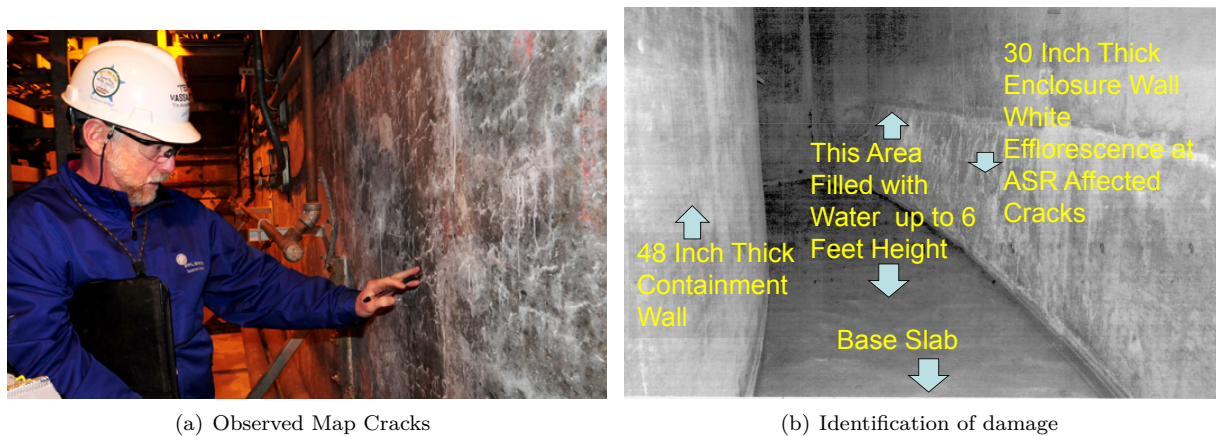


Figure 4.1: ASR in Seabrook nuclear power plant, (ML12199A300)

vided concerning the impact ASR will have on the plant as it ages, as well as the steps adopted to mitigate ASR in the plant's concrete structures, if necessary, (dailynews). Moreover, the NRC made it clear that a final decision on the license renewal application would not be announced until concrete degradation issues identified at the plant had been satisfactorily addressed, (seacoastonline).

Root cause investigation A root cause investigation was performed and led to determining that (ML13151A328):

RC1 - ASR developed because the concrete mix designs unknowingly utilized a coarse aggregate that, in the long term, would contribute to the Alkali Silica Reaction. Although testing was conducted in accordance with ASTM standards, these standards were subsequently found to be limited in their ability to predict slow reactive aggregates that produce ASR in the long term.

RC2 - Based on the long-standing belief that ASR is not a credible failure mode due to the concrete mix design, the conditions imposed on reports involving groundwater intrusion or concrete degradation, along with the structural health monitoring program, did not consider the possibility of ASR development.

One contributing cause was nonetheless identified: failure to prioritize groundwater elimination or mitigation resulted in a greater concrete area being exposed to moisture.

Material Degradation Initial testing of extracted core samples indicated reductions in the modulus of elasticity values from those assumed in the original design. The first compressive strength tests from the electrical tunnel were compared to the original test cylinders cast during construction of the Control Building in 1979. This comparison also appeared initially to indicate an approximately 22% decrease in compressive strength. Extracted cores were expected to yield compressive strength values 10% to 15% lower than cylinder test results.

When additional cores were tested from both ASR-affected and non-ASR-affected areas, the tested compressive strengths were essentially the same, a finding consistent with the industry literature, which predicts minimal impact to tested compressive strength levels at relatively low ASR expansions. The modulus of elasticity equaled approximately 47% of the expected value (ML121160422; ML13151A328).

Structural Integrity and Testing In the most recent report ML13151A328, it was stated that the purpose of testing is to assess the impact of ASR on out-of-plane shear performance and reinforcement anchorage (lap splice) performance. Test specimens will use the walls in the Electrical Tunnel as the

reference location for the Seabrook Station, and the walls will be modeled as reinforced concrete beams constructed in order to be similar to the reference location walls. It is anticipated that testing will provide data to assess the effects of ASR on shear and reinforcement anchorage performance; whenever necessary, testing will assess the effectiveness of retrofit techniques in improving the structural capacity of beams at various levels of ASR degradation.

Finite Element Studies A finite element model of the most limiting area was developed to address the potential of an adverse dynamic response associated with the apparent modulus of elasticity tests conducted on the extracted core samples. According to this model, a differential analysis of the structure with various modulus changes could be performed (**ML13151A328**). This analysis concluded that (**ML121160422**) *the maximum acceleration profiles within the structure response spectrum are not significantly affected by ASR properties and moreover that the distribution of forces and moments is not significantly altered by ASR properties. It can thus be concluded that load distribution and seismic response is negligibly affected by ASR.*

Design vs Analysis Throughout the report, safety is indeed very strictly adhered to in the spirit of the relevant codes (mostly ACI). It should be kept in mind that those codes were written primarily for the (usually linear elastic) *design* of new structures, and as a result of safety requirement, it is a binary outcome: pass or fail. Since the concepts of working stress design methods (based on allowable strength), or load resistance factor design (**asce-7**) have been adopted (ACI and AISC codes amongst others), much progress has been made. In the framework of earthquake engineering retrofitting, Performance based Earthquake Engineering was introduced (**fema445**). In this new paradigm, and through nonlinear analysis different levels of damage are considered, Fig. 4.2.

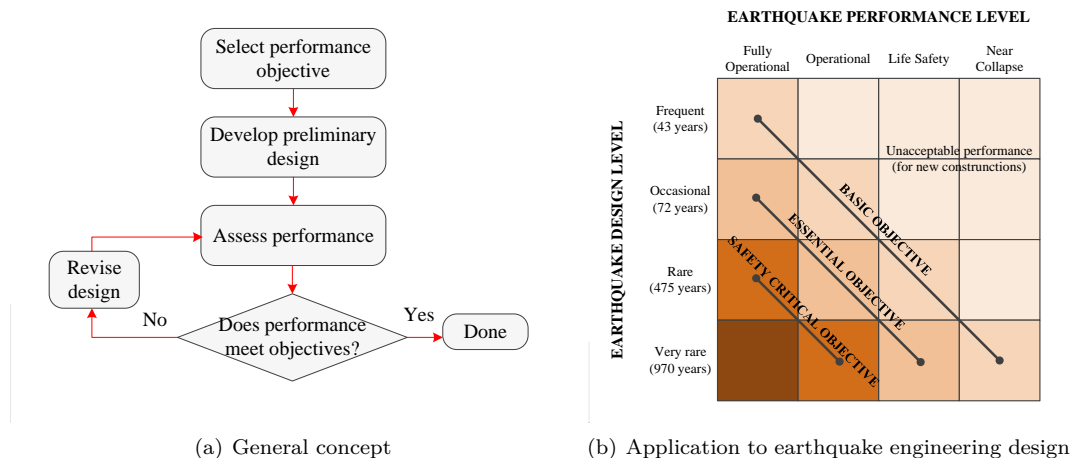


Figure 4.2: Concept of performance based earthquake engineering design, (**fema445**)

4.2 Finite Element Modeling of AAR

4.2.1 Scale and Models

The modeling of AAR expansion has been undertaken by various researchers, (**pian12**). Generally speaking, this modeling effort falls into one of three categories:

Micro Models: A single aggregate is (typically) modelled along with the cement paste. The transport equation is used to model gel, whose formation is first accommodated by its saturation of the capillary pores, (**furusawa94**), (**bazant00**), (**lemarchand01**), (**suwito02**). While essential to properly understanding the underlying phenomenon causing AAR, this level of modeling, is of little relevance to a structural analysis of AAR-affected structures (i.e. the main topic of this book).

Meso Models An extension of the previous approach, in which both particle size distribution and interaction among individual particles are taken into account, (**comby09**) (**dunant10**). More recently, innovative meso-scale modeling have been proposed by **alnaggar2013lattice** based on the so-called lattice discrete particle modeling (an extension of the lattice models). The model can indeed yield very good results at the meso-levels, albeit with a number of assumptions (such as aggregate shapes, micro-model properties) which make it difficult as a predictive tool. Finally, the application of meso-models to structures is yet to be fully and convincingly addressed.

Macro Models: This set-up avoids transport modeling, with emphasis placed on a comprehensive numerical model for the analysis of a given structure. Some (older) empirical models fully decouple structural modeling from reaction kinetics, while others couple these two effects (and may ignore the kinetics altogether).

Empirical models were first presented by **charlwood92** and **thompsonc94** who identified critical issues related to AAR, namely stress dependency, i.e. no AAR expansion under a compressive stress of around 8 MPa and an expansion akin to thermal expansion. Subsequently, more refined models were presented by **leger96**, **ournazel97**, **capra98**, and **herrador09**. In this context, the work of **huang99** stands apart since it may be one of the earliest contributions in which the kinetics are taken into account in terms of both temperature and confining stresses. Publication of **larive98**'s work brought an end to the "era" of the parametric model and opened the door to developing what came to be known as "coupled chemo-mechanical" based models.

Coupled Chemo-Mechanical are models which account (indirectly) for the time dependency of the (chemical) diffusion in the mechanical response. For the most part, these models are inspired from and calibrated with the experiments of **larive98** and **multon04**. They will be briefly reviewed in the following section.

Some current research work is seeking to develop a "grand unifying" multi-scale model that bridges the gap from micro to meso to macro in order to better capture the reaction (at the micro-scale) and its implications (on the macro scale). **puat13** is one such attempt to bridge the gap between the micro and meso levels.

4.2.2 Overview of Coupled Chemo-Mechanical Models

Broadly speaking, there are four "schools", defined as institutions, that have produced two or more publications focusing on coupled chemo-mechanical models. For the most part, these publications offer refinements of an original model.

1. One of the earliest work was by **pietruszczak1996mechanical**. This model is tightly tied to an (old) elasto-plastic model for concrete with a number of assumptions which were subsequently disproved or updated by the work of Larive (see below). Whereas the model has indeed been applied to large hydraulic structures **huang99**, its applicability over 20 years later would be questionable.
2. The work by *Laboratoire Central des Ponts et Chaussées* (LCPC) can be traced back to the research of **ulm00** followed by **li02** and later **seignol11**. The "LCPC" model was also refined by **farage04** and **fairbairn06**. In most cases these models are rooted in the theory of plasticity and implemented

within the LCPC finite element code CESAR.

3. Toulouse and EdF have had a longstanding collaboration that has given rise to what could be called the “EdF” model. As opposed to the LCPC model, the Toulouse/EdF developments are rooted in Damage Mechanics pioneered at the ENS/Cachan where Sellier performed his original work, (**sellier95**). Following a refined model for the influence of water (**pyet06**), **grimal08** developed a visco-elasto-plastic orthotropic damage model which was further refined in (**sellier2009**). These models are mainly based on Damage Mechanics (as opposed to plasticity) and implemented in EdF’s computer programming Code ASTER.
4. The *Politecnico di Milano* has also developed coupled chemo-mechanical models, similar those of Toulouse/EdF, (**comi11**) (**comi12**); they have been used to analyze some complex problems.
5. Finally, Colorado has developed a coupled model which will be described in the next chapter.
6. Others important models include the one of **meschken04**

Broadly speaking, we consider two forms of coupling:

Loose Coupling In the absence of an initial stress ($\sigma_0 = 0$) yet with an AAR induced initial strain, we have $\epsilon_0 = \epsilon_{AAR}$ where ϵ_{AAR} is the AAR strain tensor which will be defined later by Eq. 4.3. Hence,

$$\underbrace{\int_{\Omega_e} \mathbf{B}^T \mathbf{D} \mathbf{B} d\Omega}_{\mathbf{K}_e} \bar{\mathbf{u}}_e = \underbrace{\int_{\Omega_e} \mathbf{N}^T \mathbf{b} d\Omega + \int_{\Gamma_t} \mathbf{N}^T \hat{\mathbf{t}} d\Gamma}_{\mathbf{f}_e} + \underbrace{\int_{\Omega_e} \mathbf{B}^T \mathbf{D} \epsilon_{AAR} d\Omega}_{\mathbf{f}_{AAR}} \quad (4.1)$$

and the AAR strain is completely uncoupled from the constitutive model \mathbf{D} .

Tight Coupling where the inclusion of the chemical potential (which accounts for AAR) results in a fully coupled constitutive matrix without explicit expression for the AAR strains yielding

$$\underbrace{\int_{\Omega_e} \mathbf{B}^T \mathbf{D}' \mathbf{B} d\Omega}_{\mathbf{K}_e} \bar{\mathbf{u}}_e = \underbrace{\int_{\Omega_e} \mathbf{N}^T \mathbf{b} d\Omega + \int_{\Gamma_t} \mathbf{N}^T \hat{\mathbf{t}} d\Gamma}_{\mathbf{f}_e} \quad (4.2)$$

where \mathbf{D}' is the constitutive matrix which embodies both the mechanical stress strain relation and the effects of the chemical reaction, Fig. 4.3.

Henceforth, except for the Colorado model (the subject of this book), all other models rely on a single constitutive model that couples chemical (AAR expansion) and mechanical (non-linear stress strain) components. In these models,

1. One does not get only an AAR model, but also an accompanying stress-strain nonlinear constitutive model to which it is grafted. This is a clear departure from earlier models where AAR strain was accounted for as an initial strain ϵ_0 .
2. In lieu of extracting AAR strains separately, one is limited to the AAR extent (ξ) or damage.

It can indeed be argued that there is no reason a priori why AAR expansion should alter an element stiffness matrix (except for the deterioration of E), and inserting AAR within \mathbf{D} is an unnecessary complication (albeit one that leads to a very “elegant” formulation). From a conceptual perspective, this mirrors the ongoing discussion on crack modeling: smeared vs. discrete.

To the best of the author’s knowledge, the only AAR model that can be easily associated with any existing constitutive model (even linear elastic) is the one proposed in **saouma-aar-1**. Among known implementations, are **pan13**; **Mirzabozorg13**. It is this model which will be at the core of this book.

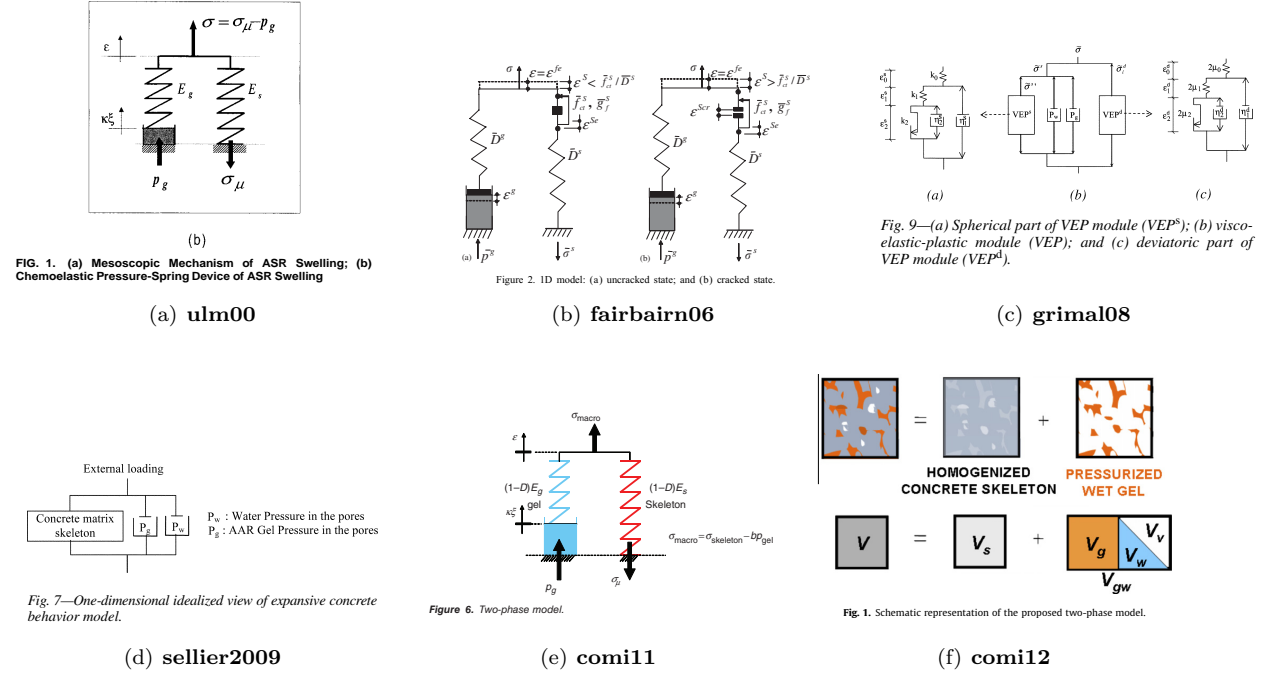


Figure 4.3: Rheological Chemo-Mechanical Models

4.2.3 Minimum Requirements for a “Modern” AAR Numerical Model

Practically any model with sufficient “cursors” can be calibrated to yield what appears to be an acceptable correlation with field-measured displacements (and at times, which implies unrealistic values for some physical parameters). This step does not necessarily make the model “correct”. Before a model can be considered adequate (in the sense of being able to generate long-term predictions), certain minimum requirements must first be met:

1. Spatial and temporal distribution of the structure temperature $T(x, y, z, t)$ and relative humidity $RH(x, y, z, t)$
2. Constitutive models (**D**) that can accommodate both a linear elastic response (for fast 3D analysis of the entire structure) and nonlinear response to account for cracking and failure.
3. Ability to properly model crack/joints. Vertical expansion is likely to cause either abutment cracking or “lift-off” of the concrete along (V-shaped) abutments or even within the inner center of rock-concrete interfaces (effect compounded by uplift). This is also required to capture the eventual closing of a sliced portion of the structure (as is often performed in dams to relieve stresses).
4. Creep to account for long-term deformation that can reduce AAR expansion.
5. Stress-induced anisotropy: confining stress will reduce expansion in the corresponding direction, but may increase it in orthogonal directions.
6. Ability to display AAR-induced strains (as opposed to the extent of AAR penetration (ξ)).
7. Should seismic excitations be of concern, then the ability to perform a **restart** with the existing state of stress and internal degradation of $f'_t(x, y, z, t)$ and $E(x, y, z, t)$

To assess AAR-equipped finite element codes, a number of benchmark problems have been proposed. Regrettably, in most or all of these problems, the analyst must perform a comprehensive analysis of a

complex structure (such as a dam), which makes it practically impossible to compare codes and pinpoint deficiencies. Accordingly, both the author and Sellier have proposed a battery of simple validation problems (of increasing complexity) in order to precisely ensure that a given code possesses all the necessary features for proper AAR modeling.

Before any finite element code can be used for AAR studies, it must therefore be verified whether some or all of the features listed above are present; moreover, it would be preferable to determine how effectively the code is able to predict in the proposed battery of benchmark problems.

4.3 Author's Model

Section adapted from **saouma-aar-book**.

A macro-based constitutive model for concrete expansion should account for: a) kinetics (i.e. time dependency) of the chemical reactions (due to ion diffusion); and b) the mechanics of the representative volume (e.g. effects of cracking and triaxial stress, property degradation). has been proposed by the first author (**saouma-perotti-2**).

To the best of the authors knowledge, this model is the most widely adopted one by other researchers. A (non comprehensive) list of implementation includes:

1. **rodriguez11** implemented the model in Abaqus and analysed an arch dam.
2. **vector3** in the Vector3 program and the analysis of reactive shear walls.
3. **Mirzabozorg13** in Iran for the analysis of Amir-Kabir arch dam in the NSA-DRI code.
4. **pan13** from Tsinghua University for the analysis of Kariba dam.
5. (**huangspencer16**) **huang15** implemented in the fully coupled Grizzly/Moose program.
6. **benftma16** Polytechnic of Montreal, and Swiss Federal Institute of Technology, Lausanne) as a model in Abaqus for the analysis of a hydraulic structure.

Henceforth, the proposed model, (**saouma-perotti-2**) is based on the following considerations:

1. AAR model is completely separate from the constitutive model (linear or nonlinear stress-strain relations).
2. AAR is a volumetric expansion and, as such, cannot be addressed unidirectionally without due regard to what may occur along the other two orthogonal directions.
3. The expansion reaction is considered to be thermodynamically driven (i.e. time-dependent and affected by temperature) and has largely been inspired by the works of **larive98** and **ulm00**.
4. AAR expansion is constrained by compression (**multon03**), and will be assumed redirected in other less constrained principal directions. This redirection will be accomplished through “weights” assigned to each of the three principal directions.
5. Relatively high compressive or tensile stresses inhibit AAR expansion due to the formation of micro (**hsu63**) or macro cracks, which absorb the expanding gel.
6. High compressive hydrostatic stresses slow the reaction, and a triaxial compressive state of stress reduces, without eliminating, expansion.
7. Accompanying AAR expansion entails a reduction in tensile strength and elastic modulus.

Based on these assumptions, the following general (uncoupled) equation for the incremental free volu-

metric AAR strain is given by:

$$\dot{\epsilon}_V^{AAR}(t, T) = \underbrace{\Gamma_t(f'_t|w_c, \sigma_I|COD_{max})\Gamma_c(\bar{\sigma}, f'_c)}_{\text{Retardation}} \underbrace{g(h)}_{\text{Humidity kinetics}} \underbrace{\dot{\xi}(t, T)}_{\text{AAR}} \underbrace{\epsilon(\infty)}_{\text{Strain}} \quad (4.3)$$

Each of these terms will be addressed separately.

4.3.1 Kinetics

One of the most extensive and rigorous AAR investigations has been conducted by **larive98**, who tested more than 600 specimens with various mixes, ambient and mechanical conditions, and proposed a numerical model that governs concrete expansion. This thermodynamically-based, semi-analytical model was then calibrated using laboratory results in order to determine two key parameters: the latency time and characteristic times shown in Fig. 4.4(a) for the normalized expansion.

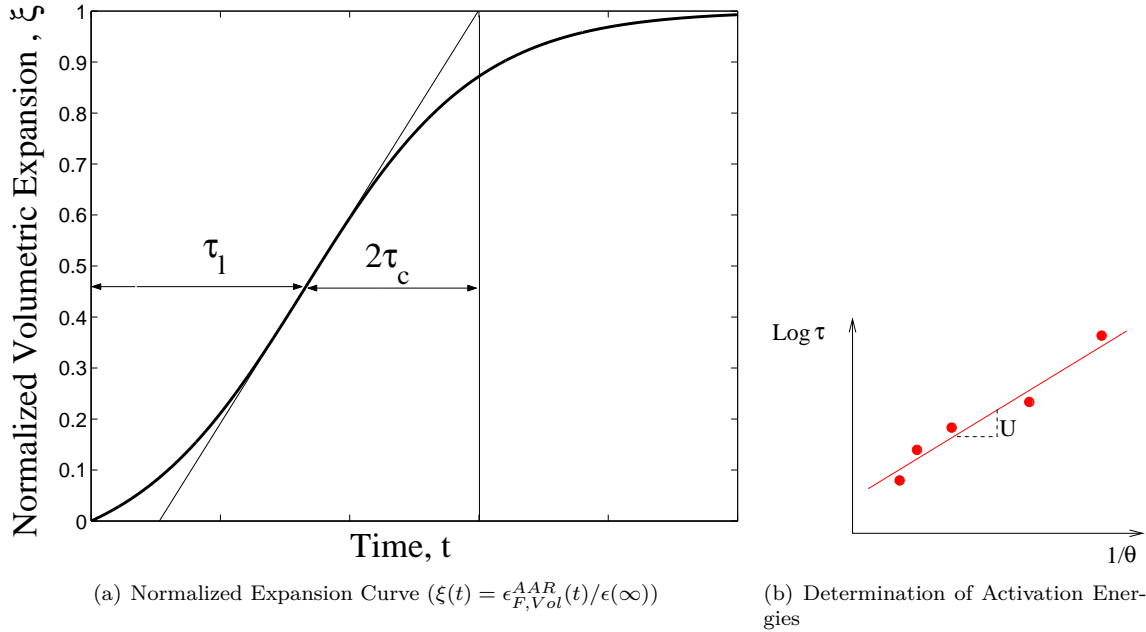


Figure 4.4: Definition of the expansion curve

$$\xi(t, T) = \frac{1 - e^{-\frac{t}{\tau_c(T)}}}{1 + e^{-\frac{(t-\tau_l(T))}{\tau_c(T)}}} \quad (4.4)$$

or in rate form

$$\dot{\xi}(t, T) = \frac{e^{t/\tau_c} \left(e^{\frac{\tau_l}{\tau_c}} + 1 \right)}{\tau_c \left(e^{t/\tau_c} + e^{\frac{\tau_l}{\tau_c}} \right)^2} \quad (4.5)$$

where τ_l and τ_c are the latency and characteristic times, respectively. The first corresponds to the inflection point, while the second is defined relative to the intersection of the tangent at τ_L with the asymptotic unit value of ξ . Like all chemical reactions, AAR is subject to Arrhenius Law (**arrhenius89**), which relates the dependence of the rate constant k of a chemical reaction on absolute temperature (T expressed in degrees

Kelvin, $T^{\circ}K = 273 + T^{\circ}C$) and activation energy E_a .

$$k = Ae^{-\frac{E_a}{RT}} \quad (4.6)$$

substituting k with τ_L and τ_C , **ulm00** has shown that these values at temperature T can be expressed in terms of the corresponding values at temperature T_0 through:

$$\begin{aligned} \tau_l(T) &= \tau_l(T_0) \exp \left[U_l \left(\frac{1}{T} - \frac{1}{T_0} \right) \right] \\ \tau_c(T) &= \tau_c(T_0) \exp \left[U_c \left(\frac{1}{T} - \frac{1}{T_0} \right) \right] \end{aligned} \quad (4.7)$$

where U_l and U_c are the activation energies required to trigger the reaction for latency and characteristic times, respectively. Activation energies can be easily determined by rewriting Eq. 4.7 in its non-exponential form:

$$\ln k = \ln \left(Ae^{-\frac{E_a}{RT}} \right) = \ln A - \frac{E_a}{RT} \quad (4.8)$$

which is the equation of a straight line with slope $-E_a/RT$ (Fig. 4.4(b)). We can thus determine the activation energy from values of k observed at different temperatures by simply plotting k as a function of $1/T$, Fig. 4.4(b). Activation energies for Eq. 4.7 were determined to be:

$$\begin{aligned} U_l &= 9,400 \pm 500K \\ U_c &= 5,400 \pm 500K \end{aligned} \quad (4.9)$$

To the best of the authors' knowledge, the only other tests for these values were performed by **scrivener05**, who obtained values within 20% of Larive's, while dependency on the types of aggregates and alkali content of the cement has not been investigated. In the absence of other tests, these values can thus be reasonably considered as representative.

It should be emphasized that not only are the latency and characteristic times temperature-dependent, but considerable variability can also be present for the same concrete specimen chosen from among others. This point is illustrated in Table 4.1 for four specimens ($\phi 13H24$ kept at $38^{\circ}C$) tested by **larive98**. Finally,

specimen		501	475	287	19	Mean	NSD (%)
$\epsilon(\infty)$	%	0.198	0.195	0.168	0.230	0.198	12.8
τ_c	days	19.9	35.3	25.8	22.0	25.7	26.5
τ_l	days	102.1	83.9	94.8	64.8	86.4	18.8
τ_l/τ_c	-	5.1	2.4	3.7	2.9	3.4	0.7

Table 4.1: Variation of $\epsilon(\infty)$, τ_c and τ_l for 4 specimens, (**larive98**)

further insight into the kinetics of the AAR reaction can be found in (**saouma-martin-2013**).

4.3.1.1 Sensitivity to Temperature

From Eq. 4.7, it is obvious that the reaction kinetics are highly dependent on temperature, which actually explains why some dams at high elevations throughout the world have exhibited AAR-induced expansion later when compared with those at lower elevations.

This temperature dependence is highlighted in Fig. 4.5(a), which illustrates the normalized expansion at four different temperatures. It is apparent that a major discrepancy exists in the expansion rate between

8^{deg} and 18^{deg}C, and then a smaller discrepancy between 18^{deg}, 28^{deg} and 38^{deg}C.

Fig. 4.5(b) illustrates the role of so-called “accelerated tests”, many of which are performed at 38°C, in inducing expansion, whereas at ambient air temperature (in this case 7°C), expansion will be extremely slow. Then, Fig. 4.5(b) illustrates the impact of temperature on both the latency and characteristic times.

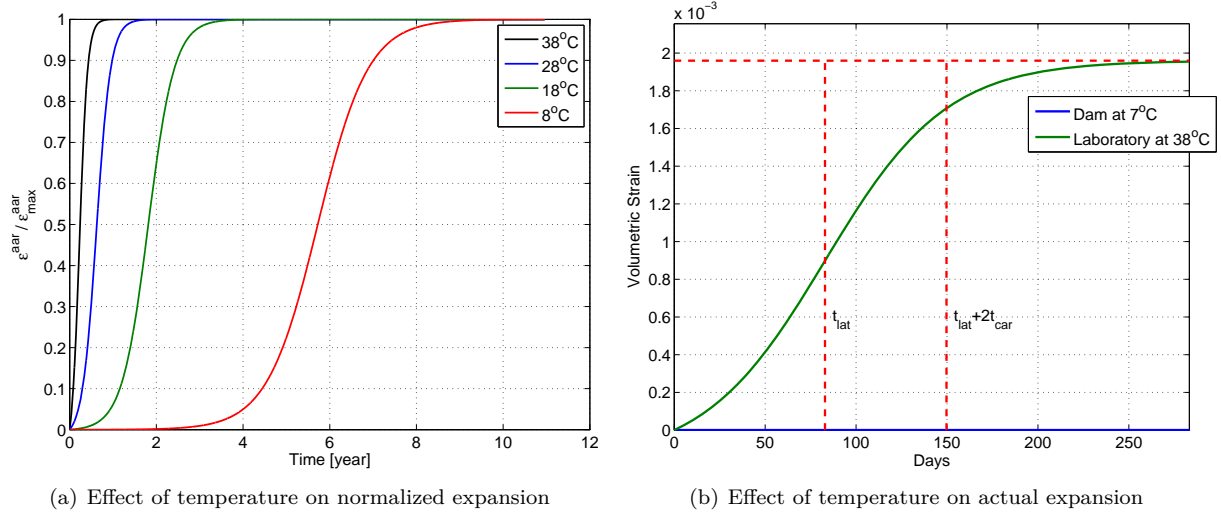


Figure 4.5: Effect of Temperature on AAR Expansion

4.3.1.2 Sensitivity to Integration Scheme

The time integration scheme may determine the expansion (in terms of temperature) through a secant approach ($\xi(t, T)$ from Eq. 4.4) or an incremental one ($\dot{\xi}(t, T)$ from Eq. 4.5). For constant or monotonically increasing temperatures, the two approaches would yield the same result. However, in the case where there may be a decrease in temperature, then erroneous results may be obtained. This will be illustrated by two simple examples. In the first, a harmonic variation of temperature is assumed over a year, and in the second an actual temperature record will be used.

For the harmonic temperature, one can assume

$$T_a = A \sin\left(\frac{2\pi(t - \xi)}{365}\right) + T_{mean} \quad (4.10)$$

where $A = 0.5(|T_{max} - T_{mean}| + |T_{min} - T_{mean}|)$, t is the time in day, ξ is the time in day at which $T_a = T_{mean}$. Fig. 4.6(a) illustrates the temperature variation for $T_{min}=14.2^\circ\text{C}$ and $T_{max}=16.2^\circ\text{C}$. The small difference is justified by the thermal inertia inside a dam. The mean and standard deviation of the concrete were selected to correspond to those assumed for a concrete dam in Coimbra (Portugal)¹ as illustrated below.

Assuming $t_{car} = 33.4$ days, $t_{lat} = 82.9$ days, $U_{lat}=9400$, $U_{car}=5400$, for a base temperature $T_0 = 48^\circ\text{C}$, the corresponding yearly variations of the latency and characteristic times are shown in Figures 4.6(b) and 4.6(c) respectively for both assumptions: constant mean temperature of 15.2°C and variable one (oscillating between T_{min} and T_{max}). The higher values (thus slower reaction) is expected since the temperature is substantially lower than the reference one of 48°C .

¹Data was retrieved from NOAA-NEEDS.

When a constant mean temperature is used, both the secant (Eq. 4.4) and incremental (Eq. 4.5) approaches yield exactly the same expansion with time, Figure 4.6(d). However, both approaches differ drastically for the variable temperature shown in Fig. 4.6(a), as illustrated in Fig. 4.6(e) (where expansion is plotted with respect to the right y axis, and temperature with respect to the left y axis). Finally, the incremental expansion first increases and then decreases smoothly in the case of a mean temperature, and irregularly if the time variation of temperature is accounted for.

Figure 4.6(f) compares variation of incremental strain for both mean and harmonic temperatures.

The same calculations are repeated for an actual dam location. Temperature record for Coimbra (Portugal) was used, and, Fig. 4.7(a) and it was determined that the mean air temperature is 15.2°C with a standard deviation of 4.9 °C. Due to the concrete thermal inertia, its temperature was estimated to have the same mean as the air, but a standard deviation of only 0.98°C.

As before, the temporal variations of both latency and characteristic times are shown in Figures 4.7(b) and 4.7(c) respectively first. Then Figures 4.7(d) and 4.7(e) compare AAR curve using mean and real temperatures. Finally, Figure 4.7(f) compares variation of incremental strain for both mean and harmonic temperatures.

From these figures, attention is drawn on the importance of using an incremental formulation for the correct AAR based expansion.

4.3.1.3 Sensitivity to Activation Energies

Given the limited laboratory data for activation energies, Fig. 4.8 shows the dependency of characteristic and latency times on a variation of their corresponding activation energies, in accordance with Eq. 4.9.

4.3.1.4 Sensitivity to Time

The effect of time is clearly displayed in Fig. 4.9. In assuming values of $\epsilon(\infty)$ equal to 1, 10, and 100, with characteristic and latency times also increasing by a factor of 10, Fig. 4.9(a) shows that for all practical purposes, a linear increase in expansion over time may occur with no indication of “softening”. This phenomenon has indeed been observed in certain dams, and Eq. 4.4 remains valid.

On the other hand, Fig. 8.1(a) illustrates the interdependency of time and temperature on the normalized expansion. It is clearly indicated that as temperature decreases, the expansion slows.

4.3.2 Retardation

A number of factors (besides temperatures) can slow the expansion of reactive concrete, namely: a) triaxial compressive stress, and b) presence of cracks. Each of these two factors will be examined separately.

By analogy with fatigue crack propagation, whereby an overstress may cause retardation of fatigue crack propagation (due to the presence of a plastic zone at the tip of the crack), the presence of micro or macro cracks will slow the expansion due to AAR. This observation is simply due to the fact that the gel generated would first have to fill the cracks before it could exert sufficient pressure to induce further expansion.

4.3.2.1 Hydrostatic Compressive Stress

It has long been established that a compressive stress (i.e. greater than about 8 MPa) will either limit or entirely prevent expansion in the corresponding direction. This finding was first stated by **Hayward88**,

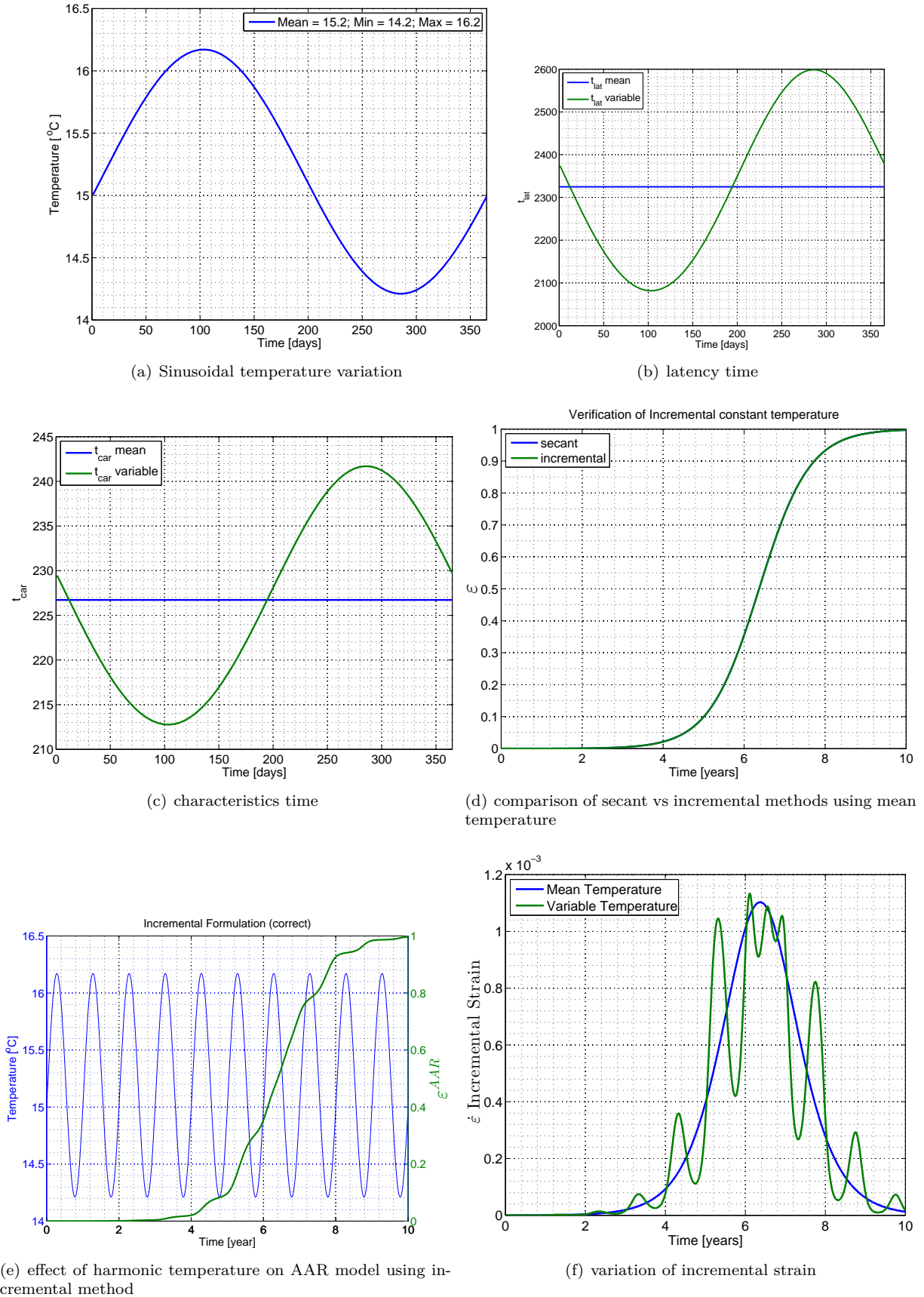


Figure 4.6: Effect of time integration scheme for a harmonic temperature variation

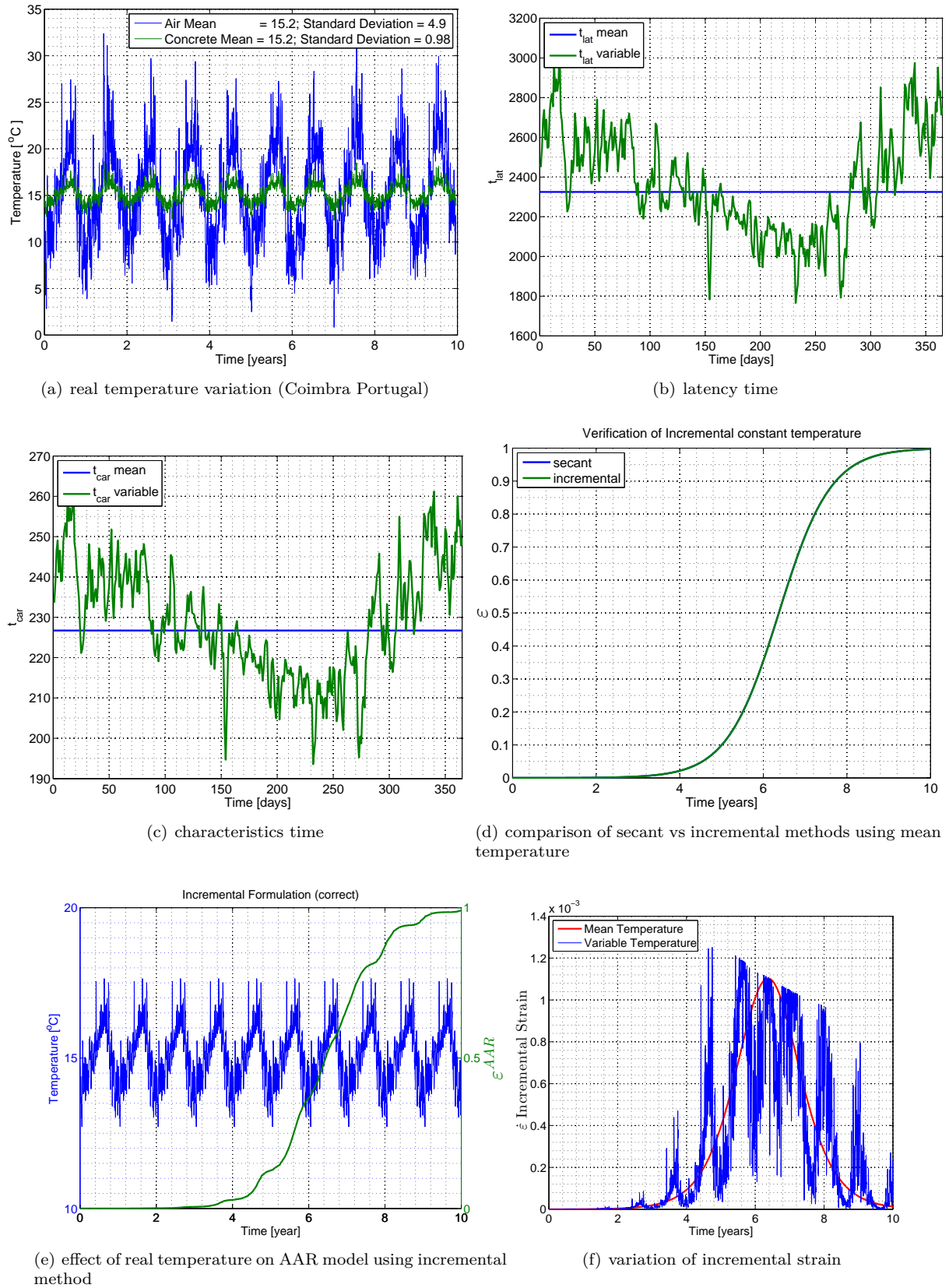


Figure 4.7: Effect of time integration scheme for temperature variation in Coimbra Portugal

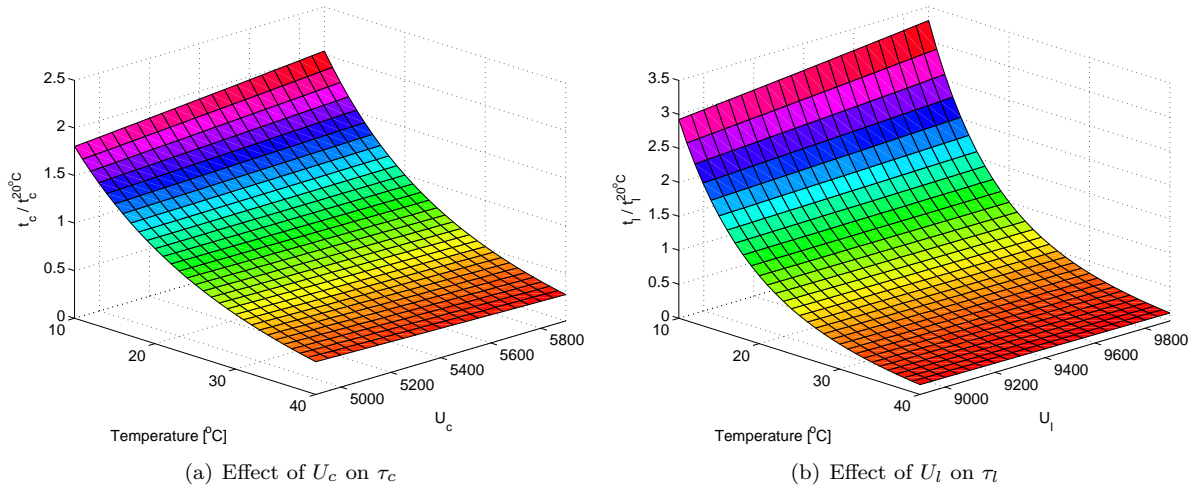


Figure 4.8: Effects of activation energy variations on characteristic and latency times

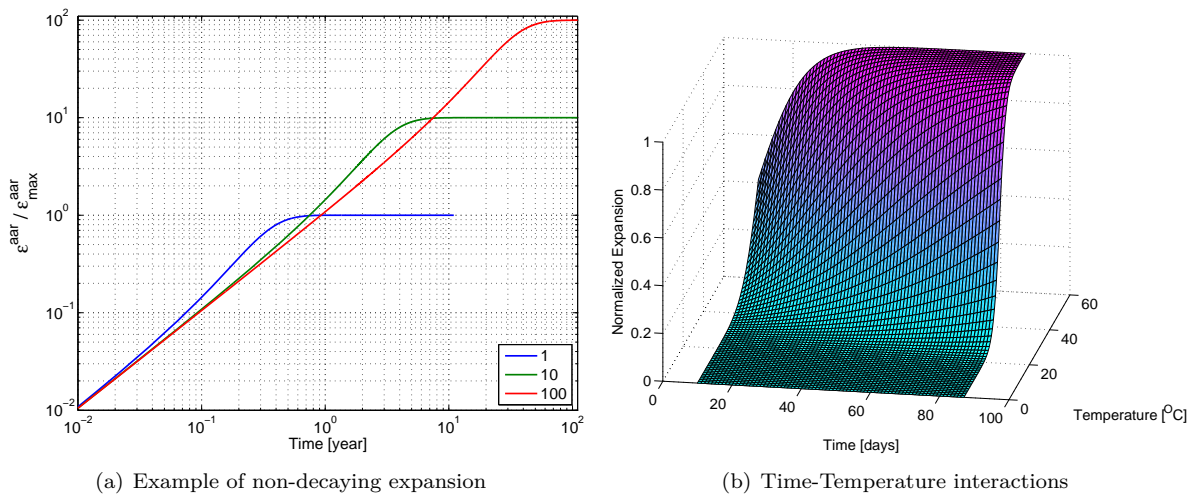


Figure 4.9: Time Evolution

as inspired by the relation between swelling pressures and swelling strains (for rocks inside tunnels) developed by **grob72** and **wittke05**. **multon03** addressed the issue of multi-axial confinement and showed

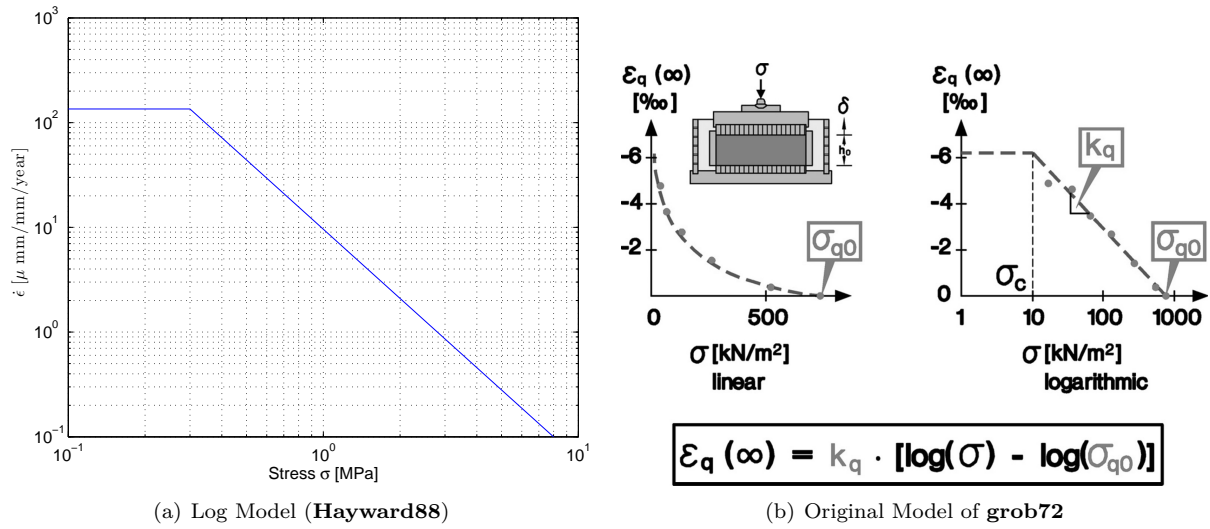


Figure 4.10: Uniaxially-restrained expansion model

that confinement in one direction will redirect expansion in the other directions (thus inducing anisotropic expansion). In these tests, the reactive concrete was cast inside a stainless steel cylinder and expansion was measured under a vertical compressive stress, Fig. 4.11. However, under triaxial compressive confinement,

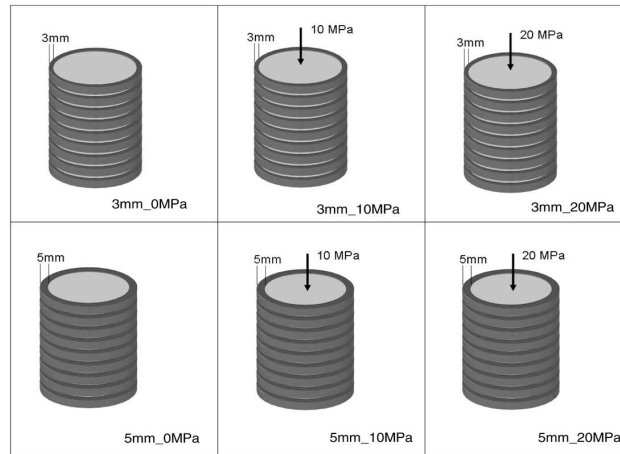


Figure 4.11: Tests on reactive concrete subjected to compressive stresses and confinement by Multon (**comi09**)

expansion is severely constrained (i.e. with room for redirecting the confined expansion), which explains the lesser expansion observed at the base of many dams, where the triaxial state of stress can be prevalent, as opposed to greater expansion in the upper part. This expansion constraint also explains why the unconstrained vertical expansion of the crest of a dam often provides a good indicator of the overall structural response for a finite element calibration, accounted for most conveniently by altering the latency time τ_l .

Hence, Eq. 4.7 can be expanded as follows:

$$\tau_l(T, T_0, I_\sigma, f'_c) = f(I_\sigma, f'_c) \tau_l(T_0) \exp \left[U_l \left(\frac{1}{T} - \frac{1}{T_0} \right) \right] \quad (4.11)$$

where:

$$f(I_\sigma, f'_c) = \begin{cases} 1 & \text{if } I_\sigma \geq 0. \\ 1 + \alpha \frac{I_\sigma}{3f'_c} & \text{if } I_\sigma < 0. \end{cases} \quad (4.12)$$

and I_σ is the first invariant of the stress tensor ($\frac{1}{3}(\sigma_I + \sigma_{II} + \sigma_{III})$), and f'_c the compressive strength.

Based on a careful analysis of **multon03**, it was determined that $\alpha = 4/3$.

4.3.2.2 Role of Cracking

As a consequence of the AAR reaction, a gel is produced. This gel will first fill the adjoining pores, interfacial transition zone around the aggregates (caused by shrinkage of the cement paste) and the cracks, Fig. 4.12. Hence, the presence of cracks proves “beneficial” for AAR as it relieves the gel-induced stresses (at first).

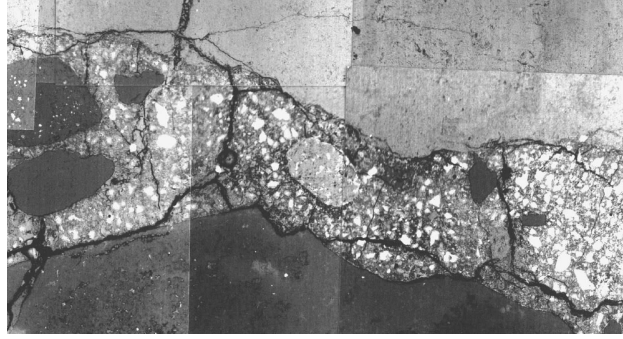


Figure 4.12: Stress-Induced Cracks with Potential Gel Absorption, (**scrivener03**)

This section will examine how macrocracks or microcracks will actually absorb the gel and thus reduce the final volumetric expansion. This phenomenon is also embedded in most modern finite element models for AAR, either explicitly (as in this model) or explicitly when simulation occurs at the micro-level as in **suwito02**, **sellier2009**.

4.3.2.2.1 Tensile Macrocrack Tensile cracks occur once the tensile stress exceeds the tensile strength. Tensile cracking is not affected by the biaxiality or triaxiality of the state of stress (as opposed to compression) (**kupfer73**), and this cracking typically results in well-localized macrocracks. Since the crack opening displacement (COD) to account for gel absorption is needed, a nonlinear simulation could be performed in order to determine the COD. Such a step can be readily determined from so-called “discrete crack” models or, with more difficulty, when the smeared crack model is adopted.

This step will be accounted for in Eq. 4.3 through $\Gamma_t(f'_t|w_c, \sigma_I|COD_{max})$

$$\text{Smeared Crack} \begin{cases} \text{No } \Gamma_t = \begin{cases} 1 & \text{if } \sigma_I \leq \gamma_t f'_t \\ \Gamma_r + (1 - \Gamma_r) \gamma_t \frac{f'_t}{\sigma_I} & \text{if } \gamma_t f'_t < \sigma_I \end{cases} \\ \text{Yes } \Gamma_t = \begin{cases} 1 & \text{if } COD_{max} \leq \gamma_t w_c \\ \Gamma_r + (1 - \Gamma_r) \gamma_t \frac{w_c}{COD_{max}} & \text{if } \gamma_t w_c < COD_{max} \end{cases} \end{cases} \quad (4.13)$$

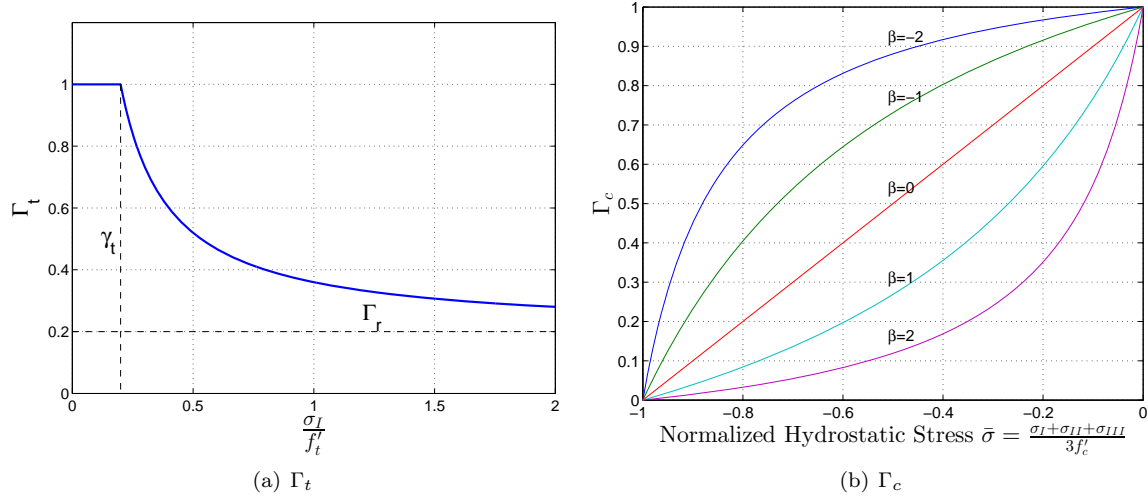


Figure 4.13: Graphical representation of normalized retardation parameters Γ_c and Γ_t

where γ_t is the fraction of tensile strength beyond which gel is absorbed by the crack, and Γ_r is a residual AAR retention factor for AAR under tension. If an elastic model is used, then f'_t is the tensile strength, and σ_I the maximum principal tensile stress. In contrast, if a smeared crack model is adopted, then COD_{max} would be the maximum crack opening displacement at the current Gauss point, and w_c the maximum crack opening displacement on the tensile softening curve, (**wittmann88**). Since concrete pores are seldom interconnected and the gel viscosity is relatively high, gel absorption by the pores is not explicitly taken into account. Furthermore, gel absorption by the pores is instead taken into account in the kinetic equation through the latency time, which depends on concrete porosity. The higher the porosity, the longer the latency time.

4.3.2.2.2 Compressive Microcracks Retardation due to compressive stresses are accounted for in Eq. 4.3 through $\Gamma_c(\bar{\sigma}, f'_c)$. Two reasons can be cited for this retardation, the first previously addressed in Sect. 4.3.2.1 caused by the maximum pressure capable of being exerted by the gel. **struble81** was among the earliest researchers to identify the maximum pressure (estimated at around 11 MPa). The second reason for this reduction is gel absorption by the microcracks, as induced by compressive stress. **hsu63** showed that microcracks develop once the compressive stresses exceed $\neq 0.45f'_c$; these microcracks may also absorb some of the gel.

$$\Gamma_c = \begin{cases} 1 & \text{if } \bar{\sigma} \leq 0. \text{ Tension} \\ 1 - \frac{e^{\beta \bar{\sigma}}}{1 + (e^{\beta} - 1) \bar{\sigma}} & \text{if } \bar{\sigma} > 0. \text{ Compression} \end{cases} \quad (4.14)$$

$$\bar{\sigma} = \frac{\sigma_I + \sigma_{II} + \sigma_{III}}{3f'_c} \quad (4.15)$$

Given that this expression will also reduce expansion under uniaxial or biaxial confinement, Fig. 4.13, these conditions are more directly incorporated below through the assignment of weights.

4.3.3 Humidity

It has long been recognized that for AAR to occur, RH must be at least equal to 0.8, hence $0 < g(h) = \frac{\epsilon(t=\infty, RH=h)}{\epsilon(t=\infty, RH=1)} \leq 1$ is a reduction function to account for humidity. A widely accepted (albeit simplistic) model was proposed by **capra98**

$$g(h) = h^m \quad (4.16)$$

where h is the relative humidity. An alternative model was proposed by **li04**, in which a lower RH reduces the maximum expansion:

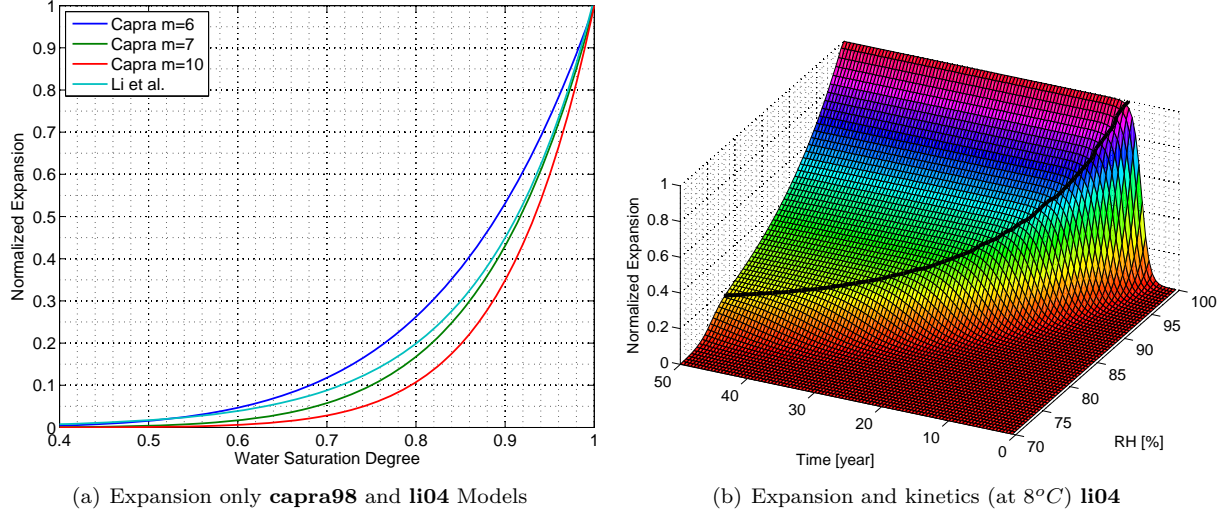


Figure 4.14: Effect of relative humidity

$$g(h) = ae^{b \cdot h} \quad (4.17)$$

These two models are contrasted in Fig. 4.14(a) and shown to be nearly identical. **li04** also altered the kinetics of the reaction through

$$\epsilon(\infty, h) = f_\infty(h_0) \cdot \epsilon(\infty, h_0) \quad (4.18)$$

$$\tau_c(h) = \alpha_c \exp(\beta_c - \gamma_c \cdot h) \cdot \tau_c(h_0) \quad (4.19)$$

$$\tau_l(h) = \alpha_l \exp(\beta_l - \gamma_l \cdot h) \cdot \tau_l(h_0) \quad (4.20)$$

In calibrating with **larive98** experiments, the coefficients are listed in Table 4.2. Fig. 8.1(b) indicates

a	b	α_c	β_c	γ_c	α_l	β_l	γ_l
0.0002917	8.156	0.325	9.508	8.375	0.139	10.761	8.807

Table 4.2: Coefficients for moisture influence on expansion and kinetics (**li04**)

that: a) the asymptotic strain is reduced with RH, and the asymptotic value is reached at a slower rate (as highlighted by the dark line). For instance, at 80% RH, the asymptotic strain has been reduced by nearly 80%, and this reduction was reached in 50 years.

Finally, in the context of a finite element analysis of a structure, separate analyses should be conducted in order to determine the spatial and temporal distribution of RH inside the structure (i.e. $RH(t, x, y, z)$).

While such an analysis may be warranted for bridges of nuclear containers, it can be reasonably assumed that for dams (where RH typically lies in the range of 90-95%) throughout (with the exception of a very small layer of the exposed concrete, which can be neglected).

More refined models addressing the influence of RH on AAR expansion can be found in **poynet06** and **comi12**.

4.3.4 AAR Strain

In Eq. 4.3, the free *volumetric* expansion $\epsilon(\infty)$ was assumed to be volumetric, hence the volumetric strain at time t is given by (Eq. refeq:expansion-xi)

$$\epsilon_V^{AAR}(t, x, y, z) = \xi(t, x, y, z)\epsilon(\infty) \quad (4.21)$$

Note that in general, but not always, $\epsilon(\infty)$ is uniform and does not exhibit a spatial distribution. This may not be the case however in some structures, where higher cement content was used in part of the structure (such as external concrete layers in dams) along with reactive aggregates.

Consequently, $\epsilon_V^{AAR}(t, x, y, z)$ should be “redistributed” along the three principal directions. In this model, the volumetric strain will be apportioned to the three principal stress directions².

The third major premise of this model is that volumetric AAR strain must be redistributed to the three principal directions according to their relative propensity to expand on the basis of a weight that is a function of the respective stresses. While the weight determination is relatively straightforward for triaxial AAR expansion under uniaxial confinement (for which some experimental data are available), it becomes less straightforward for biaxially or triaxially-confined concrete.

Mathematically speaking, the second-order engineering tensor for (small deformation) strain, at a Gauss point is defined as:

$$E_{ij} = \underbrace{\begin{bmatrix} \epsilon_{11} & \frac{1}{2}\gamma_{12} & \frac{1}{2}\gamma_{13} \\ \frac{1}{2}\gamma_{21} & \epsilon_{22} & \frac{1}{2}\gamma_{23} \\ \frac{1}{2}\gamma_{31} & \frac{1}{2}\gamma_{32} & \epsilon_{33} \end{bmatrix}}_{\text{general}}; \quad \underbrace{\begin{bmatrix} \epsilon_I & 0 & 0 \\ 0 & \epsilon_{II} & 0 \\ 0 & 0 & \epsilon_{III} \end{bmatrix}}_{\text{Principal Strains}} \equiv \left\{ \begin{array}{c} \epsilon_I \\ \epsilon_{II} \\ \epsilon_{III} \end{array} \right\} \quad (4.22)$$

where we adopted the Voigt notation for the last representation of the principal strains. The vectors of anisotropic thermal strains and the yet-to-be-determined AAR strain vector are given by:

$$\epsilon_0^{Thermal} = \left\{ \begin{array}{c} \alpha_I \Delta T \\ \alpha_{II} \Delta T \\ \alpha_{III} \Delta T \end{array} \right\} \quad \epsilon_0^{AAR} = \left\{ \begin{array}{c} \epsilon_I^{AAR} \\ \epsilon_{II}^{AAR} \\ \epsilon_{III}^{AAR} \end{array} \right\} \quad (4.23)$$

Let's focus our attention on the last vector, in knowing ϵ_V^{AAR} (which is the sum of the yet-to-be-determined ϵ_I^{AAR} , ϵ_{II}^{AAR} and ϵ_{III}^{AAR}), and the principal stresses σ_I , σ_{II} and σ_{III} . We will re-label this vector of principal stresses as $\sigma_k, \sigma_l, \sigma_m$ and assign to each of the three principal directions an AAR strain proportional to the corresponding stress through a weight.

²Strictly speaking, in nonlinear analysis, the principal strains directions are not co-aligned with the principal stress directions, hence this may be slightly erroneous.

4.3.4.1 Weights

The use of weights will control AAR volumetric expansion distribution. For instance, with reference to Fig. 4.15, let's consider three scenarios.

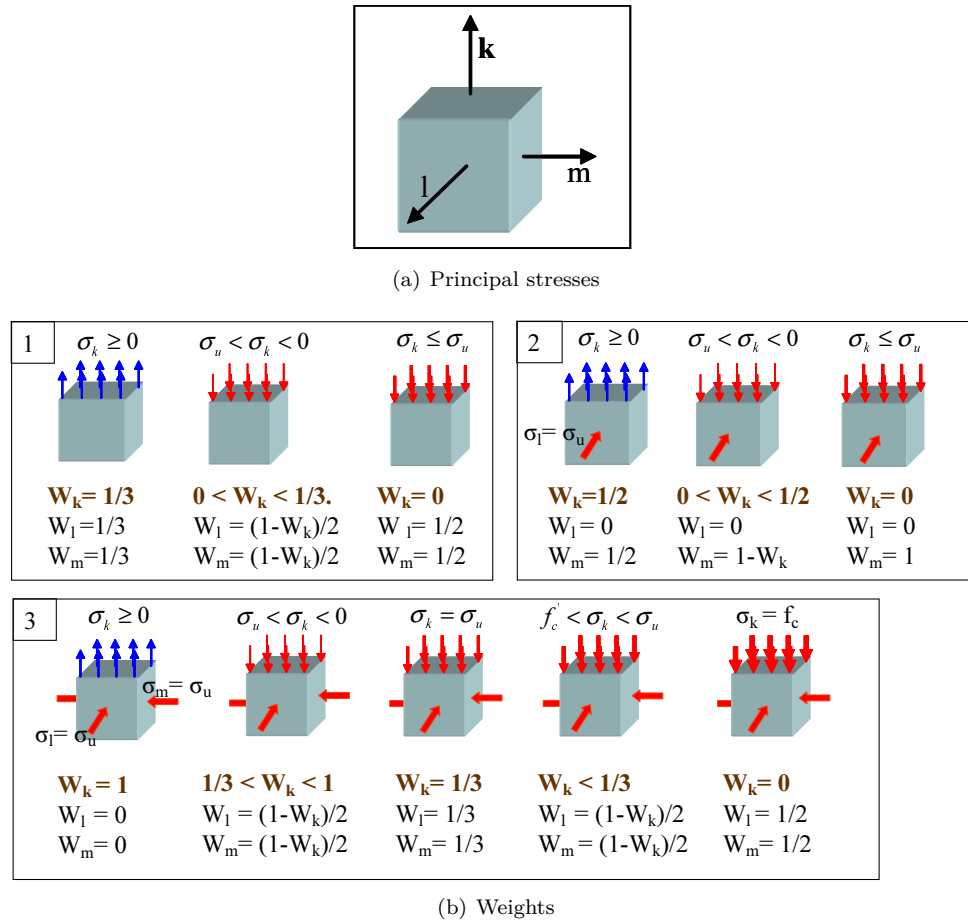


Figure 4.15: Weight of volumetric AAR redistribution in selected cases

Uniaxial State of stress, where the three following cases are distinguished:

1. According to the first case, uniaxial tension is present; hence, the volumetric AAR strain is equally redistributed in all three directions.
2. Under a compressive stress greater than the limiting stress (σ_u), the weight in the corresponding (k) direction should be less than one-third. The remaining AAR needs to be equally redistributed in the other two directions.
3. If the compressive stress is less than σ_u , then AAR expansion in the corresponding direction is prevented (i.e. weight equal to zero), and thus the other two weights must be equal one-half.

Biaxial state of stress, in which a compressive stress equals σ_u in one of the three principal directions. In this case, the corresponding weight will always be equal to zero. As for the three possible combinations:

1. Tension in one direction, equal weights of one-half.
2. Compression greater than σ_u in one direction, then the corresponding weight must be less than one-half and the remaining weight is assigned to the third direction.

3. Compression less than σ_u , then the corresponding weight is once again zero, and a unit weight is assigned to the third direction.

Triaxial state of stress, in which σ_u acts on two of the three principal directions. The five following cases can be identified:

1. Tension along direction k , then all the expansion is along k .
2. Compressive stress greater than σ_u , yielding a triaxial state of compressive stress, and the corresponding weight will lie between one and one-third. The remaining weight complement is equally distributed in the other two directions.
3. Compression equal to σ_u , hence a perfect triaxial state of compressive stress is obtained. This case produces equal weights of one-third; it should be noted that the overall expansion is reduced through Γ_c .
4. Compression less than σ_u , but greater than the compressive strength. In this case, the weight along k should be less than one-third, with the remaining weights equally distributed along the other two directions.
5. Compression equal to the compressive strength. In this case, the corresponding weight is reduced to zero, and the other two weights are each equal to one-half.

Based on the preceding discussion, this weight allocation scheme can be generalized along direction k as follows:

1. Given σ_k , identify the quadrant encompassing σ_l and σ_m , Fig. 4.16³. Weight will be determined

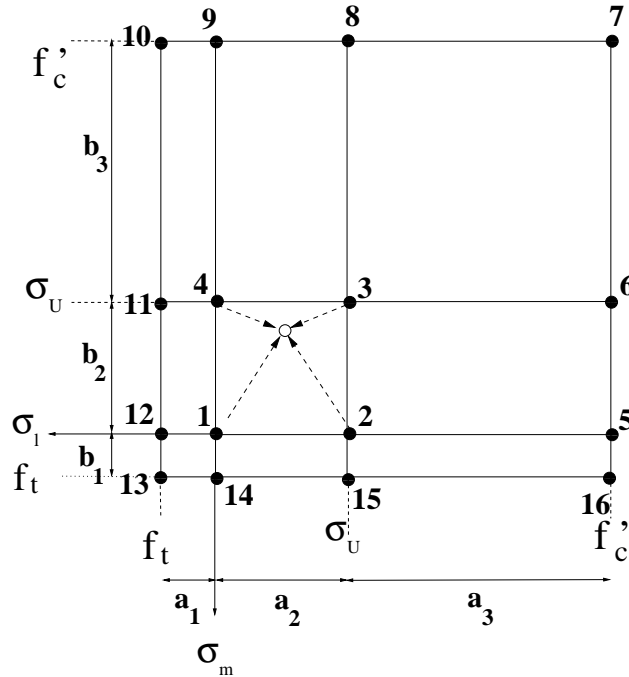


Figure 4.16: Weight domain

through a bilinear interpolation for these four neighboring nodes.

³Since compressive stresses are quite low compared to the compressive strength, we ignore the strength gained through the biaxiality or triaxiality of the stress tensor (**kupfer73**). Furthermore, the strength gain is only about 14% for equibiaxial compressive stresses, (**ceb-biaxial**).

2. Determine the weights of the neighboring nodes from Table 4.3 through a proper linear interpolation of σ_k .

Node			Weights		
No.	σ_l	σ_m	$\sigma_k \geq 0$	$\sigma_k = \sigma_u$	$\sigma_k = f'_c$
1	0.	0.	1/3	0.	0.
2	σ_u	0.	1/2	0.	0.
3	σ_u	σ_u	1.	1/3	0.
4	0.	σ_u	1/2	0.	0.
5	f'_c	0.	1/2	0.	0.
6	f'_c	σ_u	1.	1/2	0.
7	f'_c	f'_c	1.	1.	1/3
8	σ_u	f'_c	1.	1/2	0.
9	0.	f'_c	1/2	0.	0.
10	f'_t	f'_c	1/2	0.	0.
11	f'_t	σ_u	1/2	0.	0.
12	f'_t	0.	1/3	0.	0.
13	f'_t	f'_t	1/3	0.	0.
14	0.	f'_t	1/3	0.	0.
15	σ_u	f'_t	1/2	0.	0.
16	f'_c	f'_t	1/2	0.	0.

Table 4.3: Triaxial Weights

3. Compute the weight from:

$$W_k(\sigma_k, \sigma_l, \sigma_m) = \sum_{i=1}^4 N_i(\sigma_l, \sigma_m) W_i(\sigma_k) \quad (4.24)$$

where N_i is the typical two bilinear shape function used in finite element computations, given by:

$$\mathbf{N}(\sigma_l, \sigma_m) = \frac{1}{ab} \begin{bmatrix} (a - \sigma_l)(b - \sigma_m) & \sigma_l(b - \sigma_m) & \sigma_l \sigma_m & (a - \sigma_l) \sigma_m \end{bmatrix} \quad (4.25)$$

$$\mathbf{W}(k) = \begin{bmatrix} W_1(\sigma_k) & W_2(\sigma_k) & W_3(\sigma_k) & W_4(\sigma_k) \end{bmatrix}^t \quad (4.26)$$

$$a = (a_1 | a_2 | a_3) \quad b = (b_1 | b_2 | b_3) \quad (4.27)$$

$$\sigma_l = (\sigma_l | f'_c - \sigma_l) \quad \sigma_m = (\sigma_m | f'_c - \sigma_m) \quad (4.28)$$

The $i-j$ stress space is decomposed into nine distinct regions, Fig. 4.16, where σ_u is the upper (signed) compressive stress below which no AAR expansion can occur along the corresponding direction (except in triaxially-loaded cases). Hence, a and b are the dimensions of the quadrant inside which σ_i and σ_j reside.

Weights of the individual nodes are, in turn, interpolated according to the principal stress component in the third direction σ_k , Table 4.3. It should be noted that these weights are, for the most part, based on the work of **larive98** and **multon03**, but in some cases due to a lack of sufficient experimental data they are based on simple “engineering common sense”. A straightforward example of the weight evaluation is shown below.

Assuming that the principal stresses are given by $\begin{bmatrix} \sigma_l & \sigma_m & \sigma_k \end{bmatrix} = \begin{bmatrix} -5.0 & -8.0 & -5.0 \end{bmatrix}$ MPa, and that f'_c , f'_t and σ_u are equal to -30.0, 2.0, and -10.0 MPa, respectively, we seek to determine W_k .

The stress tensors place us inside the quadrant defined by nodes 1-2-3-4, whose respective weights are equal to: $W_1 = \frac{1}{2} \left(\frac{1}{3} \right) = \frac{1}{6}$, $W_2 = \frac{1}{2} \left(\frac{1}{2} \right) = \frac{1}{4}$, $W_3 = \frac{1}{3} + \frac{1}{2} \left(1.0 - \frac{1}{3} \right) = \frac{2}{3}$, and $W_4 = \frac{1}{2} \left(\frac{1}{2} \right) = \frac{1}{4}$ and b are both equal to -10 MPa, and the “shape factors” will be: $N_1 = \frac{1}{100} [(-10 + 5)(-10 + 8)] = \frac{1}{10}$, $N_2 = \frac{1}{100} [-5(-10 + 8)] = \frac{1}{10}$, $N_3 = \frac{1}{100} [(-5)(-8)] = \frac{4}{10}$, $N_4 = \frac{1}{100} [-8(-10 + 5)] = \frac{4}{10}$, and finally $W_k = \frac{1}{10} \times \frac{1}{6} + \frac{1}{10} \times \frac{1}{4} + \frac{4}{10} \times \frac{2}{3} + \frac{4}{10} \times \frac{1}{4} = 0.40833$

Based on the earlier work of **struble81**, where it was reported that no gel expansion can occur at pressures above 11 MPa (though for a synthetic gel), σ_u is set as -10 MPa. This value was also confirmed by **larive98**. f'_t and f'_c are the concrete tensile and compressive strengths, respectively.

4.3.4.2 AAR Linear Strains

The volumetric strain at a Gauss point and at time t will be given by (Eq. 4.21) $\epsilon_V^{AAR}(t, x, y, z) = \xi(t, x, y, z)\epsilon(\infty)$, and individual strains can now be obtained from

$$\epsilon_i^{AAR}(t, x, y, z) = W_i \xi(t, x, y, z) \epsilon(\infty) \quad (4.29)$$

and the resulting relative weights are shown in Fig. 4.17.

It should be noted that the proposed model will indeed result in an anisotropic AAR expansion. While not explicitly expressed in tensor form, the anisotropy stems from the various weights assigned to each of the three principal directions.

4.3.4.3 Deterioration

Since this deterioration is time-dependent, the following time-dependent nonlinear model is considered, Fig. 8.1(c).

$$E(t, T) = E_0 [1 - (1 - \beta_E) \xi(t, T)] \quad (4.30)$$

$$f'_t(t, T) = f'_{t,0} [1 - (1 - \beta_f) \xi(t, T)] \quad (4.31)$$

where E_0 and $f'_{t,0}$ are the original elastic modulus and tensile strength, β_E and β_f are the corresponding residual fractional values when ϵ_{AAR} tends to $\epsilon_{AAR}(\infty)$.

Finally, the possible decrease in compressive strength with AAR has been ignored. Most of the literature focusing on the mechanical properties of concrete subjected to AAR show little evidence of a decrease in compressive strength (as would be expected since the stresses will essentially be closing the AAR-induced cracks). Furthermore, in dams (of both the gravity and arch types), compressive stresses lie well below the compressive strength, which is quite different from tensile stresses.

4.3.5 Validation

RILEM technical committee 59-ISR has proposed a battery of tests to validate finite element codes ability to perform AAR studies. Problems include material, structural component, and structures problem, (**RILEM-Benchmark-AAR**).

To the best of the authors knowledge, the most exhaustive code validation has been submitted by them for their finite element code Merlin, (**merlin-aar**).

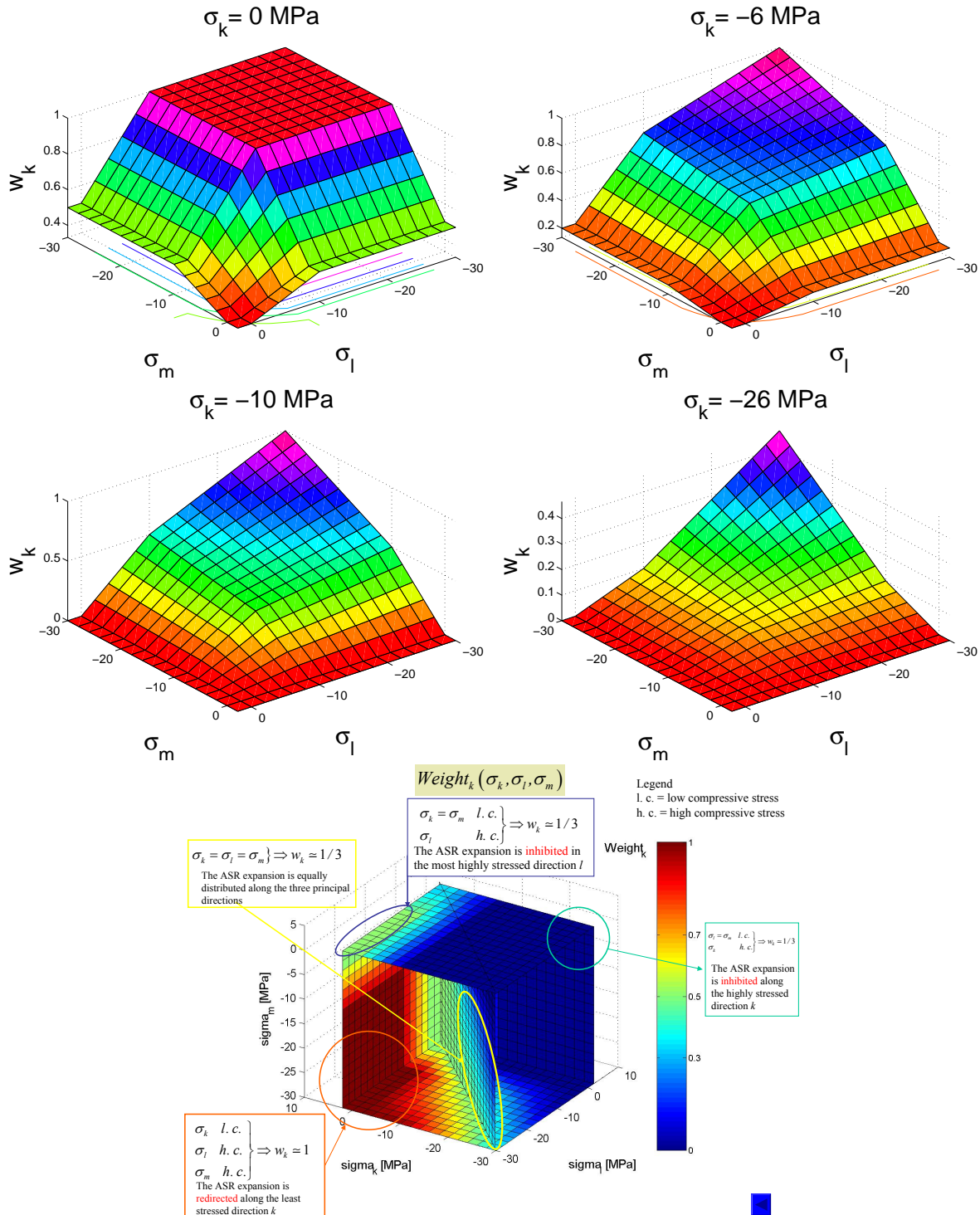
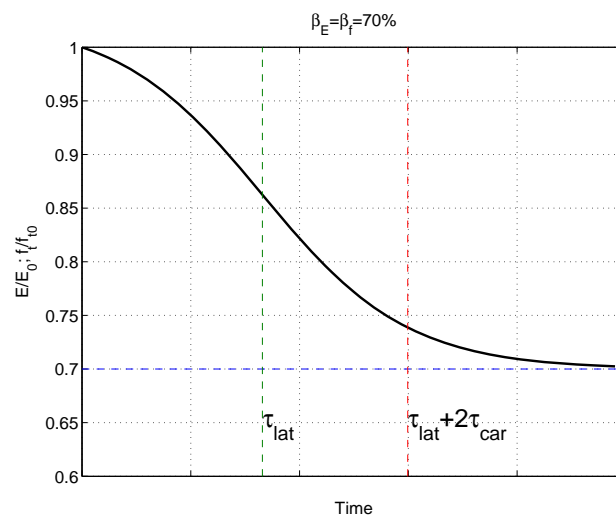


Figure 4.17: Relative Weights

Figure 4.18: Degradation of E and f'_t

Part II

Modeling

This part will extend the previously addressed Theory part into its practical application in finite element analyses. Though the guidelines are finite element code independent, the feature of the Merlin/Kumo/Spider library (developed by the Authors) will be used for illustrative purpose.

5 — Science and Art of Finite Element Modeling

5.1 Modelling

5.1.1 Introduction

This chapter provides the reader with basic recommendations prior to *any* finite element study. More specifically, how to understand and articulate and then mathematically define the problem, how to gather the required data from multiple sources and synthesize them, how to define the mathematical (finite element) model, how to identify the computer codes and assess the quality of the results, and finally how to prepare a report. Modeling is the science and art of addressing all of the above.

Coverage (albeit condensed) of the finite element method is left to any of the multiple references on the method ([Zienkiewicz and Taylor V1](#)) ([Zienkiewicz and Taylor V2](#)) ([hughes87](#)) ([belytschko00](#)).

This chapter will focus on a topic seldom addressed in the literature, that is the science and art of modeling. Cautionary note: modeling existing structure is very different from modeling new structures. In the later, one is confined (typically) with linear elastic analyses for service loads, and known material physical properties and loads (based on design specifications). In the former, typically one seeks to assess the safety margin (or factor) based on the ultimate loads. Hence, material properties must be the actual ones (may require coring), loads to be considered are different (may not simply rely on factored loads of the LRFD method). For existing structures, great caution should be exercised in addressing aging factors such as: creep, relaxation, chloride diffusion-Carbonation and possible ensuing corrosion of rebars, alkali-aggregate reactions, and other factors.

Broadly speaking, the finite element analysis of a [NCS](#) can be summarized by Fig. [5.1](#). each of the major blocks will be separately addressed below.

5.1.2 Tasks

5.1.2.1 Problem Definition

The first step consists in simply defining the problem in terms of the following:

Project Assignment is typically a document written with input from regulators, site and safety engineers and others interested in assessing the structural safety of the [NCS](#). It is typically driven by safety and regulatory requirements, and should not be unduly influenced by potential task complexity, lack of data, expertise or resources. In other words it is a “wish list”.

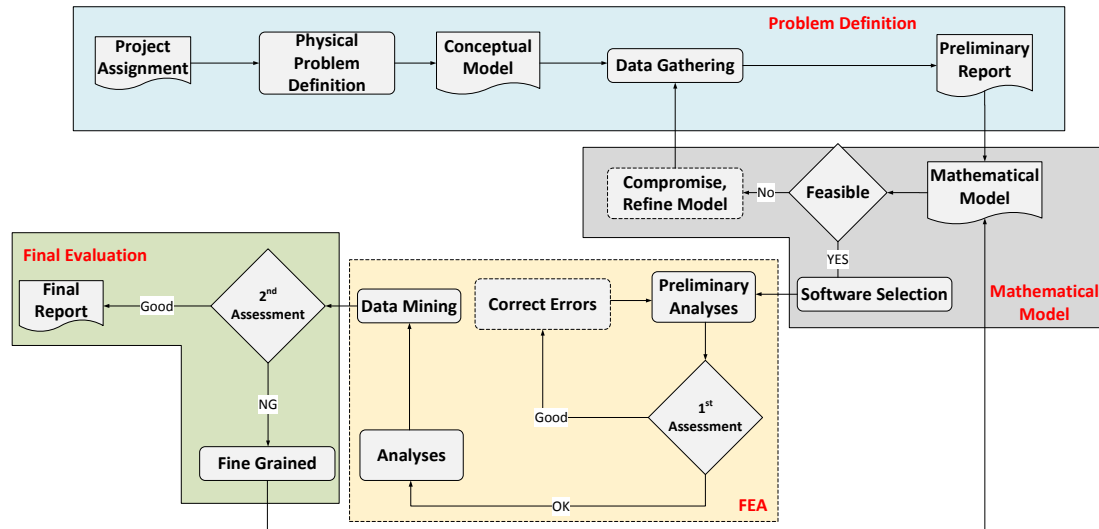


Figure 5.1: Finite Element Process (inspired by **bathe**)

Physical Problem Definition is a translation of the previous document to specific requirements of the analyses to be undertaken. It should include the specifically desired numerical results in a manner easily understood by the finite element analyst.

Conceptual Model is based on the “wish list” of the project manager for the task. It is coarse grained, does not dwell in actual details, and summarizes all assumptions, algorithms, relationships, and data that describe the reality of interest from which the mathematical model and validation experiment can be later constructed. It will also spell out the expectation, break down the project in clearly identifiable tasks, and translate what may be a partially legalistic document into an engineering one (see Sect. 5.1.4). This document should never be modified. If possible, prior to any analysis, it should include anticipated orders of magnitudes of the desired response bracketed between *minima* and *maxima* and anticipated failure modes. This will be important for subsequent “reality/sanity checks” in the first assessment.

Data Gathering is the first attempt by the analysis to translate the previous assignment into specific tasks such as:

- Are all necessary material properties available? Where could one get them (archives, site engineer, literature, others), how reliable are they?
- Is there a need to perform laboratory tests, are the financial resources available, can one easily obtain regulatory authorization to extract cores?
- Software requirements should be spelled out before identifying the one to be used. It may very well be that the “commonly used one” does not have the required features. Eventual discrepancies should be duly noted.
- Is there in-house the expertise to
 1. Perform the numerical simulation.
 2. Supervise/review the simulation performed by others.
- Identify third party independent reviewers for the project.

Preliminary Report Report on data gatherings, and repeat the anticipated results (failure modes, order

of magnitudes of results).

5.1.2.2 Mathematical Model

A mathematical model is the link between the problem statement and the actual finite element simulation. It is a fine-grained document which details of the following

Mathematical Model Based on the “marhing orders” defined previously in the Conceptual Model, and involves identifying material properties Sect. 5.1.3.4; loads and boundary conditions, Sect. 5.1.3.3 below; type of analysis (linear, nonlinear, implicit, explicit).

Assess Feasibility This is a “reality check” on whether the *desiderata* can indeed be fulfilled realistically.

Compromise If the model can not fully respond to the needs articulated in the second report, then compromises must be made, recorded, and the process of data gathering is repeated.

Software Selection is a critical step separately addressed in Sect. 5.1.3.5.

5.1.2.3 Finite Element Analyses

Preliminary Analysis usually, linear elastic to test definition of material properties, boundary conditions, and loads.

Preliminary Assessment Perform a “reality check” on the results. Are they out of bound (different orders of magnitude) of those anticipated in the preliminary report? are there blatant erroneous data entries, mixed units? are the displacements consistent with loads or boundary conditions? Is the load path realistic? are there zone of the mesh which should be refined? Should one use different number of increments, integration scheme? are the convergence criteria too tight?

Correct Errors that may have resulted in unacceptable preliminary results.

Analyses of the structure going incrementally from the simplest to the most complex.

Data Mining Is the process of extracting all relevant results from piles of output. Some software allow specific data to be dumped on disk files, others not. Data may have to be extracted wither from the graphical post-processor or from the ascii-output, and stored. It is best to store all retrieved data in an Excel sheet, and then use programs such as Matlab or Python to read the data and plot them as is best suited for the demand.

5.1.2.4 Final Evaluation

Finally a final evaluation of the series of analyses must be performed.

2nd Assessment Is a “fine grained” assessment of results to determine if they are truly meaningful and reflect a solution to the problem. If not, then the mathematical model itself must be revisited.

Final Report Should have a short executive summary, the body of the report, and typically many appendices with plots and graphs.

5.1.3 Key Considerations

5.1.3.1 Modeling

Prior to modeling a complex structure, important questions must first be addressed, as they will subsequently guide the analyst in the model.

- Can the structure be modeled as 2D or 3D? in the former should it be plane stress, plane strain, or axisymmetric? For NCS a 2D/axisymmetric model is tempting, however it will limit the ability to model buttresses, and most importantly seismic loads. Given available computational powers, a 3D model should be used when possible albeit mesh preparation time is a major consideration.
- Are we interested only in the limit state, that is only the failure load, or in the full nonlinear response. Limit states loads are either upper or lower bound solutions.
- Transient analysis is increasingly favored over Response spectrum or modal analyses. The later were *in-vogue* when computational power was in limited supply and are not suitable for nonlinear response. Hence, the nonlinear dynamic response of a structure can be obtained wither through the full power of a nonlinear transient analysis, or a simplified pushover one.
- Response can be highly dependent on damping. Rayleigh damping is essentially an artificial scheme to implicitly account for energy dissipation due to nonlinear response. it is both mass and stiffness proportional. Hence, analyst should exercise great care in selecting damping coefficients (if any) in the context of a nonlinear analysis where energy dissipation is implicitly factored in the algorithm.
- Extent of nonlinear analysis must be ascertained. Are we only interested in the peak load for safety or are we also interested in the post-peak response (softening) for ductility assessment?
- How certain are we with the loads, material properties? should one be limited to a single deterministic analysis, or should a probabilistic investigation be conducted through multiple analyses (Monte-Carlo)?

The final model is ultimately not only a compromise between requirements and time/cost constraints, but also a function of understanding of the problem, the available tools/expertise and type of results expected (very precise deterministic, or more approximate probabilistic

How should one perform an analysis where interest is in a localized zone. At a time when computational power was limited, substructuring was *in vogue* modern approach tends to focus on an “intelligent” mesh, that is one properly graded in terms of density, and assignment of material properties (linear *vs.* nonlinear).

Modeling attention to details must be uniformly distributed over the entire process, Fig. 5.2. On the one hand, one may inadvertently underestimate the importance of a modeling aspect, and this weakest link may then trigger failure. For instance bond failure may be overlooked, yet for seismic loads it is critical at the base of the container. Similarly, disproportionate effort may be spent in modeling an aspect of the structure which is unlikely to play a critical role. For instance, modeling the stiffness of the liner or of the sleeves inside which the post-tensioning cables are housed may require much effort, increase the complexity of the model and is ultimately un-necessary.

Contrarily to linear elastic solutions, there is a multitude of acceptable nonlinear solutions. Different software, models and analysts will get different results and this does not imply that they are all “wrong” (but some may be) It should be kept in mind that, often, large scale failure driven by small overlooked details which in retrospect could and should have been considered in the model while major effort may have been spent on modeling irrelevant other details. Hence, great care should be exercised in identifying what must be modeled, what is relevant, and what is not. In the end, the finite element analysis is just a tool to confirm or quantify a response anticipated through proper solid engineering judgment.

5.1.3.2 Finite Element Mesh

Convergence of a finite element analysis can be achieved by decreasing the mesh element, or increasing the interpolation order of an element (i.e.e the displacement field inside an element can be linear, or quadratic; Very seldom are higher order used). Those are referred to as *h* or *p* convergence. Typically, one would have

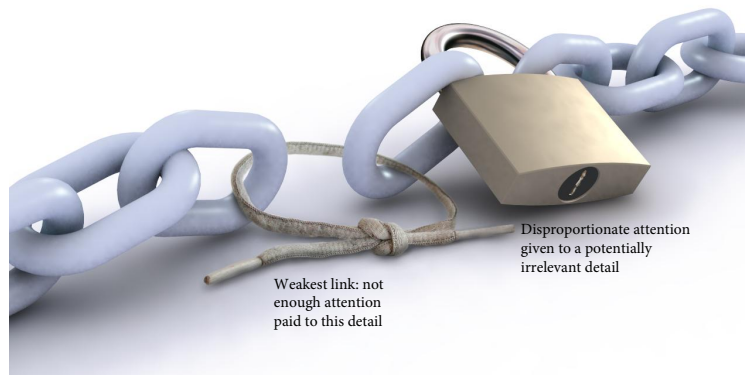


Figure 5.2: Uniformly distributed model complexity

to perform at least two analyses with two different element sizes (h) to make sure that mesh refinement is sufficient.

In modern finite element codes, nearly all elements are so-called isoparametric. That is the displacement field, and the deformed shape of the element are of the same order, linear or quadratic generally. Linear elements can be “stiff”, Fig. 5.3(a), the 8 noded quadratic, Fig. 5.3(b) are more flexible and can better represent actual deformation with fewer elements, and finally the 9 noded ones are even more flexible, Fig. 5.3(c). As a rule, it is far better to use structured mesh, Fig. 5.4(b) rather than unstructured ones, Fig. 5.4(a), as the former yield better convergence. As a rule, it is far better to model the container with solid elements as opposed to shell elements, Fig. 5.4(c).

Once a finite element mesh has been put together, it is desirable to verify its representativity. This can be assessed by comparing the finite element and experimental modal models. The former is determined from a modal analysis and the determination of the first natural frequency of the finite element model. The latter can be obtained through a forced vibration of the structure by a shaker with an eccentrically placed mass.

For NCS, at the very least, the linear elastic response of the model should reasonably well match the results obtained from the Structural/System Integrity Test (SIT) which involves pressurizing the container, and recording displacements at various locations.

Careful, “validation” on the basis of linear elastic analysis, does not imply validation of the nonlinear model. The non-linear model should be validated independently based on a representative structural component with known experimental response.

5.1.3.3 Loads and Boundary Conditions

Loads should receive special attention specially in the context of a nonlinear (incremental analysis). Point loads should be completely discarded as they will induce a localized stress concentration which may slow down the analysis. Point loads should be replaced by distributed traction over a narrow strip.

Initial loads should be carefully applied initially through one or more increments even though they are unlikely to induce any nonlinearity. This is mostly for the gravity loads and initial displacements. In all cases, too large of an increment will result in a slow convergence (assuming an implicit analysis), too small will result in increased computational time.

In a dynamic analysis time steps should be a function of the type of analysis. In an implicit one (where equilibrium is nearly enforced through iterations within an increment), the “usual” time step is 0.02 sec.

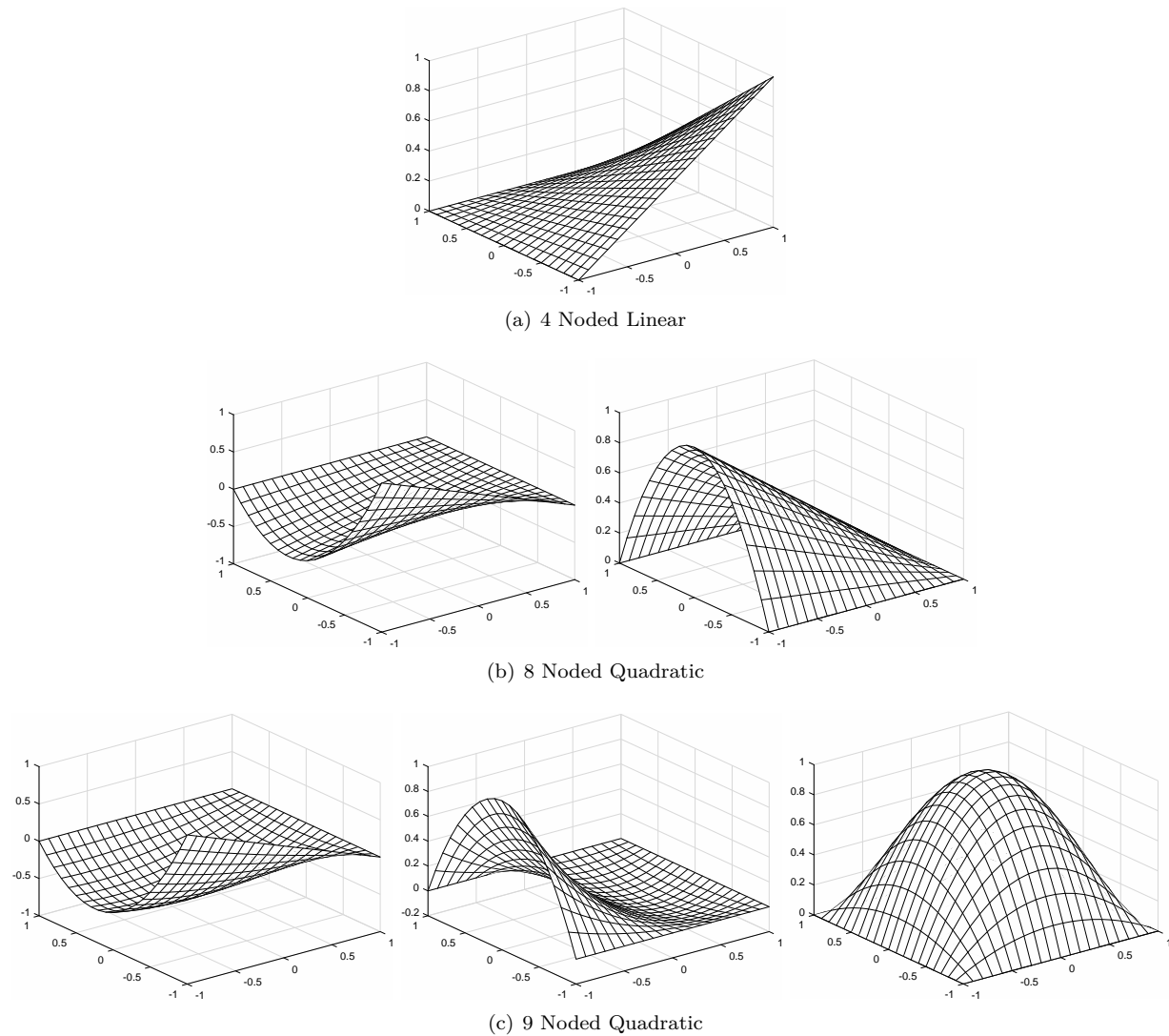


Figure 5.3: Shape functions for isoparametric. elements

Whereas in an explicit analysis, the time step should be much smaller to make ensure that a stress wave does not cross an entire element during a time step (thus computation time is in this case conditioned on the smallest element size in the mesh), (**courant67**).

Whereas *a priori* boundary conditions may not be perceived as loads, they are. Indeed a non zero fixed support will induce loads. Careful in not drastically changing the boundary conditions on an analysis without the “buffer” of a few increments to allow equilibrium to be properly recovered.

Specially in an incremental nonlinear analysis, loading of each increment should be referenced, Table 5.1.

5.1.3.4 Material Properties

Material properties for a nonlinear analysis go well beyond the traditional compressive strength f'_c . Though each plant may be governed by different codes of construction (not to be confused with codes for safety assessment), in order of importance, the following data should be gathered for multiple site locations and

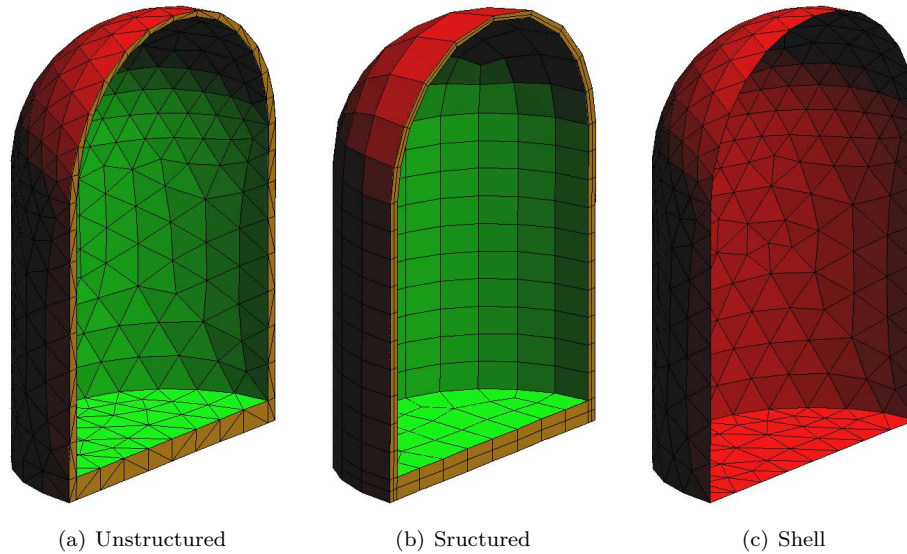
Figure 5.4: Unstructured *vs.* structured *vs.* Shell meshes (meshed with **rypl**)

Table 5.1: Sample of Excel file storing load information

Increments		Description	multirow2[4]*Comments
From	To		
1	end	B.C.: Lateral support	<i>on patch 231</i>
1	3	Initial gravity load	<i>this is a total and not an increment load</i>
4	8	Initial thermal load	
9	50	Incremental load	
51	52	Detention cable 21	
53	300	Incremental AAR load	<i>Careful about the time increment here</i>
Save and restart with removed BC			
301	20000	Seismic excitation	<i>uniform ground excitation hor. and ver.</i>

prevalent standards recommended:

Compressive strength per **aci349** or **astmC39**.

Elastic Modulus per **aci349** or **astmC469**. Ideally, the full stress-strain curve should be measured and reported. If possible, test should be conducted under strain control.

Tensile strength per **aci349** or **astmC496**.

Fracture Energy is a most important parameter for modern nonlinear analysis.

Creep Coefficients per **astmC512**.

Thermal analyses of **NCS** are seldom needed post-construction.

One should keep in mind that in a nonlinear analysis there are two types of material properties to be specified: the basic ones (typically tensile and compressive strength, elastic modulus, and Poisson's ratio), and others specific to the nonlinear constitutive model. For the first set, and specially in the context of a safety assessment investigation, one can not rely on the construction specified values, but must be determined either from cores (preferably) or from non destructive evaluations (NDE). Furthermore, material properties are likely to vary spatially within an **NCS** more specifically across vertical lifts. Hence, either probabilistic analyses should be conducted after selection of the distribution (normal, log-normal are the most common),

the corresponding mean, standard deviation of key variable. Alternatively a homogenization technique must be adopted (this methodology is still in its infancy). Finally, selection of constitutive model specific input data should be preceded by a sensitivity analysis as those are nearly never obtainable from laboratory tests.

A major tenet in the scientific and engineering community is that a paper or report should contain sufficient detail (data, figures, and others) and references to permit others to replicate the work. Hence, all input data should be clearly identified: value, symbol, value, reference and properly tabulated in an excel spreadsheet. In the context of a probabilistic analysis, the probability distribution function should also be identified along with the normalized standard deviation and the truncated values (minimum and maximum).

Data will be most efficiently stored in a multi-sheets excel file, Table 5.2 for the variables and 5.3 for the correlations.

Table 5.2: Example of Data Repository

Characteristics	Symbol	Unit	Distributional model	Mean/COV	[min, max]	Comment
Maximum volumetric strain	$(\varepsilon_{AAR}^\infty)_T$	-	Trapezoidal	-	[0.004 0.020]	From report
Characteristic time	τ_c	ATU	Trapezoidal	-	[40 75]	Curve fit lab test
Latency time	τ_l	ATU	Trapezoidal	-	[480 610]	Curve fit lab test
Activation energy for τ_c	U_C	$^\circ\text{K}$	Uniform Dist.	5,400	[4,900 5,900]	Larive paper
Activation energy for τ_l	U_L	$^\circ\text{K}$	Uniform Dist.	9,400	[8,900 9,900]	Larive Paper
Residual reduction factor	Γ_r	-	Normal Dist.	0.15/0.2	[0.1 0.2]	Assumed
Fraction of ε_t	γ_t	-	Normal Dist.	0.5/0.2	[0.3 0.7]	Assumed
Compressive strength	f_c	MPa	Uniform Dist.	-67.0	[-77.0 -57.0]	Ave. Exp. test
Tensile strength	f_t	MPa	Uniform Dist.	4.5	[4.0 5.0]	Exp. test
Shape factor	a	-	Deterministic	-2	-	-
Reference temperature	T_0	$^\circ\text{C}$	-	10.1/0.3	[2 19]	Site measurement
Upper compressive stress limit	σ_U	MPa	Deterministic	-8	-	-
Reduction fraction for E	β_E	-	Uniform Dist.	-	[0.68 0.78]	-
Reduction fraction for f'_t	β_{f_t}	-	Uniform Dist.	-	[0.10 0.41]	-

Table 5.3: Example of Correlation Between Random variables

Property	RV	1	2	3	4	5	6	7	8	9	10	11	12
Mass density	1	1											
Coefficient of thermal expansion	2	0	1										
Elastic/Young's modulus	3	0	0	1									
Poisson's ratio	4	0	0	0	1								
Tensile strength	5	0	0	0	0	1							
G_F - Exponential softening	6	0	0	0	0	0.5	1						
Compressive strength (must be negative)	7	0	0	0.5	0	0	0	1					
Compressive critical displacement	8	0	0	0	0	0.7	0	0	1				
Factor beta for return direction	9	0	0	0	0	0	0	0	0	1			
Factor e for roundness of failure surface	10	0	0	0	0	0	0	0	0	0	1		
Onset of nonlinearity in compression	11	0	0	0	0	0	0	0	0	0	0	1	
Plastic strain at compressive strength	12	0	0	0	0	0	0	0	0	0	0	0	1

5.1.3.5 Software Selection

First reaction is to assume that the readily available (in-house or with the consultant) software is adequate. This is not always correct. By the time a nonlinear analysis of a NCS must be performed, a serious and potentially grave problem exists, and the best tool should be selected.

Software fall into four major categories:

Major Commercial Abaqus, Adina, Ansys: none of them targets the civil engineering discipline (but rather aerospace, mechanical and nuclear respectively). Code Aster is worth mentioning as it was developed by the French national utility company *EdF* and must be used by all analysts. The code is practically not used outside of France.

National Laboratories LS-Dyna (originally developed at Lawrence Livermore Laboratory) has been widely publicized ([hallquist1998livermore](#)). It uses an explicit algorithm, thus results will always be obtained, but there is no assurance that equilibrium (and thus nearly correct) results are obtained, Sect. 5.2.1.1. More recently, the Idaho National Laboratory has been developing a new software to model aging of nuclear reactors, MOOSE. Built on MOOSE is Grizzly ([huang2015grizzly](#)) for concrete structures. However at this stage, it is still far from ready to run complex analysis of reinforced concrete structures.

Medium Size Specialized software for concrete such as Diana ([diana](#)) and ATENA ([atena-nuclear](#)). The former grew from the TNO research laboratory at the technical University of Delft, and the second has been developed by Cervenka. Both of them have many concrete models, and to the best of the author's knowledge only ATENA has been used for the simulation of a acNCS.

University Based Software include Merlin ([merlin](#)) developed by the author of through funding from the Electric Power Research Institute, and then from the Tokyo Electric Power Company (TEPCO); it has been used to perform nonlinear probabilistic transient analyses of both [NCSs](#) and dams, . Another code (albeit not reportedly used for [NCS](#) is OpenSees (Open System for Earthquake Engineering Simulation). it is a software framework for simulating the seismic response of structural and geotechnical systems, developed as the computational platform for research in performance-based earthquake engineering at the Pacific Earthquake Engineering Research Center. This is to some extent a “research software” extensively used to model buildings and bridges (through beam-column elements), it does have many continuum based nonlinear elements.

5.1.4 Verification and Validation *vs.* Calibration

When conducting a nonlinear analysis, it is essential that the finite element code be validated and verified if possible

Verification deals with the mathematics of the problem and is the process of determining that a model implementation accurately represents the developer's conceptual description of the model and the solution to the model by comparing numerical solutions to analytical or highly accurate benchmark solutions.

Validation on the other hand deals with the physics of the problem and is the process of determining the degree to which a model is an accurate representation of the real world from the perspective of the intended uses of the model. It compares numerical solutions to experimental data.

Calibration is the process of adjusting numerical or physical modeling parameters in the computational model for the purpose of improving agreement with experimental data.

Calibration Experiment Experiment performed for the purpose of fitting (calibrating) model parameters.

Code Verification Process of determining that the computer code is correct and functioning as intended.

Computer Model Numerical implementation of the mathematical model, usually in the form of numerical discretization, solution algorithms, and convergence criteria.

Conceptual Model Collection of assumptions, algorithms, relationships, and data that describe the reality of interest from which the mathematical model and validation experiment can be constructed.

Confidence Probability that a numerical estimate will lie within a specified range.

Error is a recognizable deficiency in any phase or activity of modeling and simulation that is not due to lack of knowledge.

Experiment Observation and measurement of a physical system to improve fundamental understanding of physical behavior, improve mathematical models, estimate values of model parameters, and assess component or system performance.

Experimental Data Raw or processed observations (measurements) obtained from performing an experiment.

Experimental Outcomes Measured observations that reflect both random variability and systematic error.

Experiment Revision The process of changing experimental test design, procedures, or measurements to improve agreement with simulation outcomes.

Fidelity The difference between simulation and experimental outcomes.

Field Experiment Observation of system performance under fielded service conditions.

Inference Drawing conclusions about a population based on knowledge of a sample.

Irreducible Uncertainty Inherent variation associated with the physical system being modeled.

Laboratory Experiment Observation of physical system performance under controlled conditions.

Mathematical Model The mathematical equations, boundary values, initial conditions, and modeling data needed to describe the conceptual model.

Model Conceptual/mathematical/numerical description of a specific physical scenario, including geometrical, material, initial, and boundary data.

Model Revision The process of changing the basic assumptions, structure, parameter estimates, boundary values, or initial conditions of a model to improve agreement with experimental outcomes.

Nondeterministic Method An analysis method that quantifies the effect of uncertainties on the simulation outcomes (also known as probabilistic method).

Performance Model A computational representation of a model's performance (or failure), based usually on one or more model responses.

Prediction Use of a model to foretell the state of a physical system under conditions for which the model has not been validated.

Pretest Calculations Use of simulation outcomes to help design the validation experiment.

Reality of Interest The particular aspect of the world (unit problem, component problem, subsystem or complete system) to be measured and simulated.

Reducible Uncertainty Potential deficiency that is due to lack of knowledge, e.g., incomplete information, poor understanding of physical process, imprecisely defined or nonspecific description of failure modes, etc.

Risk The probability of failure combined with the consequence of failure.

Risk Tolerance The consequence of failure that one is willing to accept.

Simulation The ensemble of models—deterministic, load, boundary, material, performance, and uncertainty—that are exercised to produce a simulation outcome.

Simulation Outcome Output generated by the computer model that reflect both the deterministic and nondeterministic response of the model.

Uncertainty A potential deficiency in any phase or activity of the modeling or experimentation process that is due to inherent variability (irreducible uncertainty) or lack of knowledge (reducible uncertainty).

Uncertainty Quantification The process of characterizing all uncertainties in the model and experiment, and quantifying their effect on the simulation and experimental outcomes.

Validation Experiment Experiments that are performed to generate high-quality data for the purpose of validating a model.

Validation Metric A measure that defines the level of accuracy and precision of a simulation.

Warning: Too often nonlinear finite element code are presumed as “validated” by merely capturing the experimentally observed data (displacements typically). Often times, this is accompanied with very colorful figures, and juxtapositions. It should be kept in mind that nonlinear models have sufficient variables to “tune” many of them and then obtain what is perceived as an acceptable model.

Such model should be scrutinized to make sure that all assumptions are sound and reasonable, that material properties adopted are realistic. In other words a mere superficial pictorial comparison is not sufficient.

5.1.5 Expert Selection

If a nonlinear analysis is to be performed, great care should be exercised in selecting “experts” who could perform such an analysis. Most engineers in consulting firms are accustomed to performing linear elastic analysis and code regulated design. On the other hand, there are a handful of researchers in academia who are well versed in the conduct of nonlinear analysis of a complex structure, however they often tend to simplify peripheral aspects of the model and focus on a narrow aspect.

Extraordinary problems will require extraordinary techniques to investigate by very well qualified analysts.

5.1.6 Singularities

Singularities (theoretically infinite stress) appear in many finite element models whenever there are point/line loads, sharp corner, discontinuity in boundary conditions or loads. For instance, under a point load the stress is $\propto 1/R^2$, (**boussinesq1885application**). In such cases, one should not try to excessively refine the mesh, as (by definition) this will never be fine enough. The smaller the element size, the larger the stress (i.e. “tell me what stress you want, I can get it by merely playing with the element size”), Fig. 5.5. Refinement should be avoided however one should properly interpret results from the post-processor by accounting for the non-captured singularity.

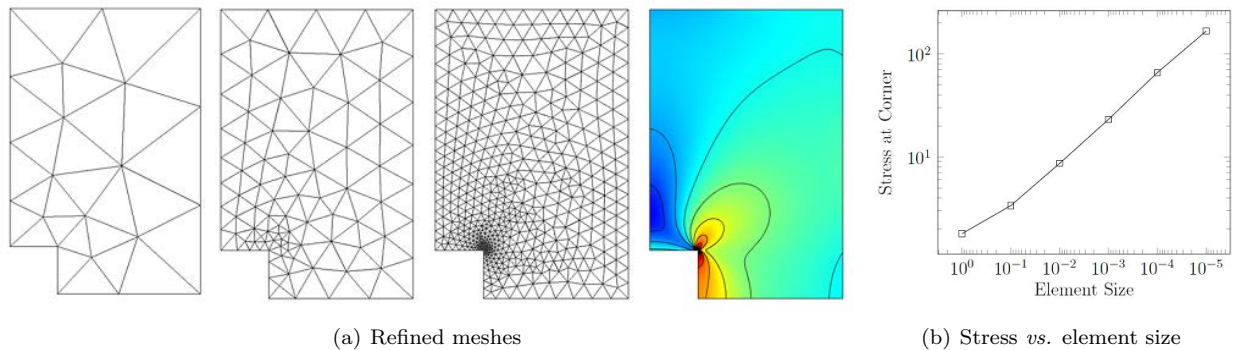


Figure 5.5: Meshing in the presence of stress singularity in a re-entry corner <https://www.comsol.com/blogs/how-identify-resolve-singularities-model-meshing/>

In the context of linear elastic analysis, high stresses will remain very localized and can be ignored. In nonlinear analyses, singularities may have a detrimental effect as they will slow the incremental solution. In either case, a stress singularity mask the stress distribution in the rest of the mesh by assigning the same color to a wide range of stresses (unless contour lines of stresses are plotted on the basis of a logarithmic scale). It should also be recognized that concrete is very resilient, a singularity is likely to cause localized micro-cracks which are inconsequential to the global safety.

5.2 Some Theoretical Considerations

5.2.1 Material Nonlinearity

Through the application of an external load, a structure deforms and develops internal deformation and corresponding internal forces (equal to the product of the stiffness matrix times the displacement vector). Per Newton's second law, equilibrium between the two must be satisfied, or the sum of external and internal forces must be equal to zero.

In linear cases, the stiffness matrix is constant, and thus the internal forces are only proportional to the displacement and the solution can be achieved in one single step.

In nonlinear cases, stiffness matrix is not constant but also a function of the displacement. Since the internal force is equal to the product of the stiffness matrix (which is also a function of displacement) and the displacement vector, the problem becomes nonlinear, and to analyze the problem, the external load has to be applied incrementally in small steps.

There are two classes of solutions explicit and implicit. Each will be discussed separately below.

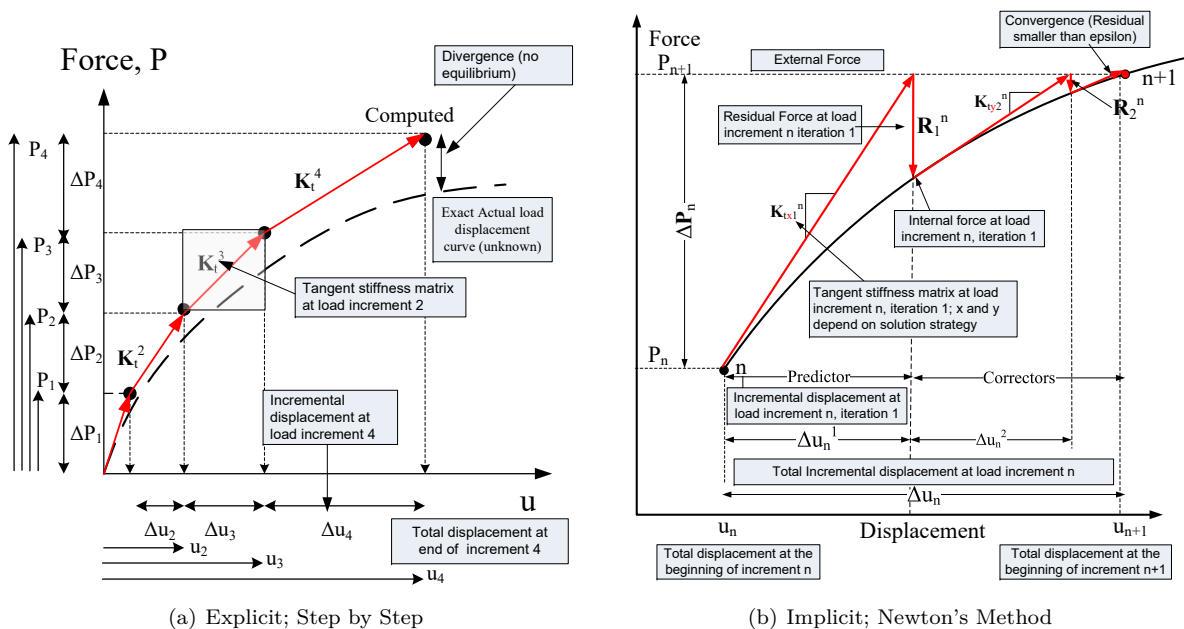


Figure 5.6: Numerical integration schemes for nonlinear structural analysis

Method	Tangent stiffness matrix computed at				Figure
	Predictor (x in K_{txi}^n)		Corrector (y in K_{tyi}^n)		
	Increment	Iteration	Increment	Iteration	
Newton-Raphson	n	1	n	i	5.7(a)
Modified Newton-Raphson	n	1	n	1	5.7(b)
Initial Stiffness	1	1	1	1	5.7(c)

Table 5.4: Highlights of integration schemes

5.2.1.1 Explicit

In an explicit integration scheme (also known as “step by step”), the load is applied incrementally and at the end of each increment: a) Compute the tangent stiffness on the basis of the current displacements, this is the slope of the load displacement curve); b) invert the stiffness matrix and multiply it by the incremental load to get the corresponding incremental displacement; c) add the incremental displacement to the sum of the previous ones to obtain the actual displacement corresponding to the actual load (sum of all previous incremental loads), Fig. 5.6(a).

The major advantage of this technique is that a solution will always be found. The major disadvantage is that the end of each increment we do not verify that equilibrium between internal and external forces is satisfied. This may result in a diverging solution as the load increases. A partial palliative to this problem, is the adoption of very small load increment to minimize errors.

This method should be used extremely carefully, as a solution will always be obtained no matter how good or bad the model and its parameters are. Unfortunately, there are some constitutive models which are very fragile when run within an implicit integration scheme, and as a result they are used (or misused) in an explicit one.

5.2.1.2 Implicit

The algorithm is illustrated in Fig. 5.6(b) which is the counterpart of the shaded zone in Fig. 5.6(a). It is essentially the same as the explicit one, however it is broken in two steps: a) A predictor (associated with an increment of load) to determine the incremental displacement as in the explicit method; and b) Corrector phase where we check for equilibrium iteratively. .

The corrector phase operates as follows: a) based on the predicted displacements, compute the corresponding internal forces (not evaluated in the explicit method); b) compute the residual force which is the difference between the external and internal forces (should be zero if equilibrium is reached); c) If the residual is larger than a user specified convergence criteria, then update the displacement by multiplying the inverse of the tangent stiffness matrix (more about this later) by the residual force; d) update the total displacement vector. Hence to each load increment, we would have multiple iterations until equilibrium is satisfied within a numerical tolerance.

There are different flavors of this so-called Newton technique. Those are associated with the tangent stiffness matrix to be considered, Table 5.4.

Those integration schemes are shown in Fig. 5.7 where in the Newton-Raphson method the tangent stiffness matrix is updated at each iteration, in the Modified Newton-Raphson it is updated at each increment, and in the Initial stiffness method there is no update.

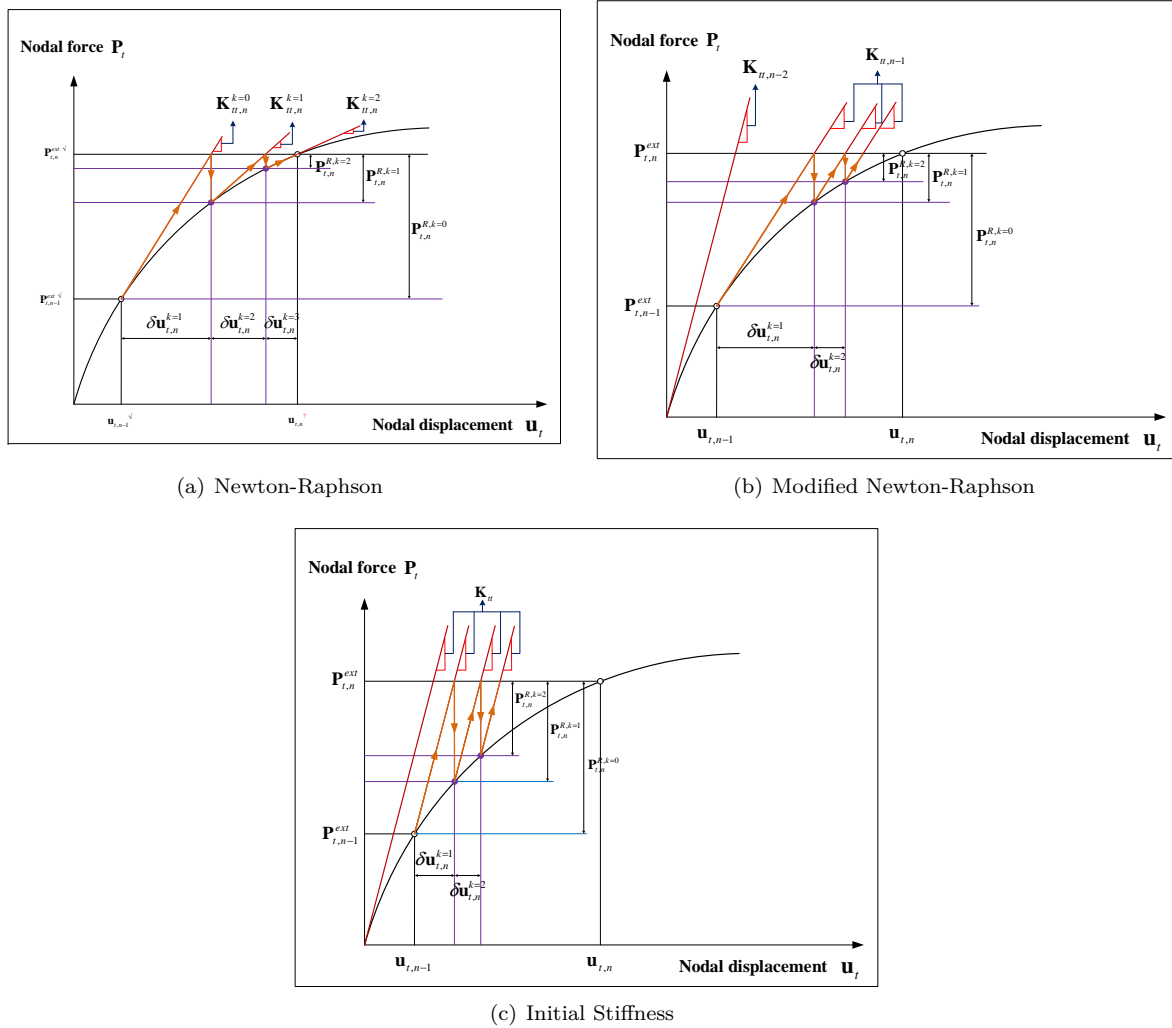


Figure 5.7: Integration schemes

5.2.2 Fracture Mechanics of Concrete

Fracture mechanics is a must consideration in modern nonlinear analysis of concrete structures. By now, most major finite element codes concrete constitutive models require the specification of the fracture energy: Abaqus ([abaqus](#)); Adina ([Adina documentation2010release](#)); ANSYS ([ANSYS documentation2010release](#)); ATENA ([vcervenk2000atena](#)); Diana ([dianafeadoc](#)); LS-Dyna ([hallquist2007ls](#)). In most of these cases, the fracture energy is used to regularize the response, that is remove the mesh sensitivity results by adjusting tensile strength in relation of the element size. In more refined models, the fracture energy is used as a parameter for a discrete crack model.

This section will first provide theoretical consideration, and then address the finite element modeling of fracture.

5.2.2.1 Theoretical Considerations

Early on, it was assumed that concrete is a brittle material that could be characterized by a fracture toughness as with metals. Yet, it was soon discovered, against expectations, that it is not, and that measured fracture

toughness had a strong dependency on the size of the specimen (**kaplan61**), (**walsh72**). Concrete is now referred to as a quasi-brittle material. Concrete fracture is characterized by a stress-crack opening width curve (and not stress-strain) which exhibits a softening past the peak load. This section will explain why.

Let us examine the response of a concrete cylinder with two strain gages: one in the upper part and the second across the likely plane of fracture. It is fixed at one end, and at the other one it is subjected to a uniformly applied normal displacement (and not traction). As the imposed displacement is increased, the strain gages will record the response shown in Fig. 5.8. The first one will report a gradual increase in force as a result of the increased displacement, and at some point (associated with the formation and opening of a crack), the gage will report a linear unloading. On the other hand, the other gage will report first an increase in force, and then during crack formation/opening a decrease in the force associated with the increase in imposed displacement. This phenomenon is referred to as softening. Similar response would be obtained if

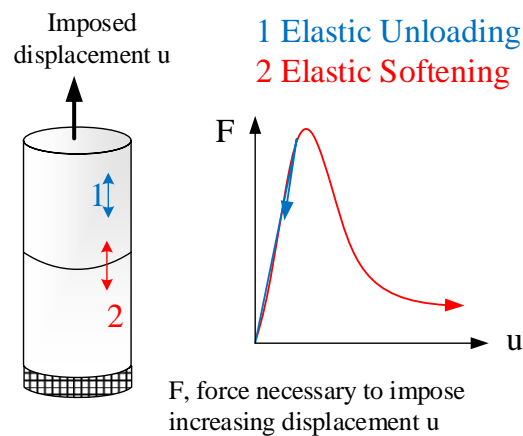


Figure 5.8: Test highlighting localization

a plate were to be subjected to a uniform displacement as in Fig. 5.9. As the plate, shown in Fig. 5.9(b) is subjected to an increased displacement, the strain across the length of the plate (units are irrelevant in this illustrative case), are shown in Figs 5.9(c) to 5.9(g) for displacement ranging from $0.5\Delta_{max}$ to Δ_{max} (arbitrarily set to 1.). At low values, the strain is uniform across the length, but then gradually it increases non-uniformly as a narrower and narrower curve until Δ_{max} .

From the previous two observations, one deduce that a fracture in concrete can carry a tensile stress that decreases from a peak equal to the tensile strength f'_t to zero at some critical crack opening displacement. **hillerborg1** presented a very simple and elegant model which capture this concrete response. In this model, the crack is composed of two parts, Fig. 5.10(a):

True or physical crack across which no stresses can be transmitted. Along this zone we have both displacement and stress discontinuities.

Fictitious crack, or Fracture Process Zone (FPZ) ahead of the previous one, characterized by:

- Peak stress at its tip equal to the tensile strength of the concrete.
- decreasing stress distribution from f'_t at the tip of the fictitious crack to zero at the tip of the physical crack.

The area under the stress crack opening is referred to as fracture energy G_F and is an indicator of the concrete ability to resist crack propagation. Hence, along the FPZ, we have displacement discontinuity and

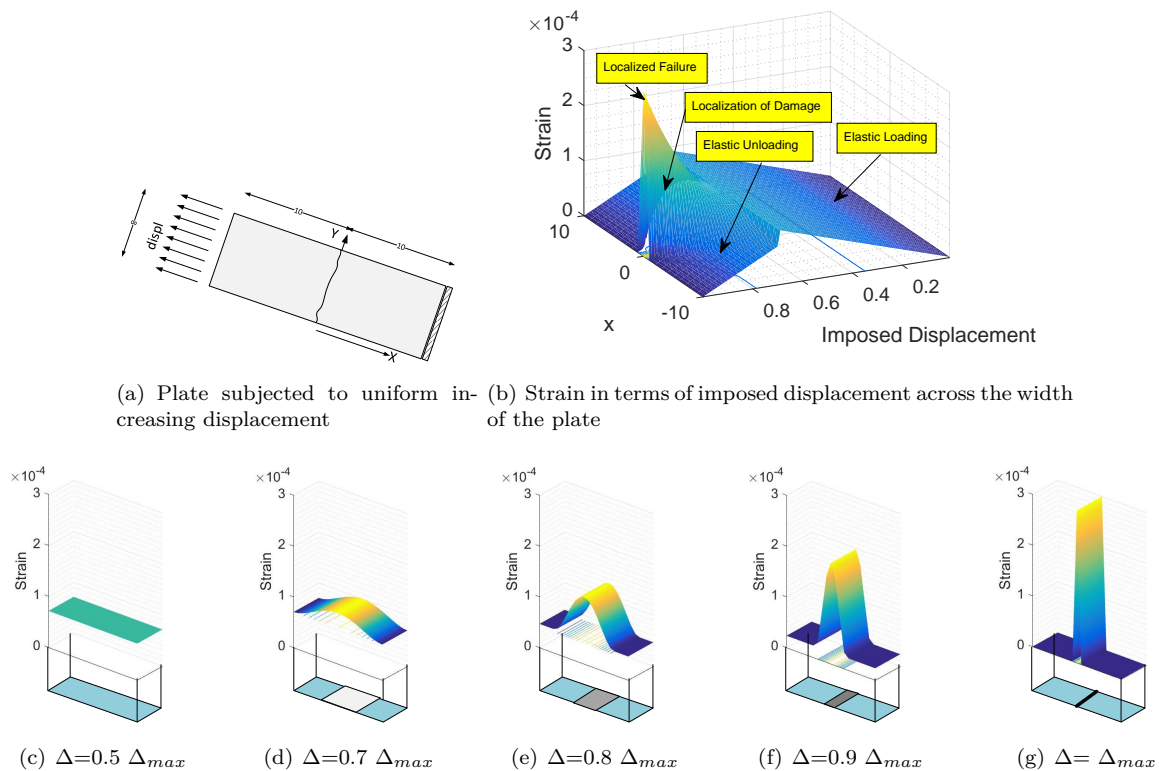


Figure 5.9: Gradual strain localization

stress continuity. In modern codes, distinction is made between G_F and G_f as shown in Fig. 5.10(b).

Regretfully, there is not yet a widely acceptable test procedure to measure the fracture energy. Most of the proposed ones address testing freshly poured concrete “brick” specimens, however in most cases one needs to test cores extracted from an existing structure. The author has been advocating the use of so-called wedge splitting tests. Specimen preparation is shown in Fig. 5.10(c) and test setup in Fig. 5.10(d).

5.2.2.2 Finite Element Modeling

Modeling of concrete failure under compression is relatively simple, however the major challenge is modeling concrete cracking where there are two approaches to model fracture in concrete: discrete and smeared models, Fig. 5.11. An excellent coverage (albeit old) of this topic can be found in (rots89).

5.2.2.2.1 Discrete Crack Model The discrete crack model treats a crack as a geometrical entity. In the FEM, unless the crack path is known in advance, discrete cracks are usually modeled by altering the mesh to accommodate propagating cracks. In the past, this remeshing process has been a tedious and difficult task, relegated to the analyst. However, newer software techniques now enable the remeshing process to be accomplished semi-automatically by the computer. A zone of nonlinear and inelastic material behavior, called the fracture process zone (FPZ), exists at the tip of a stress-free crack. One effective way to model the FPZ is to assume the existence of an additional extension of the crack in which the two sides of the crack may apply cohesive traction to each other (a fictitious, or cohesive crack). These traction are generally thought of as nonlinear functions of the relative displacements between the sides of the crack (based on extensions

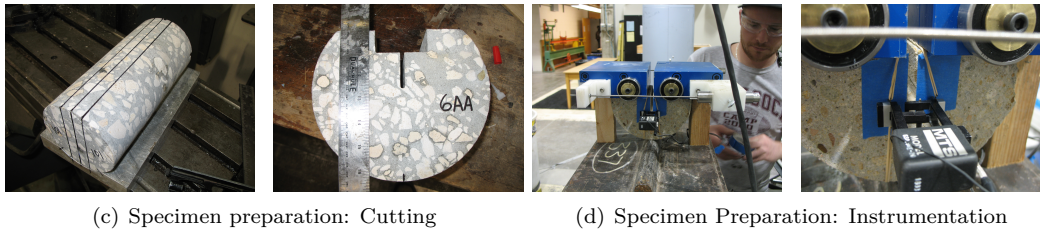
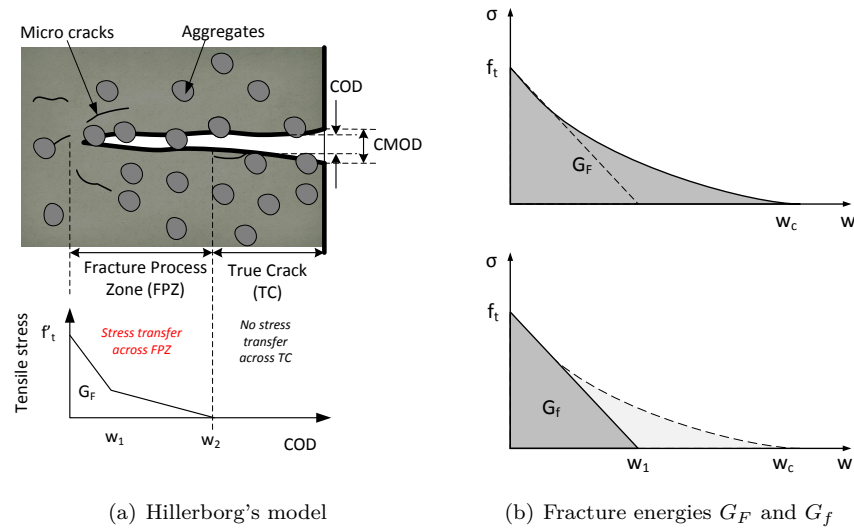


Figure 5.10: Fracture of concrete; Cohesive crack

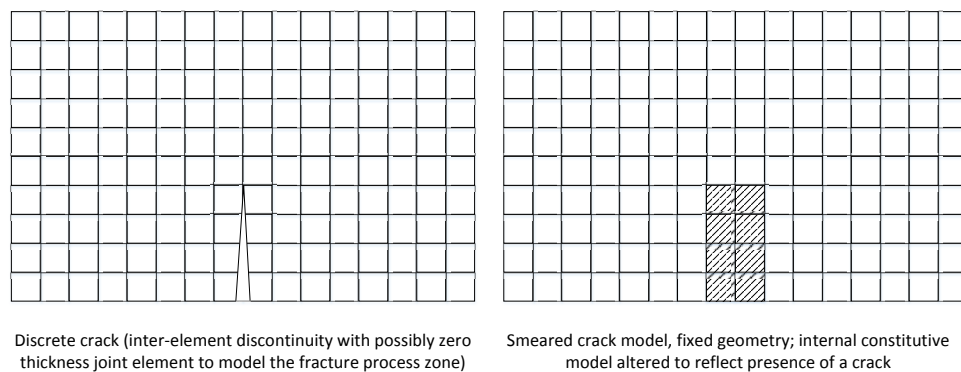


Figure 5.11: Discrete and smeared crack models in concrete

of the cohesive law model of Hillerborg).

A widely successful model for the discrete crack is the element implemented in **merlin** developed by **CervenkaKishen:1998**. Major premises upon which the model is developed are:

1. Shear strength depends on the normal stress. (Coulomb friction)
2. Softening is present both in shear and tension (Hillerborg extended)
3. Residual shear strength due to the friction along the interface, which depends on the compressive normal stress, (Coulomb).
4. Reduction in strength, i.e. softening, is caused by crack formation.

5. Zero normal and shear stiffness when the interface is totally destroyed.
6. Under compressive normal stresses neither the shear and nor the normal stiffness decrease to zero. In addition, should a compressive stress be introduced in the normal direction following a full crack opening, two faces of the interface come to contact, and both tangential and normal stiffnesses become nonzero. (contact problem).
7. Irreversible relative displacements are caused by broken segments of the interface material and by friction between the two crack surfaces, (permanent plastic damage)
8. Roughness of the interface causes opening displacements (i.e. dilatancy) when subjected to sliding displacements.
9. The dilatancy vanishes with increasing sliding or opening displacements.

The zero thickness element is inserted along potential cracks, at first it “glues” both faces to each other, and “unzip” based on the conditions described above, Fig. 5.12. The initial failure function is hyperbolic with cohesion and tensile strength. Should there be sufficient opening or sliding, then it reduces to a mere linear Mohr-Coulomb law with zero tensile strength or cohesion.

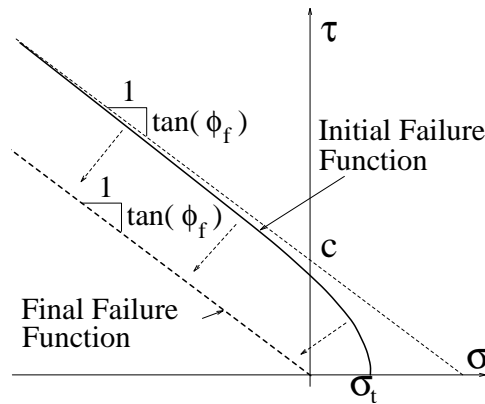


Figure 5.12: Yield function for the fracture mechanics based interface element

Whenever one is in presence of a single major structural crack, the discrete crack model should be favored.

5.2.2.2.2 Smeared Crack Model The smeared crack model was introduced by rashid68, and is a much more convenient to represent cracks by changing the constitutive properties of the finite elements than to change the topology of the finite element grid as in the discrete crack model. The approach is to change the initial isotropic stress-strain law to an orthotropic one upon crack formation, with the axes of orthotropy being determined according to a condition of crack initiation. The procedure is attractive not only because it preserves the topology of the original finite element mesh, but also because it does not impose restrictions with respect to the orientation of the crack planes. Hence, effectively, the material stiffness is dropped to zero in the direction of the principal tensile stress once the stress was calculated as exceeding the tensile capacity of the concrete. Simultaneously, the stresses in the concrete were released and reapplied to the structure as residual loads. Ideally, smeared crack models should be capable of representing the propagation of a single crack, as well as a system of distributed cracks, with reasonable accuracy. A major latent challenge of the smeared crack model is its inability to “localize” (without numerical tricks) thus resulting in a fog of cracked elements.

In the presence of multiple cracks (usually associated with reinforced concrete) then the smeared crack model should be selected, (**Rots1991**) (**saouma01-b**). For the “smeared crack” model without attempts to “localize” the crack, results will be mesh sensitive as recognized for the first time by **bazantcedolin**. Hence, most “modern” finite element codes for smeared crack models rely on a nonlocal formulation to prevent mesh sensitivity (**bazant1988nonlocal**). A valuable (but by now in dire need for revision) reference is **aci446a**.

5.2.3 Fragility Curves

Increasingly it is recognized that we can not limit ourselves to few deterministic analysis for the safety assessment analysis of existing structures. There are too many unknown parameters, yet one may assign a probability distribution function for those parameter (typically log-normal) and perform a probabilistic based analysis. Such an approach is already well established for the seismic safety assessment of buildings and bridges with FEMA (**ATC-FEMA-06**). The concept was first introduced for NCS by (**kennedy1980probabilistic**), yet to the best of the author knowledge it has not yet been formalized in nuclear codes. The analysis itself results in a so-called fragility curve which is a continuous function showing the probability of exceedance of a certain limit state (LS) for specific level of ground motion intensity measure (IM), figure 5.13(a) (**Ellingwood2009179**).

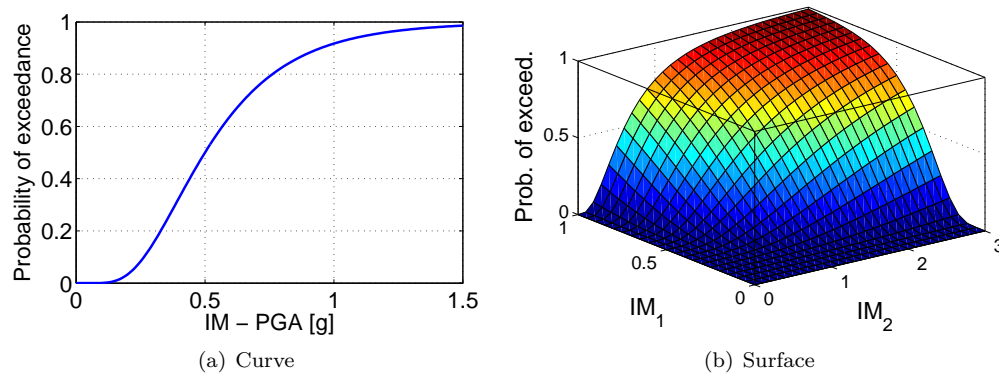


Figure 5.13: Fragility function

Generation of the curve hinges on multiple nonlinear analyses where the structure is subjected to increasing stressors (internal pressurization, seismic excitation or others). Those analyses are either based on so-called Monte-Carlo simulations or better yet on Latin-Hypercube sampling methods (**ImanConover1982**). Suffice it to say that the generation of a fragility curve is computationally expensive, and great care should be exercised in properly balancing model simplicity and structural realism.

5.3 Sensitivity Analyses

It is safe to say that practically all nonlinear constitutive models contain parameters that can not be directly measured in the laboratory. Unfortunately, in most cases the user is left with vague recommendations as to what the default value should be, and very seldom is one aware of the impact of this parameter on the overall results.

Sensitivity analysis can thus be an essential component of a detailed nonlinear investigation and is carried as follows:

1. Identify all parameters as either constants or variables.
2. To each of the n variables, assign a mean and a standard deviation (no need for a probability distribution function).
3. Prepare $2n + 1$ input data files, the first in which all variables are assigned their mean values, and then for each of the $2n$ others, all variables are assigned their mean except one that is assigned mean plus or minus standard deviation.
4. Identify a response factor (such a critical or maximum displacement).
5. For each of the n variables compare response with the one of the mean (for plus or minus standard deviation), and sort results into a so-called “tornado diagram”, Fig. 5.14.

From the tornado diagram, the impact or the sensitivity of the model to each of the variables is quantified, and one can then identify the variables to which the analysis is most sensitive and treat the others as constants.

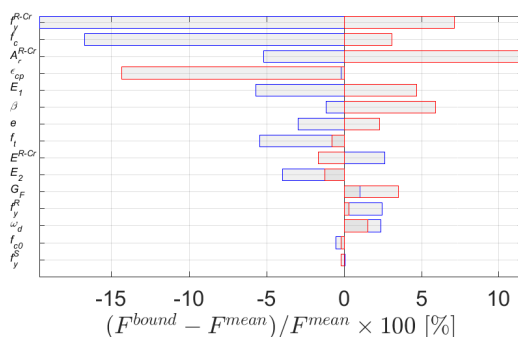


Figure 5.14: Tornado diagram for sensitivity analysis

5.4 Uncertainty Analyses or Risk Informed Conditional Assessment

Once the number of variables has been reduced to a strict minimum (see previous section), one can undertake a probabilistic analysis, or more precisely an “uncertainty analysis”, yielding the probability of an engineering demand parameter (such as deformation, expansion).

As a vehicle to illustrate the uncertainty analysis, it is assumed that the response of a major structure suffering from AAR is being investigated, and a paradigm for risk informed conditional assessment is outlined (saouma2017riskinformed). Though this paradigm is not entirely new, ellingwood2005risk it has seldom been used in the context of evaluation of structures suffering from AAR. First a few terms, commonly used in earthquake engineering will be introduced.

Stressor, S can be: 1) an incrementally-increasing, cyclic or time-dependent load (or displacement, acceleration, pressure); 2) an incrementally-decreasing resistance parameter or degradation of strength properties. In earthquake engineering, S is typically called an intensity measure (IM) parameter. For an AAR analysis, S is time. It is the increase in time (in accordance with the second law of thermodynamic) that causes aging/deterioration of the concrete.

Response, R As the name implies is merely the response of a structure to a stressor S. R may be either scalar or vectorial (single or multiple) damage variable (DV), such as drift or displacement. A limit

state (LS) may be assigned to a DV and thus define a damage index (DI); for example a stress (DV) should not exceed the strength (LS) according to a simple strength based DI. In earthquake engineering, R is often referred as an engineering demand parameter (EDP).

Capacity Function is the relationship between S and R.

Fragility Function is a continuous function showing the probability of exceedance of a certain LS for specific level of IM. This important concept was first introduced by **kennedy1980probabilistic** and is mathematically expressed as

$$\text{Fragility} = P[\text{LS} | \text{IM} = im] \quad (5.1)$$

where $P[A|B]$ is the conditional probability that A occurs given that B is equal to a particular IM.

Fig. 5.15(a) illustrates this concept, typically used in earthquake engineering: What is the probability of a LS exceeding a certain value in terms of the seismic excitation, and what would be the corresponding level of damages. Similarly, for structures affected by AAR, Fig. 5.15(b) would be a corollary that gives the probability of a volumetric expansion exceeding a value in terms of time.

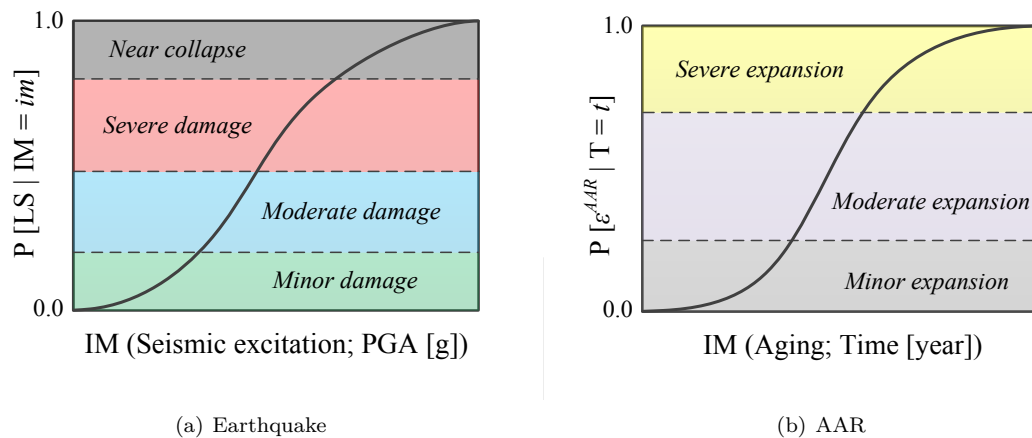


Figure 5.15: Fragility curves (**saouma2017riskinformed**)

Following a brief introduction, the uncertainty analysis proceeds as follows:

1. For the retained random variables, assign a probability distribution function (PDF), as well as upper and lower bounds.
2. Correct the mean and standard deviation to account for the bounded nature of the PDF.
3. Perform a Monte-Carlo simulation through n analyses in which in each case, variables are randomly selected from their domain. Alternatively, latin-hypercube sampling techniques can be used to reduce the number of analysis without loss of generality.

Following the analysis, the Damage index (DI) is plotted in terms of time, and 6 points are identified: the intersection of the 16th, median, and 84th fractiles with: A) a vertical line corresponding to the year 2040 and, B) a horizontal one corresponding to a DI=0.2 (or displacement of 10 mm), Fig. 5.16(a).

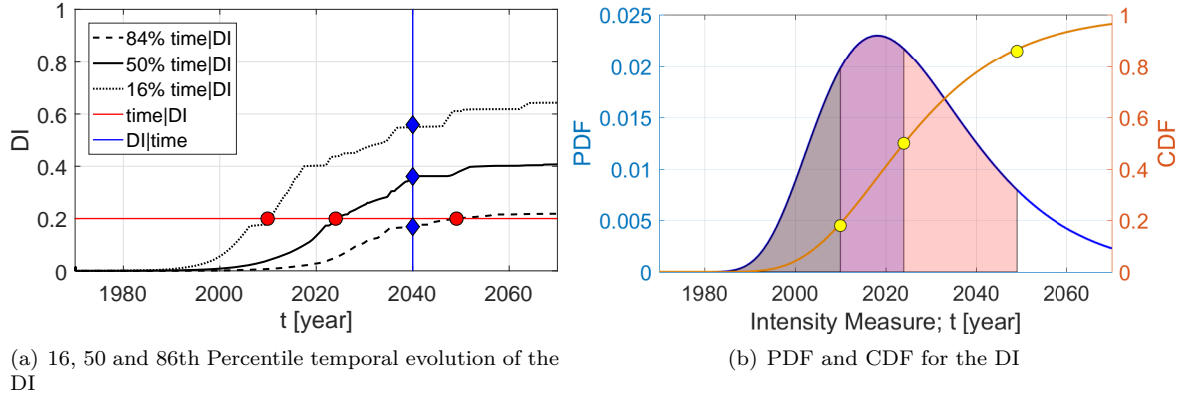


Figure 5.16: Engineering interpretation of results (**saouma2017riskinformed**)

Two conditional assessments are then extracted: 1) time|DI and 2) DI|time . The former is associated with the time needed for a given DI to occur (horizontal line), and the second with the likely of a given DI occurrence at a given time (vertical line), from the fractiles, one can estimate the mean μ and the log-normal standard deviation β , (**mood1974introduction**).

$$\mu_{\text{time|DI}} = \ln(\text{time}^{50\%}) \quad (5.2)$$

$$\beta_{\text{time|DI}} \approx \frac{1}{2} \left(\ln(\text{time}^{84\%}) - \ln(\text{time}^{16\%}) \right) \quad (5.3)$$

From these values the lognormal probability density function (PDF) and corresponding cumulative distribution function (CDF) are determined, Fig. 5.16(b).

This last curve, for all practical purposes is the fragility curve of the bridge assessed in terms of the DI of a potentially excessive displacement.

Similar curves could then be determined from other sets of quantities, and engineers could meaningfully and rationally answer such basic and important questions as: A) how long would it take for a certain degradation to occur? or B) what is the degradation likely to occur at a given time. This is the essence of RICA presented in this paper for AAR.

6 — Computational Tools for Probabilistic Analyses

6.1 Introduction

Finite element (FE) method is used for nonlinear analysis of containment structure-foundation coupled system. The family of FE-based programs that are used in this study are:

- Pre-processor: The FE analysis requires the discretization of a structure into a mathematical representation. The discretized structure is then subjected to the governing differential equation with essential (displacement) and natural (traction) boundary conditions. KumoNoSu is a graphical front end to two programs, i.e. 1) T3D a mesh generator, and 2) T3D2Merlin which enables definition of material, boundary conditions and loads.
- Processor: The discretized structure subjected to the essential and natural boundary conditions is then transferred to the main processor (called Merlin) to be analyzed.
- Post-processor: Spider is a general purpose 3D post-processor for static and dynamic nonlinear FE analysis results. It is an OpenGL implementation under Windows.

Figure 6.1 shows the interaction among the three programs and the input/output file(s) for each one. They can be summarized as:

- KumoNoSu uses: 1) `.bd` (includes all geometric information of model), 2) `.t3d` (includes all meshing information), and 3) `.ctrl` (includes material property, boundary condition, loads, analysis information), and generates `.inp` (includes all the nodes, elements, material, loads, boundary condition, analysis information) for processor (Merlin). The generated FE discretization can be saved in the form of `.eps`, `.jpeg`, and `.EMF`.
- Merlin uses `.inp` and generates: 1) `.out` (includes all the requested analysis results), 2) `.pst` (includes post-processing data for regular FE analysis), `.rtv` (includes post-processing data for Real Time View of a lengthy dynamic analysis), and 3) `.eig` (includes post-processing data to display the results of an eigenvalue analysis).
- Spider uses one of `.pst`, `.rtv`, or `.eig` and display the results. Results can be saved in the form of `.eps`, `.jpeg`, and `.EMF`.

6.2 Probabilistic Performance Assessment of Structures

The group of programs in figure 6.1, are only able to perform a single deterministic analysis. To be used within the context of the present thesis, this should be expanded to the probabilistic form. For this purpose,

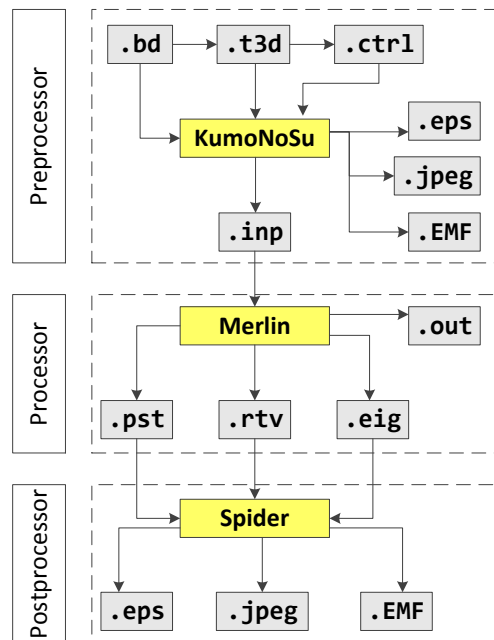


Figure 6.1: Interaction among KumoNoSu, Merlin and Spider

the Matlab-based algorithm is developed. It includes many Matlab scripts and functions facilitates the probabilistic assessment of structures. Figure 6.2 shows the general algorithm of this program and interaction among different programs. This algorithm is applicable for any types of structures and any probabilistic model (load, material, time). This algorithm is briefly explained first. Next, its application in performance based earthquake engineering (PBEE) will explore.

Major steps and features are:

- Use KumoNoSu to build a initial finite element model based on information from physical model. Hypothetical material property or load magnitude may be used in this step to develop a deterministic **test.inp**.
- The generated **test.inp** file is then broken to different sub-blocks, i.e. **Block-10.inp**, **Block-20.inp**, ...; each one includes a specific information about the FE model (e.g. analysis type, nodes, elements, material, loads, boundary condition).
- **P0.m** is used to determine the user-defined input parameters for FE model. This includes: ground motions for dynamic analysis, material property and its distributional model for uncertainty quantification, time-dependent aging and etc.
- **P1.m** uses all input blocks (i.e. **Block-10.inp**, ...) and input data from **P0.m** (**Material.mat**, **GroundMotion.mat**, ...) to generate N new input files, **test-N.inp** which have the desired probabilistic model.
- **P2.m** runs the Merlin N times and generates N **test-N.pst** and **test-N.out** (if requested **test-N.rtv** and **test-N.eig** also) files. Each of the N **test-N.pst** can be separately read by Spider and provide required graphical output.
- **P3.m** uses N **test-N.out** files (in the form of ASCII) and coverts them to **test-N.mat** files (in the form of Binary).

- P4.m further process the N `test-N.mat` files and generates N `ext-test-N.mat` files. This step includes process of the results for a specific structure, define the limit states and etc.
- P5.m uses the N `ext-test-N.mat` files and applies the probabilistic operations on them (e.g. different fractile, regression, probability of exceedance, ...). The final results can be either represented quantitatively (tabulated or central values) or graphically. Currently, this program uses one of the 1) Matlab, 2) ParaView, or 3) Ansys to show the contour plots on the FE model.

6.3 Detailed Steps

Each of the general scripts, i.e. P0.m to P5.m are explained in the context of PBEE.

6.3.1 P0.m

This script provides a set of appropriate ground motions to be used in dynamic analyses. The general steps and feature are:

- Select the type of the performance assessment: 1) intensity-based performance assessment (IBPA) assuming that the dam is subjected to a specific intensity of shaking (e.g. specific target response spectrum), 2) scenario-based performance assessment (SBPA) assuming that the dam is subjected to a specific $\langle R_{rup}, M_w \rangle$ scenario (earthquake intensity is uncertain parameter), and 3) time-based performance assessment (TBPA) assuming the uncertainty in R_{rup} , M_w and the intensity of motion.
- Select between the real (recorded) ground motions and the synthetic one (which is suitable for dam sites that there is no enough recorded signals).
- In the case of real ground motions, either use the direct ground motion selection through PEER online tool, or use a set of Matlab codes developed by Baker research group. In both cases, the selected ground motions are saved in the form of `GMList.xlsx`. The same procedure should be performed for synthetic ground motions.
- The selected ground motions can be truncated (e.g. [5%, 95%] A_I , or [5%, 75%] A_I) using `GM.Truncat.m`.

6.3.2 P1.m

Figure 6.4 shows different types of uncertainty analysis can be performed. Three sources of uncertainty in performance assessment of structures are:

- Mechanical (material): For an existing containment vessel structure, this refers to uncertainty in determination of material property and also different random variables (RV) in the constitutive model.
- Seismic: Refers to record-to-record variability of the input ground motions. Should be quantified based on seismic hazard curve.
- Time: Refers to time-dependent degradation of the material, e.g. alkali-aggregate reaction and creep.

1st degree uncertainty refers to incorporating only one of the three sources. Subsequently, 2nd and 3rd degree uncertainty refer to simultaneous effect of two or three uncertainty source.

Seismic analysis is performed in two steps: 1) static analysis with all the body forces and hydrostatic one, and 2) through a “restart”, a dynamic analysis is initiated from the preceding static one. Thus, two set of `.inp` and `.out` files will generate for each analysis. Hereafter, the static input file corresponds to N^{th} analysis refers to `test-N_dyn1.inp` and the dynamic one refers to `test-N_dyn2.inp`.

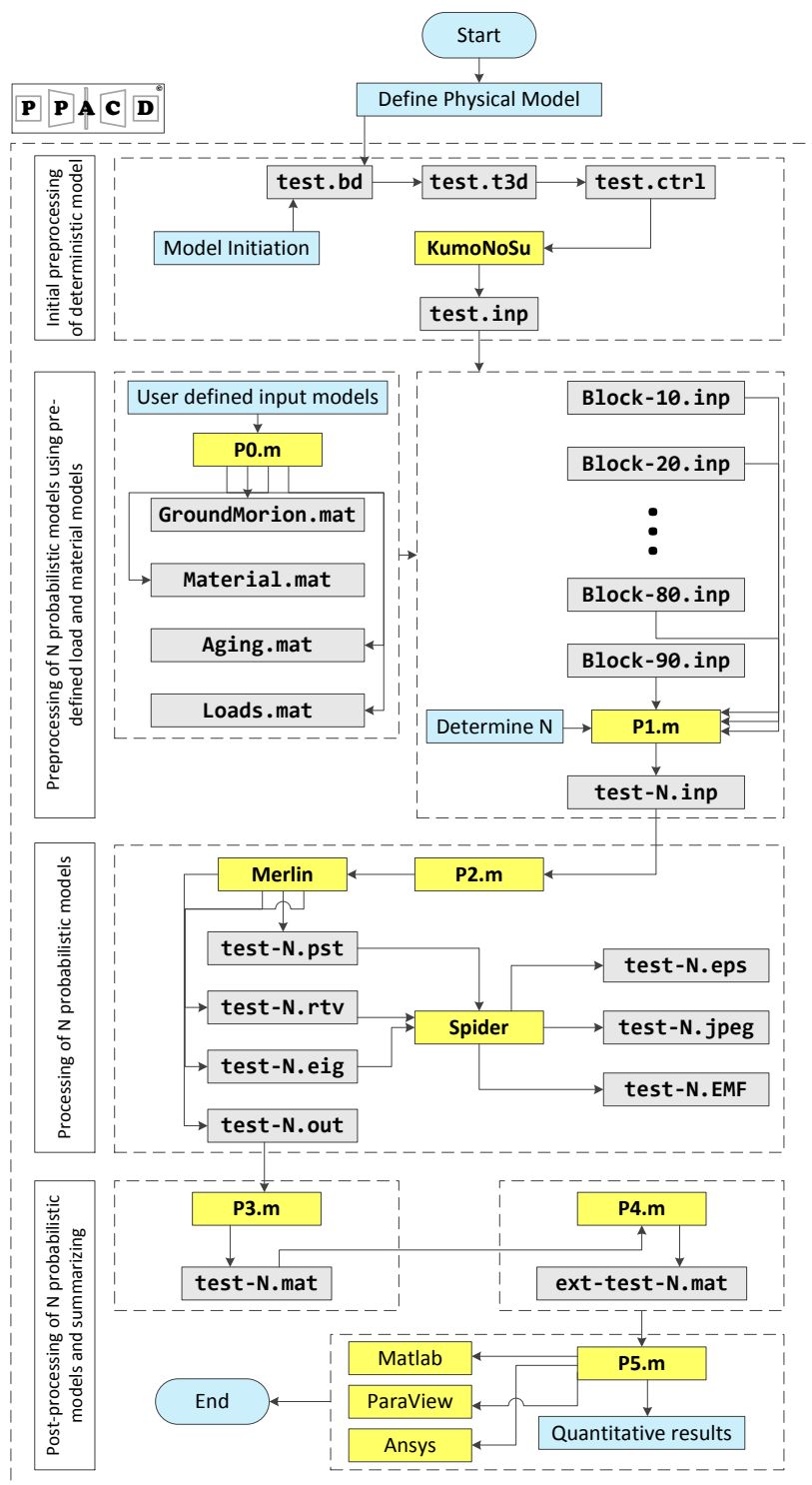


Figure 6.2: Interaction among different programs in Matlab-based code

Figure 6.5 shows the general algorithm to generate input files for static analysis. Based on figure 6.2, the initially generated input file should break into different sub-blocks as:

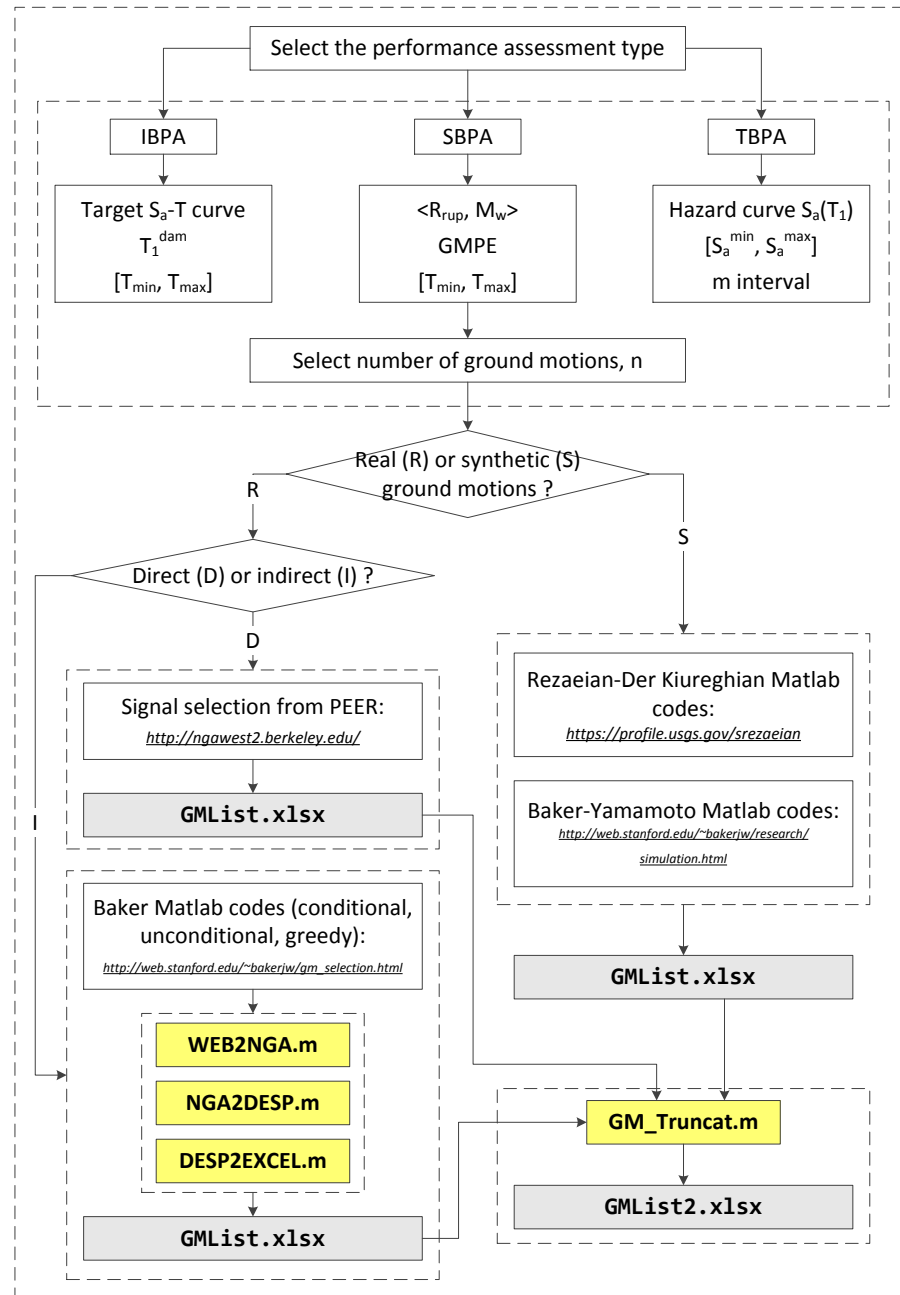


Figure 6.3: General algorithm in P0.m

- Block-Sta-10.inp: title and definition
- Block-Sta-20.inp: control block, includes number of increments, ...
- Block-Sta-30.inp: element group, includes element types and material property
- Block-Sta-40.inp: mesh group, includes nodal mass and damping, master/slave crack
- Block-Sta-50.inp: analysis control, includes iterations, error, ...
- Block-Sta-60.inp: body forces

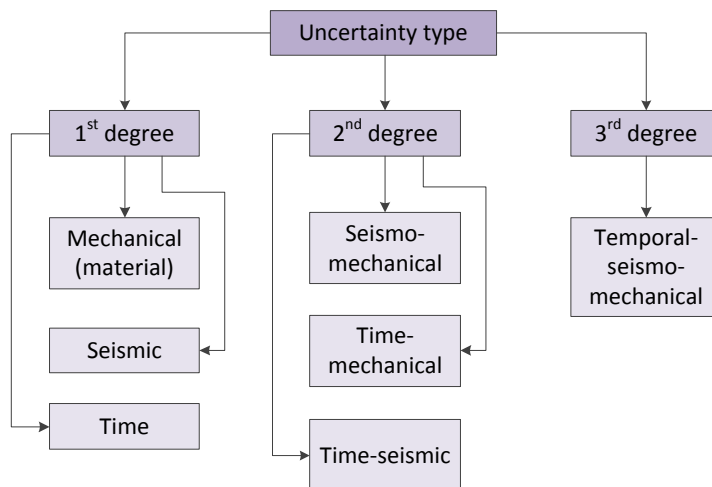


Figure 6.4: Different types of uncertainties in PPACD

- Block-Sta-70.inp: uplift model (if any)
- Block-Sta-80.inp: displacement boundary condition
- Block-Sta-90.inp: hydrostatic pressure (if any)

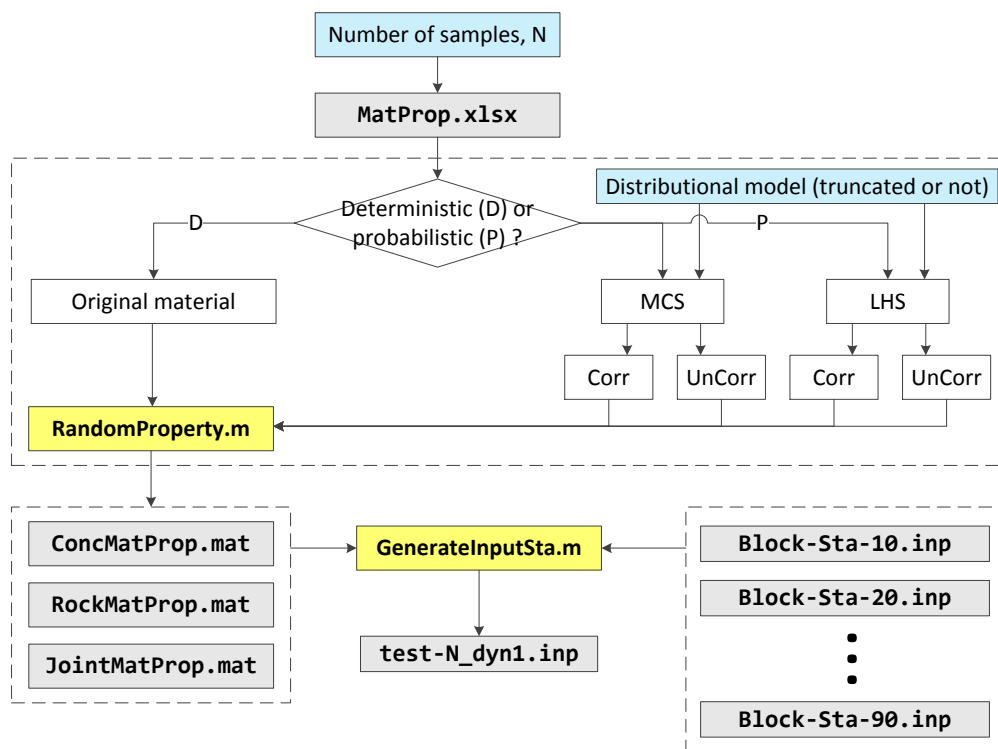


Figure 6.5: General algorithm in P1Sta.m

In figure 6.5, `RandomProperty.m` reads a user defined Excel file storing relevant data for the probabilistic based simulation and then generates N samples based on either crude Monte Carlo Simulation (MCS) or Latin Hypercube Sampling (LHS), Figure 6.6. In both cases the correlated or uncorrelated modes are

	NRV	RandType	Mean	COV	Activation	STD	BoundLimit	LowerB	UpperB	Property	Unit
Concrete	1	Normal	1	0.2	0	0	0.5	0	0	Thickness	m
Concrete	2	Normal	2.40E-06	0.05	0	0	0.5	0	0	Mass density	Gg/m^3
Concrete	3	Normal	9.90E-06	0.2	0	0	0.5	0	0	Coefficient of thermal expansion	1/C^o
Concrete	4	Normal	36,000	0.2	1	7,200	0.5	18,000	54,000	Elastic/Young's modulus	Pa
Concrete	5	Normal	0.2	0.2	0	0	0.5	0	0	Poisson's ratio	-
Concrete	6	Normal	0	0.2	0	0	0.5	0	0	Fracture toughness (LEFM)	
Concrete	7	Normal	0	0.2	0	0	0.5	0	0	Critical energy release rate (LEFM)	
Concrete	8	Normal	5,000,000	0.15	1	750,000	0.5	2,500,000	7,500,000	Tensile strength	Pa

(a) Concrete properties

	NRV	RandType	Mean	COV	Activation	STD	BoundLimit	LowerB	UpperB	Property	Unit
AAR	1	Normal	1	0.2	0	0	0.5	0	0	Model No.	-
AAR	2	Normal	0.005	0.2	1	0.001	0.5	0.0025	0.0075	Maximum volumetric strain	-
AAR	3	Normal	10.97	0.2	1	2.1932	0.5	5.483	16.449	Characteristic time	ATU
AAR	4	Normal	87.16	0.2	1	17.43	0.5	43.58	130.75	Latency time	ATU
AAR	5	Normal	5,400	0.2	0	0.0	0.5	0.0	0.0	Activation energy for char	°K
AAR	6	Normal	9,400	0.2	0	0.0	0.5	0.0	0.0	Activation energy for lat	°K
AAR	7	Normal	0.1	0.2	0	0.0	0.5	0.0	0.0	Residual red. Factor tension	-
AAR	8	Normal	0.8	0.2	0	0.0	0.5	0.0	0.0	Fraction of tension pre-AAR	-
AAR	9	Normal	-58.7	0.2	1	-11.74	0.5	-29.35	-88.05	Compressive strength	MPa
AAR	10	Normal	5.9	0.2	1	1.18	0.5	2.95	8.85	Tensile strength	MPa
AAR	11	Normal	-2.0	0.2	0	0	0.5	0	0	Shape factor for Gamma_c	-
AAR	12	Normal	10.1	0.2	1	2.02	0.5	5.05	15.15	Reference temperature test	°C
AAR	13	Normal	-8.0	0.2	0	0.0	0.5	0.0	0.0	Upper comp. stress limit	MPa
AAR	14	Normal	0.69	0.2	1	0.138	0.5	0.345	1.035	Reduction factor Young	-
AAR	15	Normal	0.48	0.2	1	0.096	0.5	0.24	0.72	Reduction factor tensile	-

(b) AAR properties

Figure 6.6: User defined Excel file with distribution models, mean, standard deviation and L/U bounds.

possible, Figure 6.7. Sampling is based on predefined distributional model (e.g. normal, lognormal, ...) by

NRV	1	2	3	4	5	6	7	8	9	10	11	12	13	14	15
1	1														
2	0	1													
3	0	0	1												
4	0.2	0	0.5	1											
5	0	0	0	0	1										
6	0	0	0	0	0	1									
7	0	0	0	0	0	0	1								
8	0	0	0	0	0	0	0	1							
9	0.8	0	0	0.5	0	0	0	0	1						
10	0	0	0	0	0	0	0	0	0.8	1					
11	0	0.5	0	0	0	0	0	0	0	0	1				
12	0	0	0	0	0	0	0	0.1	0	0	0	1			
13	0.4	0	0	0	0.7	0	0	0	0	0	0	0	1		
14	0	0	0	0	0	0	0	0	0	0	0	0.4	0	1	
15	0	0	0	0	0	0	0	0	0	0.3	0	0	0	0.7	1

Figure 6.7: User defined Excel file with possible correlation coefficients.

user for each RV. Moreover the upper and lower bounds can be defined to truncate the distributional model.

Figure 6.8(a) shows 500 samples for each of three RVs based on LHS. There is a weak correlation between Mat_1 and Mat_2 and also Mat_1 and Mat_3 ; however, the correlation is strong between Mat_2 and Mat_3 . On the other hand, figure 6.8(b) shows an un-symmetry truncation of a normal distribution in the range [18, 38] GPa.

Figure 6.9 shows the general algorithm to generate input files for dynamic analysis. Similar to static analysis, figure 6.9, there are nine blocks define the `test-N_dyn2.inp`; however, some of them are empty

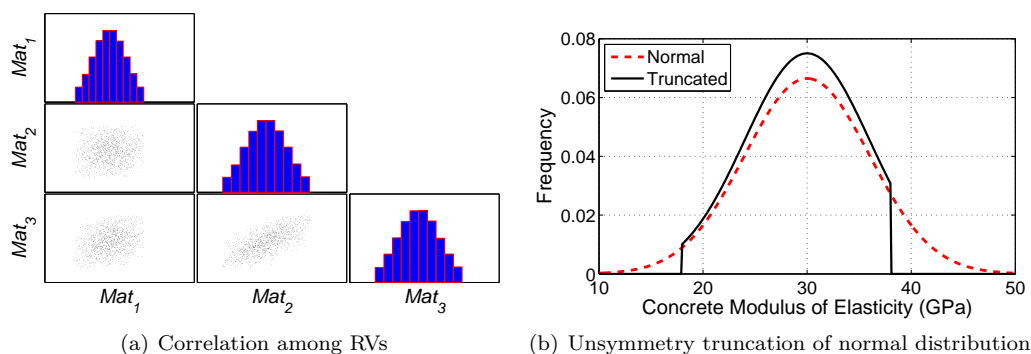


Figure 6.8: Sampling the material properties based on algorithm in figure 6.5

in dynamic analysis (e.g. material, mesh) because they already defined through the static input file. User selects the type of dynamic analysis and a **Groundmotion.mat** file is generated includes all the required seismic input with their specifications. Five types of analysis are:

- Single ground motion (SGM): only a single ground motion is used for the all N samples. If $N = 1$, this results to single deterministic analysis, and if $N = \text{“large number”}$ this is either sensitivity or material uncertainty assessment.
- Cloud analysis (CLA), figure 6.10(a): N (un-scaled) ground motions are applied to N samples. If all the samples have same characteristics, this method only shows the record-to-record variability. However, if samples are different, it accounts for epistemic uncertainty also.
- Endurance time analysis (ETA), figure 6.10(b): Only three samples are required for three acceleration functions.
- Multiple stripe analysis (MSA), figure 6.10(c): N ground motions are applied in m level ($n=N/m$ for each level).
- Incremental dynamic analysis (IDA), figure 6.10(d): N ground motions are incrementally scaled in N/n levels and applied to dam.

6.3.3 P2.m

Having the $2N$ input files (static + dynamic), **P2Sta.m** and **P2Dyn.m** are executed, sequentially. They run the Merlin (main processor) $2N$ times and generate **test-N_dyn1.out** and **test-N_dyn2.out**. Note that **test-N_dyn1.out** is used as part of input file for dynamic analysis.

6.3.4 P3.m

P3Dyn.m converts N **test-N_dyn2.out** ASCII files to **test-Dyn-N.mat** Binary files. **P3Dyn.m** is computationally expensive especially for long duration ground motions with small time step. It can be run on both PC and supercomputer (CU's 184-teraflop Dell supercomputer called Janus is used for some of the analyses; it is currently ranked 164 among the world's top-500 supercomputer sites).

6.3.5 P4.m

P4Dyn.m processes the raw data from N **test-Dyn-N.mat** files and generates N **ext-test-Dyn-N.mat** files. In the context of PBEE, two major set of post-processing are required: 1) processing the ground motion

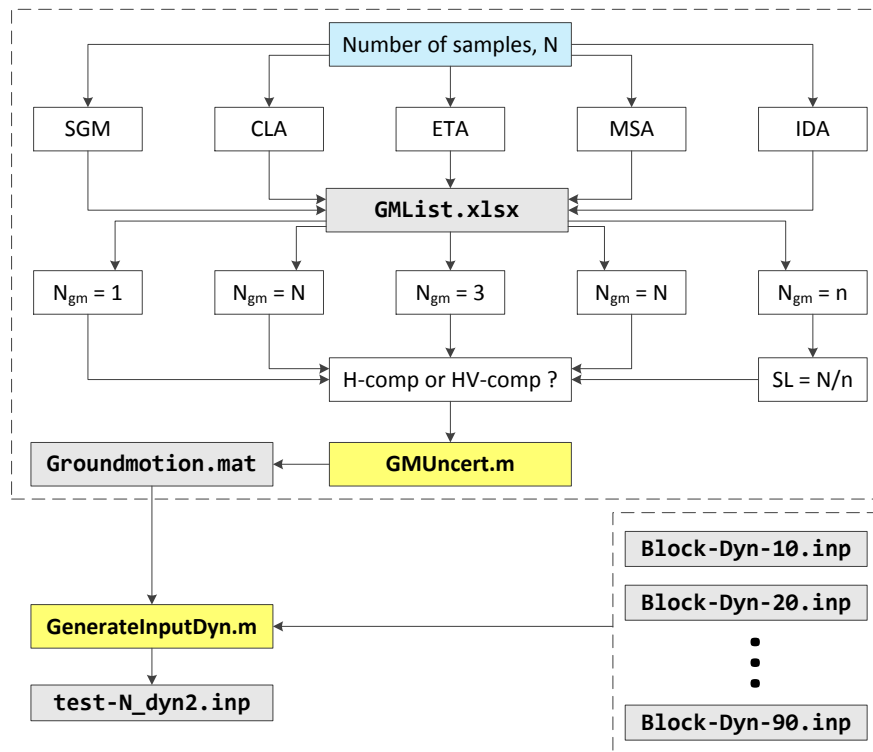


Figure 6.9: General algorithm in P1Dyn.m

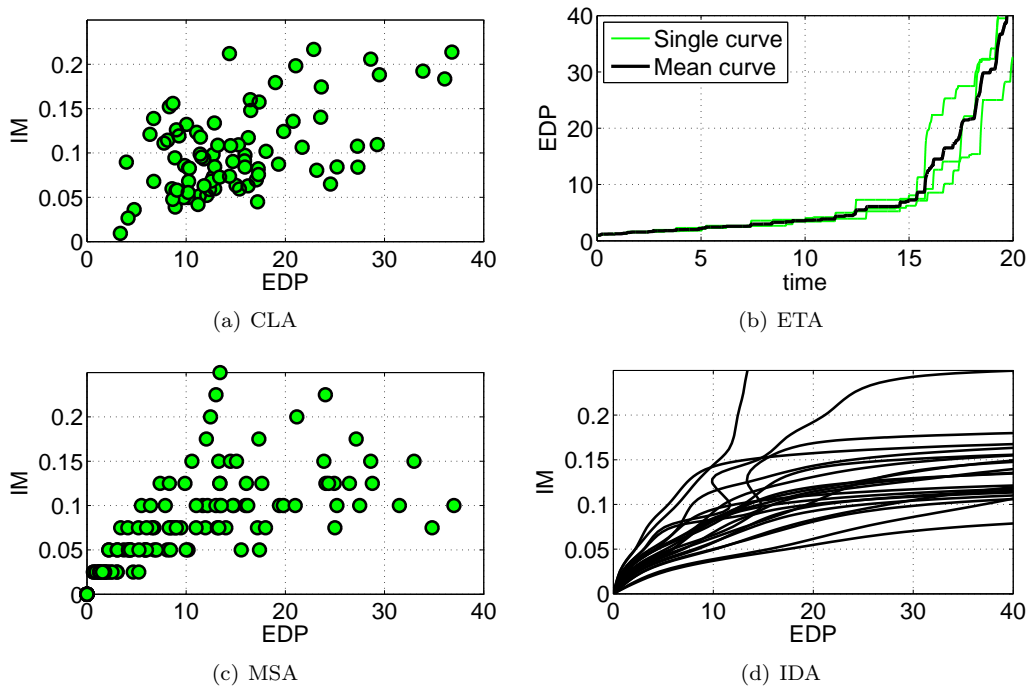


Figure 6.10: Different types of dynamic analysis methodologies in PPACD

intensity measures (IM), and 2) processing the engineering demand parameter (EDP). Figure 6.11 shows the seven category of IMs that are computed for any ground motion in P4Dyn.m. For each category, there are several individual IMs that will be explained later.

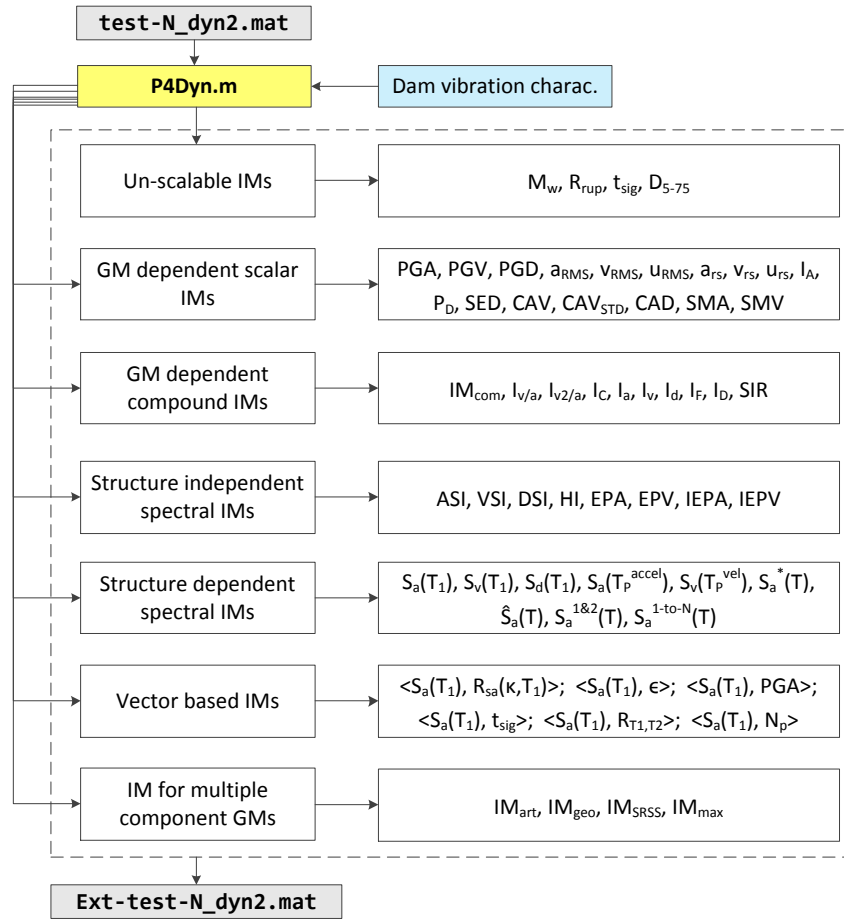


Figure 6.11: Treatment of IMs in P4.m

6.3.6 P5.m

P5.m uses N ext-test-Dyn-N.mat files and applies the probabilistic operations which depends on the type of analysis:

- CLA:
 - Determination of histograms and best fit to IM parameters
 - Determination of optimal IM in terms of efficiency, sufficiency, proficiency, and practicality
 - Determination of optimal vector IM
 - Determination of fragility curves and surfaces
- IDA:
 - Determination of capacity curves
 - Summary of capacity curve into central values and fractiles

- Determination of optimal IM parameter
- Determination of fragility curves

This page intentionally left blank.

7— Numerical Modeling for Seismic Analysis

7.1 Deconvolution

Deconvolution, addressed in section 3.1 can be complex to account for in commercial finite element code.

The procedure captured by Figure 3.5 and equations 3.11-3.13 are automated in Merlin's postprocessor Spider (**spider**) as shown in figure 7.1.

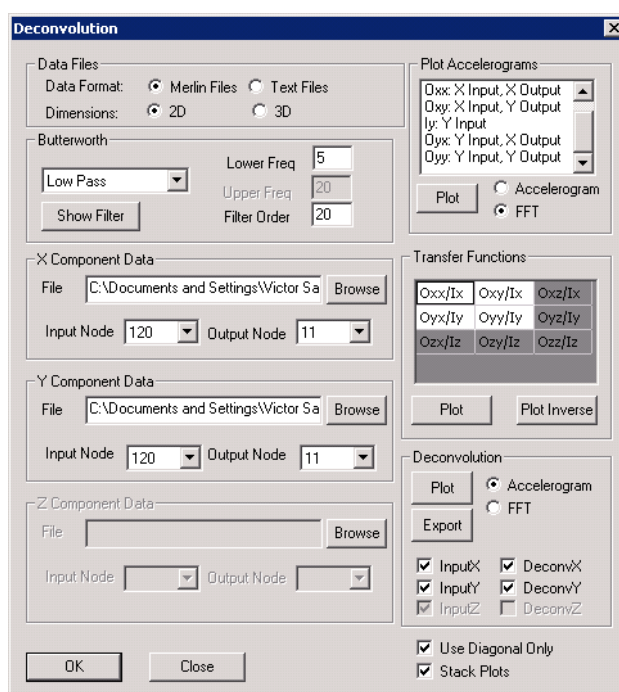


Figure 7.1: Deconvolution feature in Merlin

7.1.1 Example

Consider a structure on a foundation which is extended about three times of the structure's height in all directions. Using this applied feature in Merlin, figure 7.1, first, the recorded ground excitation (at the base of the structure) is applied at the base of the foundation and analyzed, figure 7.2. The Transfer functions

and their inverse are shown in figure 7.4. The deconvoluted signals are then computed, figure 7.3. The input signal and the deconvoluted ones are then compared, figure 7.5. Finally, we re-analyze the structure subjected to the deconvoluted signal, and we compare the computed accelerations at the base of the structure with those recorded, figure 7.6.

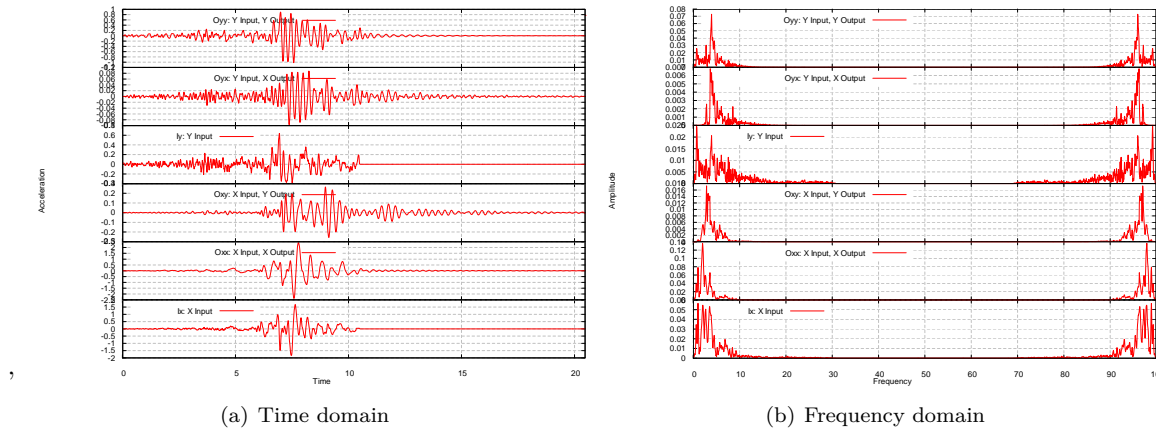


Figure 7.2: Accelerograms of the input and output

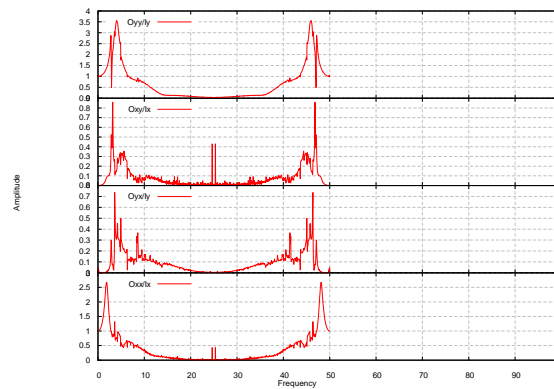


Figure 7.3: Transfer functions

7.2 Preliminary Considerations

7.2.1 Mass and Gravity

In all subsequent analysis, all material group are assigned a mass.

Gravity (which is a load) is also applied to all groups except the foundation.

7.2.2 Two Step Analysis

In the context of a seismic analysis (specially in the presence of potential non-linearities) a two step analysis must be performed.

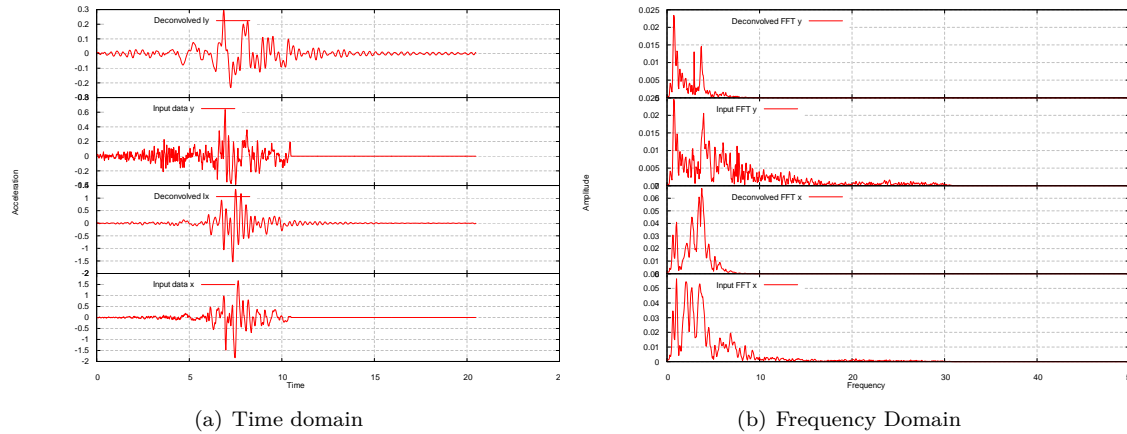


Figure 7.4: Deconvoluted signals

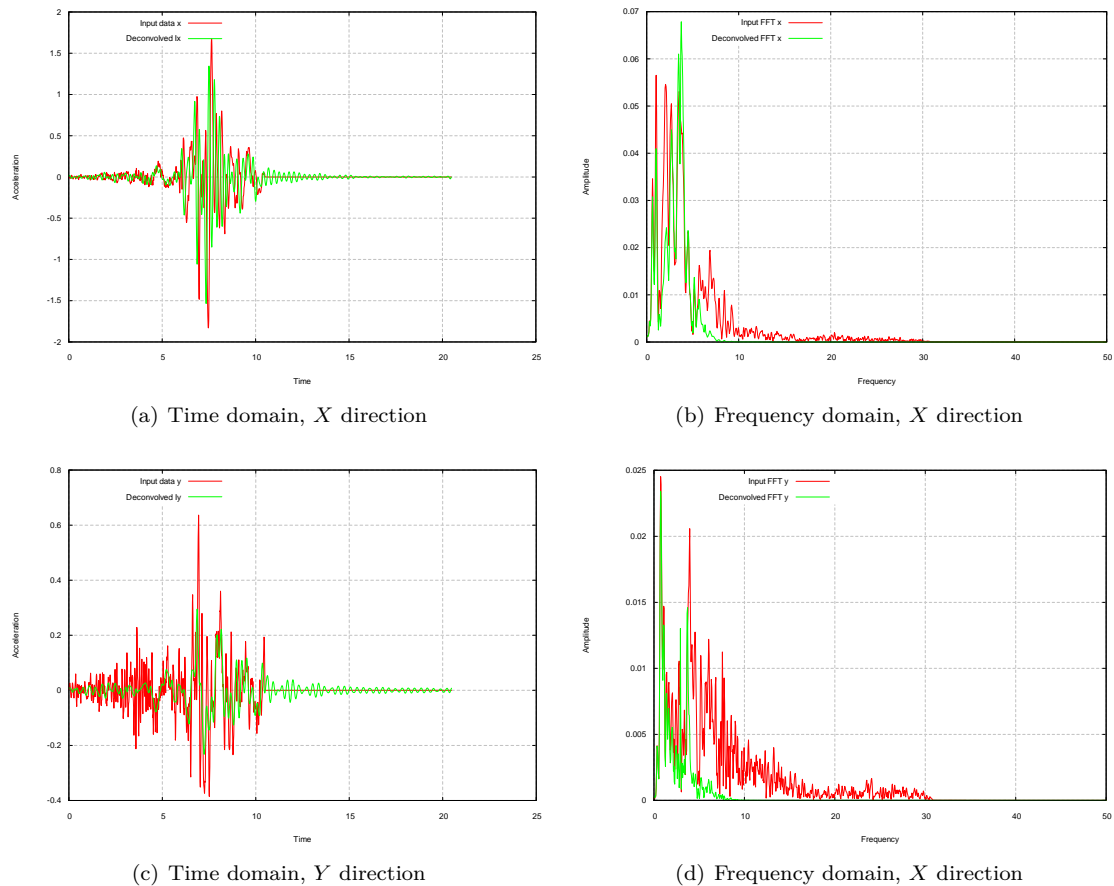


Figure 7.5: Comparison between original and deconvoluted signals

First a static on which takes into account the effects of all dead loads (gravity and others), and possible live load likely to be present during an earthquake. It should be noted that for (numerical) stability the mesh has to have constraints in all directions to prevent rigid body motion. Results are typically saved in a disk file.

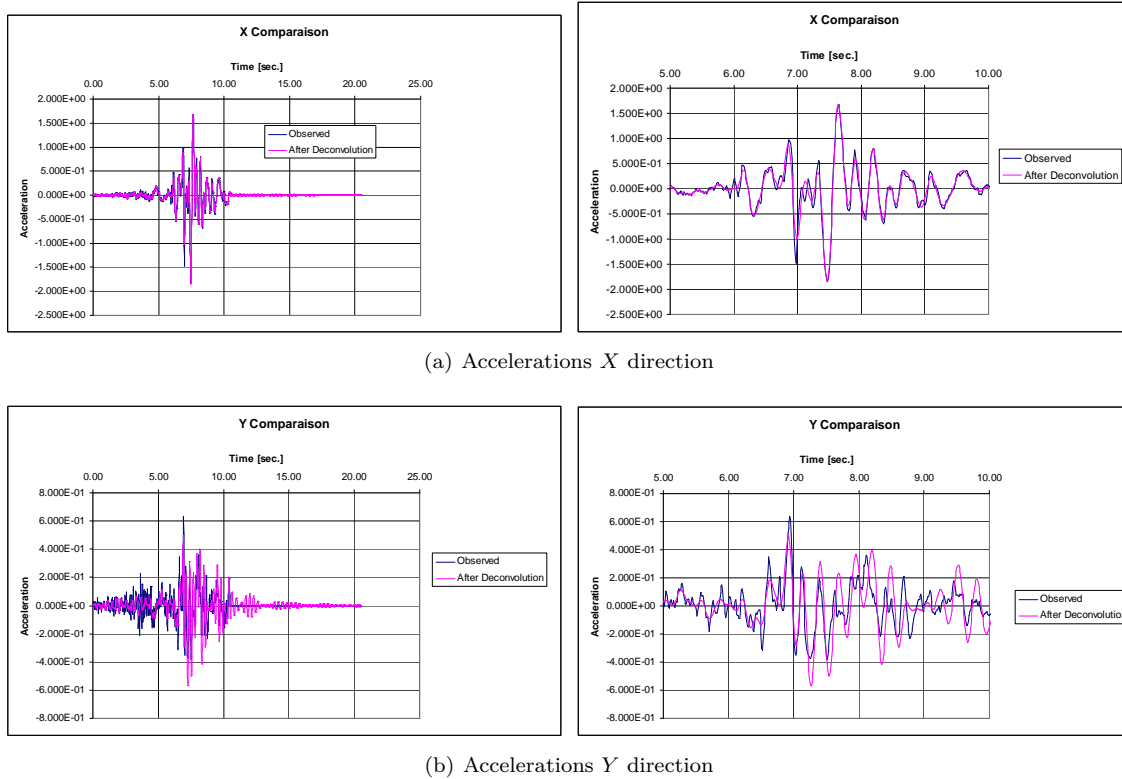


Figure 7.6: Results of deconvolution analysis

The mesh will then have to be modified to allow lateral displacements, and a dynamic analysis can start by reading the saved disk file (with the internal state variables). AT this point, it is recommended to reset all displacements to zero (without altering the initial state of stress) in order to facilitate visualization of the deformed shape (ZerroDisp).

7.2.3 Lateral Rigid Body Motion

In a dynamic analysis there is no lateral restraint as excitation is applied along this direction. As a result, visualization of deformed shapes can be problematic as the mesh is likely to undertake a rigid body motion (without loss of fidelity as the internal stresses are a function of relative displacements).

However, in a graphical post-processor this makes it difficult to visualize the deformed shape as the rigid body motion is of such a magnitude to obliterate the relative displacements.

A simple remedy to this is the insertion of lateral springs to greatly limit the rigid body motion.

In the context of Merlin/Kumo, this is automatically achieved through

$$K = \frac{EA}{t} \quad (7.1)$$

where E , A and t are the elastic modulus of the adjacent material, the tributary area of each node, and the equivalent thickness of a virtual adjacent foundation. Note that all quantities are automatically determined except for the last one.

Alternatively, user could specify directly the stiffness k .

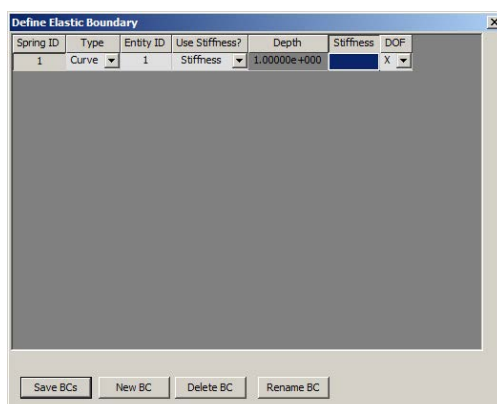


Figure 7.7: Insertion of springs to mitigate rigid body motions in a dynamic analysis

7.2.4 Rocking

Rocking can be a major issue in the dynamic analysis of massive concrete structure, yet it is not often addressed.

There are two causes for what is loosely referred to as rocking:

1. Concrete Rock Interface
2. Finite size of the foundation.

7.2.4.1 Foundation Support

If the foundation (finite size, non zero mass, zero gravity) is modeled, then the lateral inertial force will induce a “parasitic” alternating overturning moment which may not be negligible. Hence, in the context of a finite element model, the foundation support will restrain vertical displacement in both the upward (undesirable) and downward (desirable) directions. Hence, parasitic vertical elastic waves may result, Figure 7.8(a). Figure 7.8(a) highlights the issue.

A solution to this problem is the twofold analysis. First static load is applied with vertical supports. Then, prior to the restart of the dynamic analysis, the supports are all removed, and replaced by forces equal to the corresponding reactions. Indeed, in the context of a dynamic analysis (and contrarily to a static one), it is perfectly possible to omit any support.

In Merlin this process is automated through the commands:

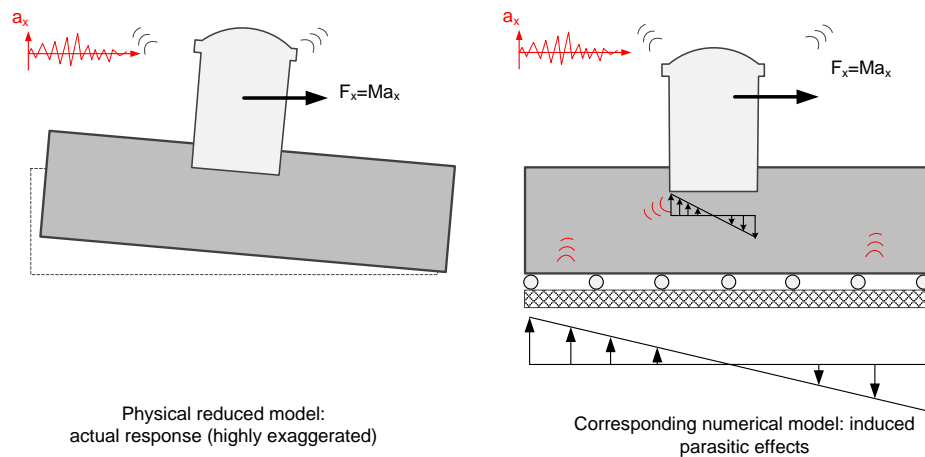
1. **SaveReacts** which saves all the reactions at a given increment into a separate external ascii data file.
2. **Reacts2Loads** within a (subsequent) increment will read the external file, and apply those reactions as nodal forces for the current increment.

7.2.4.2 Concrete-Rock Interface

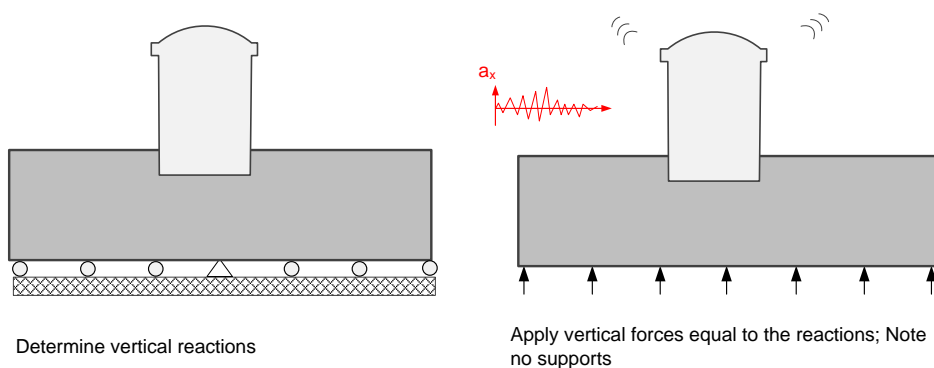
The one caused by the potential separation between the NCVS’ and the foundation though, Figure 7.9.

This would rarely occur due to the large weight of the NCVS but may be a controlling factor for strong seismic records.

This problem can be mitigated by insertion of either zero thickness joint elements or special springs along the concrete-rock interface. The most general formulation for the joint element is the one of **saouma96efm2**.



(a) The problem



(b) Mitigation

Figure 7.8: Rocking due to finite size foundation support

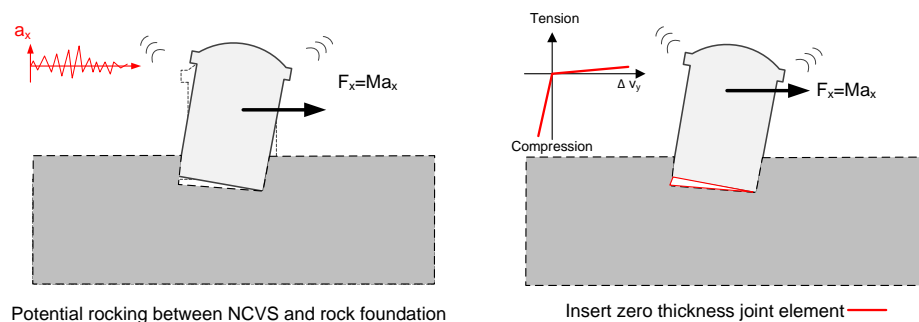


Figure 7.9: Rocking due to concrete-rock interface

Alternatively, the spring elements would have a very large stiffness in compression, and a negligibly small one in tension.

7.3 Modeling Soil Structure Interaction

Soil structure interaction is a term which came to encompass the interaction between structure and soil, as well as the dynamic interaction between foundation and the free field. Both will be separately addressed.

7.3.1 Soil-Structure

Static Model has traditionally (and most simplistically) been modeled by discrete independent linear elastic springs where the elastic pressure deflection is simply $p = kw$ where p , k and w are the pressure, the coefficient of subgrade modulus, and the deflection respectively (**winkler1867**). This model is not suited for dynamic analysis (unless different stiffnesses are assigned in tension and compression).

Joint Elements to which finite tensile strength can be assigned. They are better suited for a dynamic analysis as they may open and close, and the localized displacements can be tuned in by the element own stiffness in both compression and shear, **saouma96efm2**. For the analysis of a NCVS such elements are placed on the side of the structure.

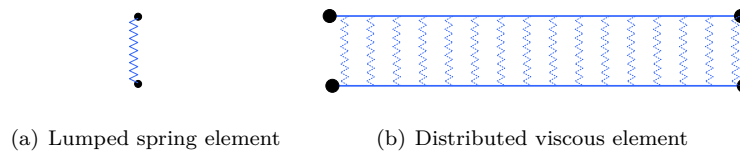


Figure 7.10: Spring joint element

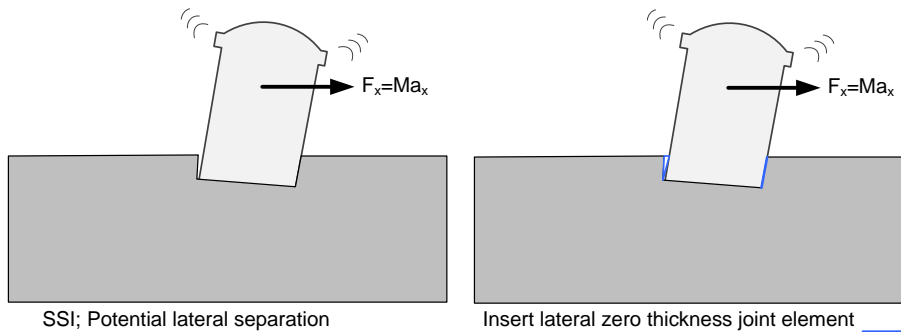


Figure 7.11: SSI: Concrete-Rock Interaction

7.3.2 Rock-Rock

Soil structure interaction has been covered in some details in section 3.2.

In the context of seismic analysis, too often is the foundation modeled as massless. This is only correct if the elastic moduli of concrete and foundation are nearly similar. Otherwise, soil structure interaction can not be ignored.

Conceptually, this is simple, yet its implementation can be challenging, particularly if rocking (discussed above) is to be avoided. The 8 possible implementations, shown in Table 7.1 will be considered and addressed

separately.

Criteria	1	2	3	4	5	6	7	8
Rocking	Y	Y	Y	N	N	Y	N	N
Radiation Damping	N	Y	Y	Y	Y	Y	Y	Y
Free Field	N	N	N	N	N	Y	Y	Y
Vertical Excitation	N	N	N	Y	Y	N	N	N
Gravity Load Transfer	N	N	N	Y	Y	N	Y	Y
Rigid Body Motion	Y	Y	N	Y	N	N	N	N

Table 7.1: Evaluation of Various Boundary Conditions

7.3.3 Model 1

This first model, Fig. 7.12, is by far the simplest, however rocking will occur and t

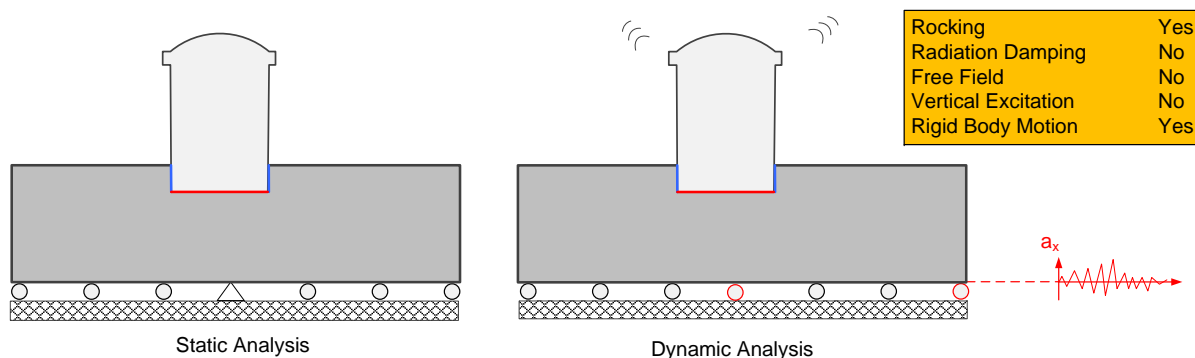


Figure 7.12: Soil structure interaction model 1

7.3.4 Model 2

Fig. 7.13

7.3.5 Model 3

Fig. 7.14

7.3.6 Model 4

Fig. 7.15

7.3.7 Model 5

Fig. 7.16

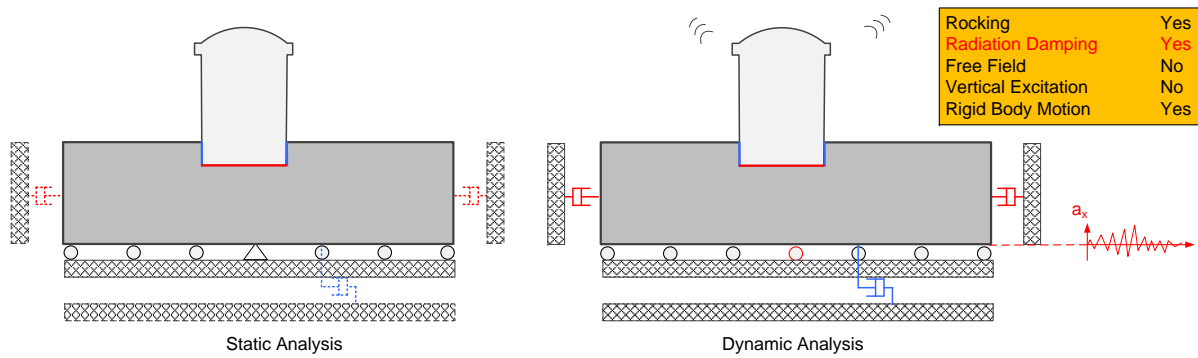


Figure 7.13: Soil structure interaction model 2

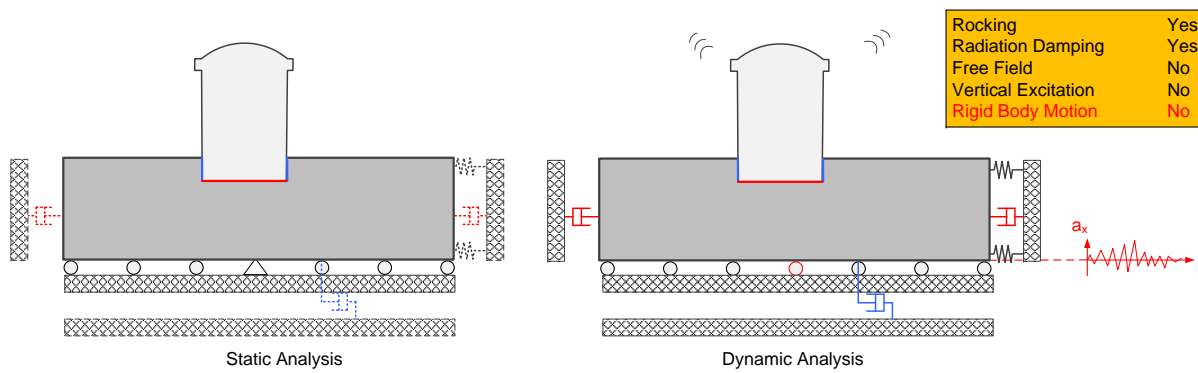


Figure 7.14: Soil structure interaction model 3

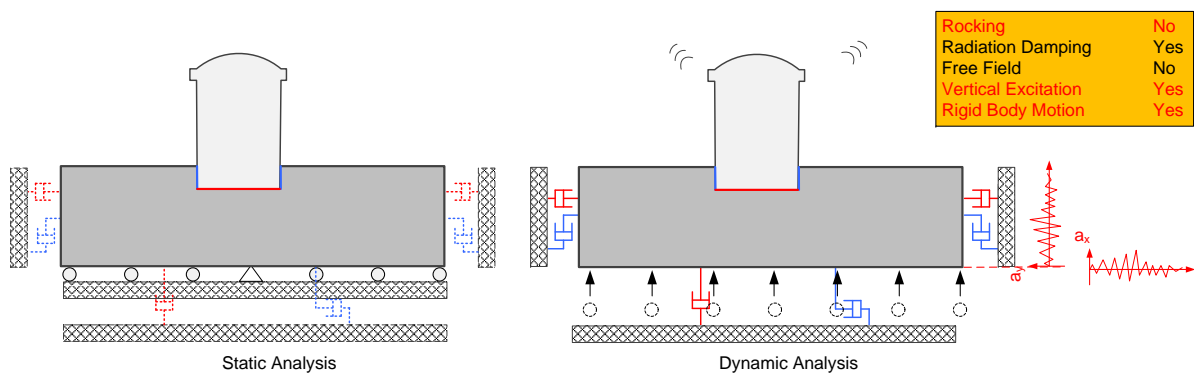


Figure 7.15: Soil structure interaction model 4

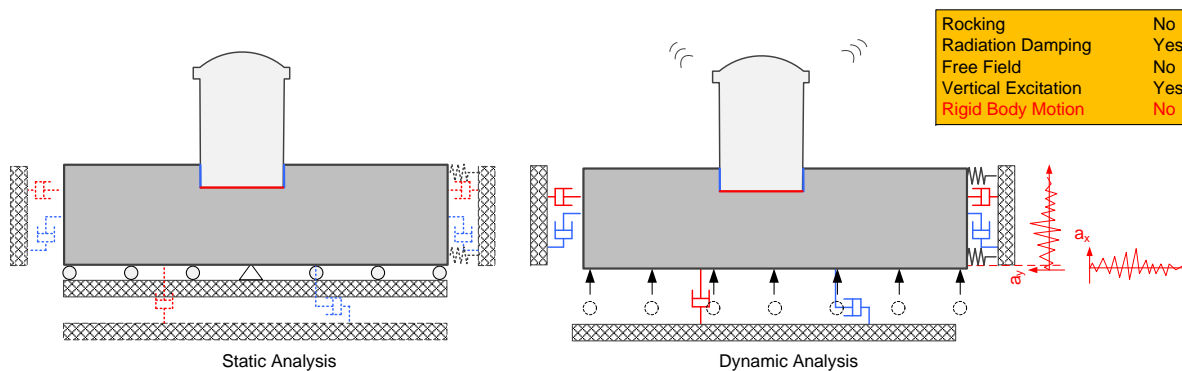


Figure 7.16: Soil structure interaction model 5

7.3.8 Model 6

Fig. 7.17

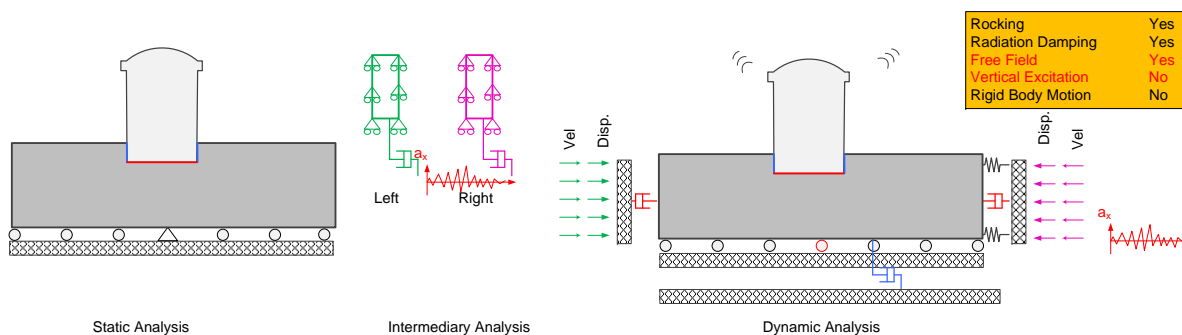


Figure 7.17: Soil structure interaction model 6

7.3.9 Model 7

Fig. 7.18

7.3.10 Model 8

Fig. 7.19

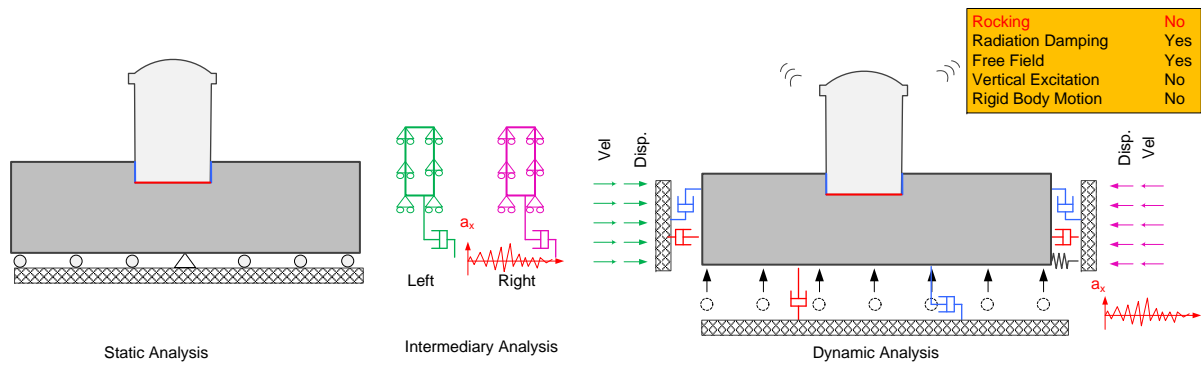


Figure 7.18: Soil structure interaction model 7

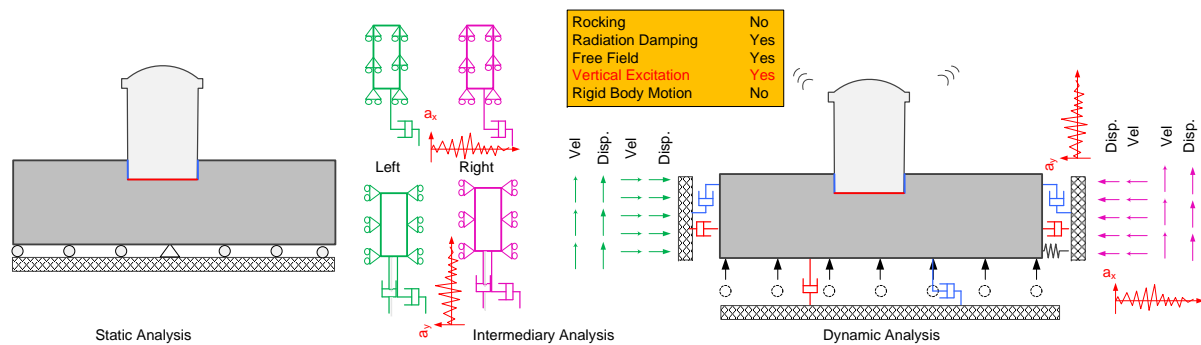


Figure 7.19: Soil structure interaction model 8

This page intentionally left blank.

8 — Modelling AAR

8.1 Introduction

Selection of AAR material properties, described in Section 4.3 can be confusing and is thus separately addressed here.

For each of the material group with AAR expansion the following data must be specified

1. ID_{group} Group ID.
2. $\varepsilon^\infty|_{T=T_0^{test}}$ Maximum volumetric strain at temperature T_0^{test} .
3. $\tau_C(\theta_0^{test})$ Characteristic time at temperature $\theta_0^{test} = 273 + T_0^{test}$.
4. $\tau_L(\theta_0^{test})$ Latency time at temperature $\theta_0^{test} = 273 + T_0^{test}$.
5. U_C Activation energy associated with $\tau_C(\theta_0^{test})$ (suggested value 5,400 K).
6. U_L Activation energy associated with $\tau_L(\theta_0^{test})$ (suggested value 9,400 K).
7. Γ_r Residual reduction factor for Γ_t .
8. γ_t Fraction of f_t prior to reduction of AAR expansion due to macro cracking.
9. f_c Compressive strength (must be negative).
10. f_t Tensile strength.
11. a Γ_2 Shape parameter (0. for straight line).
12. T_0^{test} Reference temperature ($^{\circ}\text{C}$) of tests for τ_L and τ_C .
13. σ_U Upper compressive stress beyond which there is no more AAR expansion; must be negative.
14. β_E Reduction fraction for Young's Modulus when AAR reaction ends.
15. β_f Reduction fraction for tensile strength when AAR reaction ends.

Broadly put, the data fall into one of two broad categories:

Group I are parameters which are highly dependent of the concrete and can be numerically inferred from the concrete physical properties.

Group II are those which could have been hard-wired into the model, but a lack of sufficient microscopic understanding of the concrete would compel the analyst to use “engineering judgment” to assess them.

Category, symbol, unit, and indicative values for each one of them is shown in Table 9.2.

8.2 Kinetics Related Variables

AAR, as all chemical reactions, is temperature and time dependent through the Arrhenius law. As a starter, one needs to have the reference latency and characteristic times $\tau_L(T_0)$, $\tau_c(T_0)$ in terms of the reference temperature T_0 of the tests from which these values were extracted. This is the starting point.

Table 8.1: Characteristics of the ASR model. ATU: arbitrary time unit

Parameter	Category	Symbol	Unit	Value
Reference temperature	I	T_0^{test}	°C	35
Maximum volumetric expansion at T_0^{test}	I	ε_{ASR}^∞	-	0.1%, 0.2% 0.3%
Characteristic time at T_0^{test}	I	τ_C	ATU	7.58
Latency time at T_0^{test}	I	τ_L	ATU	17.71
Activation energy for τ_C	I	U_C	K	5,400
Activation energy for τ_L	I	U_L	K	9,400
Residual reduction factor	II	Γ_r	-	0.5
Fraction of ε_t prior to reduction of ASR expansion due to macro cracking	II	γ_t	-	0.5
ASR expansion annealing stress	I	σ_U	MPa	-8
Post-ASR residual relative Young modulus	II	β_E	-	70%, 90%
Post-ASR residual tensile strength	II	β_{ft}	-	70%, 90%

8.2.1 Temperatures

Distinction must be made between relative temperature (with reference to “casting” one) and actual temperature (ΔT and T).

The former has no impact on AAR but impacts thermal stresses through the coefficient of thermal expansion α .

The later is the actual temperature at a Gauss point in the finite element. Typically it will have a spatial and temporal dependency, i.e. $T = T(x, y, z, t)$ and will be needed to compute the corresponding latency and characteristic times. User may input temperature distribution for different time steps in terms of spatial coordinates. Melin will internally perform the appropriate interpolation. Temperatures in turn may be obtained from a transient linear heat transfer analysis of the structure itself.

8.2.2 Latency and characteristic times

Then, the actual values are then transformed to $\tau_L(T)$, $\tau_C(T)$ at arbitrary temperature T at a given point in the finite element analysis¹. Transformation performed through Eq. 4.7:

$$\begin{aligned}\tau_L(T) &= \tau_L(T_0) \exp \left[U_L \left(\frac{1}{T} - \frac{1}{T_0} \right) \right] \\ \tau_C(T) &= \tau_C(T_0) \exp \left[U_C \left(\frac{1}{T} - \frac{1}{T_0} \right) \right]\end{aligned}\tag{8.1}$$

8.2.3 Activation energies

Activation energies for τ_L and τ_C have long been assumed to be universal concrete properties and are given by Eq. 4.9

$$\begin{aligned}U_L &= 9,400 \pm 500K \\ U_C &= 5,400 \pm 500K\end{aligned}\tag{8.2}$$

However, recent studies by **Katayama2016** show that both the activation energies are highly depend on the rock type and expansive model (i.e. early- moderate or late-expansive). Table 8.2 summarizes available activation energies along with estimated τ_L , τ_C and ε^∞ at two different temperatures.

¹This implies a transient thermal analysis may have to be performed prior to the stress analysis in order to get the spatial and temporal distribution of the temperature $T(x, y, z, t)$.

Table 8.2: Activation energy for different rock types (adapted from Katayama)

Sample			Activation Energy		Sigmoid Curve at 38 oC			Sigmoid Curve at 60 oC		
Expansive	Rock	Region	$U_l(K)$	$U_c(K)$	$\varepsilon_{AAR}^\infty(\%)$	τ_l (days)	τ_c (days)	$\varepsilon_{AAR}^\infty(\%)$	τ_l (days)	τ_c (days)
Early-expansive	Andesite	Japan	-	8440	0.13	0	44.1	0.14	0	10.8
Moderate-expansive	limestone	France	9400	5400	0.2	84	28	-	-	-
	cataclasite	Belgium	-	4870	0.28	90	57.9	0.15	0	20.6
		Ontario	8280	5790	0.22	97	49	0.16	17	14
		Norway	7980	8670	0.48	186.7	172.6	0.18	34.4	22.7
Late-expansive	Chert	Japan	-	10590	0.09	55.8	101.6	0.06	0	13.3
	greywacke	UK	8950	4370	0.39	233	53	0.18	36	21
	gravel	Ontario	8560	4040	0.22	282	97	0.19	46	41
	(grey-wacke, argillite)									
	quartzite	Brazil	-	7390	0.05	0	138.9	0.06	67	29
	granite-gneiss	Brazil	-	4630	0.06	54	104	0.10	72	39
	granite	Brazil	-	5510	0.04	13	74	0.05	82	23
	gravel	UK	5380	8750	0.13	119	211	0.09	38	33
	(quartzitechert)									
	gravel (rhyolite, quartzite)	Norway	13250	12620	0.45	920	399	0.14	55.5	27.5

8.3 Analysis Time Unit (ATU)

Usually, the reference values ($\tau_L(T_0)$ and $\tau_C(T_0)$) are obtained from accelerated tests (such as $T_0 = 38^\circ\text{C}$) and are thus expressed in days. However the structure being analyzed has not only a different temperature but the time increment is more likely to be in weeks, months, quarters, semesters or even years since one is typically seeking the expansion during the structure lifetime (such as 40 or 60 years). Hence, the previously defined latency and characteristic times must be expressed in corresponding time units.

Hence the procedure is as follows:

1. Select lab test temperature T_0 and corresponding latency and characteristic times ($\tau_L(T_0, \text{days})$ and $\tau_C(T_0, \text{days})$) in days.
2. Identify the activation energies U_L and U_C .
3. Select the number of increments per year n . This will correspond to the number of ATU/year.
4. Determine the number of days per ATU

$$DPATU = \frac{365}{n} \quad (8.3)$$

5. Transform the ($\tau_L(T_0, \text{days})$ and $\tau_C(T_0, \text{days})$) expressed in days to corresponding values in ATU ($\tau_L(T_0, ATU)$ and $\tau_C(T_0, ATU)$) from

$$\tau_L(T_0, ATU) = \frac{\tau_L(T_0, \text{days})}{DPTU} \quad (8.4)$$

$$\tau_C(T_0, ATU) = \frac{\tau_C(T_0, \text{days})}{DPTU} \quad (8.5)$$

Note that the computer program will internally compute the latency and characteristic times ($\tau_L(T, ATU)$ and $\tau_C(T, ATU)$) at a given time t and location x, y, z in terms of the user specified parameters.

Example:

1. Assume that one has 12 ATU/year (i.e. one increment every month), then

$$DPU = \frac{365}{12} = 30.42 \text{ days} \quad (8.6)$$

2. $\tau_L(T_0, \text{days})$ and $\tau_C(T_0, \text{days})$ are 66 and 32 days respectively, for $T_0 = 38^\circ\text{C}$, then

$$\tau_L(T_0, ATU) = \frac{66}{30.42} = 2.17 ATU \quad (8.7)$$

$$\tau_C(T_0, ATU) = \frac{32}{30.42} = 1.05 ATU \quad (8.8)$$

3. If at a given Gauss point, and a given time, the temperature is 22.5°C , then internally Merlin will compute

$$\tau_L(T, ATU) = \tau_L(T_0, ATU) \exp \left[U_L \left(\frac{1}{T} - \frac{1}{T_0} \right) \right] = 2.17 e^{[9400(\frac{1}{22.5+273} - \frac{1}{38+273})]} = 10.59 \quad (8.9)$$

$$\tau_C(T, ATU) = \tau_C(T_0, ATU) \exp \left[U_C \left(\frac{1}{T} - \frac{1}{T_0} \right) \right] = 1.05 e^{[5400(\frac{1}{22.5+273} - \frac{1}{38+273})]} = 2.61 \quad (8.10)$$

8.4 AAR; Numerical Modeling

Alkali Silica Reaction or Alkali Aggregate Reactions is a nefarious reaction between the alkali present in the cement and the alkali present in some aggregates. The reaction is sensitive to temperature and relative humidities over 80%, Fig. 8.1, and was first identified by **stanton40**. Whereas countless scientific publications have been written on the subject, a recent work stand out. **larive98** has conducted a monumental work in France which set the ground for modern understanding of the reaction, and has become the driving model for numerical codes. The author's book (**saouma2014AARBook**) does address the numerical modeling of AAR through the finite element method.

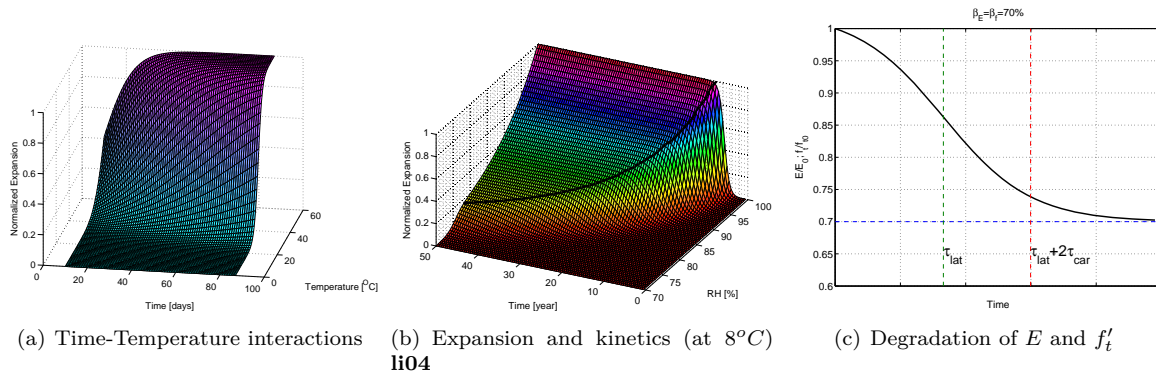


Figure 8.1: Normalized AAR expansion in terms of temperature and relative humidity (**saouma2014AARBook**)

The numerical Modeling of a structure subjected to AAR should proceed as follows:

1. Determine the inside and outside air temperatures and relative humidities over an entire year.
2. Perform a transient linear finite element analyses to determine the temporal and spatial variation of the temperature and the relative humidity inside the container over 3-5 years until a steady state regime

is found.

3. Perform an incremental time history stress analysis which should account for
 - Effect of temperature and RH (the higher, the faster the reaction).
 - Degradation of the tensile strength, elastic modulus, and to a lesser extent compressive strength with time.
 - Effect of stress redistribution: the higher the confinement, the lower the expansion in that direction.
 - Nonlinear response of the concrete.
 - Ability of the concrete to absorb gel produced by the reaction prior to expansion.
4. Extend the analysis until expansion stopped.

Analysis can be facilitated through system identification if field measurement of variables affected by AAR are recorded and can be matched by the analysis through adjustment of key parameters.

The literature is rich in publications reporting the response of a structure subjected to AAR using (dangerous) oversimplification. Matching the observed response with even a poorly formulated model is not difficult as most of them have sufficient variables which can be fine tuned. Hence, the technical committee *Prognosis of deterioration and loss of serviceability in structures affected by alkali-silica reactions* has put together a document to help engineers validate their finite element code (**RILEM-Benchmark-AAR**).

Ultimately, one must answer two critical questions

1. When will the reaction stop.
2. What is the time evolution of the reaction, the accompanying concrete degradation, and structural response. How safe will the structure be as the reaction takes place.

This page intentionally left blank.

Part III

Case Study

This page intentionally left blank.

9 — Problem Definition

9.1 Motivation

Following the extensive review of theory and numerical modeling procedures in Pats I and II, attention is now focused on a specific case study.

It is argued that whereas AAR *per se* may not seriously jeopardize the structural integrity of a nuclear containment vessel structure (NCVS) under vertical service loads, this may not be the case under strong lateral (seismic) loads. Indeed many NCVS do not have shear reinforcements, and AAR has been shown (in the accompanying experimental program) to degrade the shear strength of concrete by as much as 20%.

Hence, driven by the experimental evidence, the numerical simulation of an NCVS will be performed to assess the impact of AAR on its seismic response.

A 3D model of an NCVS, with dimensions inspired from **nureg6706**, will be subjected to 40 years of AAR expansion followed by a seismic excitation.

Results will be compared with the response of an NCVS subjected to the same seismic excitation but without prior AAR volumetric expansion (and accompanying concrete degradation).

9.2 Preliminary Considerations

For the seismic study of the NCVS to be properly performed, one has to mitigate the effects of rocking and ensure radiation damping.

Rocking is caused by the eccentricity of the center of mass that is subjected to the lateral inertial force. It will affect the soil structure interaction by potentially uplifting the base from the rock (specially if vertical excitation is accounted for), and the opening of a gap between the structure and the adjacent rock, Fig. 9.1(a). Another parasitic effect of rocking is the “hammering” of the base resulting along with a (nearly) linear uplift of the foundation base, Fig. 9.1(b).

Since the foundation base has a finite size, elastic waves will be reflected as they cross the boundary. This will cause parasitic increased seismic excitation Fig. 9.2.

These undesirable effects are mitigated by

1. Insertion of zero thickness joint elements around the concrete shell.
2. Insertion of (properly tuned) dashpots around the foundation using the model of **lysmer69**, Refer to Sect. 3.2.
3. A two step analysis procedure. First, the static (including AAR) loads are modeled with vertical supports at the base of the foundation. Then, for the dynamic analysis, those supports are removed and replaced with nodal forces, Fig. 9.3; Refer to Sect. 7.3.1.

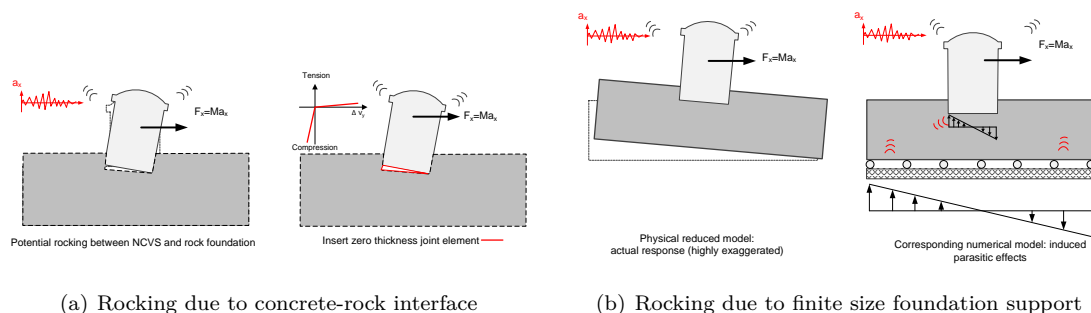


Figure 9.1: Potential rocking in a seismic analysis of a NCVS

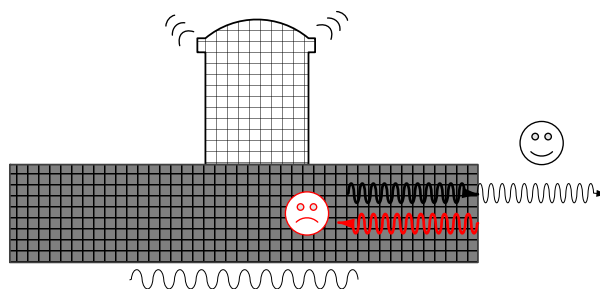


Figure 9.2: Need for radiation damping

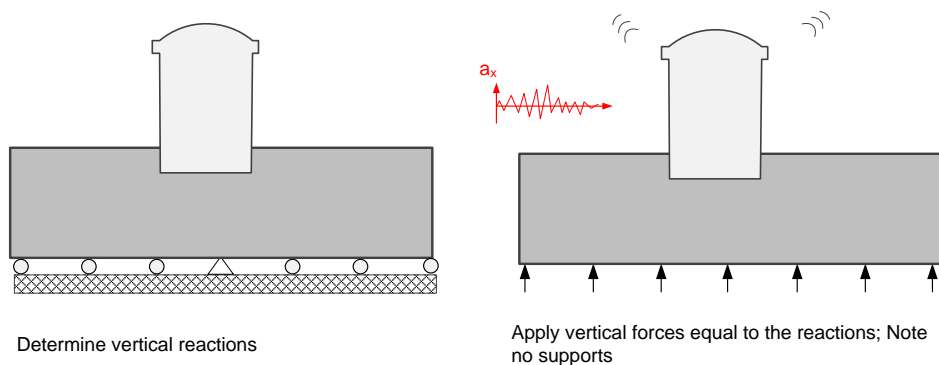


Figure 9.3: Two part analysis to mitigate effect of rocking

9.3 Geometry

The NCVS selected for case study is strongly influenced by the one illustrated in **nureg6706** and is schematically shown in Fig. 9.4.

Note that 56' of the total 122' high cylindrical part is below grade, and only the concrete underneath it will be subjected to AAR (as a result of the high RH likely to be present in the surrounding foundation).

Reinforcement ratios of 0.5% was assumed for both vertical and horizontal directions.

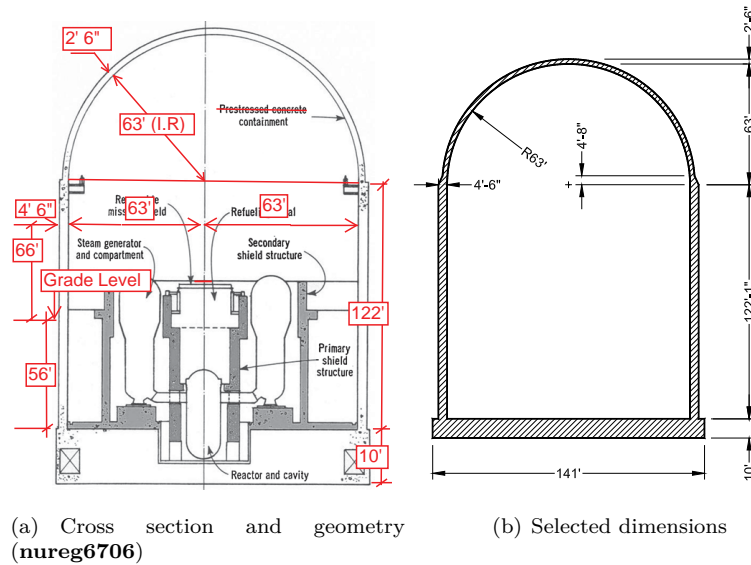


Figure 9.4: Geometry of a generic NCVS

9.4 Finite Element Model

The adopted model for our finite element code Merlin (**merlin**) is shown in figure 9.5(a)¹. The NCVS is 37 m high, has a the base mat 3.0 m thick, and an internal radius of 19.0 m. Potential separation due to rocking is shown in Fig. 9.5(b), and the foundation dimensions is shown in Fig. 9.5(c). Also shown in this last figures are the color coded 15 different material groups described in the next section.

9.5 Material Properties

15 global material groups are defined in the finite element model. More specifically:

Concrete where each of these four types can be linear elastic or nonlinear based on smeared crack model.

- 1 Base mat subjected to AAR as it is likely to be below water table.
- 2 Wall below grade (subjected to AAR as it is likely to be below water table) note two mesh densities are applied to this group.
- 3 Wall above grade without AAR, note two mesh densities are applied to this group.

4-5 Dome. Note that the dome's elastic modulus is increased to reflect the presence of reinforcement. The base is assumed to be linear, whereas the wall and the dome are modeled as nonlinear using the well tested smeared crack model (**cervenka08**) of the finite element code ATENA (**vcervenka2000atena**). Corresponding input data is shown in Table 9.1.

AAR is modeled by the model developed by **saouma-aar-1** and further illustrated in **saouma2014AARBook**.

It is worth mentioning that this possibly the most widely adopted model as it has been implemented in numerous third party codes (including LS-Dyna by NIST), Sect. 8.1. The corresponding properties are shown in Table 9.2.

Rock assumed to be linear elastic with properties shown in Table 9.3.

- 6 Foundation below the base mat.

¹Note that the analysis will use the SI units.

7 Lateral rock surrounding the NCVS.

Interface joints :

8-10 Interface between the base mat and the supporting rock.

9-11 Interface between the wall and the lateral rock.

Reinforcement modeled as elastic perfectly plastic, Table 9.4.

12 Vertical rebar.

13 Horizontal/hoop rebar.

Viscous dampers and springs for seismic analysis

14-15 Viscous dampers applied laterally around the foundation in order to prevent wave reflection according to the model of **lysmer69**

Note that nodal springs: applied on one side of the foundation, along the direction of the seismic excitation

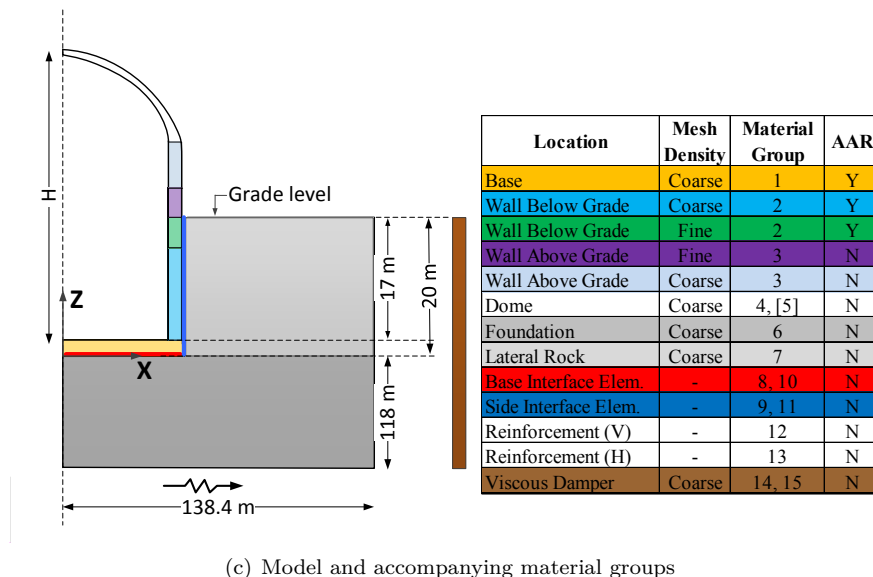
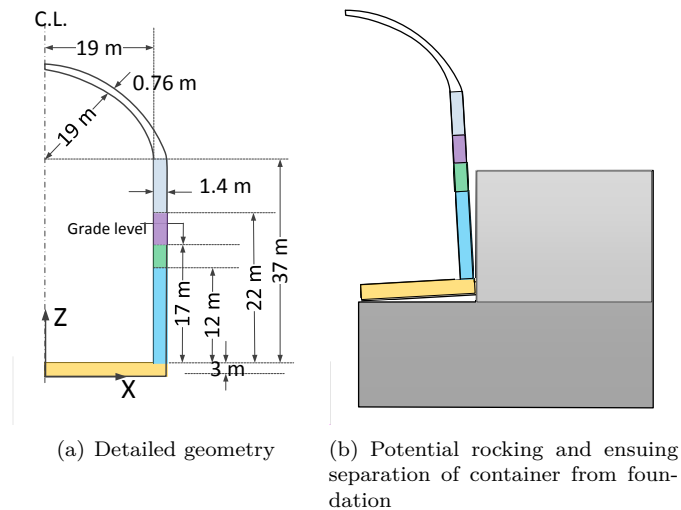


Figure 9.5: Adopted geometry of the generic NCVS

Table 9.1: Concrete mechanical properties

Characteristics	Symbol	Unit	Base	Wall below	Wall above	Dome
Mass density	ρ	Gg/m ³	0.002250	0.002250	0.002250	0.002250
Modulus of elasticity	E	MPa	39,000	39,000	39,000	39,000
Poisson's ratio	ν	-	0.2	0.2	0.2	0.2
Tensile strength	f_t	MPa	3.1	3.1	3.1	3.1
Fracture energy (Exponential softening)	G_F	MN/m	1.2e-4	1.2e-4	1.2e-4	1.2e-4
Compressive strength	f_c	MPa	-31.0	-31.0	-31.0	-31.0
Critical displacement in compression	w_d	m	-0.0005	-0.0005	-0.0005	-0.0005
Factor beta for return direction	β	-	0.0	0.0	0.0	0.0
Factor e for roundness of failure surface	e	-	0.55	0.55	0.55	0.55
Onset of nonlinearity in compression	f_{c0}	MPa	-20.0	-20.0	-20.0	-20.0
Plastic strain at compressive strength	ϵ_{cp}	-	-1e-3	-1e-3	-1e-3	-1e-3

Table 9.2: Characteristics of the ASR model

Characteristics	Symbol	Unit	Base	Wall
Reference temperature	T_0	-	18	18
Maximum volumetric expansion at T_0^{test}	ϵ_{ASR}^∞	-	0.3%	0.3%
Characteristic time at T_0^{test}	τ_C	ATU	64	64
Latency time at T_0^{test}	τ_L	ATU	160	160
Activation energy for τ_C	U_C	-	5,400	5,400
Activation energy for τ_L	U_L	-	9,400	9,400
Residual reduction factor	Γ_r	-	0.5	0.5
Fraction of ϵ_t prior to reduction of ASR expansion due to macro cracking	γ_t	-	0.5	0.5
ASR expansion annealing stress	σ_U	MPa	-8	-8
Post-ASR residual relative Young modulus	β_E	-	70%	70%
Post-ASR residual tensile strength	β_{f_t}	-	70%	70%

Table 9.3: Foundation rock mechanical properties

Characteristics	Symbol	Unit	Foundation rock	Lateral rock
Mass density	ρ	Gg/m ³	0.002600	0.002600
Modulus of elasticity	E	MPa	19,000	19,000
Poisson's ratio	ν	-	0.3	0.3

Table 9.4: rebar mechanical properties

Characteristics	Symbol	Unit	Vertical	Horizontal
reinforcement ratio	ρ	-	0.01	0.005
Modulus of elasticity	E	MPa	200,000	200,000
Poisson's ratio	ν	-	0.3	0.3
Yield stress	σ_Y	MPa	248	248

to prevent rigid body motion. Those do not impact the structural response.

9.6 Finite Element Mesh

3D finite element mesh of the buried container was generated by our pre-processor **kumo**, Fig. 9.6. An attempt was made to generate an “intelligent” mesh with properly graded elements. The elements of the foundation are coarse especially at the region far from the structure (to reduce the total computational effort), whereas the containment itself includes two types of meshes: 1) medium size elements at the base, dome and those area of the wall which are far from the rock grade, and 2) fine elements for the area in vicinity of the rock grade. The reason to use finer mesh in this location is that the structure is usually experiences high shear stresses (due to seismic action) and the damage (if any) is expected to start from this location.

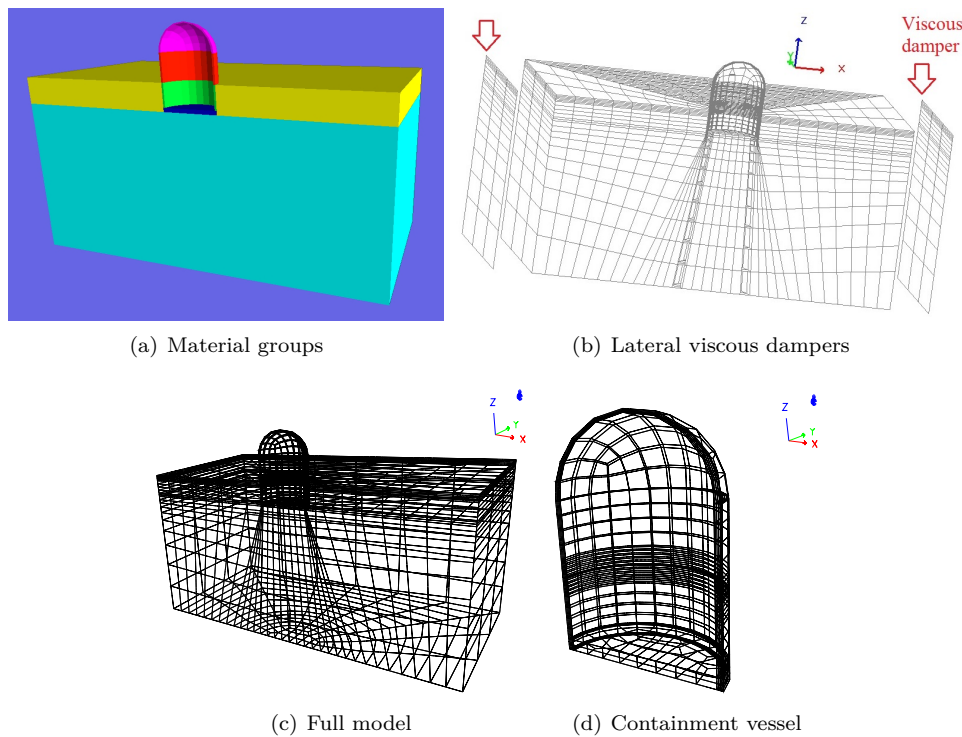


Figure 9.6: Finite element mesh of the NCVS

Reinforcement is modeled as “smeared” by altering the stiffness matrices of those continuum elements they cross. 0.5% reinforcement was assumed in both directions, resulting in the reinforcement shown in Fig. 9.7(a). This was simplified by doubling the spacing of the rebars while maintaining the same reinforcement ratio, Fig. 9.7(b).

9.7 Earthquake Characteristics

Selection of the “right” earthquake record is not a simple task, but the outcome of a sequence of carefully executed steps. Those were followed, to the extent possible, for this analysis, Sect. 2.3:

Site Characteristics It is assumed that the NCVS is located in New Hampshire, USA (coordinates $42^{\circ}53'56''N$ and $70^{\circ}51'03''W$), and the corresponding site conditions are estimated using the *open-*

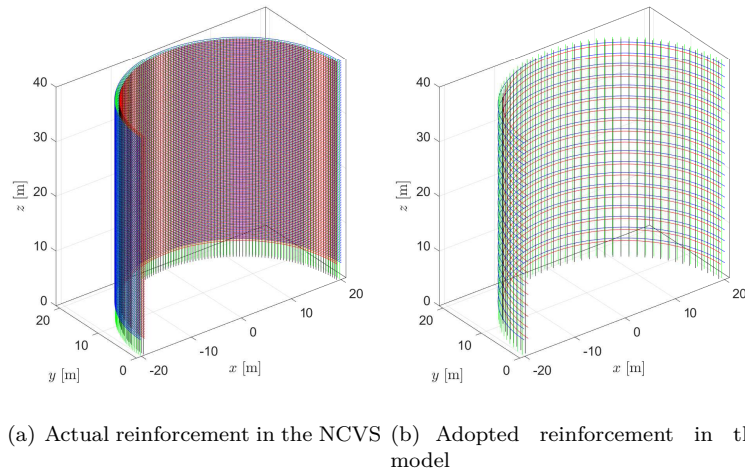


Figure 9.7: Reinforcement details

sha application (**Field2003**) which requires V_{S30} (shear wave velocity 30 m below the surface). This is obtained from the topographic slope site classification map method of **wald2007topographic**. Figure 9.8(a) shows the corresponding V_{S30} at the NCVS site, from which V_{S30} is estimated to be $\simeq 425$ m/s.

Hazard Analysis Seismic hazard is often defined as a natural phenomenon (e.g. ground shaking, fault rupture, or soil liquefaction) that is generated by an earthquake. The term “seismic hazard” in engineering practice is referred to strong ground motions produced by earthquakes that could affect engineered structures (e.g. NCVS). Furthermore, “seismic hazard analysis” refers to the estimation of earthquake-induced ground motions having specific probabilities over a given time period. A probabilistic seismic hazard analysis (PSHA) is initiated by assuming a 50-year earthquake rupture forecast duration (time intervals are usually set to 50 years since hazard maps are represented in 50-year return period)². The 50% probability of exceedance for 50 years return period vs. $S_a(g)$ plots are shown in Fig. 9.8(b) (**Field2003**).

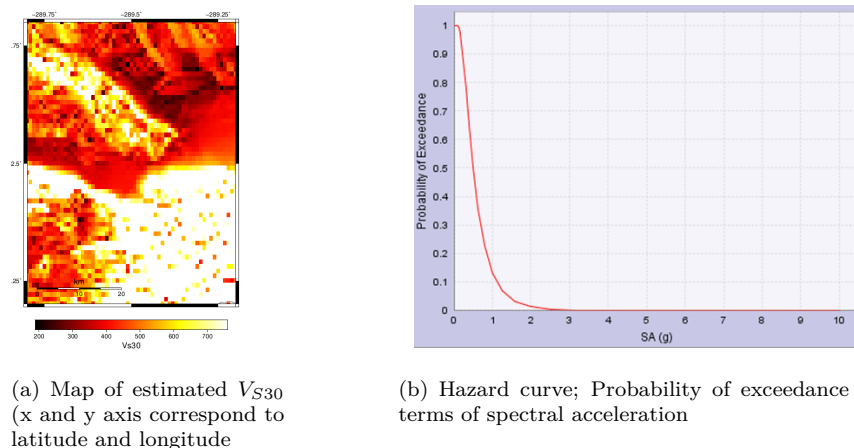


Figure 9.8: Site characterization around the NCVS site

²This choice may not correspond to NRC guidelines for seismic analysis, but is adopted for the sake of illustration.

Seismic hazard de-aggregation Seismic hazard de-aggregation plots provide a clear vision on contribution of the different parameters in record selection process. Also they can be used for the source identification controlling the hazard at the NCVS site. Selection of the ground motions (based on the earthquake magnitude, distance, and inter-event term) using 50%/50yr hazard curve (corresponding to operational base earthquake, OBE), requires seismic hazard de-aggregation plot (probability of occurrence in terms of distance and magnitude of earthquake). Using the USGS 2008 *Interactive Deaggregations service* (USGS2003), the modal distance (R), magnitude (M), and inter-event term (ϵ_0) contributing to the 50%/50yr shaking are computed. Fig. 9.9 shows a PSH de-aggregation seismic hazard plot. This was determined from (<https://earthquake.usgs.gov/hazards/interactive/>). However the site was being upgraded in the Fall 2017, and subsequent results are not exactly the corresponding ones.

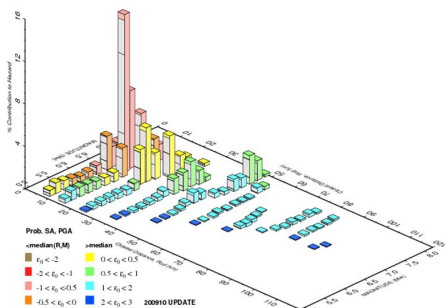


Figure 9.9: Hazard de-aggregation plot

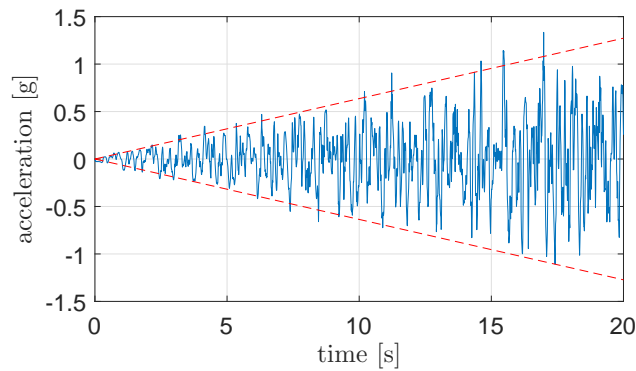
Ground motion is finally selected based on the previous step using the PEER ground-motion database (<http://ngawest2.berkeley.edu/>). As indicated above, the USGS site being deactivated in the Fall 2017, the entire procedure could not be followed, and as a temporary remedial an endurance time acceleration function was used.

Endurance Time Acceleration Function Ideally, multiple analyses with different ground motion excitations should be considered. However, this process being computationally expensive artificially generated acceleration functions are used in this study.

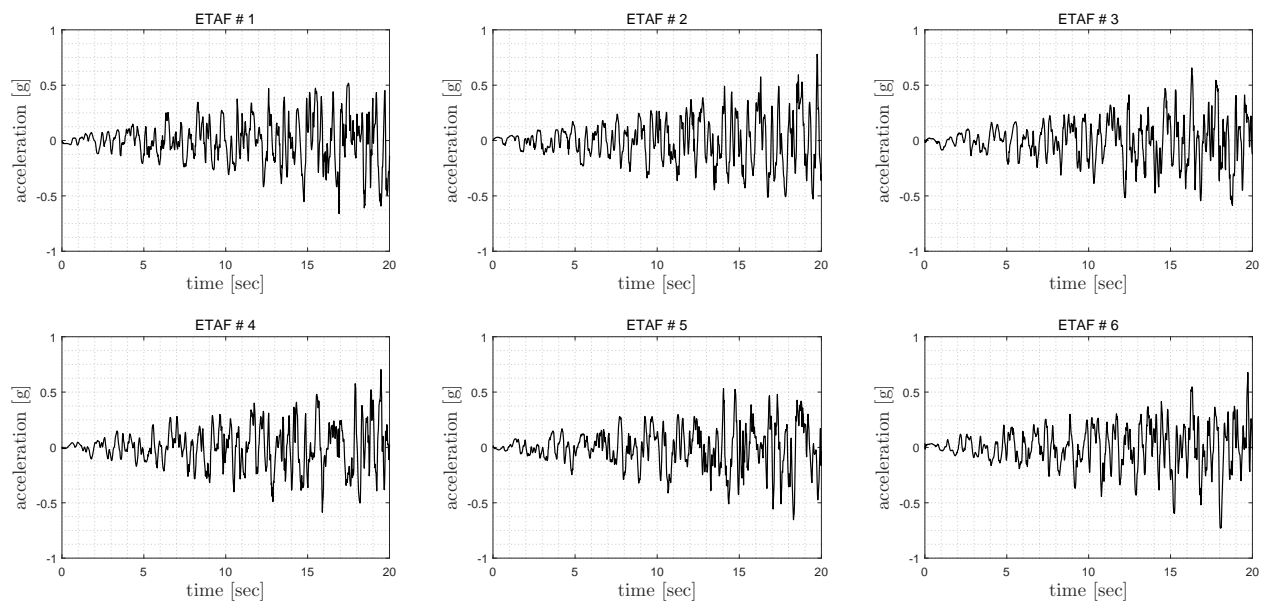
This intensifying inputs which are called endurance time acceleration functions (ETAFs) have a linear profile in time domain. They are constructed based on a stochastic process, so at least three of them are required to reduce the statistical variation. Fig. 9.10(a) shows a sample ETAF including its linear profile. ETAF enables the analyzer to study the response from linear elastic to nonlinear and final collapse of the structure **Hariri2014ES**.

9.8 AAR Volumetric Expansion

It is assumed that the NCVS is operating for 40 years during which it undergoes a relatively mild expansion of 0.3% uniformly distributed over the “contaminated” zone, Fig. 9.11. In actuality, the AAR is not so uniform and is more likely to be “spotty” to reflect the usage of reactive aggregates in some, but not all the pours. This stochastic process is not accounted for in this study. Separate studies by the authors indicate that a sparsely distributed AAR expansion may be more detrimental than a uniformly distributed one (due



(a) Highlighting the linear increase in acceleration



(b) 6 ETAF used in the analyses

Figure 9.10: Sample ETAF (endurance time acceleration functions)

to the induced strain discontinuities).

The 40 years expansion will be simulated in two weeks increments assuming a constant temperature and RH.

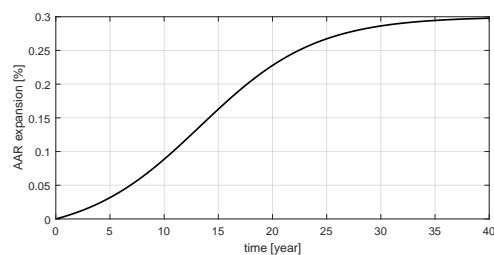


Figure 9.11: Imposed AAR expansion model (kinetics)

The external average temperature at the site is estimated to be 11°C (external face of NCVS), the internal

temperature is in turn estimated to be 25°C . Hence, an average mean yearly temperature of $(25+11)/2 = 18^{\circ}\text{C}$ is assumed.

Note that in a more refined analysis, the temperature distribution across the wall should be considered, and monthly (if not weekly) average temperatures should also be refined.

Finally, the AAR expansion is also a function of the internal RH, and a more refined analysis should take this distribution across the wall.

9.9 Index Points

The structural response of the NCVS will be assessed through the (relative) displacements and stresses (engineering demand parameters) of seven index points shown in Fig. 9.12. Displacements are reported as relative to index point # 1 (at the bottom of the base mat).

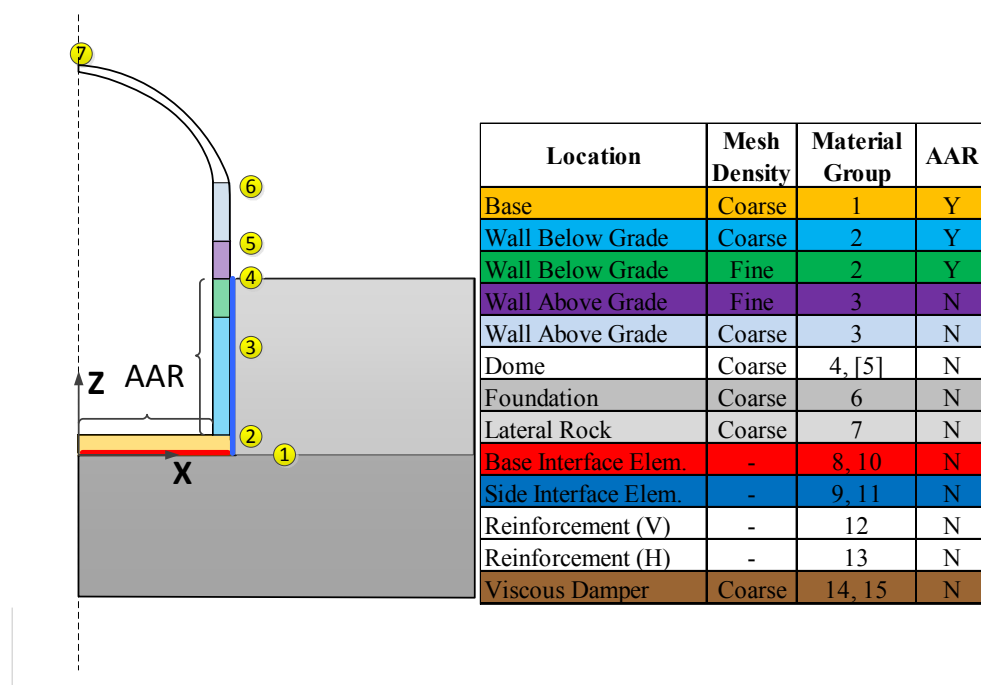


Figure 9.12: Index points to extract the displacement response

10 — Results of Analyses

10.1 Introduction

Results of the previously described analyses will be presented next. Four sets of analyses will be performed:

1. Static
2. Static + AAR
3. Static + Dynamic
4. Static + AAR+ Dynamic, Fig. 10.1.

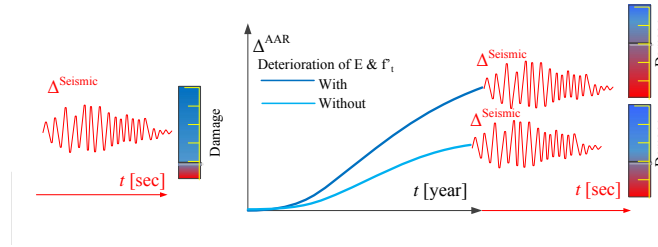


Figure 10.1: Schematic representation of analysis to be performed.

Though a very thorough analysis will be conducted, it is performed for the model previously described and the reader should be cautioned not to (yet) generalize those results to other similar NCVS.

10.2 Analyses

10.2.1 Static Analysis

This is the first initial analysis in which the NCVS is simply subjected to the self weight to ascertain the modeling assumption before a more complex analysis is performed. First a linear elastic analysis is performed, then a non-linear one. The non-linear response could be caused by either concrete cracking, or slip/opening of the joints wrapped around the NCVS.

Figure 10.2 shows the results of the nonlinear static analysis. Contour plot of vertical displacement shows a smooth displacement variation in the containment structures along with a gradual transfer of forces to the foundation.

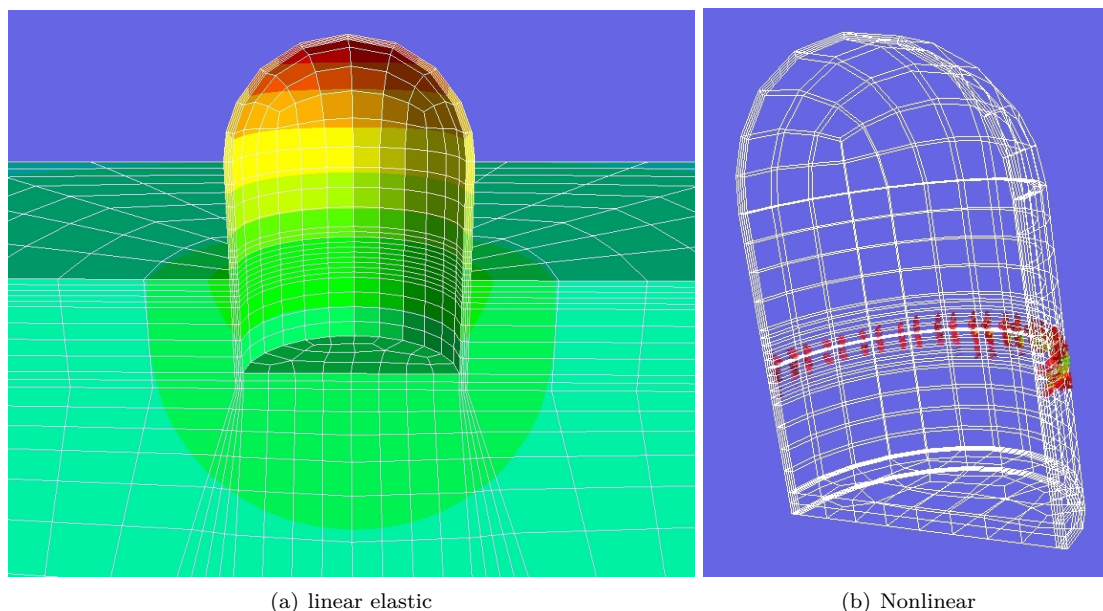


Figure 10.2: NCVS response: Static analysis

10.2.2 Static + AAR Analysis

In this second analysis, the preliminary static (dead load) analysis, is followed by the simulation of 40 years of AAR in the contaminated zone.

Swelling of the container is shown in Fig. 10.3(a) along with a closeup on the concrete-rock separation.

1. The base mat swells, but is restrained in its expansion by the cylindrical vessel, Fig. 10.3(a).
2. The wall is pushing against the adjacent rock, but is constrained by both the base mat and the upper segment of the container which does not expand, Fig. . This results in strong curvature, joint opening, and discontinuities with ensuing separation and stresses, Fig.
3. Sliding of the NCVS

10.2.3 Static + Seismic Analysis

In this analysis, the seismic analysis is performed right after the static one, i.e. there is no AAR and is used to assess the subsequent impact of AAR. As previously indicated, the seismic analysis is performed following the static one using the **restart** option of the code Merlin (**merlin**) which will safeguard the internal variables of the static analysis as it starts the dynamic one.

Fig. 10.4(a) shows a plot of NCVS and foundation deformation under the seismic excitation. Also, Fig. 10.4(b) shows the regions with high stress concentrations. As expected, the base and the the wall region near the ground level. This is confirmed with the smeared crack model as shown in Fig. 10.4. Note that this is a snapshot taken around the PGA, and a maximum stress of about 6 MPA is recorded.

10.2.4 Static + AAR + Seismic

In this last study, the NCVS is sequentially subjected to static, then AAR, and finally a ground acceleration (through the ETAF approach described above). FOr the AAR portion, two sub-cases where considered:

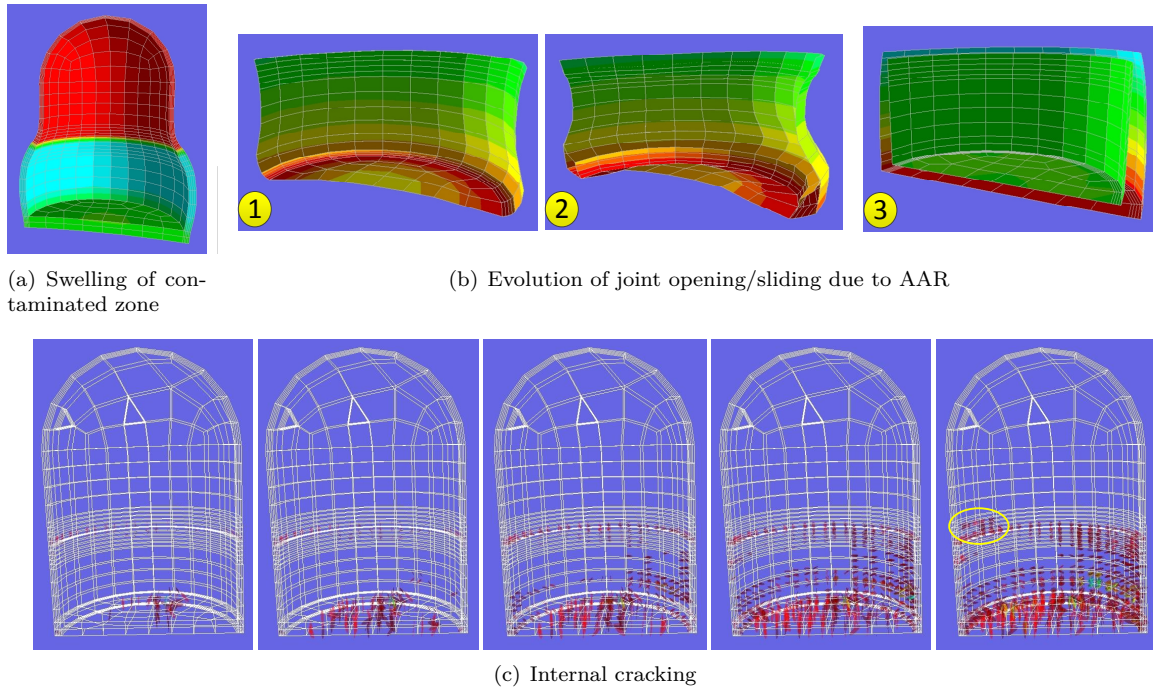


Figure 10.3: Response of NPP under AAR analysis

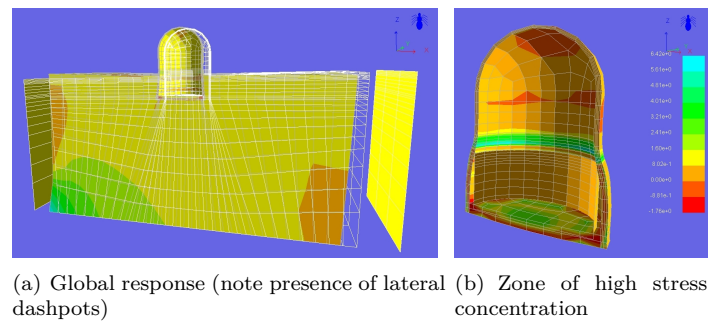


Figure 10.4: Seismic response without AAR

one with the normally anticipated E and f'_t degradations, and the other one with swelling only and no degradation.

For each of the three main models, six analyses with six different ETAFs are performed (to reduce the statistical dispersion of the results). Results associated with these analyses are not shown separately, but contrasted with the analysis scenario where AAR is not factored in.

10.3 Impact of AAR on Seismic Response of a NCVS

10.3.1 Results

The impact of AAR on the structural response of a NCVS can now be ascertained by comparing Static + Seismic and Static + AAR + Seismic for:

Displacements: The absolute value of the (horizontal) displacements corresponding to peaks in (the six) ETAF case are shown in Fig. 10.5(b). This is a ramping curve as the ground acceleration is indeed defined as a linearly increasing one (Fig. 9.10(a)). Three sets of results are shown:

1. Ground motion without AAR
2. AAR with accompanying material degradation followed by ground motion.
3. AAR without material degradation followed by ground motion.

To better ascertain the impact of AAR, responses are normalized with respect to the analysis without AAR (ground motion only), Fig. 10.5(c).

It should be noted that the displacements are all plotted as ETA functions (expression of the maximum absolute values of EDP during the time interval from 0 to t , Fig. 10.5(a), in terms of time.

$$\Omega(\text{EDP}(t)) \equiv \max \{ \text{Abs}(\text{EDP}(\tau)) : \tau \in [0, t] \} \quad (10.1)$$

Thus, an ETA function increases with time in EDP-time coordinate system. Failure in this function corresponds to a (semi-) vertical line at $t = t_{\text{failure}}$.

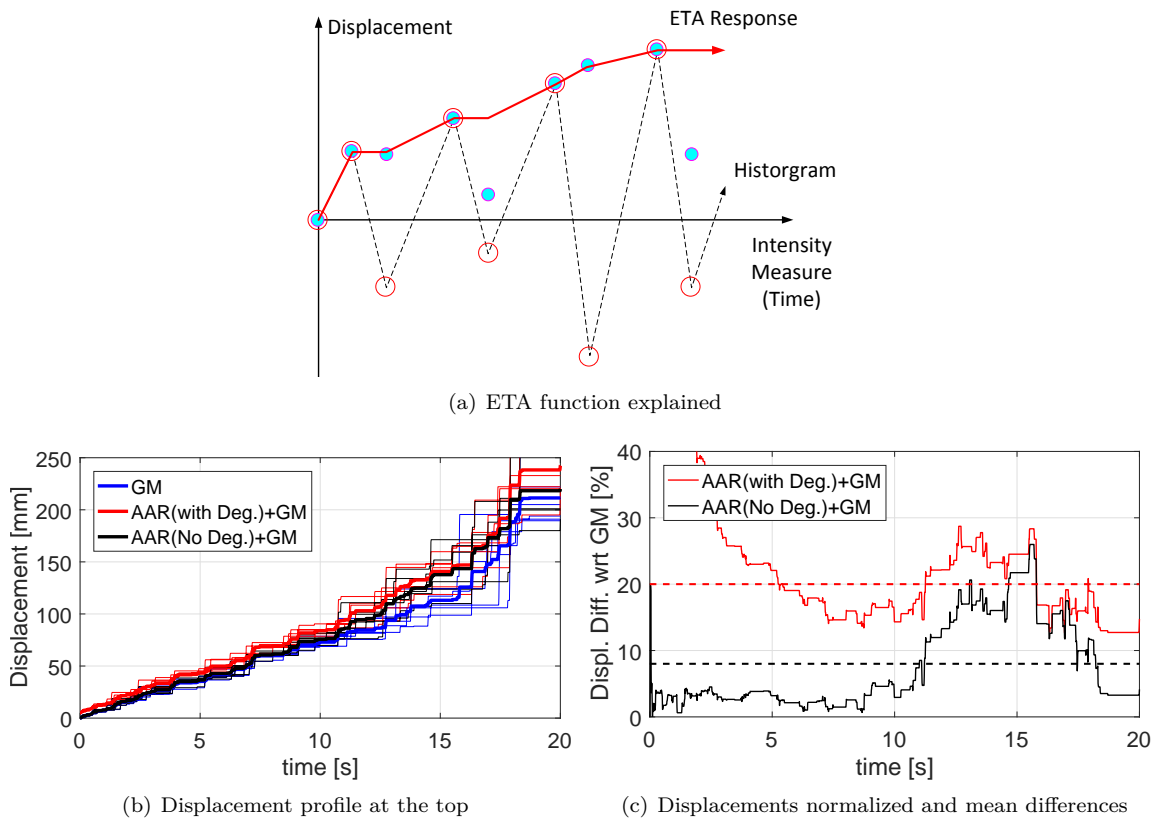


Figure 10.5: Response of NCVS under AAR and seismic

Stresses Histogram of maximum principal stresses are shown in Fig. 10.6 for various index points (Fig. 9.12) locations. Results are shown for ground motion only without AAR (in blue), and AAR (with degradation) followed by ground motion.

Cracking of the structure is shown Fig. 10.7.

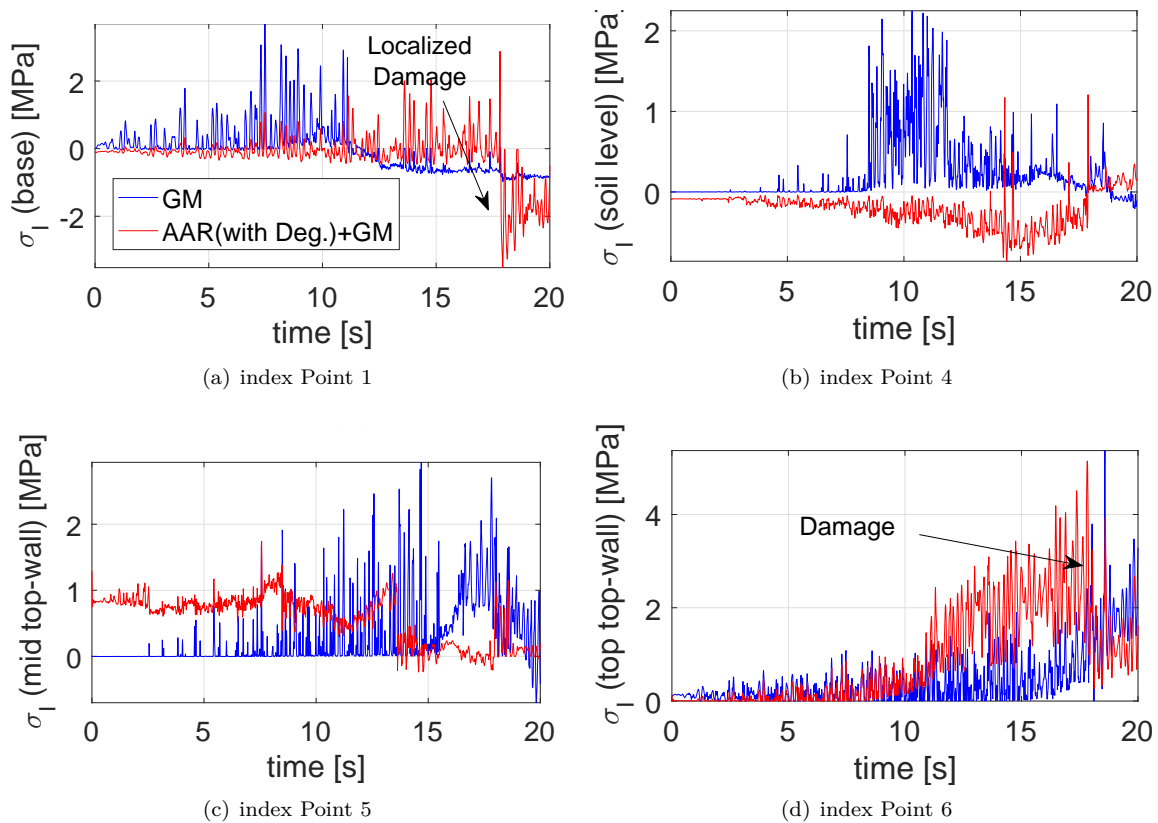


Figure 10.6: Principal stress time histories from seismic analysis

10.3.2 Observations

From the previous figures summarizing the results, the following observations can be made:

1. AAR (with material degradation) will soften the concrete resulting in lower lateral displacements.
2. If material degradation is ignored (which is an erroneous abstraction) displacements are still lower than those cases without AAR, but greater than AAR with degradation. Note that discrepancy with respect to the case without AAR starts at around 9 sec. (i.e until this point the AAR had little impact on deformation)
3. The impact of AAR (with and without degradation) is time dependent due to the complexities of the internal stress states induced by it or resulting from the seismic excitation, Fig. 10.5(c). On average, and for this case study, AAR with degradation results in 20% change, whereas the case without degradation in only 8% variation with respect to the “GM” model.
4. The principal maximum stress history profile sat various locations, Fig. 10.6, show that additional damages will be induced by the AAR (with internal damage accounted for).
 - (a) At the base, Fig. 10.6(a) max principal stresses are indeed positive, attenuate with time. Stresses are at first lower when there has been AAR expansion, but then suddenly increase with a localized damage at time $\simeq 17$ sec.
 - (b) At the grade elevation, stresses are much higher without AAR, and then gradually decrease with no indication of failure. Note that the tensile strength is 3.1 MPa. On the other hand, in the presence of prior AAR expansion, the stresses are negative, and a sudden localized failure appears

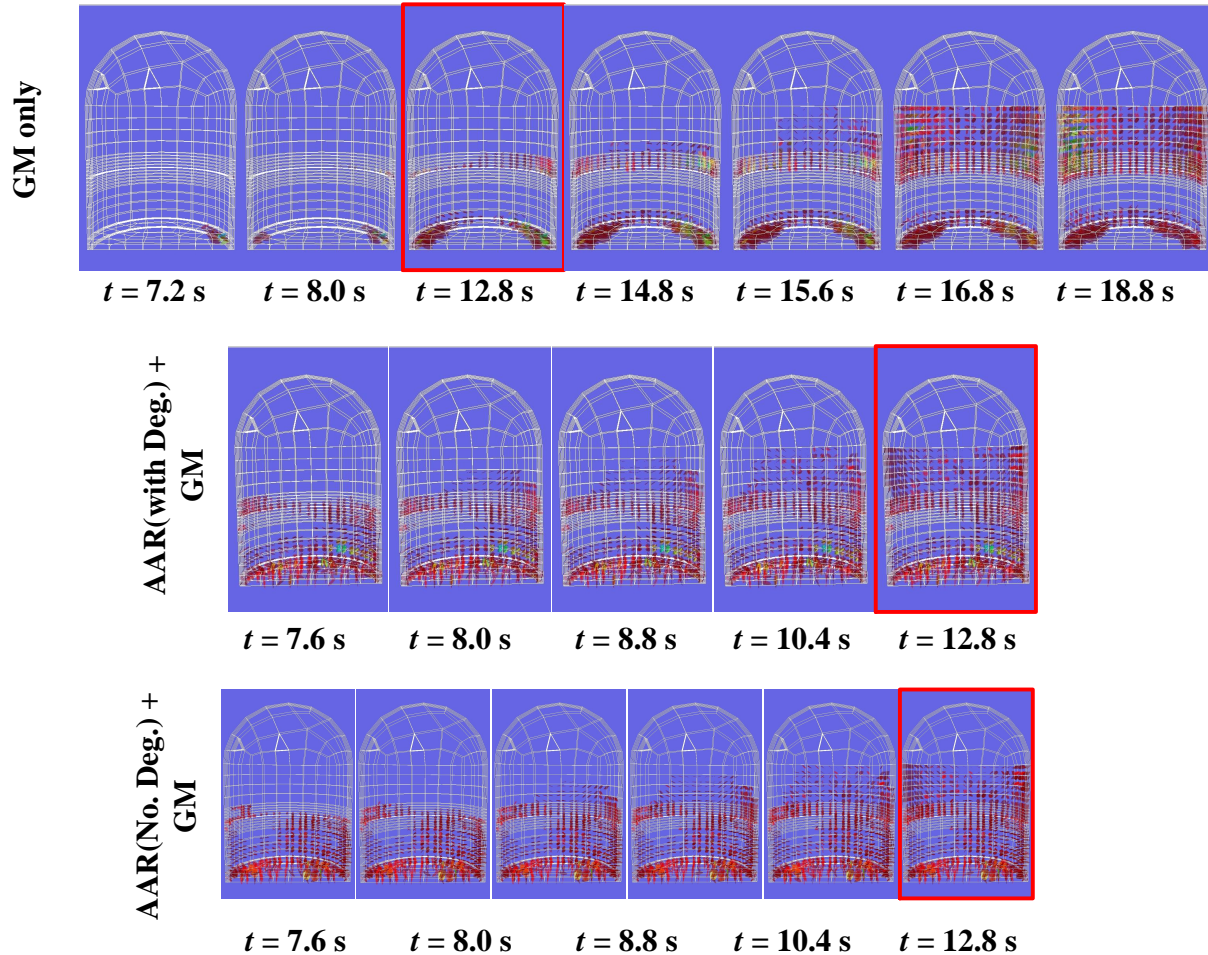


Figure 10.7: Crack profile from seismic analysis

at $t = 14$ sec.

- (c) For a point above grade, stresses are higher in the absence of AAR and there is indication of a localized failure at $t = 15$ sec. In the presence of AAR, the failure is delayed to about 17 sec.
 - (d) At the base of the dome, the AAR stresses are substantially higher than without and localized failure occurs around 17 sec.
5. For this case, AAR has reduced the stresses at the base, but substantially increased them at the base of the dome.
 6. The previous observations are qualitatively confirmed by the crack profiles shown in Fig. 10.7. Indeed, the damage index (DI), ratio of the cracked sections to the total area, is highest when AAR (with damage) preceded the seismic expansion.
 7. The AAR has a much higher impact of that portion of the NCVS below grade than above (where no AAR is modeled).

10.4 Conclusions

For this particular study, AAR will reduce the resilience of a NCVS subjected to a seismic excitation by approximately 20%.

It should be noted that this reduction, associated with 0.3% localized uniform expansion is about equal to the reduction of shear strength experimentally observed for expansions about 0.5

This page intentionally left blank.

11— Conclusions

11.1 Summary

This report is composed of two parts. First an extensive State of the Art survey of the theoretical, numerical, and modeling issues pertaining to the modern simulation of NCVS is presented.

This included:

1. Introductory remarks addressing the challenges of modern structural safety assessment of NCVS.
2. Soil structure interaction, including deconvolution, radiation damping and far field modeling.
3. Alkali-Silica Reaction focusing on the author model that has been copied and implemented by many.
4. Elements of probability.
5. Structural and Seismic modeling.
6. Non-linear modeling of concrete.

The second part included a case study of a NCVS with realistic dimensions suffering from AAR and then subjected to a strong seismic excitation. To the best of our knowledge, this is (by far) the most comprehensive and rigorous such analysis reported.

Results show that a moderate 0.3% expansion uniformly localized in that portion of concrete below grade will reduce the resilience by about 20%.

To some extent, this document can be viewed as a natural and modern extension of **nureg6906**. It is the wish of the author that it could also be published as a NUREG after some revisions.

11.2 Recommendation for Future Work

Whereas the study was quite complete and comprehensive (within the time and budgetary constraints), it would be desirable to repeat this analysis with the following additional considerations:

1. Random distribution of the AAR contaminated concrete to better reflect an actual case.
2. Deconvolution.
3. Stochastic analysis resulting in fragility curves

This page intentionally left blank.

Index

- AAR
 - Cracking, [93](#)
 - Compression, [94](#)
 - Tension, [93](#)
 - FEM Validation, [100](#)
 - Humidity, [95](#)
 - Hydrostatic Stress, [88](#)
 - Impact on Seismic, [171](#)
 - Kinetics, [85](#)
 - Model
 - Coupled, [81](#)
 - Retardation, [88](#)
 - Saouma's Model, [84](#)
 - Strain, [96](#)
 - Redistribution, [97](#)
 - Temperature, [86](#)
 - Sensitivity, [87](#)
 - Time, [88](#)
- AAR Analysis Requirements, [83](#)
- AAR Material Properties, [151](#)
- AAR Model
 - Coupled Chemo Mechanical, [81](#)
 - Meso, [81](#)
 - Empirical, [81](#)
 - Micro, [81](#)
- AAR model requirements, [83](#)
- Abaqus, [113](#)
- Activation Energies, [86](#)
- Activation energies, [88](#)
- Activation Energies, [152](#)
- Alkali Aggregate Reactions, [154](#)
- Alkali Silica Reaction, [154](#)
- Allowable Stress Design (ASD), [3](#)
- Analysis
 - Static, [169](#)
 - Static+AAR, [170](#)
 - Static+AAR+Seismic, [170](#)
 - Static+Seismic, [170](#)
- Analysis Time Unit (ATU), [153](#)
- Arbitrary Time Unit, [152](#)
- Arrhenius, [85](#)
- ASD, [3](#)
- ATENA, [113](#)
- Benchmarks, [83](#)
- Buried Container, [164](#)
- Butterworth Filter, [52](#)
- Calibration, [113](#)
- Calibration Experiment, [113](#)
- Capacity, [3](#)
- Capacity Function, [125](#)
- Capacity Functions, [35](#)
- Challenges, [2](#)
- Characteristic time, [85](#)
- Cloud Analysis, [134](#)
- Code Verification, [113](#)
- Codes
 - Philosophy, [2](#)
- Computer Model, [113](#)
- Conceptual Model, [113](#)
- Concrete
 - Fracture Energy, [111](#)
 - Concrete Creep Coefficient, [111](#)
 - Concrete Degradation, [155](#)
 - Concrete Elastic Modulus, [111](#)
 - Concrete Strength
 - Compressive, [111](#)
 - Tensile, [111](#)
 - Concrete-Rock Interface, [143](#)
- Confidence, [114](#)

- Correlation Matrix, [133](#)
- Crack, [93](#)
 - Discrete, [120](#)
 - Smeared, [122](#)
- Cracks, [94](#)
- Creep, [83](#)
- Damage Index, [36](#)
- Dams, [96](#)
- Data Gathering, [106](#)
- Data Mining, [107](#)
- De-aggregation, [166](#)
- Deconvolution
 - 1D, [54](#)
 - 3D, [55](#)
 - Application, [139](#)
 - Simplification, [55](#)
- Demand, [3](#)
- Design Codes, [5](#), [6](#)
 - Limitations, [7](#)
 - Need for New One, [7](#)
- Deterioration, [100](#)
- Dilatancy, [122](#)
- Discrete Crack, [123](#)
- Elastic Waves, [159](#)
- Endurance Time Acceleration Functions, [166](#)
- Endurance Time Analysis, [134](#)
- Engineering Demand Parameter, [124](#), [125](#), [136](#)
- Error, [114](#)
- Excel, [133](#)
- Expansion Rate, [84](#)
- Experiment, [114](#)
- Experiment Revision, [114](#)
- Experimental Data, [114](#)
- Experimental Outcomes, [114](#)
- Fidelity, [114](#)
- Field Experiment, [114](#)
- Finite Element
 - Assessment of Results, [107](#)
 - Convergence, [109](#)
 - Linear or Quadratic, [108](#)
 - Loads and B.C., [109](#)
 - Material Nonlinearity, [116](#)
 - Material Properties, [110](#)
 - Mesh Verification, [109](#)
 - Modeling, [105](#)
 - Modelling, [107](#)
 - Problem Definition, [105](#)
 - Shape Functions, [109](#)
 - Software Selection, [112](#)
 - Structured-Unstructures Meshes, [109](#)
 - Study, [107](#)
 - Tabulation Loads, [110](#)
- Finite Element Mesh, [164](#)
- First invariant, [93](#)
- Foundation Support, [143](#)
- Fourrier Transform, [52](#)
- Fracture Energy, [119](#)
- Fracture Process Zone, [119](#)
- Fracture Toughness, [118](#)
- Fragility Analyses, [38](#)
 - Analytical, [43](#)
 - Continuous Function, [40](#)
 - damage probability matrix, [40](#)
 - EDP-based, [45](#)
 - Empirical, [42](#)
 - Experimental, [42](#)
 - Fragility Curve, [38](#)
 - Fragility surface, [38](#)
 - Generalized Linear Models, [43](#)
 - Heuristic, [42](#)
 - Hybrid, [43](#)
 - IM-based, [45](#)
 - Lognormal, [44](#)
 - Treatment of Collapse, [42](#)
 - Vulnerability, [39](#)
- Fragility Curve, [4](#)
- Fragility Curves, [123](#)
- Fragility Curves, [4](#)
- Fragility Function, [125](#)
- Fragmented Knowledge, [6](#)
- Gentilly 2, [78](#)
- Geometric Nonlinearity, [5](#)
- Grizzly, [113](#)
- Ground Motion, [166](#)

- Ground Motion Intensity Measures, 136
- Hammering, 159
- Hazard Analysis, 17
 - Annual Rate of Exceedance, 22
 - Attenuation Relationships, 19
 - Deterministic Hazard Analysis, 20
 - Directivity, 20
 - Geotechnical Effects, 19
 - Ground Motion Scaling, 24
 - Ground Motion Selection, 25
 - Hazard Curves, 20
 - Intensity Measure, 26
 - Poisson Probability Model, 22
 - Probabilistic Hazard Analysis, 20
 - Seismic Environment, 18
 - Seismic Hazard De-aggregation, 23
 - Site, 18
 - Target Acceleration Response Spectra, 23
- Humidity, 95
- Hydrostatic stress, 88
- Ikata, 77
- Incremental Dynamic Analysis, 134
- Index Points, 168
- Inference, 114
- Initial AAR Strain, 82
- Integration Schemes, 117
- Intensity Measure, 124
- Irreducible Uncertainty, 114
- Joint Elements, 145
- Laboratory Experiment, 114
- Lack of Guidance, 6
- Latency And Characteristic Times, 152
- Latency time, 85
- Lateral Rigid Body Motion, 142
- Latin Hypercube Sampling, 133
- LCPC, 81
- Life Extension, 77
- Limit State, 108, 123, 125
- Load Resistance Factor Design (LRFD), 3
- Loads
 - Beyond Design Basis, 6
 - Point, 109
- LRFD, 3
- Macro, 81
- Material Nonlinearity, 5
- Mathematical Model, 107
- Mathematical Model, 114
- Merlin, 113
- Modal Analyses, 108
- Model, 114
- Model Complexity, 108
- Model Revision, 114
- Monte Carlo Simulation, 133
- Multiple Stripe Analysis, 134
- Newton-Raphson, 117
- NOAA, 87
- Nondeterministic Method, 114
- Nonlinear Analysis, 5
- Numerical Integration
 - Explicit, 117
 - Implicit, 117
- NUREG
 - 0980, 77
 - 6706, 160
 - 6906, 177
- PBEE, 4, 13
 - 1st Generation, 14
 - 2nd Generation, 15
 - IBPA, 16
 - PBA, 13
 - PBE, 13
 - PBSD, 13
 - PEER, 15
 - SBPA, 16
 - SEAOC, 13
 - TBPA, 16
 - Triple Integral, 15
- Performance Based Engineering, 3
- Performance Model, 114
- Politecnico di Milano, 82
- Prediction, 114

- Predictor, Corrector, [117](#)
Pretest Calculations, [114](#)
Probabilistic Performance Assessment Of Structures, [127](#)
Probability Distribution Function, [125](#)
Pushover Analysis, [108](#)

Quasi-brittle, [119](#)

Reality Check, [107](#)
Reality Of Interest, [114](#)
Reducible Uncertainty, [114](#)
Response, [124](#)
Response Spectrum, [108](#)
Retardation, [93](#), [94](#)
Risk, [114](#)
Risk Informed Conditional Assessment, [124](#)
Risk Tolerance, [114](#)
Rock-Rock, [145](#)
Rocking, [143](#), [159](#)

Safety Factor, [3](#)
Sanity Check, [106](#)
Seabrook, [78](#)
 Finite Element Analysis, [80](#)
 Root Cause, [79](#)
Second License Renewal, [2](#)
Seismic Analysis, [129](#)
Seismic Hazard, [165](#)
Seismic Study, [159](#)
Sensitivity Analyses, [123](#)
Sensitivity and Uncertainty Quantification, [26](#)
 Correlation, [30](#)
 Monte Carlo Simulation, [29](#)
 Sensitivity, [27](#)
 Spatial, [30](#)
 Temporal, [30](#)
 Tornado diagram, [28](#)
 Uncertainty, [28](#)
Simulation, [114](#)
Simulation Outcome, [114](#)
Single Ground Motion, [134](#)
Singularities, [115](#)
Site Characteristics, [164](#)

Smeared Crack, [123](#)
Softening, [108](#), [119](#)
Soil-Structure, [145](#)
Stressor, [124](#)
Structural Analyses, [31](#)
 Cloud Analysis, [32](#)
 Endurance Time Analysis, [34](#)
 Incremental Dynamic Analysis, [32](#)
 Multiple Stripe Analysis, [34](#)
System Identification, [155](#)

Thermal Analysis, [111](#)
Time, [88](#)
Tornado Diagram, [124](#)
Toulouse, [82](#)
Transfer Function, [53](#)
Transient Analysis, [108](#)
Two Step Analysis, [140](#)

Uncertainty, [114](#)
Uncertainty Analyses, [124](#)
Uncertainty Analysis, [129](#)
Uncertainty Quantification, [115](#)

Validation, [113](#)
Validation Experiment, [115](#)
Validation Metric, [115](#)
Verification, [113](#)
Volumetric strain, [96](#)

Wave Equation, [56](#)
Weakest Link, [108](#)
Wedge Splitting Tests, [120](#)
Weight, [96](#)

12 — Acronyms

AAR Alkali-Aggregate Reaction	6
NPP Nuclear Power Plant	77
NCS Nuclear Containment Structure	2
NRC Nuclear Regulatory Commission	2
RC Reinforced Concrete	6
SIT Structural/System Integrity Test	109